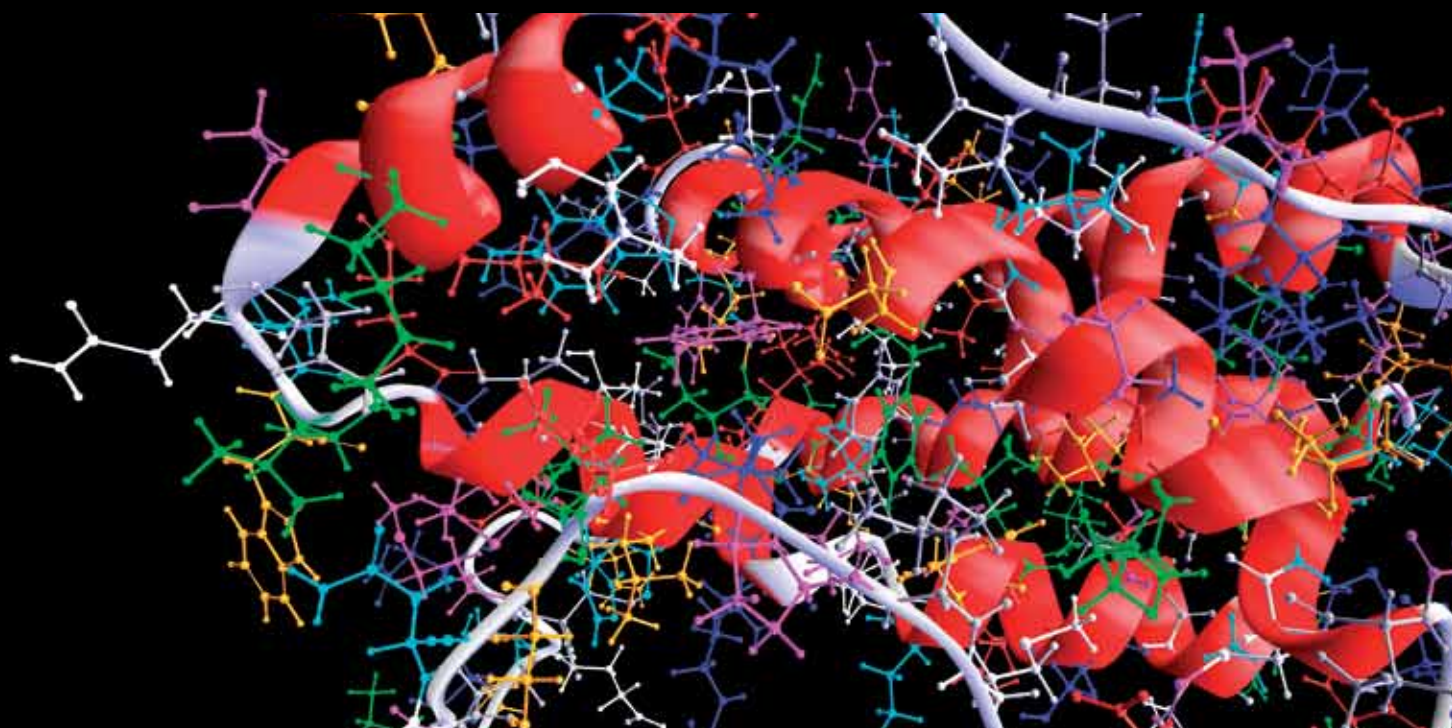# Computational Methods in Neuroengineering

Guest Editors: Chang-Hwan Im, Lei Ding, Yiwen Wang, and Sung-Phil Kim

Computational Methods in Neuroengineering

Computational Methods in Neuroengineering

Guest Editors: Chang-Hwan Im, Lei Ding, Yiwen Wang, and Sung-Phil Kim

Editorial Board

Contents

Editorial

Computational Methods in Neuroengineering

Chang-Hwan Im,[1] Lei Ding,[2] Yiwen Wang,[3] and Sung-Phil Kim[4]

[1] *Department of Biomedical Engineering, Hanyang University, 222 Wangsimni-ro, Seongdong-gu, Seoul 133-791, Republic of Korea*

[2] *School of Electrical & Computer Engineering, University of Oklahoma, Norman, OK 73019-1023, USA*

[3] *Qiushi Academy of Advanced Studies, Zhejiang University, Hangzhou 310027, China*

[4] *Research and Business Foundation, Korea University, Seoul 136-713, Republic of Korea*

Correspondence should be addressed to Chang-Hwan Im; ich@hanyang.ac.kr

Neuroengineering is an emerging discipline in the field of medical and biological engineering with the aim of understanding, modulating, enhancing, or repairing neuronal systems, which are obviously the most complex systems of the human body. During the last decade or so, neuroengineering has been growing rapidly and expanded its applications from interpreting and processing neuronal signals to interfacing the neural systems with external devices to restore lost functions. Despite its short history, neuroengineering has now become one of the most important topics in the current biomedical engineering research. As in other interdisciplinary fields, computational methods have played key roles in the development of neuroengineering.

Considering the aforementioned trends, it seems natural that neuroengineering is selected as the theme of this special issue. This special issue includes eleven high-quality, peer-reviewed articles that might provide researchers in the field of neuroscience, engineering, psychology, and computational sciences with the current state-of-the-art knowledge of this emerging interdisciplinary research field.

The paper "*Trial-by-trial adaptation of movements during mental practice under force field*" by M. N. Anwar and S. H. Khan studied how motor imagery influences trial-to-trial learning in a robot based adaptation task. The results showed that reaching movements performed with motor imagery have relatively a more focused generalization pattern and a higher learning rate in training direction.

The paper "*Evaluation of EEG features in decoding individual finger movements from one hand*" by R. Xiao and L. Ding investigates the existence of a broadband feature in EEG to discriminate individual fingers from one hand, with the significantly higher average decoding accuracy than guess level by the spectral principal component analysis (PCA).

The paper "*Coercively adjusted auto regression model for forecasting in epilepsy EEG*" by S.-H. Kim et al. proposes a coercively adjusted auto regression (CA-AR) method to forecast future values from a multivariate epilepsy EEG time series with higher accuracy and improved computational efficiency.

The paper "*A mixed L2 norm regularized HRF estimation method for rapid event-related fMRI experiments*" by Y. Lei et al. presents a new regularization framework to identify trial-specific BOLD responses in extremely rapid event-related fMRI experiments, where BOLD responses are heavily overlapped from adjacent trials. It is demonstrated that the technique significantly improves the classification accuracy in decoding brain tasks in a rapid four-category object classification experiment.

The paper "*Development of the complex general linear model in the Fourier domain: application to fMRI multiple input-output evoked responses on single subjects*" by D. E. Rio et al. describes a statistical time series analysis in the Fourier domain based on a linear time invariant model to process multivariate data from fMRI experiments, particularly for single subjects.

The paper "*Continuous- and discrete-time stimulus sequences for high stimulus rate paradigm in evoked potential studies*" by T. Wang et al. suggests using continuous-time stimulus sequences for the high stimulus rate paradigm to obtain auditory evoked potentials (AEPs) from

electroencephalography (EEG). Both the analytic results and simulation experiments revealed the advantages of using the continuous-time sequences over traditional discrete-time sequences in terms of the reliability of reconstructed AEPs.

The review paper "*A review on the computational methods for emotional state estimation from the human EEG*" by M.-K. Kim et al. summarizes the state-of-the-art computational methods used to extract features for emotional states from EEG signals and to classify those features into one of many emotional states. The readers of the journal would find this review helpful for understanding how mathematical methods are employed for affective computing based on EEG.

The paper "*Information analysis on neural tuning in dorsal premotor cortex for reaching and grasping*" by Y. Cao et al. investigates the contribution of the dorsal premotor cortex (PMd) in reaching and grasping experiments with monkeys. It is identified that, within PMd, there are neurons that only engage in reaching, neurons that only engage in grasping, and neurons that engage in both. This phenomenon is further validated in a decoding experiment using different sets/subsets of neurons in PMd.

The paper "*Modiolus-hugging intracochlear electrode array with shape memory alloy*" by K. S. Min et al. presents a novel intracochlear electrode which can deliver a more efficient electrical stimulation in human cochlea to aid people with a severe hearing loss. They propose to use a shape-memory-alloy embedded electrode to reduce the distance between the electrode and the target cells.

The paper "*Corticomuscular coherence analysis on hand movement distinction for active rehabilitation*" by X. Lou et al. evaluated corticomuscular coherence (CMC) between EEG and EMG signals recorded during voluntary hand opening tasks and found that the CMC values can detect voluntary hand opening with high accuracy. Their results suggest that CMC analysis can be a promising tool for active hand rehabilitation of patients with stroke.

The paper "*A sound processor for cochlear implant using a simple dual path nonlinear model of basilar membrane*" by K. H. Kim et al. proposed a new active nonlinear model of the frequency response of the basilar membrane in biological cochlea called the simple dual path nonlinear (SDPN) model and a novel sound processing strategy for cochlear implants (CIs) based upon this model.

Acknowledgments

Chang-Hwan Im
Lei Ding
Yiwen Wang
Sung-Phil Kim

Research Article

Development of the Complex General Linear Model in the Fourier Domain: Application to fMRI Multiple Input-Output Evoked Responses for Single Subjects

Daniel E. Rio,[1] Robert R. Rawlings,[1] Lawrence A. Woltz,[2] Jodi Gilman,[3] and Daniel W. Hommer[1]

[1] *Section of Brain Electrophysiology and Imaging, LCTS, NIAAA, National Institutes of Health, 10 Center Drive, MSC 1540, Bethesda, MD, USA*
[2] *Synergy Research Inc., 12051 Greystone Drive, Monrovia, MD, USA*
[3] *Laboratory of Neuroimaging and Genetics, Martinos Center for Biomedical Imaging, Massachusetts General Hospital, Charlestown, MA, USA*

Correspondence should be addressed to Daniel E. Rio; drio@nih.gov

A linear time-invariant model based on statistical time series analysis in the Fourier domain for single subjects is further developed and applied to functional MRI (fMRI) blood-oxygen level-dependent (BOLD) multivariate data. This methodology was originally developed to analyze multiple stimulus input evoked response BOLD data. However, to analyze clinical data generated using a repeated measures experimental design, the model has been extended to handle multivariate time series data and demonstrated on control and alcoholic subjects taken from data previously analyzed in the temporal domain. Analysis of BOLD data is typically carried out in the time domain where the data has a high temporal correlation. These analyses generally employ parametric models of the hemodynamic response function (HRF) where prewhitening of the data is attempted using autoregressive (AR) models for the noise. However, this data can be analyzed in the Fourier domain. Here, assumptions made on the noise structure are less restrictive, and hypothesis tests can be constructed based on voxel-specific nonparametric estimates of the hemodynamic transfer function (HRF in the Fourier domain). This is especially important for experimental designs involving multiple states (either stimulus or drug induced) that may alter the form of the response function.

1. Introduction

The study of human brain cognitive function has been greatly enhanced by advances made in functional magnetic resonance imaging (fMRI) over the past few decades. The most important technique developed for this purpose utilizes changes in blood oxygen level instigated by stimulus-induced neuronal activation [1]. These changes in blood-oxygen levels produce localized variations in magnetic susceptibility and can be seen in $T2^*$-weighted MRI time series data [2, 3]. These time series data, referred to as blood-oxygen-level-dependent (BOLD) fMRI, typically have a low temporal signal-to-noise-ratio (SNR) [4] as well as high temporal correlation [5] that can make them difficult to analyze.

Functional MRI data analysis from its initial development has largely been implemented in the time domain [6, 7]. The major temporal focused fMRI analysis software packages are AFNI, SPM, and FSL [7–9] although many other analysis packages are also available and in current use. Generally these temporal domain focused analyses have been extended, to incorporate the statistical methodology of general linear models (GLMs) [8, 10, 11]. While almost exclusively used to analyze group data, GLMs have also been used for individual subject analysis [12]. In either case, the GLM approach requires a number of important assumptions be meant [13], that include foremost that the noise in the time series be independent and identically distributed (i.i.d), that is, $\sim N(0, \sigma\mathbf{I})$. Since BOLD fMRI data has significant autocorrelation, it is

necessary to attempt to remove the correlation in the data or incorporate into the GLM analysis a model for the noise that takes this into account. These corrections generally take the form of prewhitening techniques [8, 10], autoregressive (AR) models [14], and restricted maximum likelihood (ReML) methods [15, 16]. However, prewhitening or AR modeling of the fMRI BOLD data has been shown to have limitations [17] and these methods may in many instances only reduce nonwhite residual to about 40% of the total voxels [13, 18].

Besides the autocorrelation problem, there are additional major sources of error in modeling BOLD responses that arise in "standard" temporal-based analysis of fMRI time series data. Primarily, *a priori* assumptions as to a general parametric form of the hemodynamic response function (HRF) are often required [19] that could vary over the brain or from experimental conditions [20]. Seldom are these assumptions tested as to their validity for each new experimental design or at every voxel to be analyzed. This incorrect modeling of the HRF can lead to increased variance in the coefficients of temporal-based GLM analyses ultimately affecting the power to detect changes in the BOLD response and in general degrading the validity of the model [21, 22]. Furthermore, it is often the case that additional parametric functions and regression coefficients are typically included in temporal-based GLM models to correct for other perceived confounds. These effects can include those of signal drift, head motion [23, 24], and time shifts errors seen in multislice acquisition of fMRI data [25]. However, it has been stated that even small errors in modeling can result in the loss of statistical power [21], and the inclusion of inappropriate effects can lead to an increase of activated voxels yet reducing the validity of the model [26].

Many of potential sources of error associated with applying the GLM framework in the temporal domain can be eliminated or mediated by implementing the GLM in the Fourier or spectral domain. An important advantage of a Fourier-based methodology [27, 28] is that the statistics at different frequencies are asymptotically independent so that statistical tests in the complex domain, that parallel those for the real domain, can be more easily and directly constructed. In particular, Brillinger [29] developed a spectral domain approach for evoked response experiments that can be adapted to the analysis of single subject BOLD fMRI time series data. In this publication, in response to experimental designs that include repeated measure data, we extend the Fourier-based methodology previously developed to analyze fMRI data for multiple input (stimuli) and single output (one fMRI run). This extension enables us to analyze evoked responses fMRI BOLD data for single subjects that have multiple stimulus inputs and multiple outputs (that is repeated runs fMRI data which we will refer to as "states"). The corresponding mathematical extensions to the theory provide the first full multivariate approach in the Fourier domain of the GLM as applied to evoked response fMRI BOLD data.

Moreover, as previously mentioned, the use of parametric models for the hemodynamic response function (HRF), somewhat separate from the statistical analysis of fMRI data is another drawback in temporal-based analysis of fMRI data [19, 20] that is naturally addressed in a spectral domain approach. As the Fourier-based GLM incorporates voxelwise

nonparametric estimates of the hemodynamic transfer function (HTF) (HRF in the frequency domain) and is focused on hypothesis testing of this estimation. Additional positive consequences of performing hypothesis testing of the HTF in the spectral domain is that signal drift corrections as implemented in the temporal domain are unnecessary as the signal mean differences are not tested; time shift errors are also of no importance since the analysis is carried out in the spectral domain; and finally motion artifacts should be mediated since the BOLD response generally has a spectral power distribution that is different than that for head motion.

Whereas it should be mentioned that some earlier papers have also used Fourier-domain-based approaches to analyze BOLD fMRI time series data, they have been of limited scope. One of the earliest attempts at a Fourier-based analysis of fMRI was that by Lange and Zeger [30] that focused on the analysis of data obtained from a block experimental design and used a parametric form of the HRF. Another early paper that analyzed fMRI data in the frequency domain was by Marchini and Ripley [31]; however, it was restricted to periodic stimuli. A more recent paper, based on the work by Brillinger [27], is that by Bai et al. [32]. It focused on obtaining unbiased estimates of the HRF using stochastic rather than deterministic input stimuli (the usual design for fMRI experiments). It uses a weighted estimate of the transfer function and appropriate chi-square statistics to analyze sample data from an fMRI experiment with a "simple" design. In contrast, our paper has deterministic inputs or stimuli and an unweighted estimate of the transfer function, an approach that provides estimates with minimum mean square error and focuses on inference testing. Thus, the paper by Bai et al. [32] is attempting to find the best estimate to the transfer function, but not necessarily carrying out multivariate statistical hypotheses testing. Therefore, as previously stated the development in this paper is toward a full "multivariate" approach for hypothesis testing to perform signal detection in the spectral domain using an extension of the general linear model methodology in the complex domain.

2. The General Linear Model in the Fourier Domain for Multivariate Output

2.1. Model. Previously, a general linear model in the Fourier, domain to model single or univariate fMRI time series was presented [33–35]. In this model, a simple scalar quantity, $\mathbf{s}(t)$, represented the fMRI time series. In order to model a repeated measures experimental design with multiple fMRI time series for a single subject, the model is extended to incorporate multivariate output as follows. Let

$$\mathbf{s}(t) = \boldsymbol{\mu} + \mathbf{r}(t) * \mathbf{a}(t) + \boldsymbol{\varepsilon}(t), \tag{1}$$

where $\mathbf{s}(t)$ now represents a matrix of size $1 \times S$ whose elements consist of multiple (S) time series or repeated BOLD fMRI runs for a single subject collected at discrete time points t ($t = 1 \cdots T$) and spatial coordinate $\underline{x} = (x, y, z)$ (or voxel position, implicit). $\boldsymbol{\mu}$ is a matrix (size $1 \times S$) whose entries consist of constant values (with respect to time) for each time

series. The fixed deterministic input stimuli represented by $\mathbf{r}(t)$ have no spatial dependency. Multiple (R) input stimuli require that $\mathbf{r}(t)$ be represented by a $1 \times R$ size matrix, and correspondingly the response function $\mathbf{a}(t)$ is represented by a matrix of size $R \times S$. The symbol $*$ represents a convolution of the entries of the matrix product of $\mathbf{r}(t)$ and $\mathbf{a}(t)$. Thus, each stimulus input type and repeated BOLD fMRI run has a single response function represented by a single matrix entry in $\mathbf{a}(t)$ and calculated at every spatial coordinate $\underline{x}$ (implicit). Each entry of the $1 \times R$ matrix $\mathbf{r}(t)$ is a time series having the same length as the collected fMRI time series and consists of 0 s or 1 s at each time point t, where a value of 1 represents a stimulus presentation at that time. The error in the data is represented by $\boldsymbol{\varepsilon}(t)$ a matrix of size $1 \times S$ and assumes that the noise is stationary with zero mean for each corresponding fMRI BOLD time series collected.

Transforming this model (via the complex Fourier transform) to the frequency domain, we have

$$\widetilde{\mathbf{s}}\left(\lambda_k\right) = \widetilde{\mathbf{r}}\left(\lambda_k\right) \widetilde{\mathbf{a}}\left(\lambda_k\right) + \widetilde{\boldsymbol{\varepsilon}}\left(\lambda_k\right), \tag{2}$$

where $\lambda_k = 2\pi k/T$ and k represents the wave or frequency number. $\widetilde{\mathbf{a}}(\lambda_k)$, the HRFs representation in the Fourier domain is henceforth referred to as the hemodynamic transfer function or HTF. Periodograms [36] are constructed from the spectral forms of the stimulus input $\widetilde{\mathbf{r}}(\lambda_k)$ and BOLD outputs $\widetilde{\mathbf{s}}(\lambda_k)$ matrices as follows:

$$\mathbf{I}_{\alpha\beta}\left(\lambda_k\right) = (2\pi T)^{-1}\widetilde{\alpha}\left(\lambda_k\right)^H\widetilde{\beta}\left(\lambda_k\right), \tag{3}$$

where $\alpha, \beta = \{\mathbf{r}, \mathbf{s}\}$, $\lambda_k = 2\pi k/T$ and the superscript H refers to the Hermitian transpose. Estimates of the cross-spectral functions are then constructed [27] as follows:

$$\widehat{\mathbf{f}}_{\alpha\beta}\left(\lambda\right) = (2m+1)^{-1}\sum_{k=-m}^{m}\mathbf{I}_{\alpha\beta}\left(\lambda_k\right), \tag{4}$$

where λ denotes the center frequency of a band of frequencies $2m+1$ in width and provides stable estimates of the cross-spectral functions. The cross-spectral functions take a slightly different form [27] for the band centered at zero frequency. However, in applications to fMRI time series data, this band is discarded because it includes artifacts (e.g., low-frequency motion drift) and is not used in this paper. The band size chosen is based on statistical power considerations and the spectrum of the input power [34].

An estimate of the hemodynamic transfer function (HTF) [27, 34, 37] is given by

$$\widehat{\mathbf{A}}\left(\lambda\right) = \left[\widehat{\mathbf{f}}_{rr}\left(\lambda\right)\right]^{-1}\widehat{\mathbf{f}}_{rs}\left(\lambda\right) \quad R \times S, \tag{5}$$

where the matrix size is included for clarity. Note that a matrix entry $\langle\widehat{\mathbf{A}}(\lambda)\rangle_{ij}$ in (5) contains the HTF associated with the ith stimulus input and the jth repeated run.

2.2. Hypothesis Testing of the Hemodynamic Transfer Function.
Consider the hypothesis

$$H_0 : \mathbf{B}a\left(\lambda\right)\mathbf{C}^T = 0, \tag{6}$$

where $\mathbf{B}$ is the matrix that allows us to construct hypothesis test for multiple input stimuli and has size $b \times R$, where b can range from 1 to R. For example, setting the $\mathbf{B}$ matrix to the identity matrix $\mathbf{I}$ (size $R \times R$) would test whether any input stimuli would evoke a response in the BOLD signal. $\mathbf{C}$ is a matrix of size $c \times S$ where c ranges from 1 to S. This matrix allows us to construct hypothesis tests associated with the S repeated runs for each subject. For example, taking $\mathbf{B} = [1 \quad 0]$ and $\mathbf{C} = [0 \quad 1 \quad 0]$ would test the HTF associated with the BOLD response to the first stimulus type and the second repeated run on a subject. Of particular interest is the case for which the $\mathbf{B}$ and $\mathbf{C}$ matrices are identity matrices, of sizes R and S, respectively. We refer to this case as the omnibus case, that is, $F_{2bc;2h}(\lambda; \mathbf{B} = \mathbf{I}, \mathbf{C} = \mathbf{I})$ which is related to how well the model generally fits the BOLD fMRI data [34].

The test of the null hypothesis (6) takes the form of the following F-distribution:

$$F_{2bc;2h}\left(\lambda\right) = \frac{h}{bc}\frac{1 - U(\lambda)^{1/d}}{U(\lambda)^{1/d}} = \frac{h}{bc}\left[U(\lambda)^{-1/d} - 1\right], \tag{7}$$

where

$$d = \begin{cases} \sqrt{\dfrac{b^2c^2 - 4}{b^2 + c^2 - 5}} & b^2 + c^2 \neq 5 \\ 1 & b^2 + c^2 = 5, \end{cases} \tag{8}$$

$$h = \left[2m + 1 - R - \left(\frac{c - b + 1}{2}\right)\right]d - \frac{bc}{2} + 1$$

at each spatial position (implicit) and band (represented by its center frequency λ). This F-distribution simplifies to a more easily recognizable form [34] in the univariate or single fMRI run case, that is the ratio of the explained (by the HTF) to unexplained variance.

The construct for the current F-distribution is based on Rao's approximation to the U-statistics [38]. The form of the complex U-statistics for the model presented is based on an extension of the multivariate general linear model [39] from the real to complex domain. It has the following form:

$$U_{2b;2c;2(2m+1+b-c-R)}\left(\lambda\right) = \frac{\det \mathbf{G}_c\left(\lambda\right)}{\det\left[\mathbf{G}_c\left(\lambda\right) + \mathbf{H}\left(\lambda\right)\right]}, \tag{9}$$

$$\mathbf{G}_c\left(\lambda\right) = \mathbf{C}\mathbf{G}\left(\lambda\right)\mathbf{C}^T, \quad c \times c, \tag{10}$$

where

$$\mathbf{G}\left(\lambda\right) = (2m+1)$$
$$\times \left\{\widehat{\mathbf{f}}_{ss}\left(\lambda\right) - \widehat{\mathbf{f}}_{sr}\left(\lambda\right)\left[\widehat{\mathbf{f}}_{rr}\left(\lambda\right)\right]^{-1}\widehat{\mathbf{f}}_{rs}\left(\lambda\right)\right\}, \quad S \times S, \tag{11}$$

$$\mathbf{H}\left(\lambda\right) = (2m+1)\mathbf{E}(\lambda)^H[\mathbf{V}\left(\lambda\right)]^{-1}\mathbf{E}\left(\lambda\right), \quad c \times c, \tag{12}$$

where

$$\mathbf{E}\left(\lambda\right) = \mathbf{B}\widehat{\mathbf{A}}\left(\lambda\right)\mathbf{C}^T, \quad b \times c,$$
$$\mathbf{V}\left(\lambda\right) = \mathbf{B}\left[\widehat{\mathbf{f}}_{rr}\left(\lambda\right)\right]^{-1}\mathbf{B}^T, \quad b \times b, \tag{13}$$

Factors of 2, associated with the degrees of freedom in (7) and (9), are required to account for the cross-spectral estimations having both real and imaginary parts. Note that all terms in (12) except that for $\widehat{\mathbf{f}}_{rr}(\lambda)$ and correspondingly $\mathbf{V}(\lambda)$ are implicit functions of the spatial coordinates $\underline{x} = (x, y, z)$ or voxel position.

3. Methods

3.1. Experimental Design and Data Acquisition. The experiment consisted of the following paradigm. An alcohol-dependent and control subject taken from a larger study using event-related fMRI [40] was investigated. The experiment consisted of obtaining three separate BOLD fMRI images per subject. During each acquisition, which we will henceforth refer to as a state, the exact same visual input stimulus sequence was presented to the subject. These visual images were chosen from the International Affective Picture System [41]. Each image was presented for two seconds with a random interstimulus interval from 0 to 8 sec. Each subject was then asked to evaluate the visual stimuli, having either positive (pos) or negative (neg) valence using one of two buttons available for them to press using three separate criteria (counterbalanced order).

Specifically, subjects were asked to:

(i) evaluate the environment of the presented image (whether it is indoor or outdoor) for which the collected BOLD time series is referred to as the cognitive state;

(ii) evaluate the emotional valence of the presented image, if you liked it or did not like it, for which the collected BOLD time series is referred to as the emotion state;

(iii) do not evaluate the image and simply press a button when presented with an image for which the collected BOLD time series is referred to as the passive state.

Henceforth, we will refer to the three BOLD fMRI time series collected for each subject as the cognitive (cog), emotion (emo), or passive (pas) state.

3.2. Experimental Scanning Parameters. Images were collected on a 3T GE MRI scanner (General Electric, Milwaukee, WI, USA), using a standard quadrature head coil. The fMRI scans consisted of 156 temporal volumes ($64 \times 64 \times 16$) consisting of 5 mm thick slices with in-plane sampling of 3.75×3.75 mm using a T2*-weighted echo-planar sequence with TR = 2 s, TE = 40 ms, and flip angle 30°. Structural scans were acquired using a T1-weighted MP-RAGE sequence with TR = 100 ms, TE = 7 ms, and flip angle 90°.

3.3. Image Preprocessing. Preprocessing of the fMRI single subject images consisted of the following steps.

(1) Spatial registration of all functional temporal volumes to the tenth-time volume collected in the passive run using the AFNI [7] program 3dvolreg. The AFNI program 3dAutomask was also used to construct a binary mask (inside brain versus outside brain) for the functional images.

(2) Within-slice (2-dimensional) spatial smoothing using a Gaussian filter 8 mm full width half-maximum (FWHM) was applied to the coregistered images produced from step 1.

(3) Structural-to-functional MRI registration and restricted-to-affine transformations within subject using the AFNI program 3dAllineate [42] were performed. That is, the tenth-time volume or BOLD image from the passive run (see step 1) was registered to the subject's own structural MRI volume image.

Notably no other preprocessing of the data was made (and none was required [34]) in contrast to standard preprocessing of fMRI data in the time domain [23–25, 43].

3.4. Analysis of Multivariate Data in the Fourier Domain. All statistical tests were performed on an Apple Mac Pro Dual-Core 2.66 GHz computer using the SRView program (unpublished) developed for general fMRI data analysis. SRView is programmed in C++, with a X11-based GUI with embedded functional calls or a batch mode that uses tcl/tk as a scripting language. C shell scripts can also be used to invoke multiple runs of SRView. Typical calculations that include all hypothesis tests usually take twenty minutes or less.

Statistical tests of the null hypothesis (6) were carried out using the corresponding F-statistics (7) with appropriate $\mathbf{B}$ and $\mathbf{C}$ matrices chosen for a specific test. A band size of 13 frequencies ($m = 6$) was chosen based on the observed spectral power distributions and from previously analyzed data results [34, 35, 37]. Once a uniform band size was chosen the partitioning of the Fourier frequencies into bands and associated center frequencies was set. The band centered at zero frequency ($\lambda = 0$) was discarded because it contains a number of low-frequency artifacts. These are most prominently associated with motion and possibly signal drift. Therefore the elimination of this band is equivalent to applying a high-pass frequency filter to the time series data. After discarding this zero-band and limiting the highest frequency band to have an upper bound less than or equal to the Nyquist frequency, we produced five bands of equal size. F-statistics (6) were then calculated as a function of the center frequency λ of these bands.

Initially, model goodness of fit was explored using the omnibus hypothesis test $H_0 : \mathbf{A}(\lambda) = 0$ using the F-test statistic (7) with $\mathbf{B}$ and $\mathbf{C}$ matrices set as identity matrices. These tests were carried out at every voxel within the scope of the brain masks produced in the preprocessing steps (see Section 3.3). These tests performed at every voxel indicated whether any of the stimuli produced a significant response at any center frequency. The resultant spatial patterns are presented using multiple P-level mask (typical for reporting fMRI activity in temporal-based analysis). A color look-up-table (LUT) is used to present these threshold values.

```
Input: Select multiple P-values P_0, ..., P_n and associated color values in LUT
Calculate corresponding F-value, F(P_0), ..., F(P_n) | dof (2bc; 2h)
Loop over voxels within brain mask
    Extract F-values at voxel, indexed by band numbers
    Loop over band numbers
        Get F for band
            if (F < F(P_0) maskPixel = 0
            if (F ≥ F(P_0) and F < F(P_1)) maskPixel = 1
                .
                .
                .
            if (F ≥ F(P_{n-1}) and F < F(P_n)) maskPixel = n
            if (F ≥ F(P_n)) maskPixel = n + 1
    End loop over band numbers
End loop over image voxels
Output: multi-value mask and associated color LUT
```

ALGORITHM 1

TABLE 1: Compilation of omnibus and interaction hypothesis tests and associated matrices with resultant figures.

Test no.	Subject type slices presented	Hypothesis test	Hypothesis matrices		Figure no.
			B	**C**	
1	Subj: control Slices: occipital, language	Omnibus	**I** (identity matrix)	**I**	2
2	Subj: alcoholic Slices: occipital, language	Omnibus	**I**	**I**	3
3	Subj: control, alcoholic Slices: all	Interaction	$\begin{bmatrix} 1 & -1 \end{bmatrix}$	$\begin{bmatrix} 1 & -1 & 0 \\ 0 & 1 & -1 \end{bmatrix}$	See text

The algorithm for production of the multiple P-level mask in the Fourier domain is shown in Algorithm 1.

To help control for multiple tests (that is limiting the number of false positives), all voxels originally sampled within the full brain mask were further restricted by statistically based "voxel limiting" spatial masks as follows. The omnibus F-test images (related to measure of model fit—see Section 2.2) at each center frequency were strictly threshold at $P = .001$ to produce binary masks for each band. These masks were then combined using a Boolean OR operation to produce one spatial binary mask, henceforth referred to as the omnibus mask. This mask enabled us to limit the number of voxels looked at with the specific inference tests for interaction, main and simple effects for the ANOVA design presented. This yielded approximately 7% of the brain mask voxels for the alcoholic subject. Next, a mask based on the interaction hypothesis test was produced. The test for interaction between stimuli and states produced a mask used to exclude those voxels in which an interaction was seen. Additional multivariate tests for state effects were also used to further spatially restrict subsequent hypothesis tests. The algorithm for application of these hierarchical embedded masks is presented in Figure 1, where we present the flow chart associated with a voxel as it is either included or excluded in a mask, whose construct is based on the specific criteria being tested. Note that less stringent criteria were applied to univariate-based hypothesis tests where only the simple omnibus test

based mask was applied so as to more easily compare the results to the previously published analysis of this data [40].

Finally, in this analysis no attempt was made to investigate the frequency structure of the response since the temporal sampling rate or TR was relatively long and only a few bands were available for testing. For a more detailed look at frequency-specific hypothesis testing, see Rio et al.'s work [34] where the TR was 400 ms and the acquired fMRI series were 1400 time points long.

4. Results and Discussion

4.1. Omnibus Hypothesis Test and Test for Interaction. The construction of the omnibus hypothesis test for the control and alcoholic subjects is performed first. This consisted in applying the F-test (6) with full-rank matrices **B** and **C** set to **I** to test the hypothesis of whether any input stimuli or output run produced a significant response. Table 1 lists the test, and selected image slices (showing relevant results) are presented in Figures 2 and 3. In both figures, we see significant activation in the occipital regions of the brain that can generally be attributed to the visual stimuli being processed. Additionally, for the alcoholic subject, we see strong activation in the languages regions (both Broca's and Wernicke's areas—bottom of Figure 3) as well as some more muted activation (associated with a larger P value) in the amygdala (top
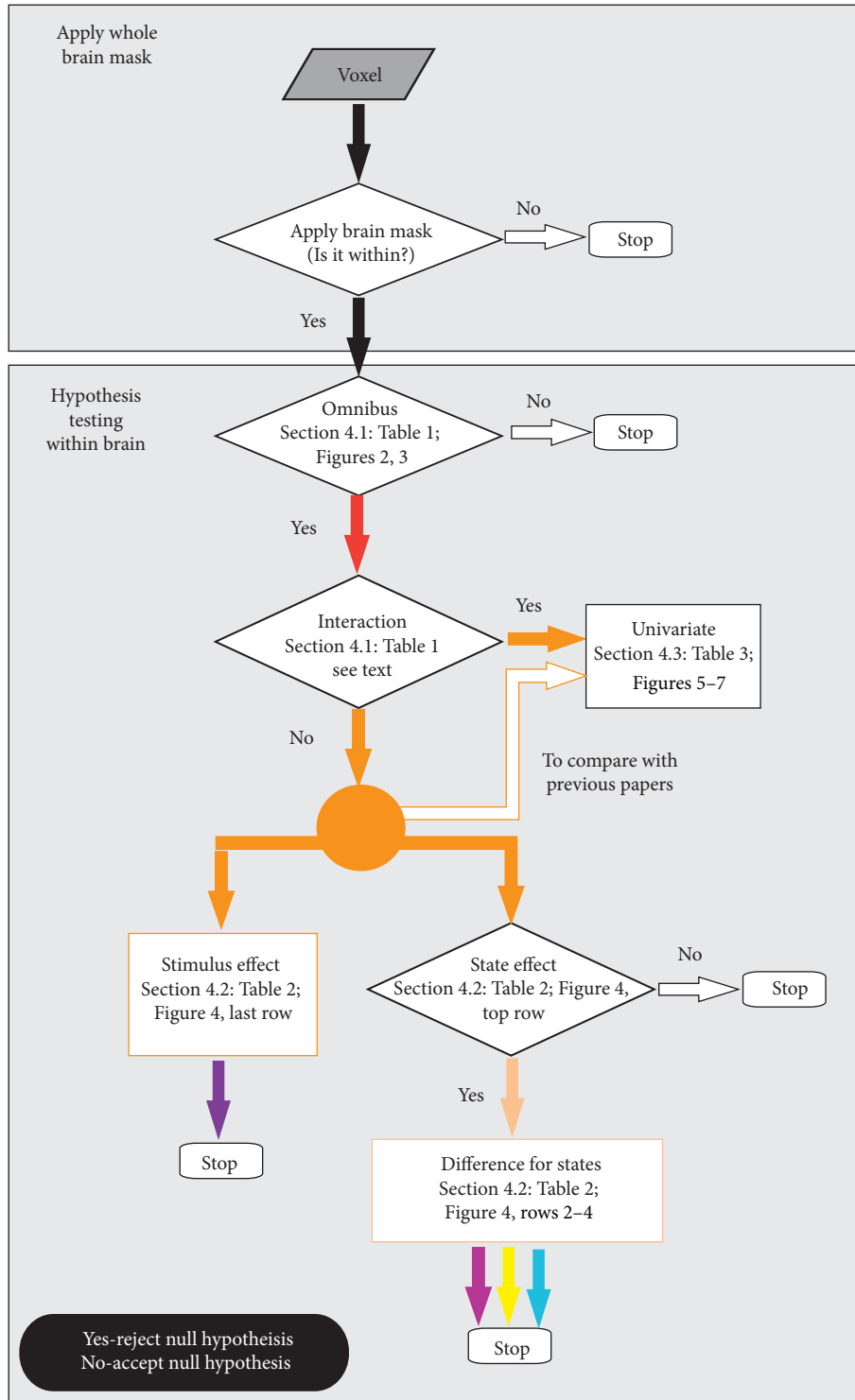
FIGURE 1: Diagram showing the sequential processing of a voxel in terms of hypotheses test applied. Only voxels for which the null hypothesis is rejected (except in the case of the interaction) proceed to the next test. For a complete description of tests and associated figures, see the indicated sections referred to in the flow chart.

of Figure 3). No such activation occurs in the control subject in the language area or in the amygdala (Figure 2).

A test for interaction was also performed (see Table 1). This test for parallel profiles based on the differential response of positive to negative stimuli for the output vector of cognitive, emotional, and passive states. This produced only a few activated voxels (not shown in any figure) in the control and alcoholic subjects. Most notably in the alcoholic subject
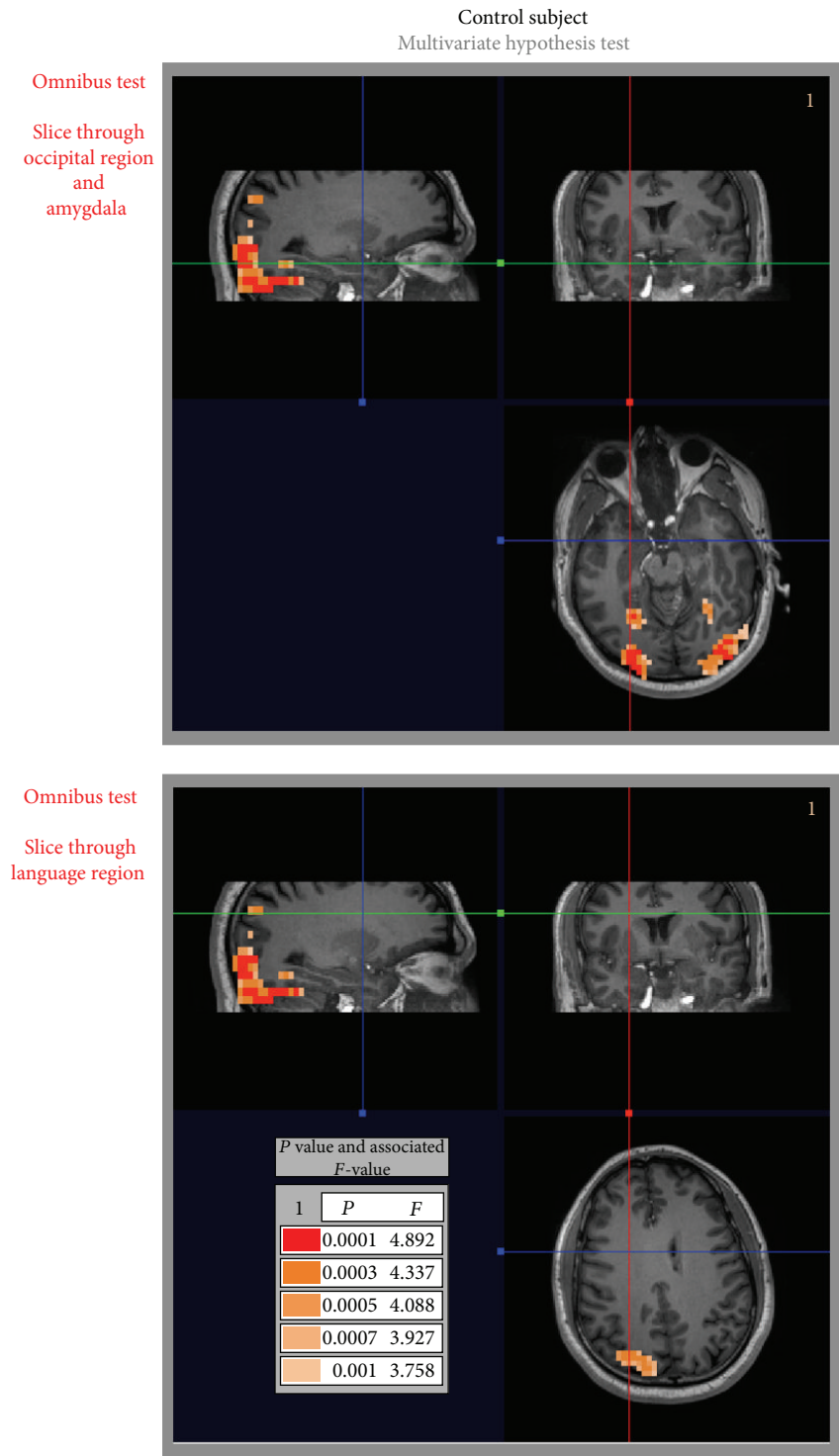
FIGURE 2: Control subject: inference results for omnibus hypothesis test shows BOLD response in the occipital region of the brain, visual stream. Note that the red blue and green lines indicate the correspondence between the orthogonal slices presented. There is no activation in the language region for the slice presented or any other slice through the language regions (not presented).

a small loosely connected set of three voxels in the left insula region that was not seen in the control subject. It is interesting to note that this is an important region of the brain linked to emotion and cognitive functioning.

4.2. Multivariate Repeated Measures Hypothesis Testing.

The main effects were investigated using multivariate repeated measures hypothesis tests (see Table 2). The images presented in Figure 4 are those for a control and alcoholic subjects for
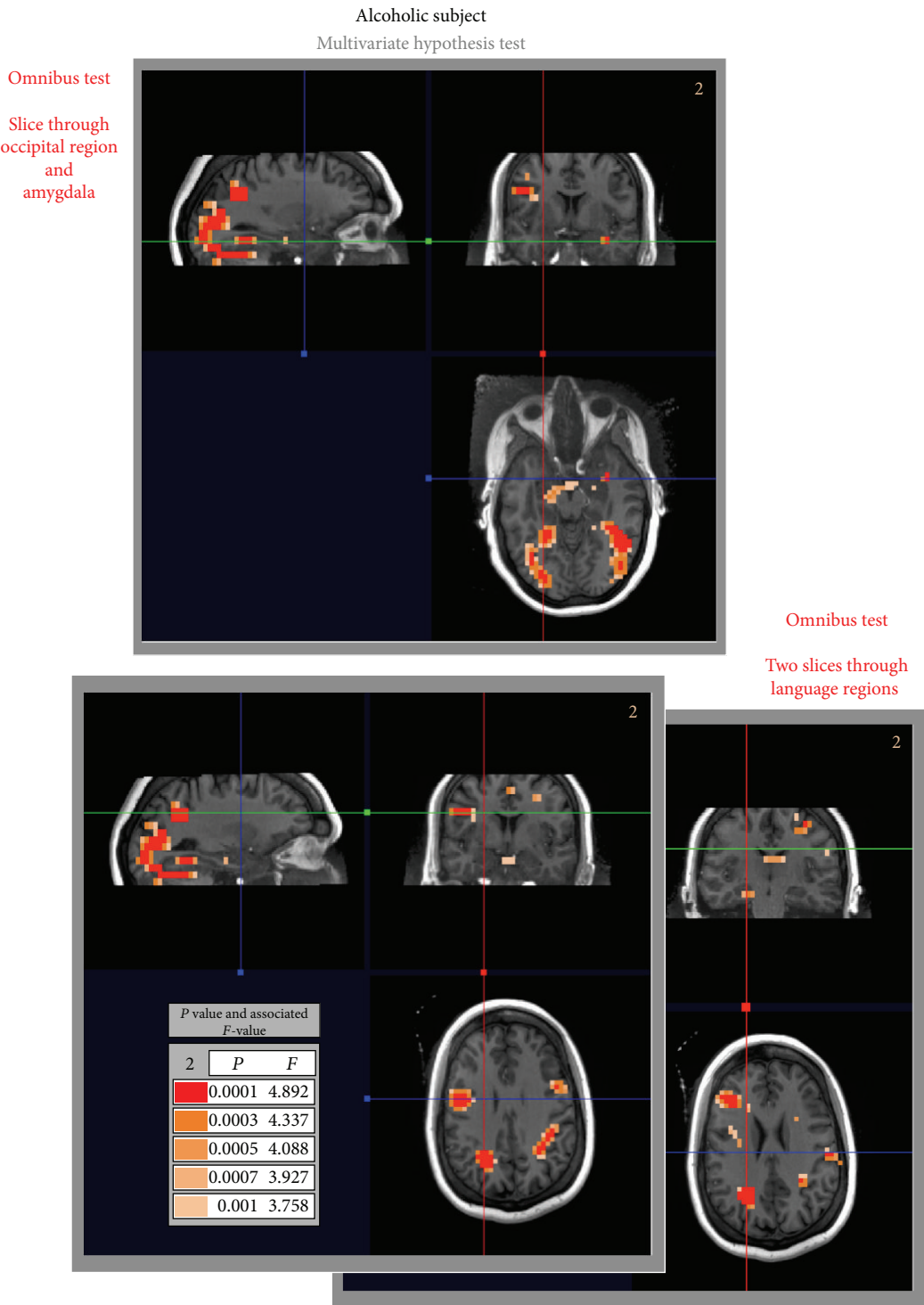
Figure 3: Alcoholic subject: inference results for omnibus hypothesis test shows BOLD response in the occipital region of the brain, visual stream. Note that the red blue and green lines indicate the correspondence between the orthogonal slices presented. Also interestingly, the amygdala and language areas for the two slices presented show a BOLD response not seen in the control subject (Figure 2).

transversal slices that cut through the occipital region of the brain posteriorly and through the amygdala in the medial anterior. The first hypothesis tested is that for the state effect, that is, whether the stimulus inputs, positive and negative, showed a differential response in the state vector consisting of

the cognitive, emotional, or passive functional MRI runs. The degrees of freedom for the F-distribution used in this test are $(4, 20)$ (with $b = 1$, $c = 2$; see Table 2, Test no. 4 and (7)). Next are presented the results for the following hypotheses: the effect between the cognitive and emotional states;

TABLE 2: Compilation of multivariate repeated measures hypothesis tests and associated matrices with resultant figures.

Test no.	Brief description of hypothesis test	Hypothesis matrices B	C	Figure no.
4	State effect differentiation between states	$\begin{bmatrix} 1 & 1 \end{bmatrix}$	$\begin{bmatrix} 1 & -1 & 0 \\ 0 & 1 & -1 \end{bmatrix}$	4
5	State effect: cog versus emo	$\begin{bmatrix} 1 & 1 \end{bmatrix}$	$\begin{bmatrix} 1 & -1 & 0 \end{bmatrix}$	
6	State effect: emo versus pas	$\begin{bmatrix} 1 & 1 \end{bmatrix}$	$\begin{bmatrix} 0 & 1 & -1 \end{bmatrix}$	4
7	State effect: cog versus pas	$\begin{bmatrix} 1 & 1 \end{bmatrix}$	$\begin{bmatrix} 1 & 0 & -1 \end{bmatrix}$	
8	Stimulus effect differentiation between stimuli	$\begin{bmatrix} 1 & -1 \end{bmatrix}$	$\begin{bmatrix} 1 & 1 & 1 \end{bmatrix}$	4

TABLE 3: Compilation of univariate hypothesis tests and associated matrices with resultant figures.

Test no.	Subject type; slices presented	Hypothesis test	Hypothesis matrices B	C	Figure no.
9	Alcoholic; occipital	Neg; emo versus pas	$\begin{bmatrix} 0 & 1 \end{bmatrix}$	$\begin{bmatrix} 0 & 1 & -1 \end{bmatrix}$	
10	Alcoholic; occipital	Neg; cog versus pas	$\begin{bmatrix} 0 & 1 \end{bmatrix}$	$\begin{bmatrix} 1 & 0 & -1 \end{bmatrix}$	5
11	Alcoholic; occipital	Neg; cog versus emo	$\begin{bmatrix} 0 & 1 \end{bmatrix}$	$\begin{bmatrix} 1 & -1 & 0 \end{bmatrix}$	
12	Control, alcoholic; occipital	Neg; pas	$\begin{bmatrix} 0 & 1 \end{bmatrix}$	$\begin{bmatrix} 0 & 0 & 1 \end{bmatrix}$	
13	Control, alcoholic; occipital	Neg; cog	$\begin{bmatrix} 0 & 1 \end{bmatrix}$	$\begin{bmatrix} 1 & 0 & 0 \end{bmatrix}$	
14	Control, alcoholic; occipital	Neg; emo	$\begin{bmatrix} 0 & 1 \end{bmatrix}$	$\begin{bmatrix} 0 & 1 & 0 \end{bmatrix}$	6
15	Control, alcoholic; occipital	Pos; emo	$\begin{bmatrix} 1 & 0 \end{bmatrix}$	$\begin{bmatrix} 0 & 1 & 0 \end{bmatrix}$	
16	Control, alcoholic; occipital	Stimulus effect; emo	$\begin{bmatrix} 1 & -1 \end{bmatrix}$	$\begin{bmatrix} 0 & 1 & 0 \end{bmatrix}$	
17	Alcoholic; occipital	State effect-cog	$\begin{bmatrix} 1 & 1 \end{bmatrix}$	$\begin{bmatrix} 1 & 0 & 0 \end{bmatrix}$	
18	Alcoholic; occipital	State effect-emo	$\begin{bmatrix} 1 & 1 \end{bmatrix}$	$\begin{bmatrix} 0 & 1 & 0 \end{bmatrix}$	
19	Alcoholic; occipital	State effect-pas	$\begin{bmatrix} 1 & 1 \end{bmatrix}$	$\begin{bmatrix} 0 & 0 & 1 \end{bmatrix}$	
20	Alcoholic; language	Neg; emo	$\begin{bmatrix} 0 & 1 \end{bmatrix}$	$\begin{bmatrix} 0 & 1 & 0 \end{bmatrix}$	7
21	Alcoholic; language	Pos; emo	$\begin{bmatrix} 1 & 0 \end{bmatrix}$	$\begin{bmatrix} 0 & 1 & 0 \end{bmatrix}$	
22	Alcoholic; language	Stimulus effect; emo	$\begin{bmatrix} 1 & -1 \end{bmatrix}$	$\begin{bmatrix} 0 & 1 & 0 \end{bmatrix}$	

the effect between the emotional, and passive states and the effect between the cognitive and emotional states. Finally, the hypothesis for stimulus effect is presented, that is, whether a differential response was seen between positive and negative input stimuli across the state vector, that is, the cognitive, emotional, or passive functional MRI runs. The degrees of freedom for the F-distribution used in these test are (2, 22) (with $b = 1$, $c = 1$; see Table 2, Tests nos. 5–8 and (7)). Generally, it is seen in Figure 4 that the alcoholic subject shows a pattern of BOLD response not seen in the control subject for any of the hypotheses tested, especially in the amygdala (medial anterior brain structure). However, no direct between-subject inference test is available for the single subject analysis presented.

4.3. Univariate Simple Effects Hypothesis Testing. The remaining hypothesis tests to be presented are simple effects tests (see Table 3). In Figure 5, we focus generally on comparisons between the output states in the amygdala, that is, the differential responses between the emotional, passive, and cognitive states for the negative stimuli input in the alcoholic subject. The largest (that is spatially extended region) differences occur between the emotional and passive states or the cognitive and passive states in this alcoholic subject. The stimulus

effect hypothesis (bottom row of Figure 5 and also presented in Figure 4) also shows a differential response between the positive and negative stimuli in this same region.

We next present some simple effects of hypothesis test results for both the control and alcoholic subjects in Figure 6 that again present results on a transversal slice that includes the amygdala. These hypothesis tests, testing simple effects associated with one or the other stimulus input and one of the output states, passive, cognitive, or emotional, show minimal activation except possibly for the emotional state. In Figure 6 (last row) is presented the activation mask associated with the stimulus effect, that is, the differential response of the input stimuli in the emotional run, which shows some differential response to the stimuli in the amygdala.

Finally, in Figure 7 are presented the results for simple effects univariate hypothesis tests. They include hypothesis tests for the negative, positive, or stimulus effect (differential response between the inputs, positive and negative stimulus inputs) for the cognitive state, emotional state and passive state for the alcoholic subject in both the amygdala and language areas of the brain. Here, we see increased activation in the emotional and passive runs as compared to the cognitive run in the amygdala and the occipital region. Particularly in the language regions, both Broca and Wernicke's (bottom two
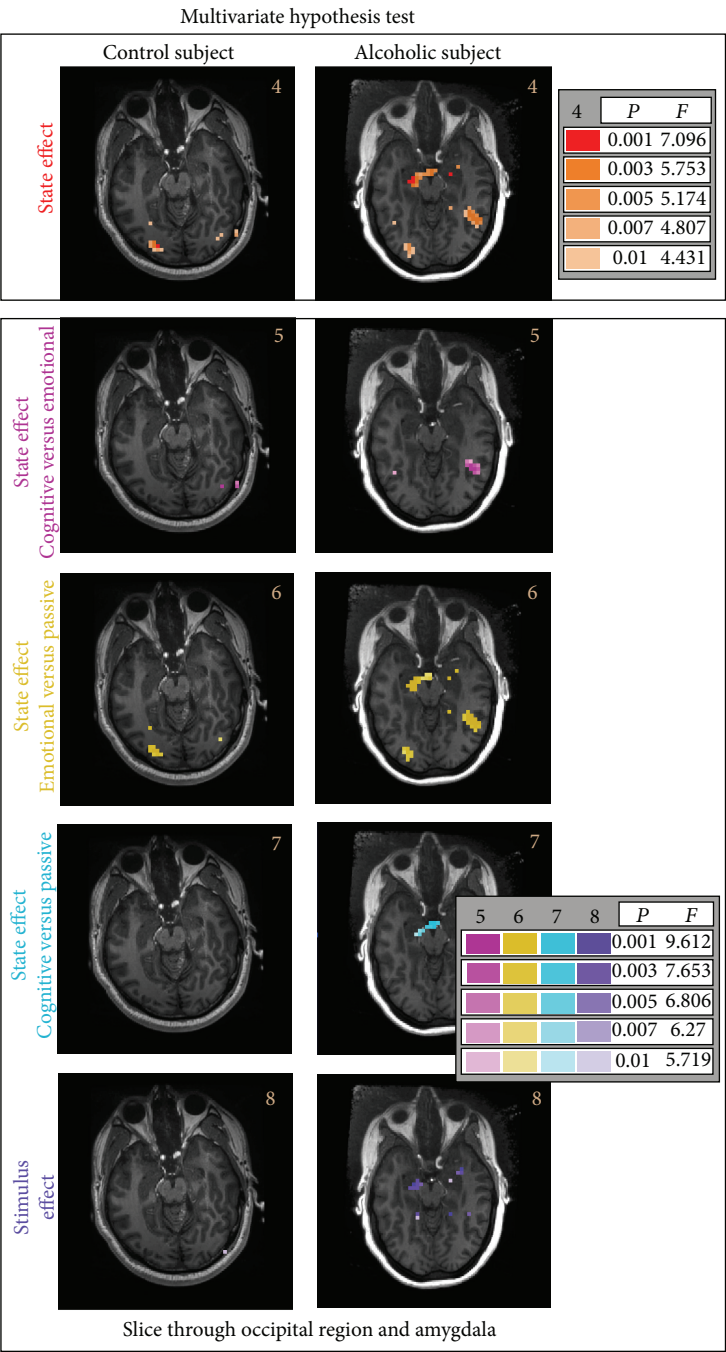
FIGURE 4: Multivariate repeated measures hypothesis tests for the control and alcoholic subjects are presented for a slice representative of the amygdala (media anterior) in the brain. The hypothesis tests show significant BOLD activation in the alcoholic subject in the amygdala for both a state effect and stimulus effect. Differences between the cognitive, emotional and passive states are also seen. Finally, while no direct hypothesis test between subjects can be made, we see in the control subject generally a more subdued BOLD response in all cases.

rows of images in Figure 7), we see substantial activation for the positive or negative stimuli and a somewhat smaller activated region for the stimulus effect (that is differential test between input stimuli) for the emotional run. The cognitive and passive runs were either not as active or generally inactive for these simple effects hypotheses tests and are not presented.

4.4. Hypothesis Testing in the Temporal Domain: A Sample Result from a Previous Study. A previous temporal-based analysis result for a slice that includes both Broca's and Wernicke's language areas of the brain for the alcoholic subject used in our Fourier-based fMRI analysis is presented. The control subject's result is not presented since our omnibus
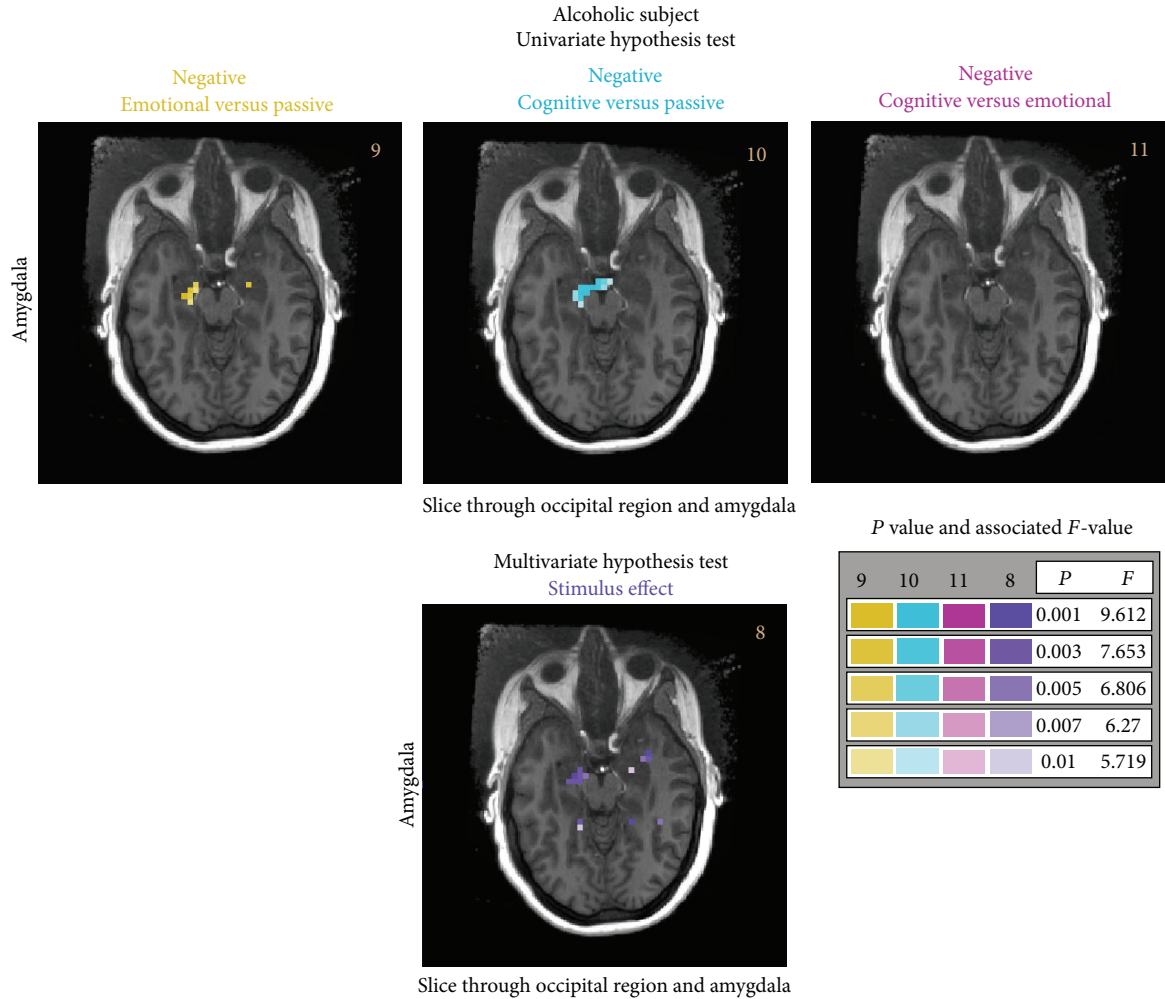
Figure 5: Univariate simple effects hypothesis test results are presented for the alcoholic subject for a slice representative of the amygdala (media anterior) in the brain. Focusing on the negative stimulus input and comparisons between the three output states, that is, emotional versus passive states, cognitive versus passive states, and cognitive versus emotional states. For context, an additional hypothesis test result (also see Figure 4) is presented showing the stimulus effect.

hypothesis test results (Figure 1) showed no activation in this region. The result presented here is the exact single subject analysis incorporated into the group analysis by Gilman et al. [40] employed to produce a major result of that paper (see Section 5). Comparison to the full group results is beyond the scope of this paper; however, a qualitative comparison can be made to the single subject alcoholic subject used in both papers. The single slice (Figure 8) covers the same anatomical regions as the slices presented in the two bottom rows of Figure 7. Activation is seen in the language area of the brain, similar to that produced in the group results [40] as well as in other regions of lesser interest in this particular subject. While no straightforward comparison of the F-statistic result (Figure 7, bottom two rows) and the t-statistics result (Figure 8) is possible, multiple P value spatial results are shown in both figures. Note that a region presented with a value of .001 means that this includes all voxels in which the statistic had a threshold in which $P < .001$. Using this as a guide, it is possible to observe similar language regions seen in both analyses; however, the temporal-based analysis seems to be

more generous in its assignments of activated region based on P values tested, especially in the hypothesis test results for the positive stimuli. This also gives rise to activated regions for the stimulus effect (last image on the right) not seen in the Fourier-based analysis method. The additional regions of activation are typical in temporal-based analysis that use less general forms for the noise error [13] and are not an indication of increased sensitivity with these tests. In fact, the group analysis using this subject corrects this problem where many of these activated regions are no longer significant. On the other hand, the language region for the emotional run, as seen in the Fourier method, is one of the major activated regions in the temporal-based group analysis that turns out to be important.

5. Conclusion

Extensions have been developed and presented to the complex general linear model with multiple inputs and outputs that provides a statistically rigorous methodology to analyze

FIGURE 6: A sampling of univariate simple effects hypothesis test results at a slice level that includes the amygdala for the control and alcoholic subjects. Focusing on the negative stimulus input for the three states (repeated BOLD fMRI image runs), passive, that is, cognitive, and emotional in the first three rows. BOLD response is most extensive in the emotional state. The fourth row shows the positive stimulus, emotional state BOLD response. Finally, in the last row is presented the stimulus response for the emotional state. See Table 3 for a description of all the matrices used to test these hypotheses.

fMRI time series data for single subjects based on the theory developed by Brillinger [27, 29]. In doing so, we have incorporated the standard notation of the general linear model in the real domain as presented by Timm [39] for multiple subjects and adapted it to the case of spectral bands. This approach allows the stochastic portion of the data to be modeled by a more general form for the noise and therefore fewer restrictions on the structure of the covariance matrix as compared to current time-based analyses. This is especially important in the analysis of single subject data where the assumptions on the noise structure can be critical to the calculation of the accompanying statistics [13].

FIGURE 7: Univariate simple effects hypothesis tests results for the alcoholic subject at three slice levels that include the amygdala and the language areas of the brain are presented. Particularly note the increased activation shown in the emotional state in the amygdala. On the bottom two rows are presented: the hypothesis tests for the emotional state for each individual input stimulus as well as the stimulus effect through slices that include both Broca's and Wernicke's language areas of the brain. The resultants indicate that the emotional state was the major contributor to the omnibus hypothesis test results shown in Figure 3 in the language area.

This methodology inherently incorporates voxel-specific nonparametric estimation of the hemodynamic transfer functions (hemodynamic response function in the time domain) that are central to the inference testing procedure. Thus, this methodology is centered on hypothesis testing of this transfer function for all constructed multivariate or univariate tests and does not require separate and possibly problematic *a priori* assumptions for the form of the hemodynamic response function as often required in time-based fMRI analysis [13, 19, 20]. In particular, the lack of a requirement to make *a priori* assumptions about the hemodynamic response function form makes this method particularly
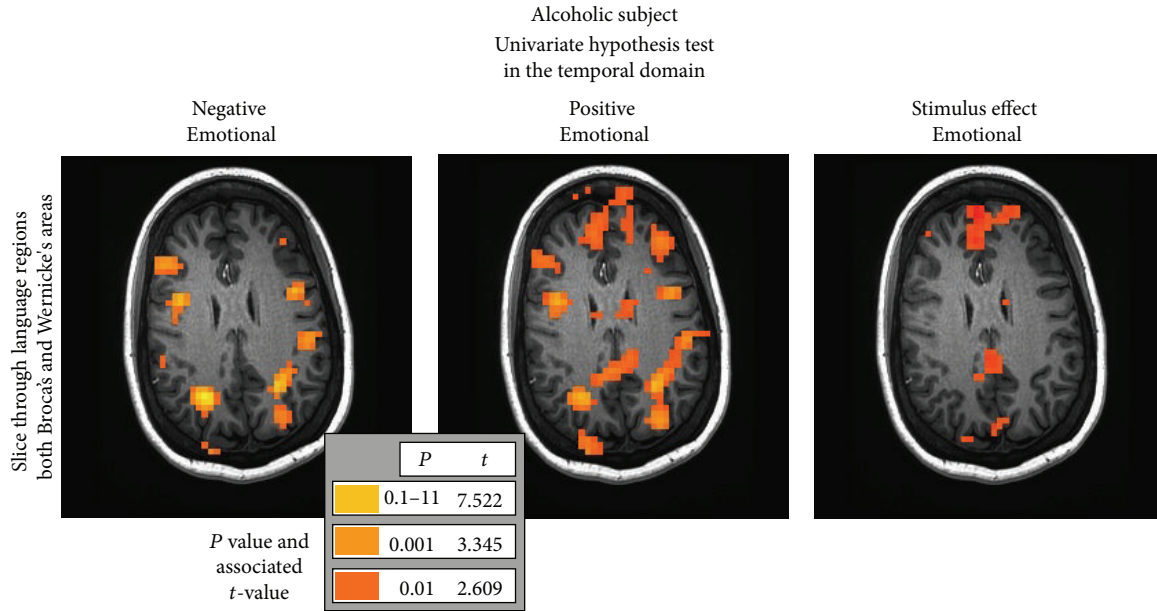
FIGURE 8: Temporal t-based statistical hypothesis test results for the emotional run in the same alcoholic subject analyzed in the Fourier domain (Figure 7, last two rows—Tests nos. 20–22). This exact single subject analysis was incorporated into the group of alcoholics used to produce a major result in the original paper by Gilman et al. [40]. Activation in both Broca's and Wernicke's language areas of the brain is shown in this single slice as well as a number of other regions of less interest.

useful in experiments designs where either drugs or the experimental manipulation itself may alter the form of the hemodynamic response function. This can, for instance happen with the introduction of a vasoactive drug, such as alcohol, to a subject during part of an experimental procedure [20].

Finally, by limiting the number of preprocessing steps and/or regressors, our Fourier-based GLM approach should mediate or eliminate many potential sources of error for single subject analysis addressed in the paper by Monti [13].

In regard to the comparison of this Fourier domain approach to the usual temporal-domain-based analyses, we can say the following. Hypotheses tested by these two methods are entirely different. In the temporal domain, a parametrically defined HRF family of functions is used to produce regressors associated with the stimulus input. Typically, amplitudes of the associated HRFs for specific stimuli provide the regression coefficients. Other regressors of noninterest are included for motion, and detrending of the time series data is also performed in this methodological approach. Statistics are then constructed to test the null hypothesis, essentially that the coefficient of the stimuli associated HRFs are zero. In contrast, the Fourier-based method for single subject hypothesis tests completely different. We focused on comparing the entire shape of the HTFs rather than simply comparing the amplitude of HRFs with a similar underlying shape as is often done in the temporal domain. This is accomplished by constructing hypothesis tests is directly on the HTF shape as represented by its spectral profile. Here voxel-specific HTFs are estimated as a direct response to the stimuli presented. That is, a spatially varying measure of the response to the stimuli is presented by the hemodynamic system

associated with the brain. The specific and general advantages to this approach are mentioned in previous paragraphs.

From an experimental design chosen to demonstrate the use of this methodology, we have presented the analysis of a single control and alcoholic subject. This design incorporated multiple visual stimuli input and acquired multiple-output state fMRI data. While not rigorously comparable, we see that this analysis shows similar regions of BOLD response to those seen in the original temporal-based group analysis of this data. This can best be summed up by quoting from the conclusion of the original paper by Gilman et al. [40], "Alcoholic patients appear to use brain language areas more than non-alcoholics while making judgments about the setting or liking of emotionally arousing visual images. This increased activation may reflect a compensatory recruitment of brain regions to perform simple decision-making tasks." Of additional importance, the choice of this experimental design for use in our demonstration has also allowed us to present a systematic approach to avoiding bias in multivariate hypothesis testing by incorporating hierarchical embedded restricting masks. This is an important step in controlling the number of false positives in multivariate-based analysis of fMRI imaging data. Planned extensions would also incorporate a method of false discovery proportion across voxels to further enhance results.

In conclusion, the results obtained from this analysis provide additional confirmation that this methodological approach, previously applied to an experimental design with multiple input stimuli and one output with a fast sampling rate (TR = 400 ms) and Poisson's distributed stimuli [34] can be applied to an experimental design with a more typical design matrix and slower sampling rate (TR = 2 s) that also

incorporates multiple (or repeated) fMRI runs for each subject. Having now incorporated multiple input and output hypothesis testing into the Fourier-based GLM approach, this paper provides a foundation to extend this development to the analysis of subject groups in the Fourier domain. Finally while group-based extensions to this methodology will be presented in future publications, let us end by quoting a comment made by Savoy [44], "That ironically it may someday turn out that the information from a few brains, thoroughly studied, will reveal more about universal aspects of human brain function and organization than the current torrent of studies from large collections of brains."

References

[1] S. Ogawa, T.-M. Lee, A. S. Nayak, and P. Glynn, "Oxygenation-sensitive contrast in magnetic resonance image of rodent brain at high magnetic fields," *Magnetic Resonance in Medicine*, vol. 14, no. 1, pp. 68–78, 1990.

[2] S. Ogawa, D. W. Tank, R. Menon et al., "Intrinsic signal changes accompanying sensory stimulation: functional brain mapping with magnetic resonance imaging," *Proceedings of the National Academy of Sciences of the United States of America*, vol. 89, no. 13, pp. 5951–5955, 1992.

[3] K. K. Kwong, J. W. Belliveau, D. A. Chesler et al., "Dynamic magnetic resonance imaging of human brain activity during primary sensory stimulation," *Proceedings of the National Academy of Sciences of the United States of America*, vol. 89, no. 12, pp. 5675–5679, 1992.

[4] K. Murphy, J. Bodurka, and P. A. Bandettini, "How long to scan? The relationship between fMRI temporal signal to noise ratio and necessary scan duration," *NeuroImage*, vol. 34, no. 2, pp. 565–574, 2007.

[5] M. W. Woolrich, B. D. Ripley, M. Brady, and S. M. Smith, "Temporal autocorrelation in univariate linear modeling of FMRI data," *NeuroImage*, vol. 14, no. 6, pp. 1370–1386, 2001.

[6] K. J. Worsley and K. J. Friston, "Analysis of fMRI time-series revisited-again," *NeuroImage*, vol. 2, no. 3, pp. 173–181, 1995.

[7] R. W. Cox, "AFNI: software for analysis and visualization of functional magnetic resonance neuroimages," *Computers and Biomedical Research*, vol. 29, no. 3, pp. 162–173, 1996.

[8] K. J. Friston, A. P. Holmes, K. J. Worsley, J.-P. Poline, C. D. Frith, and R. S. J. Frackowiak, "Statistical parametric maps in functional imaging: a general linear approach," *Human Brain Mapping*, vol. 2, no. 4, pp. 189–210, 1994.

[9] M. Jenkinson, C. F. Beckmann, T. E. J. Behrens, M. W. Woolrich, and S. M. Smith, "FSL," *NeuroImage*, vol. 62, no. 2, pp. 782–790, 2011.

[10] K. J. Worsley, C. H. Liao, J. Aston et al., "A general statistical analysis for fMRI data," *NeuroImage*, vol. 15, no. 1, pp. 1–15, 2002.

[11] C. F. Beckmann, M. Jenkinson, and S. M. Smith, "General multi-level linear modeling for group analysis in FMRI," *NeuroImage*, vol. 20, no. 2, pp. 1052–1063, 2003.

[12] H. Zhang, W. Luo, and T. E. Nichols, "Diagnosis of single-subject and group fMRI data with SPMd," *Human Brain Mapping*, vol. 27, no. 5, pp. 442–451, 2006.

[13] M. M. Monti, "Statistical analysis of fMRI time-series: a critical review of the GLM approach," *Frontiers in Human Neuroscience*, vol. 5, pp. 1–13, 2011.

[14] E. Bullmore, C. Long, J. Suckling et al., "Colored noise and computational inference in neurophysiological (fMRI) time series analysis: resampling methods in time and wavelet domains," *Human Brain Mapping*, vol. 12, no. 2, pp. 61–78, 2001.

[15] K. J. Friston, W. Penny, C. Phillips, S. Kiebel, G. Hinton, and J. Ashburner, "Classical and Bayesian inference in neuroimaging: theory," *NeuroImage*, vol. 16, no. 2, pp. 465–483, 2002.

[16] K. J. Friston, K. E. Stephan, T. E. Lund, A. Morcom, and S. Kiebel, "Mixed-effects and fMRI studies," *NeuroImage*, vol. 24, no. 1, pp. 244–252, 2005.

[17] J. L. Marchini and S. M. Smith, "On bias in the estimation of autocorrelations for fMRI voxel time-series analysis," *NeuroImage*, vol. 18, no. 1, pp. 83–90, 2003.

[18] A. T. Smith, K. D. Singh, and J. H. Balsters, "A comment on the severity of the effects of non-white noise in fMRI time-series," *NeuroImage*, vol. 36, no. 2, pp. 282–288, 2007.

[19] M. A. Lindquist, J. Meng Loh, L. Y. Atlas, and T. D. Wager, "Modeling the hemodynamic response function in fMRI: efficiency, bias and mis-modeling," *NeuroImage*, vol. 45, supplement 1, pp. 187–198, 2009.

[20] M. Luchtmann, K. Jachau, C. Tempelmann, and J. Bernarding, "Alcohol induced region-dependent alterations of hemodynamic response: implications for the statistical interpretation of pharmacological fMRI studies," *Experimental Brain Research*, vol. 204, no. 1, pp. 1–10, 2010.

[21] J. M. Loh, M. A. Lindquist, and T. D. Wager, "Residual analysis for detecting mis-modeling in fMRI," *Statistica Sinica*, vol. 18, no. 4, pp. 1421–1448, 2008.

[22] L. Waldorp, "Robust and unbiased variance of glm coefficients for misspecified autocorrelation and hemodynamic response models in fMRI," *International Journal of Biomedical Imaging*, vol. 2009, Article ID 723912, 11 pages, 2009.

[23] J. Tanabe, D. Miller, J. Tregellas, R. Freedman, and F. G. Meyer, "Comparison of detrending methods for optimal fMRI preprocessing," *NeuroImage*, vol. 15, no. 4, pp. 902–907, 2002.

[24] T. Johnstone, K. S. Ores Walsh, L. L. Greischar et al., "Motion correction and the use of motion covariates in multiple-subject fMRI analysis," *Human Brain Mapping*, vol. 27, no. 10, pp. 779–788, 2006.

[25] R. Sladky, K. J. Friston, J. Tröstl, R. Cunnington, E. Moser, and C. Windischberger, "Slice-timing effects and their correction in functional MRI," *NeuroImage*, vol. 58, no. 2, pp. 588–594, 2011.

[26] M. Razavi, T. J. Grabowski, W. P. Vispoel et al., "Model Assessment and Model Building in fMRI," *Human Brain Mapping*, vol. 20, no. 4, pp. 227–238, 2003.

[27] D. R. Brillinger, *Time Series: Data Analysis and Theory*, Holden-Day, San Francisco, NC, USA, 1981.

[28] R. H. Shumway and D. S. Stoffer, *Time Series Analysis and Its Applications: With R Examples*, Springer, New York, NY, USA, 2006.

[29] D. R. Brillinger, "The general linear model in the design and analysis of evoked response experiments," *Journal of Theoretical Neurobiology*, vol. 1, no. 1, pp. 105–119, 1981.

[30] N. Lange and S. L. Zeger, "Non-linear Fourier time series analysis for human brain mapping by functional magnetic resonance imaging," *Journal of the Royal Statistical Society C*, vol. 46, no. 1, pp. 1–29, 1997.

[31] J. L. Marchini and B. D. Ripley, "A new statistical approach to detecting significant activation in functional MRI," *NeuroImage*, vol. 12, no. 4, pp. 366–380, 2000.

[32] P. Bai, Y. Truong, and X. Huang, "Nonparametric estimation of hemodynamic response function: a frequency domain

approach," in *Optimality: The Third Erich L. Lehmann Symposium*, vol. 57 of *IMS Lecture Notes-Monograph Series*, pp. 190–215, 2009.

[33] D. E. Rio, R. R. Rawlings, L. A. Woltz, J. B. Salloum, and D. W. Hommer, "Single subject image analysis using the complex general linear model—an application to functional magnetic resonance imaging with multiple inputs," *Computer Methods and Programs in Biomedicine*, vol. 82, no. 1, pp. 10–19, 2006.

[34] D. E. Rio, R. R. Rawlings, L. A. Woltz, J. Gilman, and D. W. Hommer, "Analysis of fMRI single subject data in the Fourier domain acquired using a multiple input stimulus experimental design," *Journal of Signal and Information Processing*, vol. 3, no. 4, pp. 469–480, 2012.

[35] D. E. Rio, R. R. Rawlings, and D. W. Hommer, "Application of a linear time invariant model in the Fourier domain to perform statistical analysis of functional magnetic resonance images," in *Proceedings of the Medical Imaging: Physiology and Function from Multidimensional Images (SPIE '00)*, pp. 265–275, February 2000.

[36] M. S. Barlett, "Periodogram analysis and continuous spectra," *Biometrika*, vol. 37, no. 1-2, pp. 1–16, 1950.

[37] D. Rio, R. Rawlings, L. Woltz, J. Gilman, and D. Hommer, "An application of the complex general linear model to analysis of FMRI single subjects multiple stimuli input data," in *Proceedings in Medical Imaging: Biomedical Applications in Molecular, Structural, and Functional Imaging*, vol. 7262, February 2009.

[38] C. R. Rao, *Linear Statistical Inference and Its Applications*, John Wiley & Sons, New York, NY, USA, 2nd edition, 1973.

[39] N. H. Timm, "Multivariate analysis of variance of repeated measurements," in *Handbook of Statistics: Analysis of Variance*, P. R. Krishnaiah, Ed., vol. 1, pp. 41–87, North-Holland, Amsterdam, The Netherlands, 1980.

[40] J. M. Gilman, M. B. Davis, and D. W. Hommer, "Greater activation in left hemisphere language-related regions during simple judgment tasks among substance-dependent patients in treatment for alcoholism," *Alcoholism*, vol. 34, no. 2, pp. 331–341, 2010.

[41] P. J. Lang, M. M. Bradley, and B. N. Cuthbert, *International Affective Picture System (IAPS): Technical Manual and Affective Ratings, the Center for Research in Psycho-Physiology*, University of Florida, Gainsville, Fla, USA, 1995.

[42] Z. S. Saad, D. R. Glen, G. Chen, M. S. Beauchamp, R. Desai, and R. W. Cox, "A new method for improving functional-to-structural MRI alignment using local Pearson correlation," *NeuroImage*, vol. 44, no. 3, pp. 839–848, 2009.

[43] G. H. Glover, T. Li, and D. Ress, "Image-based method for retrospective correction of physiological motion effects in fMRI: RETROICOR," *Magnetic Resonance in Medicine*, vol. 44, no. 1, pp. 162–167, 2000.

[44] R. L. Savoy, "Using small numbers of subjects in fMRI-based research," *IEEE Engineering in Medicine and Biology Magazine*, vol. 25, no. 2, pp. 52–59, 2006.

Research Article

Information Analysis on Neural Tuning in Dorsal Premotor Cortex for Reaching and Grasping

Yan Cao,[1,2] Yaoyao Hao,[1,2] Yuxi Liao,[1,2] Kai Xu,[1,2] Yiwen Wang,[1,3] Shaomin Zhang,[1,3] Qiaosheng Zhang,[1,2] Weidong Chen,[1] and Xiaoxiang Zheng[1,2,3]

[1] *Qiushi Academy for Advanced Studies, Zhejiang University, Hangzhou 310027, China*
[2] *Department of Biomedical Engineering, Zhejiang University, Hangzhou 310027, China*
[3] *Key Laboratory of Biomedical Engineering of Ministry of Education, Zhejiang University, Hangzhou 310027, China*

Correspondence should be addressed to Yiwen Wang; eewangyw@zju.edu.cn

Previous studies have shown that the dorsal premotor cortex (PMd) neurons are relevant to reaching as well as grasping. In order to investigate their specific contribution to reaching and grasping, respectively, we design two experimental paradigms to separate these two factors. Two monkeys are instructed to reach in four directions but grasp the same object and grasp four different objects but reach in the same direction. Activities of the neuron ensemble in PMd of the two monkeys are collected while performing the tasks. Mutual information (MI) is carried out to quantitatively evaluate the neurons' tuning property in both tasks. We find that there exist neurons in PMd that are tuned only to reaching, tuned only to grasping, and tuned to both tasks. When applied with a support vector machine (SVM), the movement decoding accuracy by the tuned neuron subset in either task is quite close to the performance by full ensemble. Furthermore, the decoding performance improves significantly by adding the neurons tuned to both tasks into the neurons tuned to one property only. These results quantitatively distinguish the diversity of the neurons tuned to reaching and grasping in the PMd area and verify their corresponding contributions to BMI decoding.

1. Introduction

Motor brain-machine interfaces (mBMIs) interpret the motor intents from neural signals to control the external devices, such as the computer curser and the robot arm [1–5]. In the previous studies, the subjects, usually nonhuman primates, are required to manipulate a joy stick in a 2D plane or 3D space to track the target, which mostly focus on the arm movement [6, 7]. Thanks to the occurrence of the artificial prostheses with multi-degrees of freedom and the stable recoding systems, we could step into more complicated paradigms. A few researchers have started to work on elaborate grasping tasks [8–10], which involve the movement of fingers with different gestures.

Previous studies have shown that there are several cortical areas relevant to the reaching and the grasping movements, such as the primary motor cortex (M1), the ventral premotor cortex (PMv), and the dorsal premotor cortex (PMd) [10–13].

Specially, neurophysiological studies have manifested that the PMd area mostly relates to the proximal arm movements [14, 15]. Some neurons fire more frequently when moving towards the preferred direction. Burnod et al. have found that when the initial arm position varied across the working space, the directional preferences of the PMd neurons changed significantly [14]. Messier and Kalaska have proposed a bootstrapping method to estimate the probability that neurons were tuned based on the intertrial variability when the monkey was performing a whole-arm reaching movement in a plane. Significant directional tuning of the neurons in PMd was relatively constant throughout the trials [15]. But recently, some studies have reported that there are also some neurons related to grasping in PMd [16, 17]. Raos et al. firstly found that when the monkey was grasping different shaped objects, the recorded neuron firings in PMd were sensitive for a preferred type of shape [16, 17]. Some researchers suggest that in the PMd area the neural representations of reaching are

not completely separated from grasping [17, 18], that is, there are grasp-related neurons in this area. This phenomenon indicates the existence of the neurons tuned to both reaching and grasping tasks. To study their combined representation, Stark et al. performed a mixed paradigm which required the monkey to grasp one of three different objects in six directions [12]. He found that there are neurons related to reaching as well as grasping in PMd. However, the paradigm in [12] combined reaching and grasping in the same trial, which may influence each other because the reaching is always preshaped by the grasping gesture.

In this paper, we are interested in studying the tuning property of the PMd neurons related to reaching and grasping, respectively. Two experimental paradigms are designed to separate these two factors. Two monkeys are instructed to reach in four directions but grasp the same object in the first experiment, named as "Reaching task." In the second experiment, the monkeys are instructed to grasp four different objects with different gestures but reach in the same direction, named as "Grasping task." Activities of neuron ensemble in PMd are collected while performing the tasks. We propose to use mutual information (MI) to quantitatively discriminate the neurons tuned to reaching and grasping, respectively. In order to verify the contribution of the tuned neurons in PMd, a support vector machine (SVM) is implemented to decode the activities of the tuned neurons to the corresponding movement and compared with the performance by full ensemble in both reaching and grasping tasks. The decoding is further used to validate if there exist neurons tuned to both tasks, and how much they contribute to the motor decoding. The experimental setup and data acquisition are shown in Section 2.1, followed by the introduction of the mutual information method measuring the neurons' tuning characteristic and the implementation of the decoding algorithm SVM. Results are shown and explained in Section 3. Conclusion and discussion are in Section 4.

2. Materials and Methods

2.1. Experimental Setup. The paradigm of motor brain-machine interface was designed and implemented in Qiushi Academy for Advanced Studies at Zhejiang University. Two rhesus macaques (male), named B03 and B04, were trained separately to perform two different tasks: the Reaching task and the Grasping task with one of their dominant hands (right hand for B03 and left hand for B04), as illustrated in Figures 1(a) and 1(b). In the Reaching task, four identical objects are fixed on the four corners of a transparent resin glass board, and the monkeys are required to stretch out to grasp the target object in different directions. While in the Grasping task, one object with a certain shape is fixed on the same position of the board (indicating the same direction), and the monkeys are required to grasp it with a specific gesture in each trial. There are four objects in our experiment, namely, a small cylinder, a rectangle plate, a ring, and a cone. One object is grasped for a certain number of trials and changed to another.

During the task, the monkey sits in a primate chair with his head fixed. An LCD monitor is mounted behind the board to illuminate the target object area, as a cue to instruct the monkeys to start the trial. The trial sequence is shown in Figure 1(c).

The monkey sits in darkness during the intertrial interval (1~2.5 s) with his hand resting on the clapboard. When the cue is on (Light ON), the monkey is required to stretch out and grasp the target object within 600 ms, and hold it for 1~2 s until the cue is off (Light OFF). After Light OFF, the monkey releases the object and withdraws his hand to the rest position. When a trial is completed successfully, the monkey would receive water rewards. The training durations are 2~3 months before the monkeys successfully perform the tasks.

2.2. Neural Data Acquisition. The neural data are collected from the Utah microelectrode array (Blackrock, 96 channels) chronically implanted in the hand area of PMd, contra-lateral to the trained hand (left hemisphere for B03 and right hemisphere for B04). The surgical procedures are the same as described in [19]. All experimental procedures in this study conformed to the Guide for the Care and Use of Laboratory Animals (China Ministry of Health) and were approved by the Animal Care Committee at Zhejiang University, China.

Neural activities are recorded by the Cerberus data acquisition system (Blackrock, USA). Signals were amplified and analog-filtered by the Butterworth band-pass filter at 0.3–7500 Hz and further digitized (14 bit resolution, 30 kHz sample rate) and digitally filtered (Butterworth high pass filter) at 250 Hz. The spike activities were detected from the filtered signal by a threshold value method (the threshold was −5.5 times of the root mean square of the baseline signal). And the spike timings were recorded. Spike activities were sorted by Offline Sorter (Plexon, USA). Different spike waveforms were discriminated by a time-amplitude discriminator and a principle component analysis (PCA) algorithm [20]. Each neuron was identified by observing the spike waveforms and the channel locations based on the above spike sorting method. In addition, the event timings of Light ON, Light OFF, and rewarding were also recorded synchronously via the digital input port of the Cerberus system.

2.3. Data Analysis. To analyze neural activities in the two tasks, we mainly focus on the period from the resting state to stretch out, grasp, and hold. For each trial, we extract 0.5 s before Light ON to 1.7 s after Light ON for Monkey B03 and 1.3 s after Light ON for B04 (B04 moved faster than B03).

For the desired period, neurons' firing rates are binned in a 100 ms window. Firstly, a one-way ANOVA test is applied to observe whether the neurons fire significantly different from the rest state when performing the tasks. Then a quantitative method, mutual information, is introduced to measure the information amount between the neural firings and the target task. In order to directly exploit the timing of the neurons' firing, we examine the spike indicator (whether there is a spike or not) every 10 ms. The mutual information between

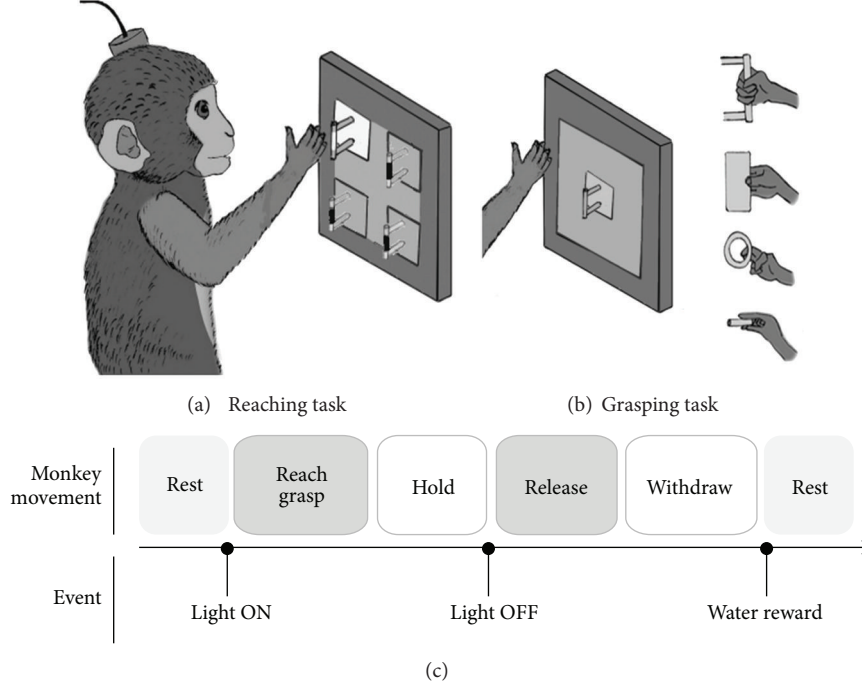(a) Reaching task   (b) Grasping task

(c)

FIGURE 1: Experimental setup and the trial sequence. (a) The Reaching task. The monkeys were trained to grasp the identical objects in four directions. (b) The Grasping task. The monkeys were trained to grasp four different objects, namely, a small cylinder, a rectangle plate, a ring, and a cone, in the same direction. (c) The time sequence of a single trial.

the neural activities and the task (reaching or grasping) is defined as

$$I(\text{spk}; y) = \sum_{y=y_1, y_2, y_3, y_4} p(y) \sum_{\text{spk}=0,1} p(\text{spk} \mid y) \\ * \log_2 \left(\frac{p(\text{spk} \mid y)}{p(\text{spk})} \right), \tag{1}$$

where y_1, y_2, y_3, and y_4 represent four different actions in either task, and $p(y)$ represents the probability of the corresponding action (in our experiments, it is 1/4 due to the same trial numbers); $p(\text{spk} \mid y)$ represents the conditional probability of the corresponding firing rate (0 or 1) for a certain action; and $p(\text{spk})$ represents the probability of the corresponding firing rate of the target task. Please refer to [21, 22] for details. We calculate the cumulative sum of the neurons' MI according to a descending order for each task. When the cumulative sum of the MI reaches 90 percent of the total amount, the last MI that has been added is regarded as the threshold for the task. The threshold is applied to divide the neurons into the tuned ones and nontuned ones and calculated session by session, respectively.

An SVM is implemented as a decoder to quantify the contribution of the tuned neurons to the BMI decoding. Firstly, a subset of the tuned neurons according to the thresholds described above is used in classification, compared with the decoding by full ensemble, respectively, for the two tasks. Noticing that there might be overlaps between the neurons tuned to reaching and the neurons tuned to grasping, that is, the neurons tuned to reaching as well as grasping,

we separate them from the neurons tuned to one property only and compare the decoding performance including or excluding them.

An SVM model maps the neural data into a high-dimension space by a kernel function, and different categories are divided by a hyper plane. For a specific SVM model, the hyper plane is optimized by (2), according to the statistical learning theory [23]:

$$\min_{u,b,\varepsilon_i} \quad \frac{1}{2}\|u\|^2 + C\sum_{t=1}^{N} \varepsilon_t \\ \text{subject to:} \quad y_t \left(u^T X_t + b \right) \geq 1 - \varepsilon_t, \\ t = 1,\dots,N; \quad \varepsilon_t \geq 0, \quad t = 1,\dots,N, \tag{2}$$

where y_t represents the category of different movements, and X_t represents the neural firing rate, which is an n by m vector (n is the number of neurons in a session, and m is the number of bins). In our experiment, m is 18 for B03 and 14 for B04. The parameters u and b indicate the normal vector of a hyper plane and its offset. The goal of (2) is to find an optimal separation plane which is farthest away from the nearest neural data in both classes. The parameter ε_t is a dummy variable. The regularization term makes sure that the neural data in the training set is misclassified with a cost, because there is noise and other measurement errors. The parameter C is used for controlling the balance between the overtraining and the generalization in testing. In our experiment, we take radial basis function as the kernel function. And the parameters of the radial function γ and C are determined

by a 2-fold cross validation. The algorithm is implemented in MATLAB using open source library LIBSVM [24]. We would like to remark at this point that SVM is not the only option to evaluate the decoding performance. Any effective classifier may work here.

3. Results

The goal of this work is to find out how a certain neuron in the PMd area is tuned to reaching and grasping, and this section shows some example neurons with different tuning characteristics, followed by the quantitative analysis of the neurons' tuning properties for different tasks; and the last step is to verify the contribution of the tuned neurons to the BMI decoding.

5 sessions of neural signals for each monkey were obtained during a period of half a month. In each session, monkeys were required to do both Reaching task (100 trials divided in 25 trials for each reaching direction) and Grasping task (200 trials divided in 50 trials for each grasping gesture). For Monkey B03, neural data were recorded from 96 channels, and for Monkey B04, neural data were recorded from 64 channels. After offline sorting, 22–47 neurons (from B03) and 30–66 neurons (from B04) were isolated in each session.

3.1. Observing Neurons' Tuning Activities in Time. To give an intuitively view of the neurons' tuning characteristic in the Reaching and the Grasping tasks, we average the firing rates across trials in one session for each task. Here, we plot four example neurons (Figure 2) which show different firing patterns during the tasks. The average firing rates in each task are aligned by the time of Light ON and plotted in the same figure. Neurons A and B are selected from one session of B03, and Neurons C and D are selected from one session of B04. We can see that Neuron A fires significantly higher than the baseline in the two tasks. And the four curves both in the Reaching task (corresponding to the four reaching directions) and the Grasping task (corresponding to the four grasping gestures) are scattered. Therefore, we consider Neuron A as tuned to both tasks. For Neuron B, the firing curves in the Reaching task can be discriminated but grouped together in the Grasping task. We consider it as tuned to reaching only. The firing pattern of Neuron C is just contrary to Neuron B, and we regarded it as tuned to grasping only. And for Neuron D, which fires at the baseline level in both tasks, is regarded as no-tuning.

To inspect whether the neurons' tuning properties commonly exist or not, a one-way ANOVA test ($P < 0.05$) has been carried out [25]. Task-related responses of each neuron are statistically assessed by comparing the firing rates between the movement state and the rest state. In the reaching task, 80.96% of the neurons from B03 show significant difference in the firing rate relative to the baseline. The percentage is 72.41% for B04. These neurons are classified as reaching-related ones. In the Grasping task, the percentages are 88.02% and 86.59%, respectively, for B03 and B04. These neurons are classified as grasping-related ones (one-way ANOVA, $P < 0.05$). Among the reaching-related neurons, a large fraction (84.04% for B03 and 68.26% for B04) further shows reaching

tuning property (the firing rates for at least one reaching direction in at least two bins were significantly different to the others). This situation is the same as the grasping-related neurons, 92.03% and 73.88% for B03 and B04 show grasping tuning property, respectively, (one-way ANOVA, $P < 0.05$). These results show that a majority of the neurons show tuning property to the Reaching and the Grasping tasks.

3.2. Mutual Information Analysis. To evaluate the neurons' tuning characteristic quantitatively, the mutual information (MI) between each neuron and the corresponding task is calculated. For each neuron there are two MI values respectively for the reaching and the grasping task.

Figure 3 displays the MI values for the two tasks in one session. The MI values in the two tasks reflect some characteristics. Some neurons exhibit large MI in reaching (blue bar) while very small MI in grasping (red bar), suggesting that they are more sensitive to the reaching task. By contrast, some display large MI in grasping while small MI in reaching, suggesting they are involved in grasping. Besides, there are also some neurons presenting large MI in both tasks, which indicates that they are related to both conditions.

Note that the four example neurons shown in Figure 2 are marked by the asterisks in the above figure, and the corresponding neuron signs are instructed by the arrows under the *x*-axis. Neuron A, ranking first in the upper panel, which is regarded as tuned to both conditions in Figure 2, shows large MI values in both tasks. Neuron B, which tuned to reaching only, exhibits large MI in reaching while small MI in grasping. Neuron C, ranking 23 in the bottom panel, displays large MI only in grasping. And Neuron D shows small MI in both conditions. This demonstrates that a neuron's tuning to a task reveals large MI in the corresponding task, and the MI can indicate a neuron's tuning property.

A threshold method on MI is employed to quantitatively evaluate a neuron's tuning property. If the MI values in reaching and grasping exceed the thresholds of both tasks, the neuron is tuned to both conditions. If the MI of one task is greater than the task's threshold but the MI of another task is below the task's threshold, the neuron is defined as tuned to one condition only. Table 1 shows the contribution of the tuned neurons in the corresponding task, that is, the percentage of the information provided by the tuned neurons, which are averaged across five sessions. The number of the corresponding tuned neurons is also given in the brackets. Take Monkey B03 as an example, in the Reaching task, the information provided by the neurons tuned only to reaching and those tuned to both conditions, respectively, accounts for 30.74% and 54.81%. And in the Grasping task, the proportion is 27.77% and 60.94%, respectively, for the neurons tuned only to grasping and the neurons tuned to both conditions. The information distribution for Monkey B04 is similar to B03.

It is interesting to notice that the contribution of the neurons tuned to both conditions is much larger than that of the neurons tuned to only one property in both tasks. One possible reason may be the number of the neurons tuned to both conditions is averagely greater than the number of the neurons tuned to one property only. The reveal of the large number of the neurons that tuned to both conditions
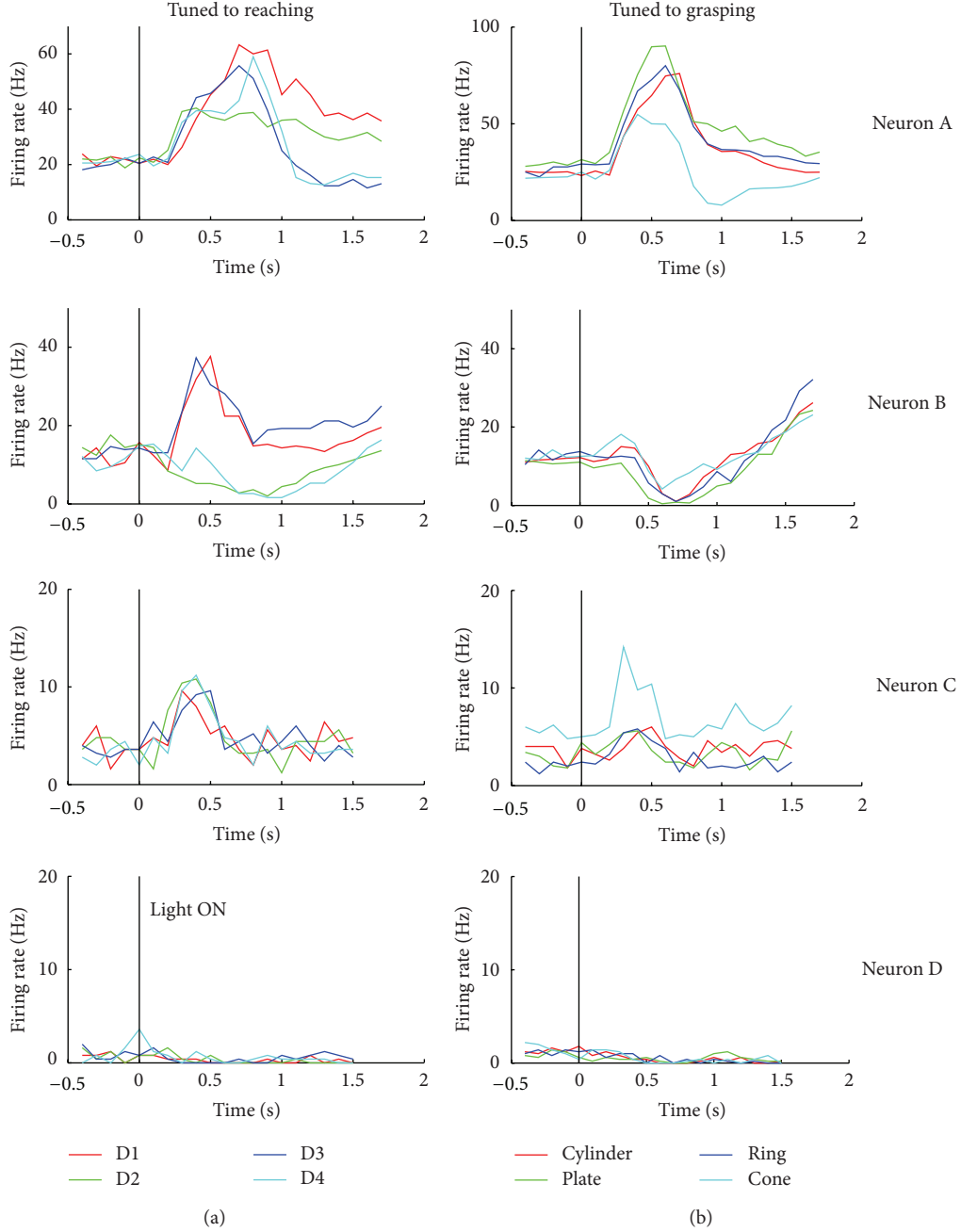
FIGURE 2: The tuning activities of four example neurons from both monkeys during the Reaching and the Grasping tasks. The x-axis represents the times (in seconds) from the rest state (about 0.4-0.5 s) to the movement state (about 1.4–1.7 s). The y-axis represents the firing rate (in Hz). The vertical line in each panel represents the time of Light ON, which is defined as 0 s. Each row shows the variation of the same neuron's firing rates in the two tasks (left: the Reaching task; right: the Grasping task). Neurons A and B are from the first session of B03, and Neurons C and D are from the third session of B04. The four different colors in one plot represent four different actions of a task. Specifically, in the Reaching task, the red color indicates reaching to the direction of upper-left corner (D1), the green color indicates reaching to the direction of upper-right corner (D2), the blue color indicates reaching to the direction of lower-left corner (D3), and the light blue color indicates reaching to the direction of lower-right corner (D4). In the Grasping task, the red color indicates grasping the cylinder, the green color indicates grasping the plate, the blue color indicates grasping the ring, and the light blue color indicates grasping the cone.

is consistent with the study [12] that shows there exist PMd neurons that tuned to grasping as well as reaching.

3.3. Decoding Verification. To verify the correlation between the neurons' tuning property and the tasks, we adopt the SVM

to check the decoding performance by full ensemble versus the tuned neuron subset versus the top 10 well-tuned neurons. The decoding results are depicted in **Figure 4**.

Compared with the decoding by full ensemble, the tuned neuron subset achieves quite close accuracy in both tasks
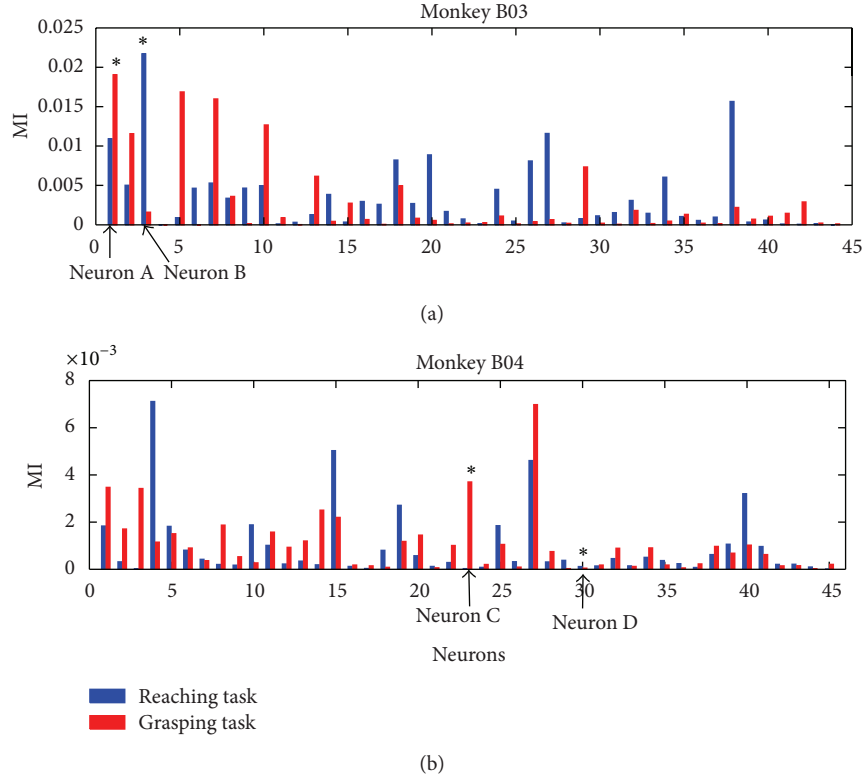
FIGURE 3: The mutual information in one session for the two tasks. The x-axis represents the neurons, and the y-axis represents the MI values in the Reaching and the Grasping tasks. The blue bars represent the Reaching task, and the red bars represent the grasping task. The upper panel is for Monkey B03, and the bottom one is for B04. The asterisks represent the four neurons shown in **Figure 2**, which are instructed by four arrows under the x-axis.

TABLE 1: The percentage of the information provided by the tuned neurons in the Reaching and the Grasping task. The number shown in the brackets represents the corresponding tuned neurons.

| Monkey | The contribution of the tuned neurons in the two tasks | | | |
| | Reaching task | | Grasping task | |
	Tuned only to reaching (averaged number of neurons)	Tuned to both conditions (averaged number of neurons)	Tuned only to grasping (averaged number of neurons)	Tuned to both conditions (averaged number of neurons)
B03	30.74% (7)	54.81% (9)	27.77% (5)	60.94% (9)
B04	23.16% (9)	65.51% (14)	30.4% (9)	57.89% (14)

for the two monkeys, and even using the top 10 well-tuned neurons can get a comparable performance. These results suggest that the tuned neurons contain the majority of the information related to the corresponding task, and even a small subset of well-tuned neurons is able to achieve an excellent decoding performance.

In Figure 4, the tuned neuron subset in each task contains two types of tuned neurons, that is, the neurons tuned to one property only and the neurons tuned to both conditions. To investigate the role of the neurons tuned to both conditions, we further compare the decoding by adding them into the neurons tuned only to one property.

Figure 5 includes three neurons subsets, namely, the subset a, the subset b, and the subset c, representing, respectively, the neurons tuned only to reaching, the neurons tuned only

to grasping, and the neurons tuned to both conditions. The light blue bars represent the decoding by the subset tuned only to one property (i.e., the subset a in the Reaching task and the subset b in the Grasping task), and the yellow bars represent the decoding by two types of tuned neurons (the neurons tuned to one property only plus the neurons tuned to both conditions, that is, the subset a plus the subset c in the Reaching task and the subset b plus the subset c in the Grasping task). Adding the subset c to the subset a or the subset b, the decoding accuracy significantly increases both in the Reaching and the Grasping tasks, and the improvement is about 50.9%–70.6%. For the significant decoding performance improvement, one possible reason is the greater number of the neurons for the combination of the two types of tuned neurons. Another possibility is that the tuned
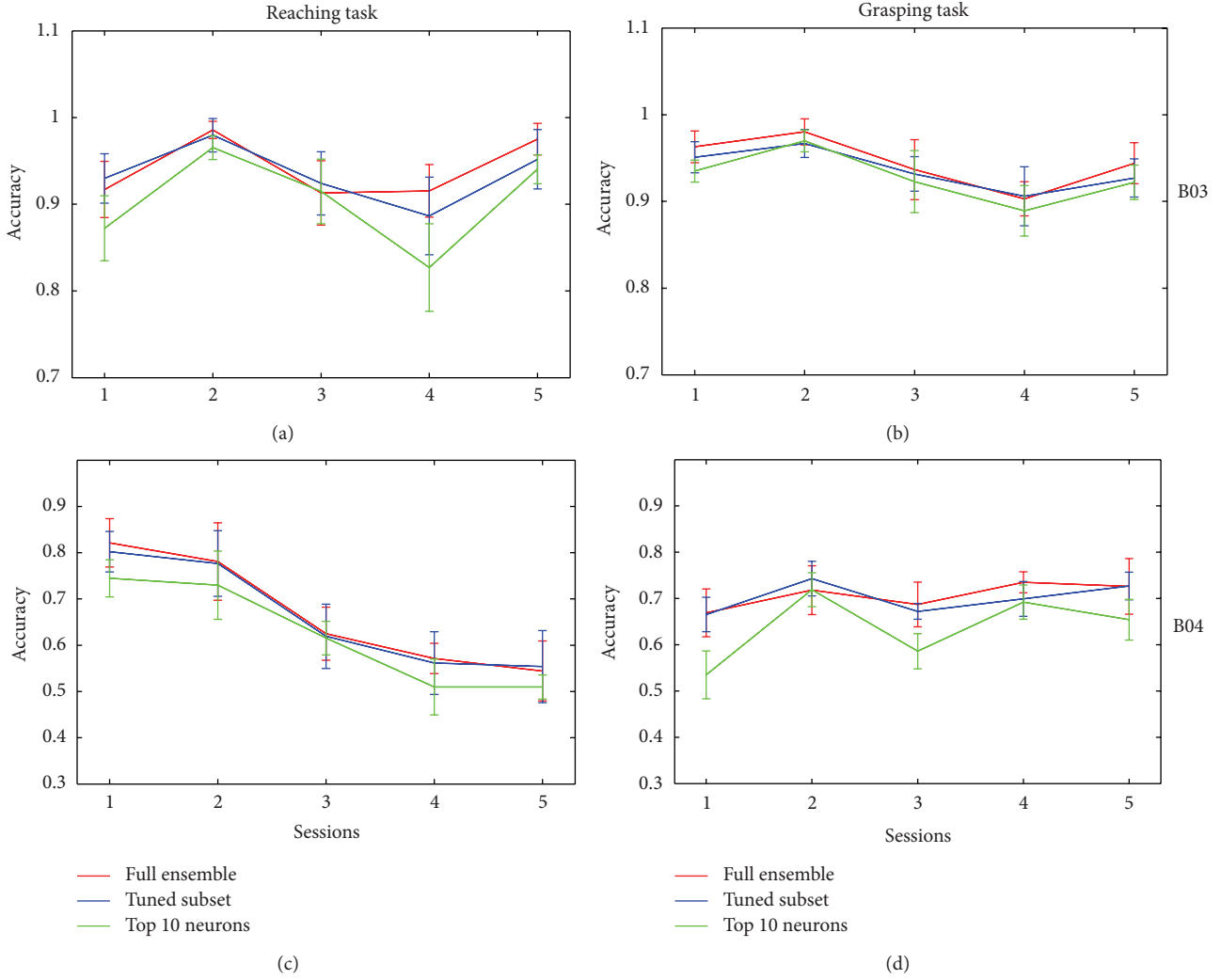
FIGURE 4: The decoding results by full ensemble versus the tuned neuron subset versus the top 10 well-tuned neurons. The x-axis represents the sessions, and the y-axis represents the decoding accuracy. The red line represents the decoding by full ensemble, the blue line represents the decoding by the tuned neuron subset, and the green line represents the decoding by the top 10 well-tuned neurons. The top two panels show the decoding in the Reaching (left) and the Grasping tasks (right) for Monkey B03. The bottom panels are for B04.

neurons in the combined group make a better integration of the neuron circuits that can form a complete and more complicated reaching and grasping action. Hoshi and Tanji in their reviews have demonstrated that the neurons in PMd receive multiple aspects of motor information (including arm use, target location, and instructed movement direction) that encodes in a circuit to form an appropriate action [26–29]. These studies indicate that the PMd has played a major role in integrating multi-information to formulate a complicated movement. Therefore, the combined groups of the tuned neurons may make a better integration of different information that eventually achieves a precise prediction of the output movement.

4. Conclusion and Discussion

In the current work, we have studied the tuning characteristic of the neurons in the PMd area in reaching and grasping,

respectively. We design two BMI behavior paradigms which keep one factor constant but change another. The first condition is a "Reaching task" which requires the monkeys to reach in four different directions but grasp the same object. The other condition is a "Grasping task" which requires the monkeys to grasp four different objects but reach in the same direction. We propose to utilize mutual information (MI) to quantitatively evaluate the neurons' tuning property in both tasks. We find that there exist neurons in PMd that are tuned only to reaching, tuned only to grasping, and tuned to both tasks. When applied with a support vector machine (SVM), the movement decoding accuracy by the tuned neuron subset in either task is quite close to the performance by full ensemble. Our results demonstrate the diversity of neural tuning to reaching and grasping in the PMd area. The tuning characteristic of the PMd neurons in the Reaching and the Grasping tasks can be significant. The tuned neurons contain more information related to the movement.

An interesting phenomenon is that the MI of the neurons tuned to both conditions is larger than that of the neurons tuned to one property only in both tasks. One possible reason may be that the number of the neurons tuned to both conditions is greater than the number of the neurons tuned to one property only. The reveal of the large number of the neurons that tuned to both conditions is consistent with the study [12] that shows there exist PMd neurons that tuned to grasping as well as reaching. The larger number may also cause improvement of the decoding performance when combining such neurons tuned to both conditions with the subset tuned to one property only. Furthermore, the tuned neurons in the combined group may make a better integration of the neuron circuits that can form a more complicated reaching and grasping action, which can contribute to the better decoding of multimotor information from PMd neurons. The mechanism of neural activities for the reaching or grasping task requires further study.

Acknowledgments

References

[1] L. R. Hochberg, M. D. Serruya, G. M. Friehs et al., "Neuronal ensemble control of prosthetic devices by a human with tetraplegia," *Nature*, vol. 442, no. 7099, pp. 164–171, 2006.

[2] J. M. Carmena, M. A. Lebedev, R. E. Crist et al., "Learning to control a brain-machine interface for reaching and grasping by primates," *PLoS Biology*, vol. 1, no. 2, 2003.

[3] M. A. Lebedev, J. M. Carmena, J. E. O'Doherty et al., "Cortical ensemble adaptation to represent velocity of an artificial actuator controlled by a brain-machine interface," *Journal of Neuroscience*, vol. 25, no. 19, pp. 4681–4693, 2005.

[4] M. Velliste, S. Perel, M. C. Spalding, A. S. Whitford, and A. B. Schwartz, "Cortical control of a prosthetic arm for self-feeding," *Nature*, vol. 453, no. 7198, pp. 1098–1101, 2008.

[5] L. R. Hochberg, D. Bacher, B. Jarosiewicz et al., "Reach and grasp by people with tetraplegia using a neurally controlled robotic arm," *Nature*, vol. 485, no. 7398, pp. 372–375, 2012.

[6] J. Wessberg, C. R. Stambaugh, J. D. Kralik et al., "Real-time prediction of hand trajectory by ensembles of cortical neurons in primates," *Nature*, vol. 408, no. 6810, pp. 361–365, 2000.

[7] D. M. Taylor, S. I. H. Tillery, and A. B. Schwartz, "Direct cortical control of 3D neuroprosthetic devices," *Science*, vol. 296, no. 5574, pp. 1829–1832, 2002.

[8] P. K. Artemiadis, G. Shakhnarovich, C. Vargas-Irwin, J. P. Donoghue, and M. J. Black, "Decoding grasp aperture from motor-cortical population activity," in *Proceedings of the 3rd International IEEE EMBS Conference on Neural Engineering*, pp. 518–521, May 2007.

[9] C. E. Vargas-Irwin, G. Shakhnarovich, P. Yadollahpour, J. M. K. Mislow, M. J. Black, and J. P. Donoghue, "Decoding complete reach and grasp actions from local primary motor cortex populations," *Journal of Neuroscience*, vol. 30, no. 29, pp. 9659–9669, 2010.

[10] Y. Hao, Q. Zhang, S. Zhang et al., "Decoding grasp movement from monkey premotor cortex for real-time prosthetic hand control," *Chinese Science Bulletin*, vol. 58, no. 1, pp. 1–9, 2013.

[11] M. Saleh, K. Takahashi, and N. G. Hatsopoulos, "Encoding of coordinated reach and grasp trajectories in primary motor cortex," *Journal of Neuroscience*, vol. 32, no. 4, pp. 1220–1232, 2012.

[12] E. Stark, I. Asher, and M. Abeles, "Encoding of reach and grasp by single neurons in premotor cortex is independent of recording site," *Journal of Neurophysiology*, vol. 97, no. 5, pp. 3351–3364, 2007.

[13] B. R. Townsend, E. Subasi, and H. Scherberger, "Grasp movement decoding from premotor and parietal cortex," *Journal of Neuroscience*, vol. 31, no. 40, pp. 14386–14398, 2011.

[14] Y. Burnod, P. Grandguillaume, I. Otto, S. Ferraina, P. B. Johnson, and R. Caminiti, "Visuomotor transformations underlying arm movements toward visual targets: a neural network model of cerebral cortical operations," *Journal of Neuroscience*, vol. 12, no. 4, pp. 1435–1453, 1992.

[15] J. Messier and J. F. Kalaska, "Covariation of primate dorsal premotor cell activity with direction and amplitude during a memorized-delay reaching task," *Journal of Neurophysiology*, vol. 84, no. 1, pp. 152–165, 2000.

[16] V. Raos, G. Franchi, V. Gallese, and L. Fogassi, "Somatotopic organization of the lateral part of area F2 (dorsal premotor cortex) of the macaque monkey," *Journal of Neurophysiology*, vol. 89, no. 3, pp. 1503–1518, 2003.

[17] V. Raos, M. A. Umiltá, V. Gallese, and L. Fogassi, "Functional properties of grasping-related neurons in the dorsal premotor area F2 of the macaque monkey," *Journal of Neurophysiology*, vol. 92, no. 4, pp. 1990–2002, 2004.

[18] R. P. Dum and P. L. Strick, "Frontal lobe inputs to the digit representations of the motor areas on the lateral surface of the hemisphere," *Journal of Neuroscience*, vol. 25, no. 6, pp. 1375–1386, 2005.

[19] Q. S. Zhang, S. M. Zhang, Y. Y. Hao et al., "Development of an invasive brain-machine interface with a monkey model," *Chinese Science Bulletin*, vol. 57, no. 16, pp. 2036–2045, 2012.

[20] M. A. L. Nicolelis, A. A. Ghazanfar, B. M. Faggin, S. Votaw, and L. M. O. Oliveira, "Reconstructing the engram: simultaneous, multisite, many single neuron recordings," *Neuron*, vol. 18, no. 4, pp. 529–537, 1997.

[21] Y. Wang, J. C. Principe, and J. C. Sanchez, "Ascertaining neuron importance by information theoretical analysis in motor Brain-Machine Interfaces," *Neural Networks*, vol. 22, no. 5-6, pp. 781–790, 2009.

[22] Y. Wang and J. C. Principe, "Instantaneous estimation of motor cortical neural encoding for online brain-machine interfaces," *Journal of Neural Engineering*, vol. 7, no. 5, Article ID 56010, 2010.

[23] V. N. Vapnik, *Statistical Learning Theory*, Wiley-Interscience, 1998.

[24] C. C. Chang and C. J. Lin, "LIBSVM: a Library for support vector machines," *ACM Transactions on Intelligent Systems and Technology*, vol. 2, no. 3, article 27, 2011.

[25] M. A. Umilta, T. Brochier, R. L. Spinks, and R. N. Lemon, "Simultaneous recording of macaque premotor and primary motor cortex neuronal populations reveals different functional contributions to visuomotor grasp," *Journal of Neurophysiology*, vol. 98, no. 1, pp. 488–501, 2007.

[26] E. Hoshi and J. Tanji, "Distinctions between dorsal and ventral premotor areas: anatomical connectivity and functional properties," *Current Opinion in Neurobiology*, vol. 17, no. 2, pp. 234–242, 2007.

[27] E. Hoshi and J. Tanji, "Functional specialization in dorsal and ventral premotor areas," *Progress in Brain Research*, vol. 143, pp. 507–511, 2004.

[28] A. R. Mitz, M. Godschalk, and S. P. Wise, "Learning-dependent neuronal activity in the premotor cortex: activity during the acquisition of conditional motor associations," *Journal of Neuroscience*, vol. 11, no. 6, pp. 1855–1872, 1991.

[29] S. T. Grafton, A. H. Fagg, and M. A. Arbib, "Dorsal premotor cortex and conditional movement selection: a PET functional mapping study," *Journal of Neurophysiology*, vol. 79, no. 2, pp. 1092–1097, 1998.

Research Article

A Mixed L2 Norm Regularized HRF Estimation Method for Rapid Event-Related fMRI Experiments

Yu Lei, Li Tong, and Bin Yan

China National Digital Switching System Engineering and Technological Research Center, Zhengzhou 450002, China

Correspondence should be addressed to Bin Yan; tom.yan@gmail.com

Brain state decoding or "mind reading" via multivoxel pattern analysis (MVPA) has become a popular focus of functional magnetic resonance imaging (fMRI) studies. In brain decoding, stimulus presentation rate is increased as fast as possible to collect many training samples and obtain an effective and reliable classifier or computational model. However, for extremely rapid event-related experiments, the blood-oxygen-level-dependent (BOLD) signals evoked by adjacent trials are heavily overlapped in the time domain. Thus, identifying trial-specific BOLD responses is difficult. In addition, voxel-specific hemodynamic response function (HRF), which is useful in MVPA, should be used in estimation to decrease the loss of weak information across voxels and obtain fine-grained spatial information. Regularization methods have been widely used to increase the efficiency of HRF estimates. In this study, we propose a regularization framework called mixed L2 norm regularization. This framework involves Tikhonov regularization and an additional L2 norm regularization term to calculate reliable HRF estimates. This technique improves the accuracy of HRF estimates and significantly increases the classification accuracy of the brain decoding task when applied to a rapid event-related four-category object classification experiment. At last, some essential issues such as the impact of low-frequency fluctuation (LFF) and the influence of smoothing are discussed for rapid event-related experiments.

1. Introduction

In the last decade, multivoxel pattern analysis (MVPA) has become a widely used analysis method in cognitive neuroscience especially in decoding brain activities at different states [1–4]. MVPA mainly focuses on single-trial blood-oxygen-level-dependent (BOLD) responses to identify different brain states. In some experiments, to obtain an effective and reliable classifier or computational model, numerous samples should be collected using rapid event-related designs [3]. However, for rapid event-related designs, the overlapping of BOLD signals in the time domain encumbers the extraction of a real trial-specific BOLD response, which is important for MVPA. Hence, the accurate estimation of a trial-specific BOLD response is a challenging problem in rapid event-related MVPA.

Traditional estimating approaches are mainly classified into two groups. Model-based methods involve prior hemodynamic response function (HRF), whereas model-free methods have no assumptions on the shape of HRF. Model-based methods differ in the assumptions of the shape of HRF,

such as the canonical double gamma function [5], Poisson function [6], radial basis function [7], and inverse logit function [8]. Previous reports revealed the capability of HRFs in the traditional univariate statistical analysis especially in activation-based analysis. However, most brain state decoding experiments or information-based analysis aim to obtain fine-grained spatial activation patterns that can help improve the performance of our decoding model [9]. Therefore, an accurate estimation that reflects real neural activities is necessary to obtain more fine-grained spatial activation patterns. In these cases, we cannot ignore the high variation in the temporal responses of different voxels across individuals as well as across tasks, regions of the brain, and different days within individuals [10]. Hence, model-free methods that are more sensitive and accurate have been widely used [11, 12].

For a model-free method, a voxel-specific HRF contains one free parameter for each time point. Thus, an HRF of arbitrary shape of each voxel that provides much more flexibility in data analysis can be obtained. In a model-free method, the first step is always to estimate a voxel-specific

HRF and use this HRF to deconvolve BOLD signals [13]. When estimating a voxel-specific HRF, the BOLD response is often assumed to be a linear time-invariant (LTI) system [14]. Then, one of the main solutions is to represent the HRF with a linear combination of basis functions [15, 16]. Another solution is to treat the HRF at each point as a free parameter [17]. This paper alternatively focuses on the latter one. Modeling low-frequency fluctuation (LFF) is another problem in HRF estimation that should be addressed [18]. The linear drift in the obtained images is a challenging problem in fMRI data analysis because of the poor HRF estimates. A simple strategy for removing linear drift is to detrend time-series data as a preprocessing step [19, 20]. Alternatively, LFF may be modeled in a nuisance matrix consisting of some basis functions as regressors. This strategy enables not only linear detrending but also LFF removal to some extent [21], resulting in a more flexible and efficient detrending model.

Given that BOLD images have high noise, regularization is a popular technique that allows constraints to be imposed on HRF estimates to suppress the impact of noises when employing a parameter-free model. The smooth finite-impulse response (FIR) method [22] is a good example of regularization to smooth estimates. Tikhonov regularization may also be used to impose smoothness [23]. In [24, 25], Tikhonov regularization is combined with generalized cross-validation (GCV) to reduce the computational burden involved in parameter selection. Accordingly, Tikhonov regularization is also used in this paper. However, smoothness is only one of the local features of a signal, which could not reflect the global structure of a signal. Therefore, in extremely rapid event-related experiments, considering only smoothness is not enough to suppress the overlapping of different events, resulting in deformed HRF shape. Hence, we add an additional L2 regularization component into the estimation model with Tikhonov regularization, called mixed L2 norm (MN) regularization. Using this regularization method, we cannot only retain the smooth feature of HRFs but also prevent the significant overlapping of adjacent events. Furthermore, this method is a parameter-free model, indicating that it is adaptive to the variability of HRFs across voxels and individuals.

We first outlined the HRF and response estimation methods, especially the proposed MN estimation method and the classification approach used to assess their performances. All methods were applied to four-category object classification data to compare the classification accuracy. We also compared the classification performances between object responsive (OR) voxels and voxels in the early visual cortex. Finally, we discussed the role of LFF and the impact of smoothness in MVPA.

2. Materials and Methods

2.1. Subjects. Ten healthy subjects (six males and four females) participated in this fMRI study. The study was approved by the Institutional Review Board of China National Digital Switching System Engineering and Technology Research Center. All subjects provided written informed consent and had normal vision.

2.2. Stimuli. The stimuli consisted of four categories (car, animal, building, and human face) of color images, including 50 different images in each category. All images were cropped to the center (700 pixels × 700 pixels) and placed onto a gray-scale background.

Visual stimuli were rear-projected onto a screen in the scanner bore using a luminance-calibrated LCD projector driven by a PC. The subjects viewed the screen from a mirror. The display resolution was 1024 × 768, and the stimulus presentation script was written using MATLAB (The Mathworks) and Psychtoolbox 3.0 (http://psychtoolbox.org/).

2.3. Experimental Design. Each subject participated in three task runs, four localizer runs, and one retinotopic mapping run. In the task runs, images were presented in a 4 s stimulus trial. In each trial, an image was first presented for 2 s, and the gray background was presented for the last 2 s. Each presentation consisted of an image being periodically flashed ON-OFF, where ON corresponds to the presentation of the image for 200 ms and OFF corresponds to the presentation of the gray background for 200 ms. The first two task runs consisted of 70 distinct images randomly presented once for each time. The last task run consisted of 60 distinct images also randomly presented once for each time. After every five stimulus trials, a blank trial that lasted for 4 s was conducted as a break.

In localizer runs, the subjects were presented with blocks of images for each category. Each run consisted of 12 blocks, with 6 task blocks and 6 control blocks. The task block lasted the same time as the control block for 30 s. Each localizer run consisted of six images randomly selected from the same image category. Each task block consisted of an image being periodically flashed ON-OFF, where ON corresponds to the presentation of the image for 200 ms and OFF corresponds to the presentation of the gray background for 200 ms. The OR voxels were a set of voxels that were strongly activated in at least one localizer run (*t*-test, $P = 0.005$, family-wise error corrected).

Another standard retinotopic mapping run with polar stimuli was performed to delineate the early visual areas on a flattened cortex.

2.4. Data Acquisition. The data were collected using a 3-T GE Discovery 750 (General Electric, Fairfield, CT, USA) scanner with a standard head coil at the Imaging Center of Henan Province. For each subject, a standard gradient-echo-planar imaging series was used to collect functional images with the following parameters: repetition time (TR), 2000 ms; echo time (TE), 30 ms; field of view, 220 mm × 220 mm; matrix size, 64 × 64; 39 slices; slice thickness, 3.5 mm; flip angle (FA), 80°; and voxel size, 3.4 mm × 3.4 mm × 3.5 mm. In addition, a high-resolution three-dimensional T1-weighted anatomical image was acquired (TR, 8.268 ms; TE, 3.24 ms; FA, 12°).

2.5. Data Preprocessing. All fMRI data were preprocessed with SPM8 (Statistical Parametric Mapping, http://www.fil.ion.ucl.ac.uk/spm/software/spm8/) and REST (http://www.restfmri.net/). The first 10 volumes of each run were discarded because of the instability of initial magnetic resonance

imaging signal and adaptation of subjects to the circumstance. Then, slice timing was performed on all functional images. The images were realigned to the first image in the first run for motion correction. We used REST to remove the linear drift in each run.

For retinotopic mapping analysis, FreeSurfer (http://surfer.nmr.mgh.harvard.edu/) was used to reconstruct a T1-weighted anatomical image. Then, the realigned retinotopic mapping images were registered to the anatomical image to obtain the registration file. The following retinotopic analysis was consistent with [26].

2.6. HRF Estimation

2.6.1. Basic Model. In our model, the BOLD signal is assumed to be an LTI system with respect to the stimulus. Then, the measured BOLD time series is modeled as the convolution of an input signal. The hemodynamic response function is as follows:

$$y(t) = h(t) * s(t) = \sum_{k=0}^{L-1} h(k) s(t-k), \tag{1}$$

where $y(t)$ represents the fMRI time series, $h(t)$ represents the HRF, $s(t)$ represents the stimulus vector, and L indicates the discrete time length of the HRF. This model can also be rewritten in matrix form:

$$\mathbf{y} = \mathbf{Sh}, \tag{2}$$

where $\mathbf{y}$ is a column vector of length N (N being the number of time points of the fMRI time series), $\mathbf{S}$ is the stimulus convolution matrix with a dimension of $N \times L$, and $\mathbf{h}$ is a column vector of length L. The stimulus convolution matrix consists of shifted versions of a binary sequence, where ones indicate event occurrences.

Considering LFF and other noises, additional nuisance parts should be added to the above model. In this case, a set of Legendre polynomials of degrees 0 through 3, which are pairwise orthogonal, is used as regressors to compensate for LFF [21]. An autoregressive stochastic process of order one is also added [27]. Upon the incorporation of the nuisance parts, the HRF estimating model can be written as follows:

$$\mathbf{y} = \mathbf{Sh} + \mathbf{Pb} + \boldsymbol{\epsilon}, \tag{3}$$

where $\mathbf{P}$ represents the nuisance matrix of dimension $N \times B$ consisting of Legendre polynomials of degrees 0 through 3, $\mathbf{b}$ is a column nuisance parameter vector of length 4, and $\boldsymbol{\epsilon}$ represents the stochastic noise.

2.6.2. Least-Square Estimation with AR (1) (LSAR) Noise Model. The LSAR of the HRF estimation problem can be achieved through the following steps (details can be found in [28]):

(1) perform the ordinary least squares (OLS) method on $= \mathbf{W}[\mathbf{h} \ \ \mathbf{b}]^{\mathrm{T}} + \boldsymbol{\epsilon}$, where $\mathbf{W} = [\mathbf{S} \ \ \mathbf{P}]$, to obtain $\boldsymbol{\epsilon}$;

(2) use $\boldsymbol{\epsilon}$ to create a transformation matrix $\mathbf{L}$ with autocorrelation coefficients. Then, transform the original

regression model $\mathbf{y} = \mathbf{W}[\mathbf{h} \ \ \mathbf{b}]^{\mathrm{T}} + \boldsymbol{\epsilon}$ using $\mathbf{L}$ to $\mathbf{Ly} = \mathbf{LW}[\mathbf{h} \ \ \mathbf{b}]^{\mathrm{T}} + \mathbf{L}\boldsymbol{\epsilon}$;

(3) conduct an OLS regression on the transformed formulation $\widetilde{\mathbf{y}} = \widetilde{\mathbf{W}}[\mathbf{h} \ \ \mathbf{b}]^{\mathrm{T}} + \widetilde{\boldsymbol{\epsilon}}$ to obtain the real $\widehat{\mathbf{h}}$.

2.7. MN Estimation. Regularization is a common scalarization method for solving problems such as in the above-mentioned basic model. The most common form of regularization is called Tikhonov regularization, which results in a convex optimization problem [29]:

$$\text{minimize } \|\mathbf{Ax} - \mathbf{b}\|^2 + \delta \|\mathbf{x}\|^2. \tag{4}$$

For various values of $\delta > 0$, this problem has the following analytical solution:

$$\mathbf{x} = \left(\mathbf{A}^{\mathrm{T}}\mathbf{A} + \delta \mathbf{I}\right)^{-1} \mathbf{A}^{\mathrm{T}}\mathbf{b}. \tag{5}$$

This optimization problem can be extended in several ways. One useful extension is to add a regularization term with the form of $\|\mathbf{Dx}\|$ in place of $\|\mathbf{x}\|$. In many cases, the matrix $\mathbf{D}$ represents an approximate differentiation or second-order differentiation operator; so $\|\mathbf{Dx}\|$ represents a measure of the variation or smoothness of $\mathbf{x}$. In the HRF estimation, we assume that it is smooth; so the second-order differentiation operator $\mathbf{D}$ is used in the regularization term to achieve a smooth result:

$$\text{minimize } \|\mathbf{Ax} - \mathbf{b}\|_2 + \delta \|\mathbf{Dx}\|_2. \tag{6}$$

Another problem in the HRF estimation of rapid event-related experiments is the overlapping of adjacent events. When the interstimulus interval (ISI) is extremely short (e.g., 2 s), overlapping encumbers the calculation of the hemodynamic response function because the BOLD responses evoked by different events could not be separated successfully. To address the instability of the estimate, we also assume that the BOLD responses evoked by pulsed stimuli quickly return to the baseline. In this study, we assume that the BOLD responses return to the baseline 10 s after pulsed stimuli. In addition, the HRF should start from zero. Based on these assumptions, we can use a regularization term to constrain the solution. In our study, we aim to suppress the impact of overlapping, retaining the profile of HRF. Thus, to depict the character of the hemodynamic response, we use a regularization term as follows:

$$\text{minimize } \|\mathbf{Ax} - \mathbf{b}\|_2 + \gamma \sum_{i=1, i>10} x(i)^2. \tag{7}$$

This formulation can be written in matrix form as follows:

$$\text{minimize } \|\mathbf{Ax} - \mathbf{b}\|_2 + \gamma \|\mathbf{Cx}\|_2, \tag{8}$$

where

$$\mathbf{C} = \begin{bmatrix} 1 & & & & & & \\ & 0 & & & & & \\ & & \ddots & & \mathbf{0} & & \\ & & & 0 & & & \\ & \mathbf{0} & & & 1 & & \\ & & & & & \ddots & \\ & & & & & & 1 \end{bmatrix}. \tag{9}$$

FIGURE 1: Simulation results of the HRF estimates using Tikhonov regularization. The x-axis indicates the time relative to the event onset (TR = 2 s), and the y-axis indicates the BOLD signal. Each HRF estimate was normalized by dividing it by its maximum value.

Considering the above-mentioned regularization terms, the mixed L2 norm (MN) regularization could be written as

$$\text{minimize } \left\| \mathbf{Sh} + \mathbf{Pb} - \mathbf{y} \right\|_2^2 + \delta^2 \left\| \mathbf{Dh} \right\|_2^2 + \gamma^2 \left\| \mathbf{Ch} \right\|_2^2. \quad (10)$$

Then, the HRF estimator derived is

$$\widehat{h} = \left(\mathbf{S^T J S} + \delta^2 \mathbf{D^T D} + \gamma^2 \mathbf{C^T C} \right) \mathbf{S^T J y}, \quad (11)$$

where $\mathbf{J} = (\mathbf{I} - \mathbf{P P^T})$. δ and γ are trade-off parameters to adjust the weight of the different regularization terms.

Using this new regularization term, smoothness and prior information about the HRF shape can be added to the estimation process. Hence, the noise caused by short ISI is removed.

2.8. Simulation Study: Tikhonov Regularization versus MN Regularization. To understand the difference between Tikhonov regularization and MN regularization, we first compared the HRF estimation result in a simulation study. Figure 1 shows the result of this simulation study using Tikhonov regularization, where the ISI was set to 2 s and the duration of stimuli was also set to 2 s. Time series was produced by convolving the stimulus vector with canonical double gamma HRF. Then, the Gaussian white noise of different signal-to-noise ratios (SNRs) was added to it. The result implied that with decreasing SNR, the overlapping

increasingly destabilized the tail of the HRF estimates. Figure 2 shows the result of the same simulation study using MN regularization. Compared with Figure 1, the result shows that when an additional regularization term was employed, most of the instability in the HRF estimates was suppressed. Based on this simulation study, the MN regularization method showed a great improvement in estimating HRF in a rapid event-related experiment.

2.9. Response Estimation Method. When voxel-specific HRFs are computed, we should deconvolve the time-series with the HRFs to obtain the real trial-specific BOLD responses. Reference [13] compared many deconcolving methods for multivoxel pattern classification analysis, such as FIR, ridge regression, partial least square, and support vector regression. In the following section, we will focus on the least square separate (LS-S) model.

In a rapid event-related fMRI data analysis, the traditional general linear model (GLM) suffers from collinearity induced by the correlation between trial-specific regressors. This collinearity could result in highly variable and unreliable estimates because of the lack of information that is unique to specific trials [13]. To reduce collinearity, we can modify the strategy of regressor construction or use regularization methods such as ridge regression [30] and partial least square [31]. In this paper, we use a regressor construction strategy called LS-S [13], which runs a GLM for each trial. The trial
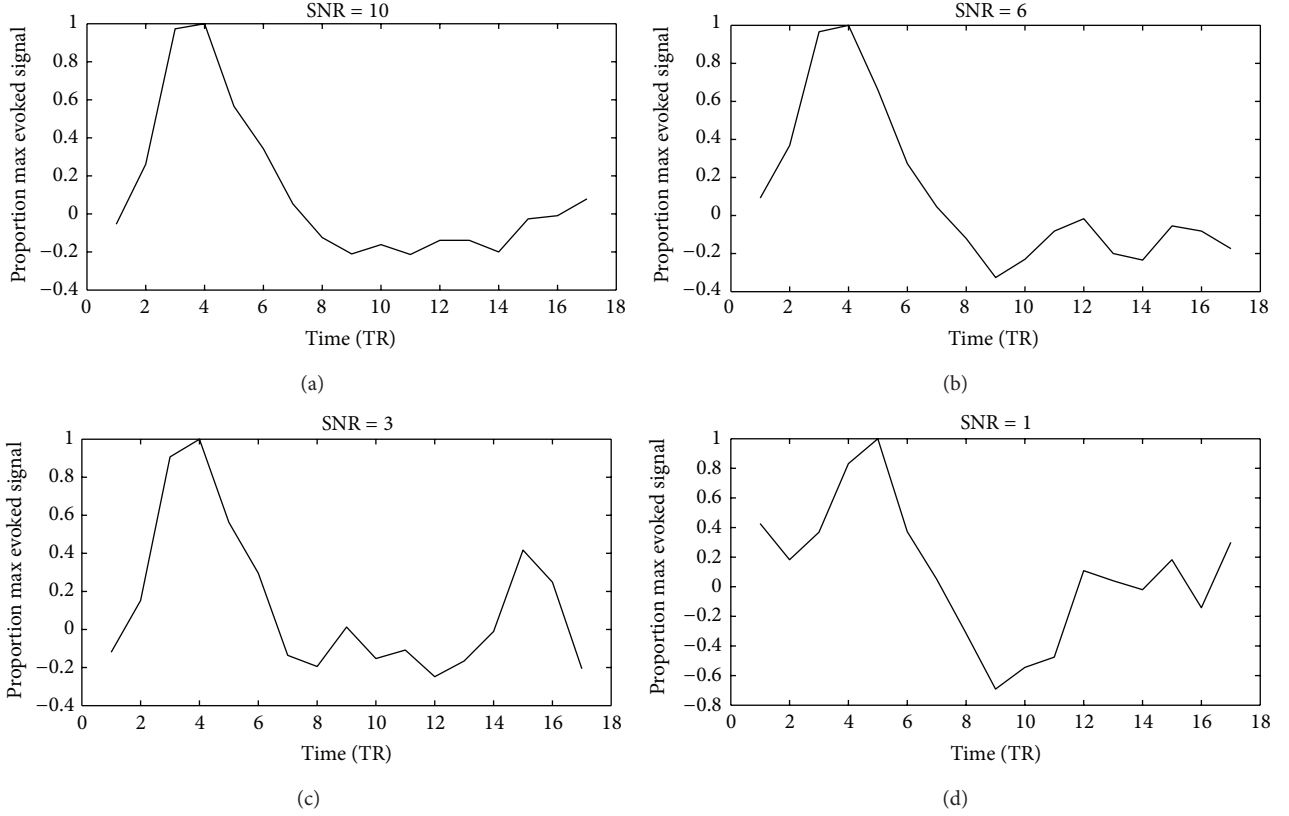
(a)

(b)

(c)

(d)
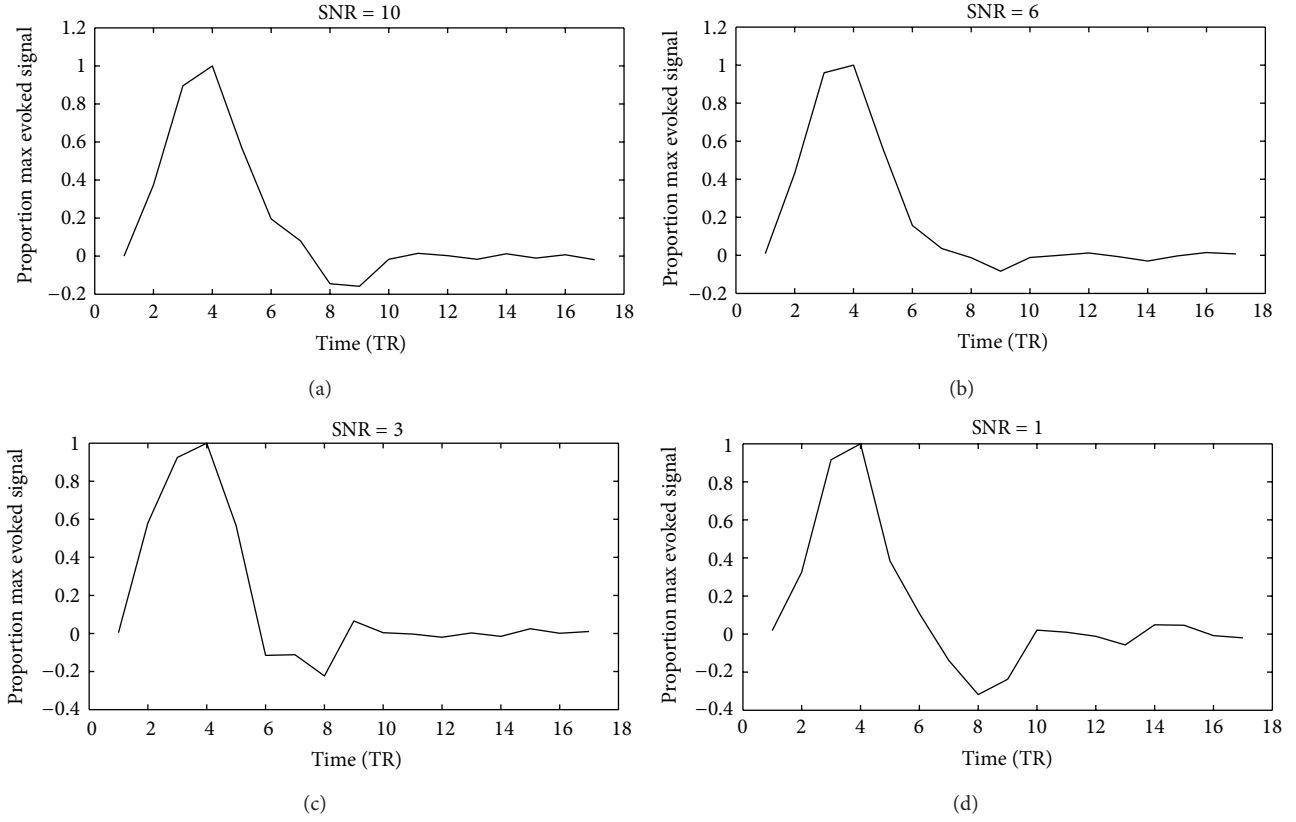
FIGURE 2: Simulation results of the HRF estimates using mixed-norm regularization. The x-axis indicates the time relative to the event onset (TR = 2 s), and the y-axis indicates the BOLD signal. Each HRF estimate was normalized by dividing it by its maximum value.
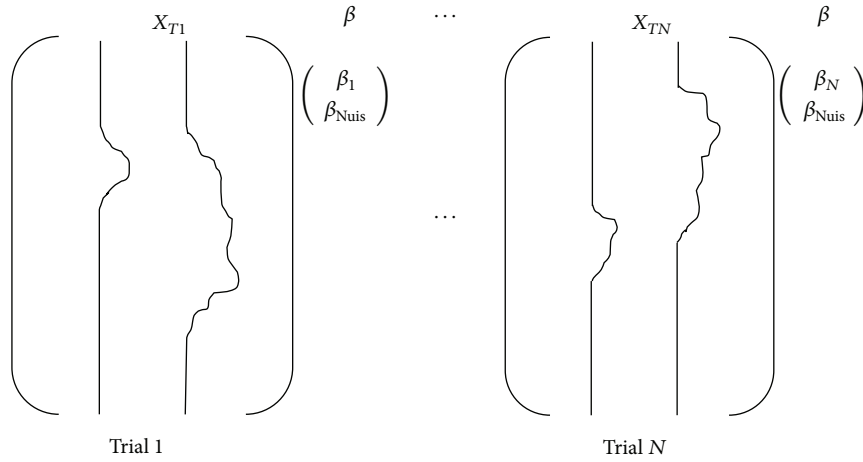
FIGURE 3: LS-S model. The design matrix has two regressors, one for the trial of interest and another for all other trials simultaneously. X_{T1} aims to obtain the activation estimate for trial 1. Therefore, a regressor is conducted for trial 1, and a second regressor is conducted for all other trials. The estimate for β_1 based on this design is the estimate activation for trial 1. This method is repeated N times to obtain the estimates for all N trials.

is modeled as the regressor of interest, and all other trials are combined into a single nuisance regressor. Thus, if we have N trials, we need to run the LS-S model N times to obtain each trial-specific response. The LS-S model is illustrated in Figure 3.

2.10. Classification Method and Statistical Analysis. As a widely used linear classifier, linear support vector machine (SVM) has been proved efficient in handling high-dimensional data. In our study, we also used the linear SVM based on LIBSVM [32] to compare the classification

TABLE 1: Mean number of voxels across all subjects used in different methods. Unselected voxels were all located in OR areas or early visual areas. Voxels were selected from the unselected voxel set based on the selection criterion. Object responsive (OR) voxels were strongly activated in localizer runs (t-test, $P = 0.005$, familywise error corrected). Retinovoxels were located in the early visual area, which was delineated via retinotopic mapping analysis.

	OLS	LS-AR (1)	MN
OR			
Unselected	2682	2682	2682
Selected	387 ± 127	425 ± 163	1334 ± 246
Retino			
Unselected	1290	1290	1290
Selected	221 ± 103	276 ± 112	721 ± 175

performances of the different estimation methods. The dataset was divided into five parts, and a fivefold "leave-one-out" cross-validation was applied to obtain the average classification accuracy. Lastly, the classification performances of the different methods were statistically compared using Wilcoxon signed-rank pair test.

3. Results and Discussion

This study aims to find an efficient method for estimating voxel-specific HRFs in a rapid event-related design fMRI study, which could deconvolve the BOLD time series to obtain the real BOLD activation signals associated with specific stimuli. The three task runs are divided into two parts. The third task run with 60 images is used to estimate voxel-specific HRFs and the other two task runs are used for classification analysis. In the following, we present the results of the analysis. Some essential aspects of this problem are also discussed.

3.1. Comparison of Different HRF Estimation Methods. To evaluate the performance of different HRF estimation methods in decoding brain states, we compared the classification accuracy of OLS, LS-AR (1), MN, and canonical double gamma HRF. Given the noise of the fMRI BOLD signals, we found that not all of the estimated HRFs of the voxels are acceptable. Considering this problem, we proposed a voxel selection criterion based on the prior knowledge about the BOLD responses. We assumed that $h(0)$ was near zero and that the minimum value of normalized $h(t)$ could not be less than -1. Furthermore, after 12 s, the BOLD responses should fall to the baseline. In other words, the voxel should be removed if it satisfies the following condition: $|h(0)| > 0.3$, $\max(h(t \mid t > 12 \text{ s})) > 0.4$, and $\min(h(t)) > -1$, where $h(t)$ is the estimated HRF of a voxel.

Table 1 shows the mean number of voxels across all subjects before and after selection. The result indicates that good HRF estimates for all voxels could not be obtained in OR areas or early visual areas because of the noise in the time series. Therefore, invalid voxels were eliminated under the above-mentioned selection criterion. In addition, owing

to the regularization, we obtained more voxels using the new MN estimation method.

In the simulation study, the MN method showed its capability in rapid event-related experiments. Here, the HRF estimation of the different methods was compared using real data. Figure 4 shows one of the subjects' estimated HRFs in the OR areas. Figures 4(a) and 4(b) show the significant overlapping of the time series and a fake peak in the end of the estimated HRF using the OLS or LS-AR (1) method. However, in the MN estimation method, the fake peak was strongly suppressed because of the additional regularization term, as shown in Figure 4(c). Figure 4(d) shows the canonical double gamma function [33].

The shape of the estimated HRFs intuitively showed the difference of the investigated methods. However, the shape could not be used to quantify this difference. Therefore, the classification accuracy based on real data was used to compare quantitatively the different methods. Figure 5 shows the mean classification accuracy of the different HRF estimation methods across all subjects. For the different estimation methods, the classification results were 80.96%, 72.25%, 69.76%, 72.74%, 72.25%, and 71.51%. The results indicate that MN performed significantly better than the other five methods (Wilcoxon signed-rank pair test, $P = 0.01$).

The number of voxels after selection by different methods was different. The effect of the size of voxel set should therefore be considered. We applied MN to the voxel set selected by OLS or LSAR to investigate the impact of the size of voxel set. Figure 6 shows that MN also performed significantly better than OLS and LSAR using the voxels selected by LSAR or OLS (Wilcoxon signed-rank pair test, $P = 0.01$). For the different estimation methods, the classification results were 80.96%, 72.25%, 69.76%, 79.59%, and 78.88%. This result indicates that the MN estimation method improved the classification accuracy and not the number of voxels.

Recent studies have illustrated the shape of HRF [5]. As a widely known model, the canonical HRF has been successfully used in fMRI studies, especially in univariate analysis or activation-based analysis. However, with the development of high-resolution fMRI, information-based analysis was applied for brain decoding [34]. In the present study, when voxel-specific HRFs were used, the classification accuracy significantly increased.

Many studies suggested that the fMRI time series has temporal autocorrelation between residual errors [27]. However, the present results indicated no significant differences in the classification accuracy between the least-square models with and without AR (1).

In our MN estimation method, no assumption is made on the noise model, and the only task is the selection of regularization parameters. Considering that the selection of proper regularization parameters is one of the most important steps in solving regularization problems, many articles focused on the regularization parameter selection strategy to improve the performance of regularization, such as generalized cross-validation (GCV) [35], Bayesian information criterion (BIC) [36], and Akaike information criterion (AIC) [37]. In the present study, to simplify the problem, we selected the best

(a)

(b)

(c)

(d)
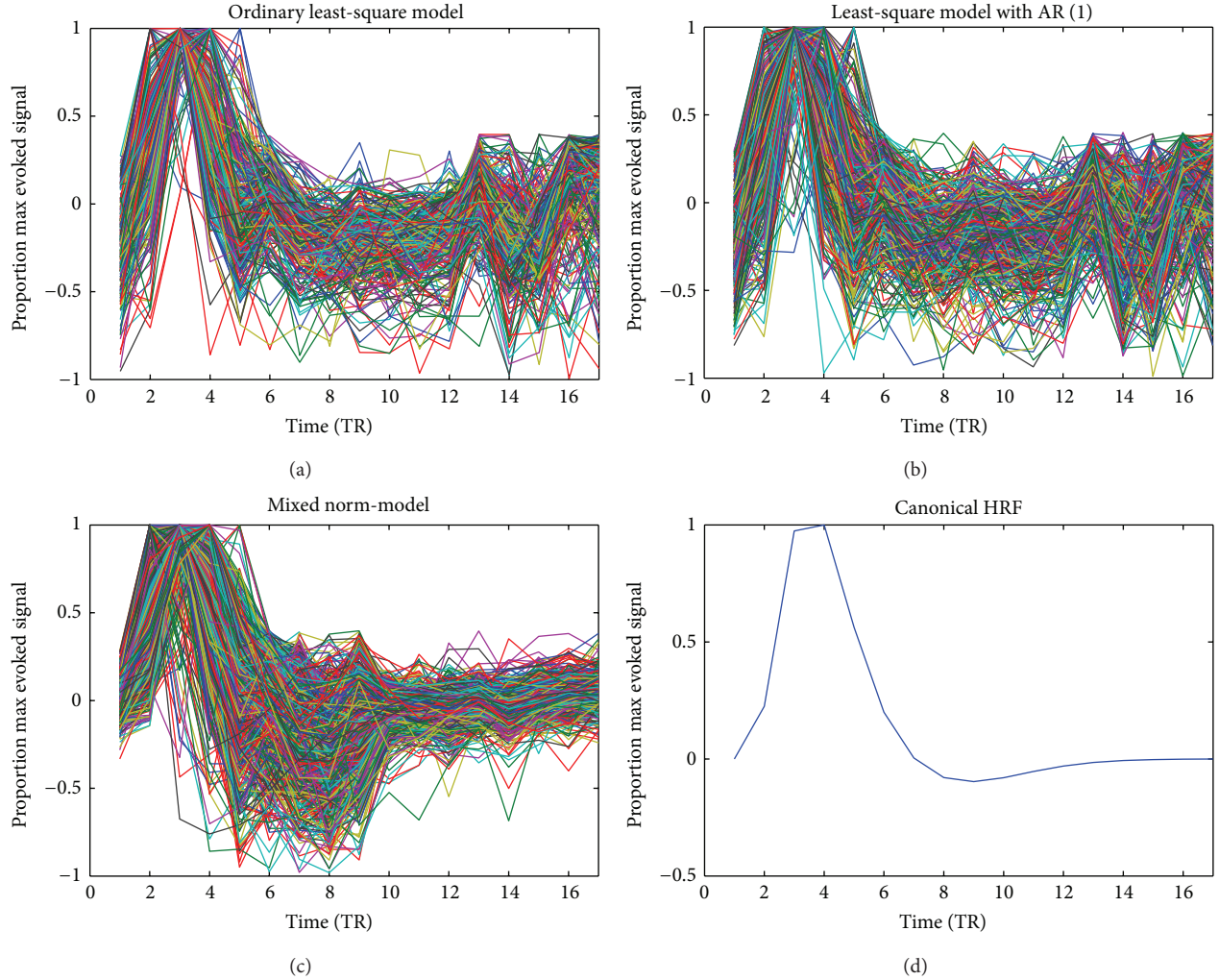
FIGURE 4: Inspection of the HRF estimates of the different methods. The lines in different colors represent the different HRF estimates of the voxels. The x-axis indicates the time relative to the event onset (TR = 2 s), and the y-axis indicates the BOLD signal. Each HRF estimate was normalized by dividing it by its maximum value.

one from a set of parameters. Although this strategy might not identify the best parameters, this method also performed significantly better than the other methods.

3.2. Impact of Smoothing on Brain Decoding. We compared the classification accuracy of the smoothed and unsmoothed data to investigate the impact of smoothing on brain decoding. Figure 7 shows the classification accuracies of the different HRF estimation methods. For the smoothed data, the classification results were 81.03%, 69.74%, 67.23%, 74.39%, 72.49%, and 70.3%. For the unsmoothed data, the classification results were 80.96%, 72.25%, 69.76%, 72.74%, 72.25%, and 71.51%. The results implied no significant difference between the smoothed and unsmoothed data in brain decoding (Wilcoxon signed-rank pair test, $P = 0.01$). This conclusion is consistent with the finding of a previous study [38].

Smoothing is a standard preprocessing step in traditional activation-based or univariate analysis. However, in MVPA,

whether smoothing should be conducted is unclear [38–40]. Many studies smooth the fMRI data before analysis to increase the SNR [41–43]. However, considering that smoothing may blur data, some studies omitted smoothing in analysis [1–3]. To preserve fine-grained pattern information, [39] suggested that smoothing should be omitted or strongly reduced.

Our result in this study implies that smoothing may not decrease the sensitivity and performance of brain decoding. However, this result does not mean that smoothing does not blur the fine-grained weak spatial information across voxels. A detailed explanation is given by [40]. If a study does not focus on subvoxel information sources or fine-grained information, smoothing would not matter.

3.3. Effect of LFF. The LFF compensation model is widely used in estimating voxel-specific HRFs. Figure 8 shows a comparison of the estimated HRF using LS-AR (1) with and without the LFF model in one of our subjects. Based on the
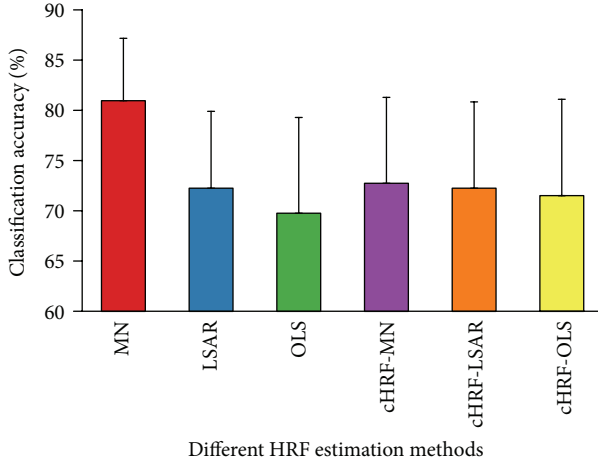
FIGURE 5: Bars show the classification accuracies of the different HRF estimation methods (cHRF-MN, canonical HRF with voxels selected by MN; cHRF-LSAR, canonical HRF with voxels selected by LSAR; and cHRF-OLS, canonical HRF with voxels selected by OLS). Error bars show the standard error of the mean classification accuracy across subjects.
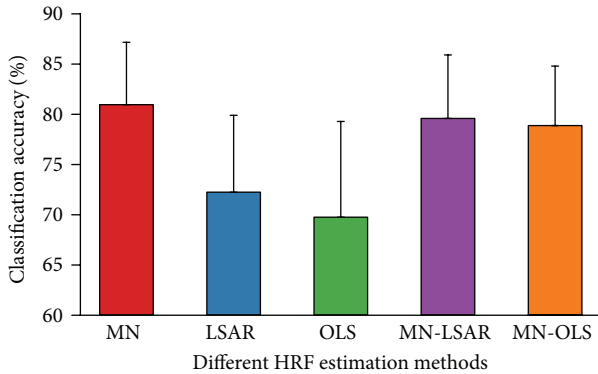
FIGURE 6: Effect of the size of voxel set. MN-LSAR, mixed-norm estimation was applied to the voxel set selected by LSAR; MN-OLS, mixed-norm estimation was applied to the voxel set selected by OLS. Error bars show the standard error of the mean classification accuracy across subjects.

results, LFF had a large impact on HRF estimates. However, when we deconvolved the BOLD response from the fMRI time series, the impact of LFF was ignored. By contrast, in the MVPA analysis, wherein one of our goals is to exploit the information of weakly activated voxels, LFF significantly reduced the classification accuracy.

In the current study, we compared the classification performances of the response estimation method with and without the LFF compensation component. Figure 9 illustrates the effect of LFF in brain decoding. For the model with LFF, the classification results were 80.96%, 72.25%, 69.76%, 72.74%, 72.25%, and 71.51%. For the model without LFF, the classification results were 73.81%, 65.04%, 63.3%, 72.09%, 71.1%, and 69.23%. These results indicated that the model with LFF compensation performed significantly better than that

FIGURE 7: Comparison of smooth and unsmooth data. Classification accuracies estimated with fivefold leave-one-out cross-validation. Each method was applied to both unsmooth and smooth data to investigate the impact of smoothing. cHRF-MN, canonical HRF with voxels selected by MN; and cHRF-LSAR, canonical HRF with voxels selected by LSAR; cHRF-OLS, canonical HRF with voxels selected by OLS. Error bars show the standard error of the mean classification accuracy across subjects.

without LFF compensation (Wilcoxon signed-rank pair test, $P = 0.01$). Interestingly, no significant difference was found between the models with and without the LFF compensation component using canonical HRF. Our results implied that LFF plays an important role not only in HRF estimation but also in response estimation.

3.4. Classification Performances of Different Masks. For each subject, we defined a mask of OR voxels in the occipital and temporal cortex that responded strongly in at least one of the four localizer runs. Then, nearly 3000 voxels were selected for each subject. The voxels in these areas were previously shown to provide information about object category [1, 44]. We also tested the classification accuracy in early visual areas, which were delineated by retinotopic mapping [26]. The classification accuracies in both masks are summarized in Figure 10. The classification results for the OR voxels were 80.96%, 72.25%, 69.76%, 72.74%, 72.25%, and 71.51%. The classification results for the retinovoxels were 79.99%, 65.59%, 64.67%, 68.83%, 66.24%, and 66.05%. The results showed that the OR voxels performed better than the retinovoxels in all six cases (significantly better in LSAR, OLS, cHRF-MN, cHRF-LSAR, and cHRF-OLS. Wilcoxon signed-rank pair test, $P = 0.05$).

These results demonstrated that the object category information has a distributed representation in the occipital and temporal areas. This information could improve the performance of classification. Therefore, localizer runs are necessary in object-related brain decoding experiments. Furthermore, in a brain-computer interface system with visual information, the spatially distributed information in large areas should not be ignored to obtain a better result.

(a)

(b)
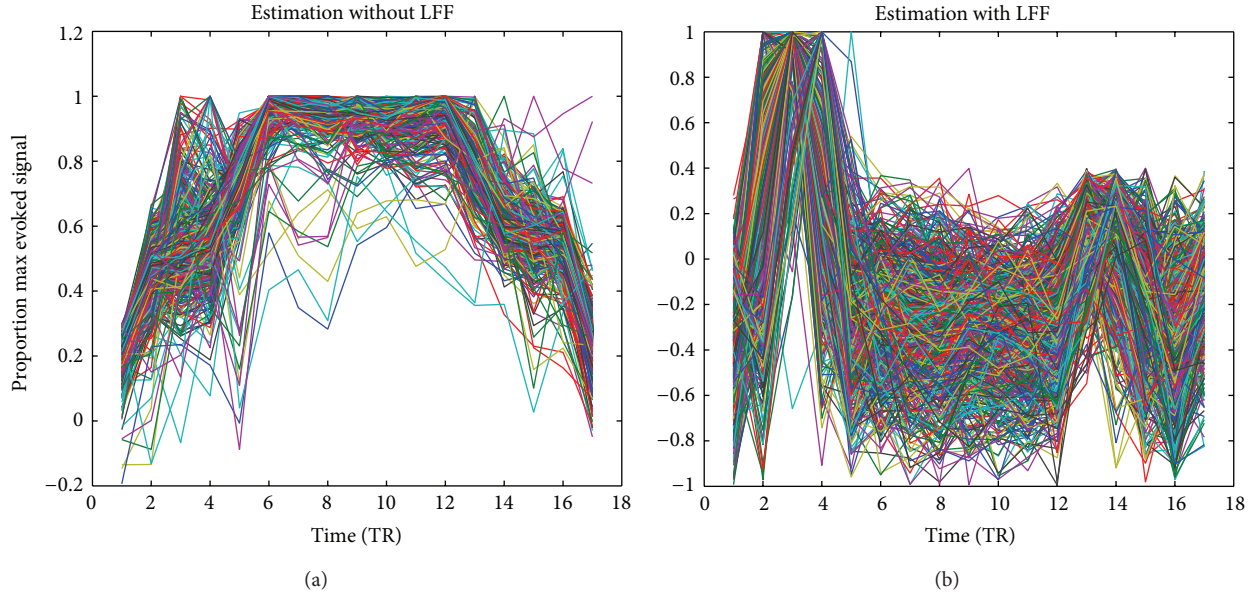
FIGURE 8: Comparison of HRF estimates with and without LFF. The lines in different colors represent the different HRF estimates of the voxels. The x-axis indicates the time relative to the event onset (TR = 2 s), and the y-axis indicates the BOLD signal. Each HRF estimate was normalized by dividing it by its maximum value.
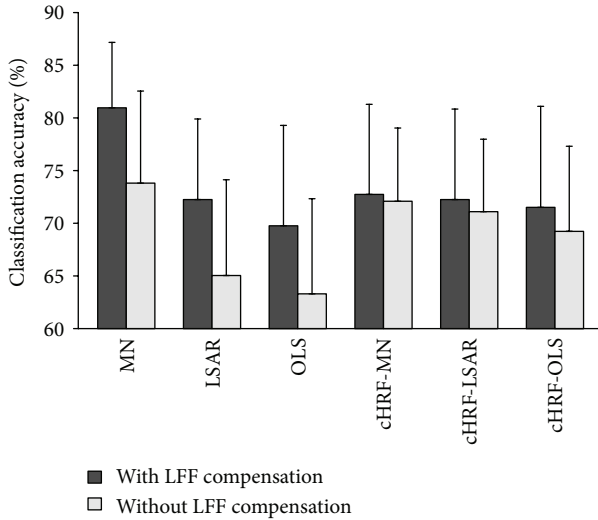
FIGURE 9: Comparison of classification accuracies with and without the LFF compensation component. Classification accuracies estimated with fivefold leave-one-out cross-validation. Each method was applied to both models with and without LFF data to investigate the impact of LFF. cHRF-MN, canonical HRF with voxels selected by MN; cHRF-LSAR, canonical HRF with voxels selected by LSAR; and cHRF-OLS, canonical HRF with voxels selected by OLS. Error bars show the standard error of the mean classification accuracy across subjects.
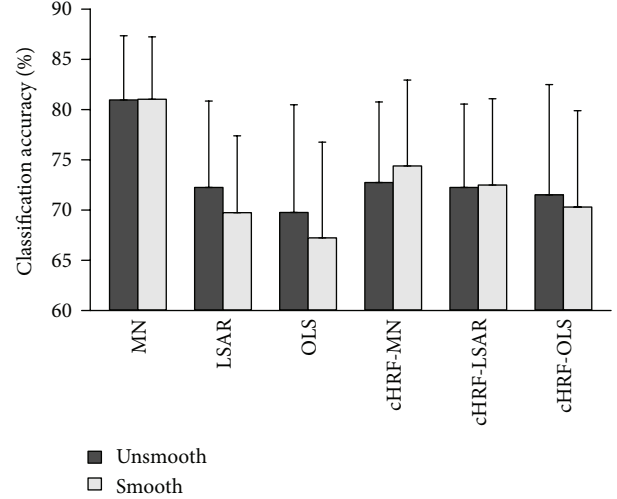

FIGURE 10: Comparison of classification accuracies in object responsive (OR) or early visual areas. OR voxels were strongly activated in localizer runs (t-test, $P = 0.005$, family-wise error corrected). Retinovoxels were located in the early visual area, which was delineated via retinotopic mapping analysis. Classification accuracies estimated with fivefold leave-one-out cross-validation. cHRF-MN, canonical HRF with voxels selected by MN; cHRF-LSAR, canonical HRF with voxels selected by LSAR; and cHRF-OLS, canonical HRF with voxels selected by OLS. Error bars show the standard error of the mean classification accuracy across subjects.

4. Conclusions

In this paper, we propose a new HRF estimation method that uses Tikhonov regularization and additional shape regularization term to address the HRF estimation problem in

rapid event-related experiments and suppress the overlapping of adjacent events. To test its performance, we applied this method to four-category object classification data. The results showed a significant improvement in classification performance, which proved that the new MN regularization HRF

estimation method was more efficient than the others. Some essential issues in MVPA were also discussed in this paper, including the role of LFF in response estimation, the effect of data smoothing, and the differences in the classification accuracy between OR voxels and retinovoxels. Based on this work, we conclude that LFF compensation is necessary in MVPA analysis and that smoothing is an alternative. Moreover, spatially distributed information should be considered to obtain the best classification performance.

Acknowledgment

References

[1] J. V. Haxby, M. I. Gobbini, M. L. Furey, A. Ishai, J. L. Schouten, and P. Pietrini, "Distributed and overlapping representations of faces and objects in ventral temporal cortex," *Science*, vol. 293, no. 5539, pp. 2425–2430, 2001.

[2] Y. Kamitani and F. Tong, "Decoding the visual and subjective contents of the human brain," *Nature Neuroscience*, vol. 8, no. 5, pp. 679–685, 2005.

[3] K. N. Kay, T. Naselaris, R. J. Prenger, and J. L. Gallant, "Identifying natural images from human brain activity," *Nature*, vol. 452, no. 7185, pp. 352–355, 2008.

[4] T. Naselaris, R. J. Prenger, K. N. Kay, M. Oliver, and J. L. Gallant, "Bayesian reconstruction of natural images from human brain activity," *Neuron*, vol. 63, no. 6, pp. 902–915, 2009.

[5] K. J. Friston, O. Josephs, G. Rees, and R. Turner, "Nonlinear event-related responses in fMRI," *Magnetic Resonance in Medicine*, vol. 39, no. 1, pp. 41–52, 1998.

[6] K. J. Friston, P. Jezzard, and R. Turner, "Analysis of functional MRI time-series," *Human Brain Mapping*, vol. 1, no. 2, pp. 153–171, 1993.

[7] J. J. Riera, J. Watanabe, I. Kazuki et al., "A state-space model of the hemodynamic approach: bonlinear filtering of BOLD signals," *NeuroImage*, vol. 21, no. 2, pp. 547–567, 2004.

[8] M. Lindquist and T. Wager, "Modeling the hemodynamic response function using inverse logit functions," in *Proceedings of the Human Brain Mapping Annual Meeting*, 2005.

[9] E. Formisano, F. de Martino, and G. Valente, "Multivariate analysis of fMRI time series: classification and regression of brain responses using machine learning," *Magnetic Resonance Imaging*, vol. 26, no. 7, pp. 921–934, 2008.

[10] M. M. Monti, "Statistical analysis of fMRI time-series: a critical review of the GLM approach," *Frontiers in Human Neuroscience*, vol. 5, article 28, 2011.

[11] A. M. Wink, H. Hoogduin, and J. B. T. M. Roerdink, "Data-driven haemodynamic response function extraction using Fourier-wavelet regularised deconvolution," *BMC Medical Imaging*, vol. 8, article 7, 2008.

[12] T. Zhang, F. Li, L. Beckes, C. Brown, and J. A. Coan, "Nonparametric inference of the hemodynamic response using multisubject fMRI data," *NeuroImage*, vol. 63, no. 3, pp. 1754–1765, 2012.

[13] J. A. Mumford, B. O. Turner, F. G. Ashby, and R. A. Poldrack, "Deconvolving BOLD activation in event-related designs for multivoxel pattern classification analyses," *NeuroImage*, vol. 59, no. 3, pp. 2636–2643, 2012.

[14] G. M. Boynton, S. A. Engel, and D. J. Heeger, "Linear systems analysis of the fMRI signal," *NeuroImage*, vol. 62, no. 2, pp. 975–984, 2012.

[15] M. W. Woolrich, T. E. J. Behrens, and S. M. Smith, "Constrained linear basis sets for HRF modelling using Variational Bayes," *NeuroImage*, vol. 21, no. 4, pp. 1748–1761, 2004.

[16] G. K. Aguirre, E. Zarahn, and M. D'Esposito, "The variability of human, BOLD hemodynamic responses," *NeuroImage*, vol. 8, no. 4, pp. 360–369, 1998.

[17] A. M. Dale, "Optimal experimental design for event-related fMRI," *Human Brain Mapping*, vol. 8, pp. 109–114, 1999.

[18] A. M. Smith, B. K. Lewis, U. E. Ruttimann et al., "Investigation of low frequency drift in fMRI signal," *NeuroImage*, vol. 9, no. 5, pp. 526–533, 1999.

[19] J. Tanabe, D. Miller, J. Tregellas, R. Freedman, and F. G. Meyer, "Comparison of detrending methods for optimal fMRI preprocessing," *NeuroImage*, vol. 15, no. 4, pp. 902–907, 2002.

[20] C. Chu, J. Mourão-Miranda, Y. C. Chiu, N. Kriegeskorte, G. Tan, and J. Ashburner, "Utilizing temporal information in fMRI decoding: classifier using kernel regression methods," *NeuroImage*, vol. 58, no. 2, pp. 560–571, 2011.

[21] K. N. Kay, S. V. David, R. J. Prenger, K. A. Hansen, and J. L. Gallant, "Modeling low-frequency fluctuation and hemodynamic response timecourse in event-related fMRI," *Human Brain Mapping*, vol. 29, no. 2, pp. 142–156, 2008.

[22] C. Goutte, F. A. Nielsen, and L. K. Hansen, "Modeling the haemodynamic response in fMRI using smooth FIR filters," *IEEE Transactions on Medical Imaging*, vol. 19, no. 12, pp. 1188–1201, 2000.

[23] V. A. Vakorin, R. Borowsky, and G. E. Sarty, "Characterizing the functional MRI response using Tikhonov regularization," *Statistics in Medicine*, vol. 26, no. 21, pp. 3830–3844, 2007.

[24] R. Casanova, L. Yang, W. D. Hairston, P. J. Laurienti, and J. A. Maldjian, "Evaluating the impact of spatio-temporal smoothness constraints on the BOLD hemodynamic response function estimation: an analysis based on Tikhonov regularization," *Physiological Measurement*, vol. 30, no. 5, pp. N37–N51, 2009.

[25] R. Casanova, S. Ryali, J. Serences et al., "The impact of temporal regularization on estimates of the BOLD hemodynamic response function: a comparative analysis," *NeuroImage*, vol. 40, no. 4, pp. 1606–1618, 2008.

[26] J. Belliveau, T. Brady, B. Rosen, and R. Tootell, "Borders of multiple visual areas in humans revealed by functional magnetic resonance imaging," *Molecular Biology*, vol. 228, p. 619, 1992.

[27] M. W. Woolrich, B. D. Ripley, M. Brady, and S. M. Smith, "Temporal autocorrelation in univariate linear modeling of FMRI data," *NeuroImage*, vol. 14, no. 6, pp. 1370–1386, 2001.

[28] I. Rustandi, *Estimation of Hemodynamic Response Function in Rapid Interval Event-Related fMRI Trials*, 2004.

[29] S. Boyd and L. Vandenberghe, *Convex Optimization*, Cambridge University Press, New York, NY, USA, 2004.

[30] A. E. Hoerl and R. W. Kennard, "Ridge regression: biased estimation for nonorthogonal problems," *Technometrics*, vol. 12, no. 1, pp. 55–67, 1970.

[31] P. Geladi and B. R. Kowalski, "Partial least-squares regression: a tutorial," *Analytica Chimica Acta*, vol. 185, pp. 1–17, 1986.

[32] C. C. Chang and C. J. Lin, "LIBSVM: a library for support vector machines," *ACM Transactions on Intelligent Systems and Technology*, vol. 2, no. 3, article 27, 2011.

[33] K. J. Friston, P. Fletcher, O. Josephs, A. Holmes, M. D. Rugg, and R. Turner, "Event-related fMRI: characterizing differential responses," *NeuroImage*, vol. 7, no. 1, pp. 30–40, 1998.

[34] N. Kriegeskorte and P. Bandettini, "Analyzing for information, not activation, to exploit high-resolution fMRI," *NeuroImage*, vol. 38, no. 4, pp. 649–662, 2007.

[35] P. Craven and G. Wahba, "Smoothing noisy data with spline functions—estimating the correct degree of smoothing by the method of generalized cross-validation," *Numerische Mathematik*, vol. 31, no. 4, pp. 377–403, 1978.

[36] G. Schwarz, "Estimating the dimension of a model," *The Annals of Statistics*, vol. 6, pp. 461–464, 1978.

[37] H. Akaike, "A new look at the statistical model identification," *IEEE Transactions on Automatic Control*, vol. 19, no. 6, pp. 716–723, 1974.

[38] H. P. O. de Beeck, "Against hyperacuity in brain reading: spatial smoothing does not hurt multivariate fMRI analyses?" *NeuroImage*, vol. 49, no. 3, pp. 1943–1948, 2010.

[39] M. Mur, P. A. Bandettini, and N. Kriegeskorte, "Revealing representational content with pattern-information fMRI—an introductory guide," *Social Cognitive and Affective Neuroscience*, vol. 4, no. 1, pp. 101–109, 2009.

[40] Y. Kamitani and Y. Sawahata, "Spatial smoothing hurts localization but not information: pitfalls for brain mappers," *NeuroImage*, vol. 49, no. 3, pp. 1949–1952, 2010.

[41] S. Song, Z. Zhan, Z. Long, J. Zhang, and L. Yao, "Comparative study of SVM methods combined with voxel selection for object category classification on fMRI data," *PLoS ONE*, vol. 6, no. 2, Article ID e17191, 2011.

[42] C. Cabral, M. Silveira, and P. Figueiredo, "Decoding visual brain states from fMRI using an ensemble of classifiers," *Pattern Recognition*, vol. 45, no. 6, pp. 2064–2074, 2012.

[43] L. Reddy, N. Tsuchiya, and T. Serre, "Reading the mind's eye: decoding category information during mental imagery," *NeuroImage*, vol. 50, no. 2, pp. 818–825, 2010.

[44] L. Reddy and N. Kanwisher, "Category selectivity in the ventral visual pathway confers robustness to clutter and diverted attention," *Current Biology*, vol. 17, no. 23, pp. 2067–2072, 2007.

Research Article

Modiolus-Hugging Intracochlear Electrode Array with Shape Memory Alloy

Kyou Sik Min,[1] Sang Beom Jun,[2,3] Yoon Seob Lim,[1,4] Se-Ik Park,[1] and Sung June Kim[1]

[1] *School of Electrical Engineering & Computer Science, Seoul National University, 1 Gwanak-ro, Gwanak-gu,*
  Seoul 110-742, Republic of Korea
[2] *Department of Electronics Engineering, Ewha Womans University, 52 Ewhayeodae-gil, Seodaemun-gu,*
  Seoul 120-750, Republic of Korea
[3] *Department of Brain & Cognitive Sciences, Ewha Womans University, 52 Ewhayeodae-gil, Seodaemun-gu,*
  Seoul 120-750, Republic of Korea
[4] *Cognitive and Neural Systems, Boston University, 677 Beacon Street, Boston, MA 02215, USA*

Correspondence should be addressed to Sang Beom Jun; juns@ewha.ac.kr

In the cochlear implant system, the distance between spiral ganglia and the electrodes within the volume of the scala tympani cavity significantly affects the efficiency of the electrical stimulation in terms of the threshold current level and spatial selectivity. Because the spiral ganglia are situated inside the modiolus, the central axis of the cochlea, it is desirable that the electrode array hugs the modiolus to minimize the distance between the electrodes and the ganglia. In the present study, we propose a shape-memory-alloy- (SMA-) embedded intracochlear electrode which gives a straight electrode a curved modiolus-hugging shape using the restoration force of the SMA as triggered by resistive heating after insertion into the cochlea. An eight-channel ball-type electrode array is fabricated with an embedded titanium-nickel SMA backbone wire. It is demonstrated that the electrode array changes its shape in a transparent plastic human cochlear model. To verify the safe insertion of the electrode array into the human cochlea, the contact pressures during insertion at the electrode tip and the contact pressures over the electrode length after insertion were calculated using a 3D finite element analysis. The results indicate that the SMA-embedded electrode is functionally and mechanically feasible for clinical applications.

1. Introduction

During the past several decades, cochlear implant systems have been established as a successful treatment for people suffering from severe hearing impairment due to hair cell loss. In general, a cochlear implant system consists of a multichannel intracochlear electrode, electronics in a hermetic package, and an external speech processor with a signal and power transmission coil. Briefly, the system converts sound signals into electrical signals and divides into multiple channels with different frequencies at the external speech processor. These signals then are radio-frequency- (RF-) modulated and transferred to the receiver/stimulator ASIC chip in a hermetic package through a transcutaneous coil link. After demodulation, the signals generate stimulating current pulses for each channel. Through the intracochlear electrode array, the current pulses stimulate ganglion cells in the inner ear, inducing auditory sensations in the recipients. The most important parts of the functionality of a cochlear implant are design of electrode array. Todays, insertion of a cochlear electrode array becomes far more important because it is required that newly developed electrode array can preserve residual hearing, be inserted deeper region of scala tympani, and stimulate targets more efficiently [1].

One of the challenges to improve the current cochlear implant system is to realize spatially high-resolution electrical stimulation to restore sound perception close to normal hearing. To achieve this goal, it is essential to locate the intracochlear electrode array close to the spiral ganglia, the target of the electrical stimulation, because the current will

diffuse and stimulate a large number of ganglia with low specificity if the electrode is located far from the target cells. In general, the electrode of a cochlear implant is inserted into the scala tympani because it has the largest cross-sectional area and an easy surgical operation site as shown in Figure 1. Stimulating currents flowing from the electrode site stimulate the ganglion cells located in the direction of the cochlear modiolus. Therefore, it is desired that the electrode is located close to the modiolus, as depicted in Figure 1(b), to reduce the distance between the electrode and the ganglia and increase the spatial specificity of the electrical stimulation [2]. When implanting the electrode array into the scala tympani, however, a straight shape is desirable to facilitate insertion by surgeons. If the electrode array is straight after molding with elastic silicon rubber, the electrode array is located along with the outer wall radius of the scala tympani due to the elastic restoration force of the electrode (Figure 1(a)).

Several strategies have been developed and employed for commercial cochlear implant systems to locate the electrode close to the modiolus. Advanced Bionics, Inc. and Cochlear Ltd. have developed modiolus-hugging electrodes using a preformed carrier which is held straight by an internal stylet before and during the insertion process [3]. After the partial insertion of the electrode and stylet, the electrode is pushed to its full insertion depth while holding the stylet at the same position. The electrode returns to its original spiral shape while being pushed toward the modiolus [4, 5]. Accordingly, the insertion depth of the stylet is critical in modiolus-hugging electrode array surgery. If the stylet is inserted far deeper into the cochleostomy, the electrode tip will come into contact with the cochlear outer wall, which may damage the spiral ligament or penetrate into the scala vestibuli. On the other hand, if the insertion depth of the stylet is too short, the apical curve of the electrode will curl before the first turn of the scala tympani [6]. Another method for modiolus-hugging was to insert an additional silastic structure called a positioner along the outside of the electrode after its insertion. The positioner pushes the electrode toward the modiolus, which locates the electrode sites in the vicinity of the ganglion cells [7]. However, when using this method, surgeons must undertake a precise insertion process twice. In addition, it was reported that the enlarged hole for the additional insertion of the positioner can cause meningitis [8].

In order to overcome these disadvantages, it was proposed to make the stylet with shape memory alloy (SMA), which converts its initial straight shape into a curved shape at the body temperature [9]. With this method, the electrode hugs the modiolus once it is inserted into the scala tympani by the restoration force of SMA stylets, during which the modiolus-hugging shape is memorized. However, it is not easy to pull out the electrode or to reinsert it once it is inserted because the SMA force always exists at the temperature of the human body. The heat from the surgeon's hands may also trigger SMA transformation before the insertion of the electrode.

In the present study, we propose an intracochlear electrode embedded with SMA without the drawbacks related to the transition temperature of the human body. Similar to the previous method, the SMA is pretreated to have a modiolus-hugging shape above its transition temperature. However, because the SMA is transformed into its memorized shape slightly above the body temperature, the electrode can be handled by a surgeon without SMA transformation during the insertion process. The transformation into the modiolus-hugging shape can be controlled by heating via an electrical current to the SMA after the insertion. We developed an eight-channel intracochlear electrode in which SMA wire is embedded. A finite element analysis was performed to verify the mechanical safety of the electrode array compared with conventional electrode arrays.

2. Materials and Methods

2.1. Shape Memory Alloy. The shape memory alloy (SMA) has two different phases: martensite and austenite. Martensite is the relatively soft and easily deformable phase of shape memory alloys, and it exists at a lower temperature. Austenite, the stronger phase of shape memory alloys, occurs at higher temperatures. Above a specific temperature, the deformed SMA in martensite is transformed into the austenite phase, which is configured as the original shape of the wire. The temperatures at which the transformation begins and ends are defined as T_m and T_a (Figure 2), respectively. In this study, T_m is defined as higher than the temperature of the human body in order to prevent the SMA from being transformed by heat from the surgeon's hands or by the patient's body while inserting the electrode into the cochlear scala tympani. T_a is defined as low as possible so as not to cause tissue damage by the heat generated from the SMA. Using titanium-nickel alloy, the SMA is prepared such that T_m is 40°C and T_a is 45°C (Jin-Sung Ltd., Eui Wang, Korea).

The human cochlear canal is a spiral structure with 2.5 turns. If straightened, its length is approximately 32 mm from the base to the apex of the cochlea. However, the maximum insertion angle of the intracochlear electrodes is usually 360° and less than 25 mm in length, as shown in the modeling result of the trace of the electrode tip in Figure 3. In Figure 3(b), the smallest radius of curvature of the trace is 2.38 mm. To simplify the fabrication of SMA wires to be embedded in electrodes, the displacement on the z-axis (0.336 mm) was ignored because it is much smaller than those of the x- and y-axes, as depicted in Figure 3. The SMA wires (0.1 mm diameter) were fabricated in the shape of a spring whose curvature is 4.7 mm in diameter so that it can ensure that the curvature hugs the modiolus. The SMA spring was cut to have a length of 15 mm and an angle of 360°.

2.2. Electrode Fabrication and Transformation Test. An eight-channel intracochlear electrode array was fabricated. In this process, the ball-shaped sites are made from Teflon-coated 25 μm (dia.) 90% Pt/10% Ir-alloy wire (A-M systems, Inc., USA) by melting the wire with an oxygen/acetylene minitorch. The diameter of the ball sites is 420 μm. The balls are fixed at a hole in the bottom mold, as depicted in Figure 4, using silicone elastomer MED 4211 (Nusil, Ltd., USA). Both ends of the SMA wire are soldered with the same wires as the electrodes. The SMA wire is straightened and is then
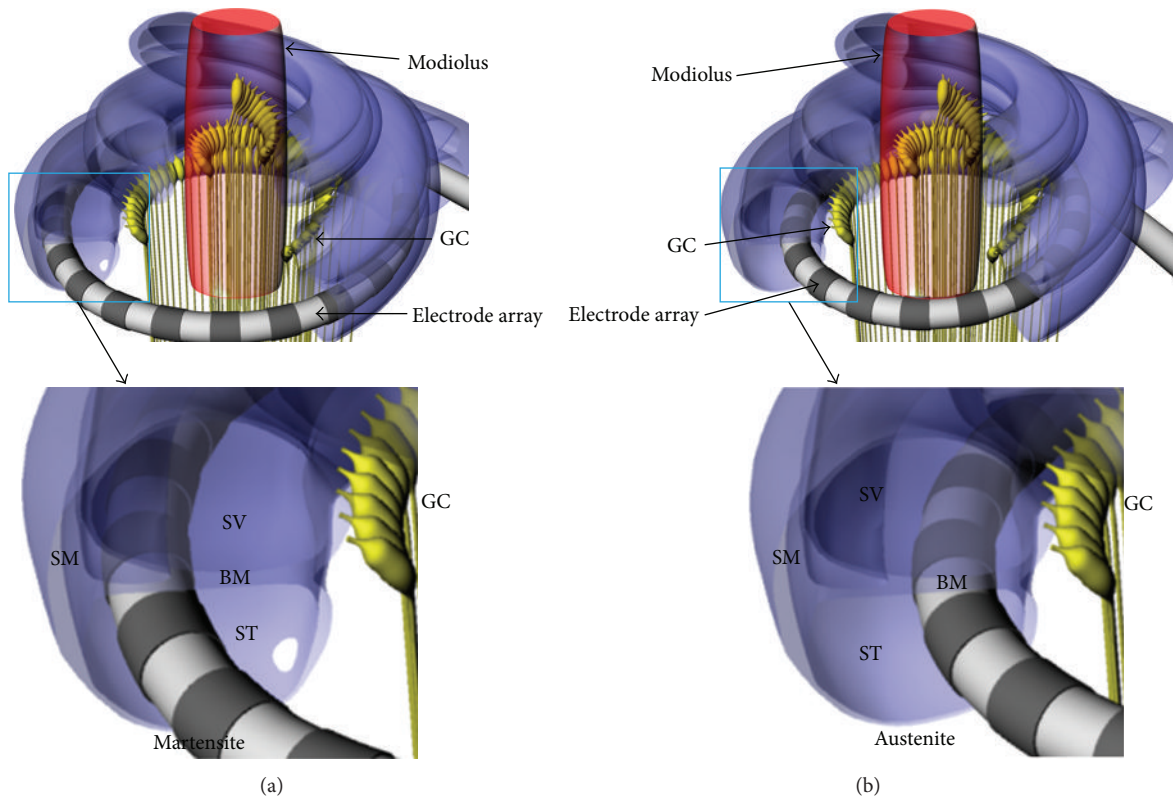
FIGURE 1: 3D models of intracochlear electrode arrays inserted into the cochlea for stimulation on ganglion cells. (a) Straight intracochlear electrode without modiolus-hugging characteristics. (b) Modiolus-hugging intracochlear electrode (GC: ganglion cell, SM: scala media, SV: scala vestibuli, ST: scala tympani, and BM: basilar membrane).
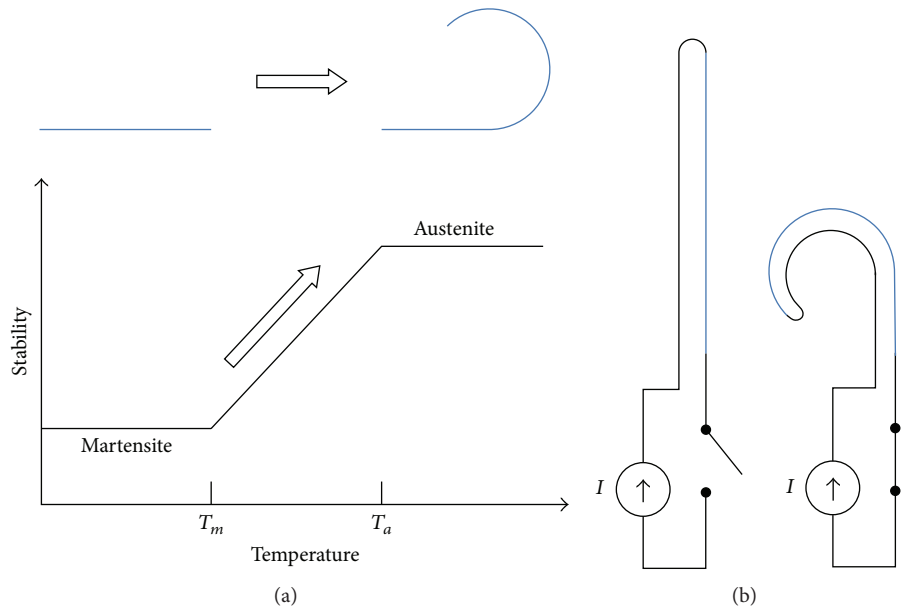
FIGURE 2: Transformation of shape memory alloy (SMA): (a) SMA changes its straight shape (martensite) into the modiolus-hugging shape (austenite), (b) the SMA transformation is triggered by resistive heating of electrical current.

(a)

(b)
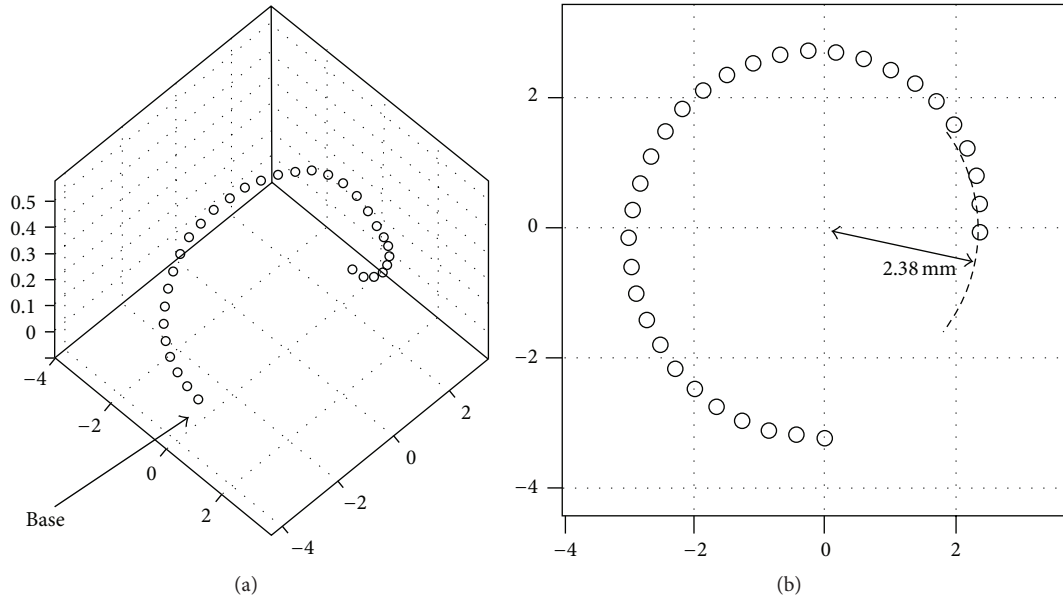
FIGURE 3: Trace of electrode tip during the insertion into scala tympani of human cochlea (all units are mm in this picture): (a) 3D trajectory of the electrode tip and (b) the trajectory of the electrode tip projected on x-y plane.

(a)

(b)
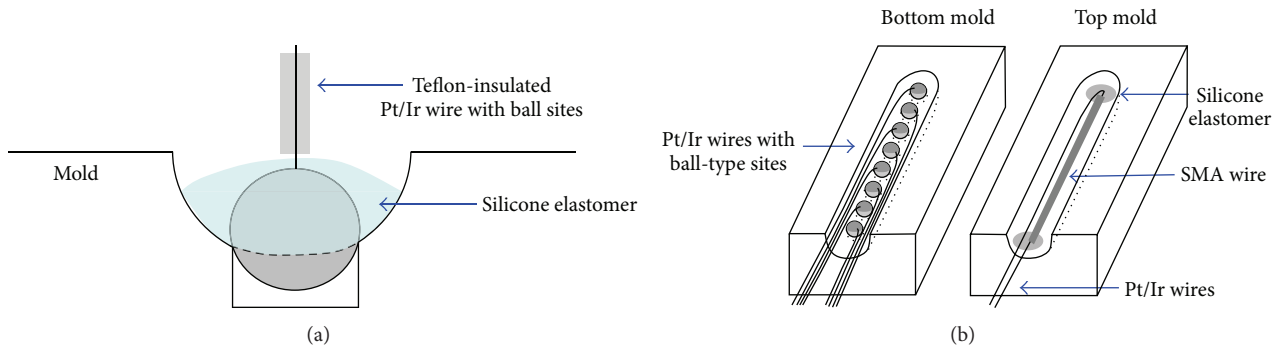
FIGURE 4: Fabrication of the SMA-embedded ball-type intracochlear electrode: (a) ball site fixation at a hole in the bottom mold and (b) fixation of eight-channel ball electrodes and the SMA wire at bottom and top molds, respectively.

fixed at the top mold with the elastomer. After joining two molds, degassed silicone elastomer is injected into the inlet. To prevent the SMA from being transformed, the elastomer is cured at room temperature for 2 days and then at 150°C for 30 minutes to complete the curing. The distance between adjacent sites is 1.8 mm. The total length of the electrode to be inserted into the cochlea is 21.5 mm. The electrode diameters were 0.6 mm at the apex and 0.8 mm at the base.

To determine if the fabricated SMA-embedded electrode array is transformed into the modiolus-hugging shape, various amplitudes of electrical current are applied to wires connected to both ends of the SMA. The electrode is also inserted into a clear human cochlear model, and the restoration force of the SMA triggered by resistive heating is applied to verify that the electrode can change its shape into a modiolus-hugging shape.
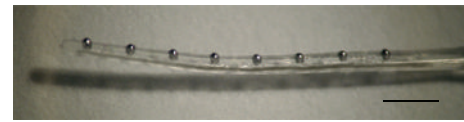
FIGURE 5: Eight-channel SMA-embedded intracochlear electrode array (scale bar: 2 mm).

2.3. Electrode Insertion Simulation. It was reported that the insertion of a cochlear electrode may cause trauma at the basilar membrane, which is very thin and soft [10–12]. Researchers inserted electrodes into the cochleae of human cadavers or the cochleae of animals in an effort to prove the mechanical safety of the electrodes [13–15]. It is also known that the trauma can be predicted by the stiffness

of the electrodes [6]. We performed a finite element analysis on the pressure generated by electrode insertion using a three-dimensional simulation (ANSYS 14 Workbench, ANSYS, Inc., USA). The three-dimensional human cochlear model is reconstructed using Rhinoceros (Robert McNeel & Associates, USA). First, a human scala tympani image is used for the base model of the cross-section of the entire scala tympani. The outline of the cross-section of the scala tympani is arranged along a curve defined in cylindrical coordinates as follows:

$$R = 1.14987e^{0.075458\varphi},$$
$$h = 3.23203e^{-0.126636\varphi}, \quad (1)$$

where R is radius from the central axis of cochlear spiral, h is height along the spiral axis and φ is cochlear angle ($0\sim5\pi$).

The patterns are then rescaled so that the areas fit cross-sectional areas along the depths [16]. The centers of the mass of the rescaled patterns are positioned along the aforementioned cochlear curve. The surface of the scala tympani is generated by connecting the closed curves. The electrode is modeled with diameters of 0.6 mm at the apex and 0.8 mm at the base. Eight platinum-iridium wire models are linearly arranged along the z-axis, which is parallel to the modiolus. The nitinol (Ti-Ni alloy) wire is modeled at the bottom of the platinum-iridium wire arrays. Table 1 depicts the material properties used in the finite element analysis. Because the SMA-embedded electrode array is designed to be inserted under the martensite temperature (T_m), the mechanical parameters of martensite are used for the SMA. The stress-strain value of the SMA-embedded electrode can be expressed by the following equation using the nonlinear uniaxial stress-total strain relationship [17]:

$$\sigma(\varepsilon) = \left(\frac{E_c}{1 + (E_c\varepsilon/2f_c)^2} \right.$$
$$\left. + \frac{E_s}{1 + (E_s\varepsilon/2f_s)^2} + \frac{\sum E_w}{1 + (E_w\varepsilon/2f_w)^2} \right)\varepsilon, \quad (2)$$

where σ = stress at strain ε, E_c, E_s, E_w = Young's modulus of silicone elastomer, SMA, and Pt/Ir wire, respectively, and f_c, f_s, f_w = the ultimate compressive strengths of silicone elastomer, SMA, and Pt/Ir wire, respectively.

Based on the stress-strain formula, the pressure at the electrode tip during the insertion process is calculated because insertion trauma tends to occur at the interface of the electrode tip and the cochlear tissue. The pressure over the electrode is also simulated by a time-lapse method. After completing the insertion process, the contact pressures are obtained along the electrode length. The displacement and fixed constraints are defined at the base plane of the electrode array and the scala tympani, respectively. The electrode array is inserted from the center of the cross-section of the scala tympani at 80°. The electrode array model is rotated by 10° on the z-axis. The electrode model is inserted to 18 mm, which is 360° in terms of the cochlear angle. In the analysis, the stress intensity at the interface of the electrode is calculated.

Table 1: Mechanical parameters of human cochlea and materials of intracochlear electrodes.

Material	Elastic modulus	Poisson's ratio
Bone (cochlear inner wall) [18]	20 GPa	0.3
Pt/Ir/PTFE [19]	8.27 GPa	0.3
Silicone elastomer [20]	0.45 MPa	0.5
TiNi (martensite) [21]	28 GPa	0.33

3. Result

The SMA-embedded eight-channel electrode array is fabricated as shown in Figure 5. The SMA wire is seen through the transparent silicone elastomer envelope. The electrical current through the SMA wire is increased while observing the electrode's shape. The electrical current-generated resistive heat at the SMA begins to induce the transformation of the electrode shape from a current level of approximately 150 mA, as shown in Figure 6(a). When the current level was increased to 208 mA, the transformation was completed by changing the electrode into the modiolus-hugging shape as memorized in the SMA wire (Figure 6(d)). This result indicates that the SMA phase is shifted from martensite to austenite by the resistive heat generated by the electrical current. During this heating process, the maximum power dissipation was 75 mW.

The electrode without SMA is located along the outer wall of the transparent scala tympani model (Figure 7(a)). For an electrode with an SMA stylet, the electrode hugs the central z-axis of the model, as shown in Figure 7(b), after applying electrical current through the SMA. In order to mimic an actual surgical situation, the cochlear model was filled with lubricant prior to the insertion of the electrode [2].

The trajectories of the electrode array with the SMA are visualized in a 2D cross-section of the scala tympani (Figure 8). The insertion process begins from the location with a cochlear angle of 80° (Figure 8(a)) and is performed up to 18 mm in depth representing a cochlear angle of 360°. The electrode initially came into contact with the wall of the cochlea at a cochlear angle of 135° when it was inserted to a depth of 6 mm. As it was inserted further into the cochlea, the electrode continued to bend and conform to the curvature of the cochlear outer wall. The insertion was finished when the tip reached the position with a cochlear angle of 360° (Figure 8(d)) and a total insertion depth of 18 mm. The stress applied to the electrode is shown in different colors in Figure 8.

In order to verify the feasibility of SMA-embedded electrodes, two mechanical parameters are evaluated using a finite element analysis. First, the contact pressures at the electrode tip during insertion are shown in Figure 9. Second, after the insertion is completed, the contact pressure distribution is calculated along the length of the electrode array and shown in Figure 10. To compare conventional electrode arrays, for both tests, 16-channel electrode arrays are employed with different arrangements of wires. Previously, it was reported that the maximum and the minimum contact pressure levels

(a) 150 mA   (b) 180 mA   (c) 195 mA

(d) 200 mA
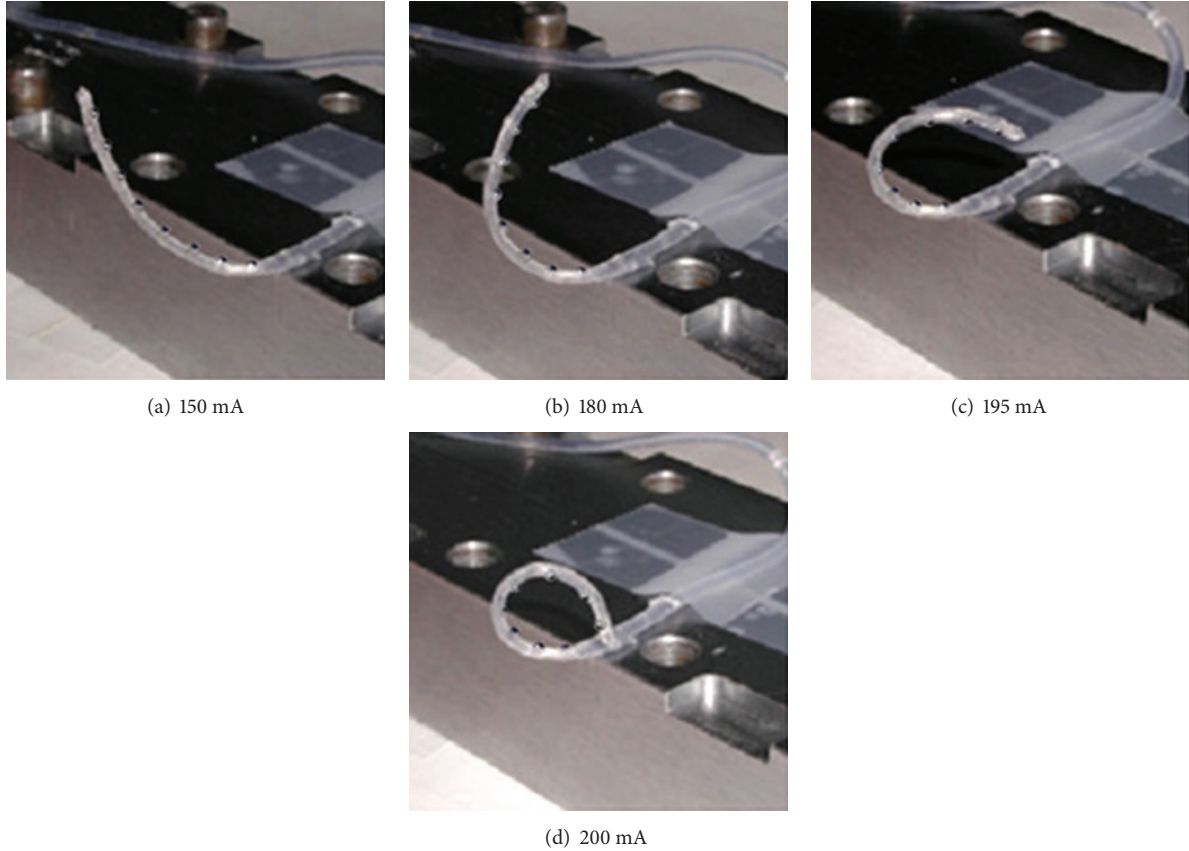
FIGURE 6: Electrode transformation induced by resistive heating of electrical current through the embedded SMA wire.

(a)   (b)
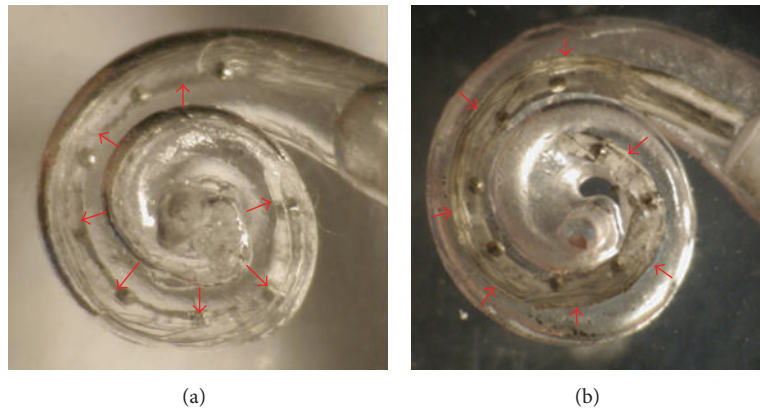
FIGURE 7: Insertion test into a transparent plastic cochlear model: (a) electrode without SMA: (b) electrode with a modiolus-hugging SMA.

occur when the wires in the electrode are assembled along the vertical and horizontal planes, respectively [16]. The contact pressures at the electrode tip are evaluated because it was previously reported that most traumatic events arose between the electrode tip and basilar membrane.

As shown in **Figure 9**, the contact pressure increased steeply after the electrode tip initially came into contact with the inner wall at a cochlear angle of approximately 100°. The maximum value of the contact pressure is 1.58 MPa during insertion at 180°. It decreased and converged to 0.9 MPa during the rest of insertion process. In terms of the electrode position and deformation, this result indicates that the maximum contact pressure at the electrode tip is attributed to the initial bending of the straight electrode. Moreover, the pressure becomes constant once the electrode bends to fit to the curvature of the cochlear outer wall from its original straight shape. After the completion of the electrode insertion process, as depicted in **Figure 10**, the maximum pressure occurs approximately at 200°, where the deformation begins. The pressure decreased from

(a)

(b)

(c)

(d)
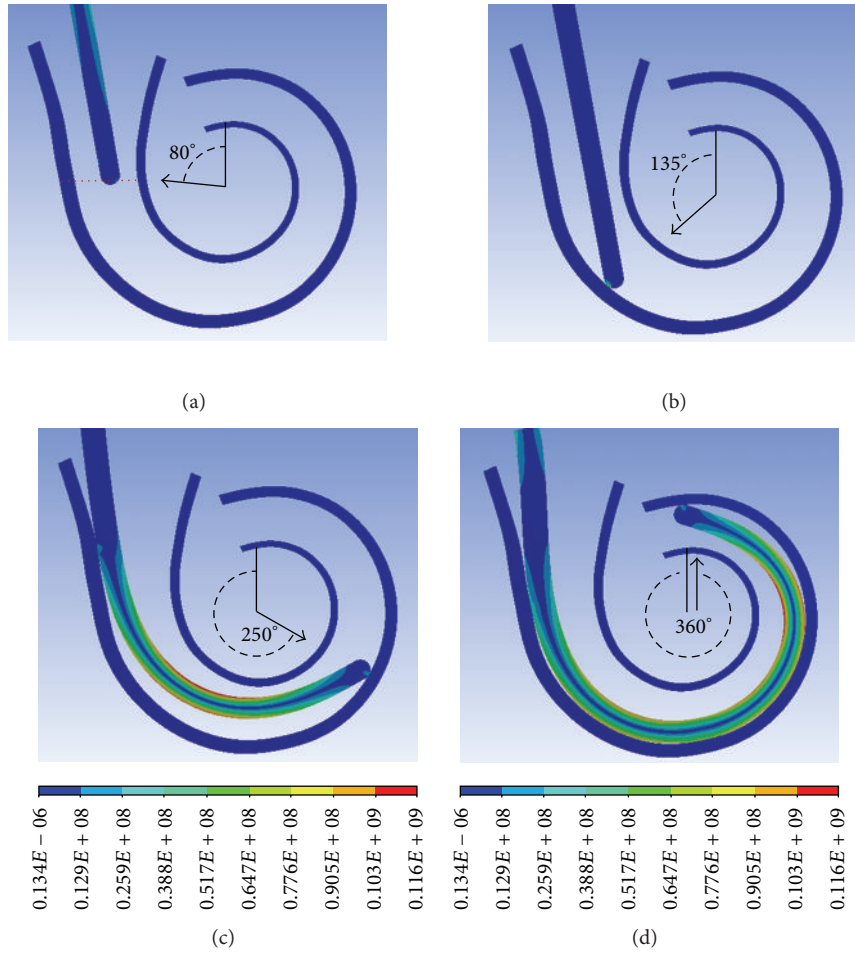
Figure 8: Cross-sectional views of 3D simulation of pressure distribution on the electrode during electrode insertion into cochlea.

$200°$ to $275°$ and increased again to the apical region of the electrode.

4. Discussion

In this study, we developed an eight-channel, SMA-embedded, intracochlear electrode. The intracochlear electrode could be located in the vicinity of spiral ganglion cells via the formation of a modiolus-hugging shape of the SMA. When using this method, the electrode maintains a straight shape during the insertion process and then transforms into a curved shape which can surround the cochlear modiolus. This proposed method reduces the distance between stimulation electrode sites and the targeted spiral ganglion cells, which enables an effective stimulation with lower power while increasing the operation time using a battery. Moreover, the discrimination between channels is also improved due to the reduced amount of current spreading. The proposed intracochlear electrode has advantages in that it does not produce a vacant lumen due to the stylet removal process, creating a possible infection route, and does not require the insertion of an additional
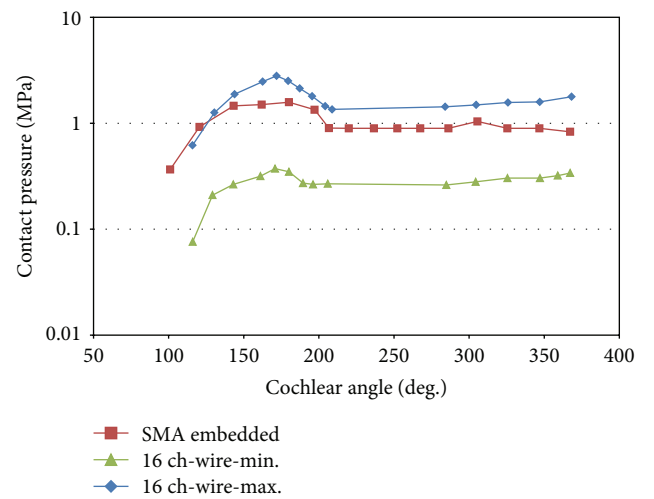
Figure 9: Contact pressures at the electrode tip during insertion.

insert structure to fill the cavity of the scala tympani, which has been used commercially for modiolus-hugging.

On the other hand, there are other factors to consider. There is a possibility that the heat generated by the electrical
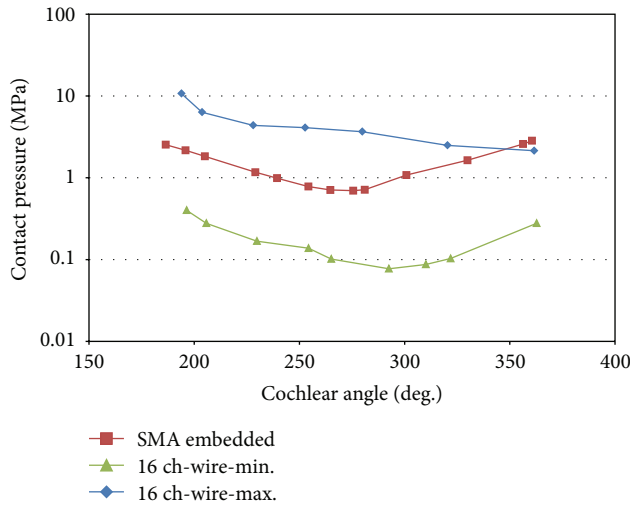
FIGURE 10: Contact pressure distributions along the length of the electrode after insertion.

current can damage the tissue surrounding the electrodes. However, the transition temperature was adjusted from 40°C to 45°C, which is close to the body temperature, and the SMA wire is insulated by thick silicone rubber. Though not proved in this paper, redundant heat accumulation can be avoided by applying current pulses instead of a constant current flow. Electrical safety should be also considered. In this study, the transformation of the SMA required about 200 mA of DC electrical current. This amount was much higher than the stimulation current, with its maximum amplitude of only several mA. In order to avoid stimulating adjacent cells with this large amount of current, it should be ensured that the entire current path is perfectly insulated properly at least during the implantation process. Using the proposed technique, advanced intracochlear electrodes with segmented SMAs can also be developed. If each SMA segment is converted to a curved shape of the martensite phase in an orderly process from the apex to the base, electrode insertion into the scala tympani can be done with little insertion force. In addition, even after complete insertion, the position of the electrode can be adjusted by applying electrical current through specific SMA segments if necessary [22].

In this study, three-dimensional modeling of the scala tympani is done using a cross-sectional outline of an actual cochlear image to calculate the contact pressure during and after electrode insertion. This is a simplified model of the human cochlea because the cochlear duct does not consist of only the scala tympani. Although the scala tympani model is sufficient to draw a conclusion about general insertion safety, a full cochlear model is required to analyze complicated failure modes. To generate a realistic cochlear model, the cross-sections should be reconfigured including the basilar membrane and other canals such as the scala media and scala vestibuli.

The simulation results indicate that the eight-channel SMA-embedded electrode has a comparable stiffness as 16 channel cochlear electrode which was reported previously [16]. The stiffness of the intracochlear electrodes is one

of the most important parameters determining the safety of electrode insertion, as a stiffer electrode incurs greater risk of penetrating through the basilar membrane during the insertion process. Using the typical method of cochlear electrode fabrication of molding metal wires with a silicone rubber carrier, the stiffness of the electrode is determined by the number and the diameter of the metal wires. In this study, to show the feasibility of the modiolus-hugging SMA-embedded electrode, an electrode with eight channels is fabricated instead of more than 10 channels. In order to achieve a SMA-embedded electrode with more channels, the diameter of the SMA wire needs to be increased to ensure sufficient restoration force, or the diameters of the individual metal wires should be decreased. In addition, the overall stiffness of the electrode needs to be within a range such that safe insertion is ensured without damage to the cochlea.

As an alternative method to realize a high-density cochlear electrode array with SMA, a micropatterned electrode array based on thin film can be employed [23]. Using this method, a SMA-embedded electrode can be fabricated without a reduction of the number of channels because the thin-film-based electrode can have a much larger number of channels without increasing the stiffness of the electrode, unlike a wire-based electrode array. However, the mechanical insertion behavior of an electrode based on a thin-film array should be evaluated, including the stiffness, insertion depth, and rotation of the electrode tip in an *in vitro* study or via a simulation.

To employ this method in clinical cochlear implant procedures, the biocompatibility of the SMA material should be proven during long-term implantation assessments. Due to the superelasticity and the large deformation capability of TiNi SMA, it has been used for several medical applications, such as orthodontic arch wires; orthopedic implants; and stents for coronaries, esophagi, or large intestines. Despite these applications, the toxicity of TiNi alloys has remained controversial for long-term applications due to the high nickel content. However, recent studies have reported that TiNi can be implanted into the human body for long-term use because an oxidized layer of TiO_2 on the TiNi surface prevents the possible loosening of nickel. This type of passivated TiO_2 layer is known to be very stable chemically and mechanically [24]. Therefore, TiNi SMA is expected to be used in regular medical applications such as cochlear implants in the near future [25, 26].

References

[1] S. J. Rebscher, A. Hetherington, B. Bonham, P. Wardrop, D. Whinney, and P. A. Leake, "Considerations for design of future cochlear implant electrode arrays: electrode array stiffness, size, and depth of insertion," *Journal of Rehabilitation Research and Development*, vol. 45, no. 5, pp. 731–748, 2008.

[2] S. J. Rebscher, M. Heilmann, W. Bruszewski, N. H. Talbot, R. L. Snyder, and M. M. Merzenich, "Strategies to improve electrode positioning and safety in cochlear implants," *IEEE Transactions on Biomedical Engineering*, vol. 46, no. 3, pp. 340–352, 1999.

[3] A. A. Eshraghi, N. W. Yang, and T. J. Balkany, "Comparative study of cochlear damage with three perimodiolar electrode designs," *Laryngoscope*, vol. 113, no. 3, pp. 415–419, 2003.

[4] E. Pasanisi, V. Vincenti, A. Bacciu, M. Guida, and S. Bacciu, "The nucleus contour electrode array: an electrophysiological study," *Laryngoscope*, vol. 112, no. 9, pp. 1653–1656, 2002.

[5] C.-G. W. Treaba, F. Dadd, D. I. Darley, and J. L. Parker, "Cochlear implant electrode array," 2002, United States Patent.

[6] S. J. Rebscher, A. Hetherington, B. Bonham, P. Wardrop, D. Whinney, and P. A. Leake, "Considerations for design of future cochlear implant electrode arrays: electrode array stiffness, size, and depth of insertion," *Journal of Rehabilitation Research and Development*, vol. 45, no. 5, pp. 731–748, 2008.

[7] N. W. Yang, A. V. Hodges, and T. J. Balkany, "Novel intracochlear electrode positioner: effects on electrode position," *The Annals of Otology, Rhinology & Laryngology*, vol. 185, pp. 18–20, 2000.

[8] W. Arnold, G. Bredberg, W. Gstöttner et al., "Meningitis following cochlear implantation: pathomechanisms, clinical symptoms, conservative and surgical treatments," *Journal for Oto-Rhino-Laryngology and its Related Specialties*, vol. 64, no. 6, pp. 382–389, 2002.

[9] F. Dadd, D. I. Darley, P. Gibson, J. L. Parker, and C. Treaba, "Double stylet insertion tool for a cochlear implant electrode array," 2007, U.S. Patent No. 7,269,461.

[10] D. W. Kennedy, "Multichannel intracochlear electrodes: mechanism of insertion trauma," *Laryngoscope*, vol. 97, no. 1, pp. 42–49, 1987.

[11] D. B. Welling, R. Hinojosa, B. J. Gantz, and J. T. Lee, "Insertional trauma of multichannel cochlear implants," *Laryngoscope*, vol. 103, no. 9, pp. 995–1001, 1993.

[12] P. S. Roland and C. G. Wright, "Surgical aspects of cochlear implantation: mechanisms of insertional trauma," *Advances in Oto-Rhino-Laryngology*, vol. 64, pp. 11–30, 2006.

[13] A. A. Eshraghi, N. W. Yang, and T. J. Balkany, "Comparative study of cochlear damage with three perimodiolar electrode designs," *Laryngoscope*, vol. 113, no. 3, pp. 415–419, 2003.

[14] P. Wardrop, D. Whinney, S. J. Rebscher, J. T. Roland Jr., W. Luxford, and P. A. Leake, "A temporal bone study of insertion trauma and intracochlear position of cochlear implant electrodes. I: comparison of nucleus banded and nucleus ContourŮ electrodes," *Hearing Research*, vol. 203, no. 1-2, pp. 54–67, 2005.

[15] P. Wardrop, D. Whinney, S. J. Rebscher, W. Luxford, and P. Leake, "A temporal bone study of insertion trauma and intracochlear position of cochlear implant electrodes. II: comparison of spiral clarionŮ and hiFocus IIŮ electrodes," *Hearing Research*, vol. 203, no. 1-2, pp. 68–79, 2005.

[16] Y. S. Lim, S. I. Park, Y. H. Kim, S. H. Oh, and S. J. Kim, "Three-dimensional analysis of electrode behavior in a human cochlear model," *Medical Engineering and Physics*, vol. 27, no. 8, pp. 695–703, 2005.

[17] D. Kachlakev, T. Miller, S. Yim, K. Chansawat, and T. Potisuk, "Finite element modeling of reinforced concrete structures strengthened with FRP laminates," Final Report SPR 316, 2001.

[18] G. J. Baker, C. R. Steele, J. A. Tolomeo, and D. E. Zetes-Tolometo, "Cochlear mechanics," in *The Biomedical Engineering Hanbook*, CRC Press LLC, New York, NY, USA, 2nd edition, 2000.

[19] T. G. McNaughton and K. W. Horch, "Mechanical testing of metallic and polymeric intrafascicular electrodes," in *Proceedings of the 16th Annual International Conference of the IEEE Engineering in Medicine and Biology Society, Engineering Advances: New Opportunities for Biomedical Engineers*, vol. 2, pp. 806–807, November 1994.

[20] D. W. van Krevelen and K. te Nijenhuis, *Properties of Polymers: Their Correlation with Chemical Structure; Their Numerical Estimation and Prediction from Additive Group Contributions*, Elsevier Science, Amsterdam, The Netherlands, 2009.

[21] W. contributors, "Nickel titanium," 2013, http://en.wikipedia.org/w/index.php?title=Nickel_titanium&oldid=535331827.

[22] S. B. Jun and S. J. Kim, "Fabrication method for intracochlear electrodes," 2002, South Korea Patent 2002-23390.

[23] J. H. Kim, K. S. Min, H. S. Lee, M. H. Park, S. H. Oh, and S. J. Kim, "A polymer based intracochlear electrode for low cost, but highly effective cochlear implantation," in *Proceedings of the Conference on Implantable Auditory Prostheses*, Asliomar, Calif, USA, 2011.

[24] P. Filip, J. Lausmaa, J. Musialek, and K. Mazanec, "Structure and surface of TiNi human implants," *Biomaterials*, vol. 22, no. 15, pp. 2131–2138, 2001.

[25] I. P. Lipscomb and L. D. M. Nokes, *The Application of Shape Memory Alloys in Medicine*, 1996.

[26] M. H. Wu, D. E. Hodgson, and R. J. Biermann, "Shape memory alloys," in *Metals Handbook*, vol. 2, pp. 897–902, ASM International, Ohio, Ohio, USA, 1990.

Research Article

Trial-by-Trial Adaptation of Movements during Mental Practice under Force Field

Muhammad Nabeel Anwar and Salman Hameed Khan

Human Systems Laboratory (HSL), Department of Biomedical Engineering and Sciences, School of Mechanical &
Manufacturing Engineering, National University of Sciences & Technology, Islamabad 44000, Pakistan

Correspondence should be addressed to Muhammad Nabeel Anwar; nabeel@smme.nust.edu.pk

Human nervous system tries to minimize the effect of any external perturbing force by bringing modifications in the internal model. These modifications affect the subsequent motor commands generated by the nervous system. Adaptive compensation along with the appropriate modifications of internal model helps in reducing human movement errors. In the current study, we studied how motor imagery influences trial-to-trial learning in a robot-based adaptation task. Two groups of subjects performed reaching movements with or without motor imagery in a velocity-dependent force field. The results show that reaching movements performed with motor imagery have relatively a more focused generalization pattern and a higher learning rate in training direction.

1. Introduction

Mental simulation of various actions can be used as a tool for studying theoretical concepts about cognitive neuroscience. Motor imagery, a subcategory of mental simulation, is an internal reproduction of a specific motor action without any overt motor output and is widely used for improving the motor performance. In relation to it, the underlying neurological mechanisms activated by mentally rehearsing motor actions are quite similar to the ones activated during actual physical movements [1]. There is a high overlap between the active brain regions of subjects undergoing movement execution and the movement imagination [2]. It provides the idea that motor imagery might help the CNS in the learning process and can be used in conjunction with physical training to improve motor performance [2–5]. As an example, it is used for improving the performance of athletes and sports men [6]; experienced musicians have used motor imagery for improving coordination between complex spatial and timing components of a musical composition [2]. It is also used, for speeding up the recovery process of stroke patients and neurological rehabilitation [7], for motion accuracy, and for

adaptation to the changing dynamics and arm kinematics [5, 8].

In the current study we consider a task in which subjects make series of reaching movements in the presence of external dynamics, that is, an externally imposed force field from a mechanical robot. The force field introduces significant errors in contrast to the movements that take place in the absence of any external force field. These errors gradually fade out with practice as the nervous system adapts to the newly imposed dynamics; this recovery of performance is "*motor adaptation*" [9]. The force field is switched off unexpectedly in some trials during adaptation; these trails are termed as "*catch trials*" and they help in investigating the properties of internal model that human nervous system updates to predict and neutralize the error. The trajectories formed during the catch trials are quite similar in shape but opposite in direction to the trajectories that are observed at the sudden introduction of force field (also termed as "*after effects*"). This supports the notion that model-based motor commands are generated by central nervous system (CNS). There are predominantly two modes in human motor control mechanism: feedback and feedforward. During the early learning stage, internal model

is evolved and learning is achieved through sensorimotor feedback mechanism. After sufficient practice, motor systems adapt with external environment and operate autonomously in feedforward mode; this is called as "late learning" [10].

Human brain formulates internal model in such a way that motor learning in one direction has a positive impact on learning in other adjacent directions. This effect gradually decreases as the difference in directions increases. The ability to apply what has been learned in one context to other contexts is termed as the "*generalization*" of motor learning. When generalization increases learning in some contexts, it is called as "*transfer.*" In some contexts, generalization diminishes learning and it is said to be causing an "*interference*" [11]. It shows that the model evolved by human nervous system learns beyond the boundaries of training data and its output is broadly adapted across the state space of motor commands [9]. In the contexts where generalization is detrimental, it is usually due to the large alteration in the learning problem associated with comparatively small contextual changes. This is relevant to our experiment where a large change in direction, that is, around 135° to 180°, has an associated small change in context. This is also true in general; for example, driving car in the reverse direction or counting backward is difficult as compared to normal routine.

The current work is focused on how CNS learns to control and compensate errors in imagined reaching movements and how an error experienced in one direction can affect the reaching movements in other directions, with or without motor imagery. In other words, an investigation is made to answer how mental practice affects the generalization pattern of internal learning model developed by CNS. Up to the best of our knowledge, the relation between generalization and motor imagery in reaching movements has not been studied explicitly. By motor imagery, we mean that the individual subjects imagine the subsequent movement before actually performing it (MI group). The group of subjects without any conscious intent before starting movement or has not mentally rehearsed the upcoming movement constitutes the no motor imagery group (No-MI group).

At this stage we develop our initial hypothesis as follows.

(1) The motor imagery affects the generalization function in such a way that it transfers the learning in nearby directions.

(2) The group of subjects who rehearsed the task mentally prior to their physical action will have a high learning rate in the direction of training and associated directions.

(3) The group of subjects who rehearsed the task mentally prior to the physical action will have a more focused generalization pattern with respect to the No-MI group.

The composition of the remaining paper is as follows. Section 2 describes the related work. Methods and materials are explained in Section 3. Results are outlined in Section 4. The conclusion and future work are included in Section 5.

2. Related Work

Mussa-Ivaldi and Bizzi studied the possible ways in which the information about force field dynamics was perceived by the CNS. Finding the movement path based on perception of force field is a complex inverse dynamics problem, and brain forms an internal model composed of motor primitives to solve this inverse problem. This internal model is updated regularly to conform with the ever-changing environmental and physical dynamics [12]. Robotic manipulandum systems are widely used to study the underlying dynamics of motor commands issued by CNS [13].

Previous studies suggest that motor imagery has a constructive effect on the human motor performance. It has been argued that the covert mental practice is a cost effective, easily accessible strategy to improve motor performance of affected body parts after stroke [14]. Gentili et al. have studied the associated question of how imagination and mental execution of physical activities can help in learning process. It is found that although subjects with physical training (without imagery) have good learning rate than the subjects undergoing mental training (without any sensorimotor feedback), yet the movement rhythms and adaptation rates were identical. Authors proposed that the internal forward model of human brain provides state estimation to improve motor performance during imagery [5].

3. Materials and Methods

3.1. Experimental Setup. We considered a behavioral task for studying the effect of motor imagery on trial-by-trial motor learning. The subjects performed center out reaching movements by using a robotic manipulandum. An external force field was generated by the robotic manipulandum for desired perturbations in a plane during the movements. The subjects, then, had to adapt to the new environment. This helped in studying the adaptive capabilities of human motor system Figure 1(a).

The experimental setup shown in Figure 1(a) was the same as [8]. In this setup the *Braccio di Ferro* robot (see [15] for details) was used to generate the forces and record the motion paths. The plane of motion was restricted to only two dimensions for the ease of analysis. Fourteen-channel EEG was recorded using gold cup electrodes (g.EEGcap g.tec, Guger Technologies OEG, Graz, Austria). The electrodes were placed at central locations (C3, C1, Cz, C2, and C4), frontal locations (F3, Fz, and F4), parietal locations (P3, Pz, and P4), and temporal locations (T3 and T4) by adapting international 10–20 electrode placement system. Left earlobe and right earlobe were used as reference and ground, respectively. Analogue EEG signals were amplified and band-pass filtered (0.1–100 Hz) by the EEG amplifier (g.BSamp g.tec, Guger Technologies OEG, Austria). The signals were then sampled at 256 Hz (NIDAQ 6040-E) and were stored for later offline analysis. The online feedback was provided by a software application based on BCI2000 [16].

(a) Robotic manipulandum system was used to deliver required perturbations during the course of reaching movement. A setup for 2D movements was used to record the trajectories followed by different subjects under the application of external force field. This movement onset was controlled through a feedback mechanism involving EEG

(b) Eight possible motion directions are shown. All paths are spaced at regular intervals of 45°. Anticlockwise force field was turned on/off during the experiment

(c) Timeline for each trial is shown. Total duration is subdivided into several intervals bounded by commands issued by the controller

Figure 1: Experimental setup and trial protocol.

3.1.1. Subjects. Total 12 subjects participated in this experiment. Eleven of the subjects were right handed, while one left handed subject was present. Before undertaking the experiment, a screening process was performed in which EEG patterns of all subjects were analyzed. During this process, each subject was asked to rest for 3 seconds (base line) followed by imagining hand movements for 2 seconds, and a total of 96 trials were conducted in this way. Then,

for each subject, we identified the spectral bandwidth and the electrode locations that correlated most with the motor imagery. The most responsive spectral bandwidth and electrode locations were then used for online feedback. We also calculated the "coefficient of determination" for each subject. It acts as a measure to determine the quality of human intention that can be inferred from the EEG signal. It is expressed as a correlation coefficient defined over a bivariate

signal composed of EEG signal x during motor imagery and a task condition signal y that consists of EEG signal during rest period:

$$r^2 = \frac{\sigma(x,y)^2}{\sigma^2(x) \cdot \sigma^2(y)}, \tag{1}$$

where r^2 value was calculated from each electrode. After screening, the subjects were randomly assigned to two experimental protocols as folows: "with imagery" (6 subjects, 1 M and 5 F, mean age 23 ± 1.5 years) and "no imagery" (6 subjects, 3 M and 3 F, mean age 25 ± 2.8 years).

3.2. Experimental Procedures.

The subjects sat on a chair in front of the manipulandum. The height and position of the seat were adjusted so that the arm could be kept horizontally at shoulder level pointing towards the center of the work space. In normal position, the elbow and the shoulder joints were flexed about $90°$ and $45°$, respectively. The experimental protocol was displayed to the subjects on a $19''$ LCD computer screen placed about 1 m away at eye level. The subjects performed 10 cm reaching movements with dominant hand. The targets were displayed on a black background as white circles of 1 cm diameter appeared at one of the eight random locations ($0°$, $45°$, $90°$, $135°$, $180°$, $225°$, $270°$, and $315°$). The current position of the hand along with target was continuously displayed on the computer screen.

The experiment was organized into sets; each set consisted of a sequence of 48 target presentations, with target appeared at 8 different positions, 6 times each. Every set lasted for approximately 7 $\sim$ 8 minutes, and the subjects were allowed to take rest between sets. Each movement started from the center of the work space. In order to initiate a movement, the subject had to hold the cue at the starting point (initial position of the target). Once the cue is in center of the target, the target changed its color to gray; after 4 s it shifted to one of the eight random outer positions and turn into red. At this point, the "imagery" group subjects were required to "imagine" the hand movement toward the target. EEG signals were continuously recorded and after every 300 ms a spectral estimate in the most responsive frequency band was calculated. This value was compared with the threshold value to detect the presence/absence of event-related EEG desynchronisation (ERD). The binary signal was transmitted to the robot and used for changing the color of the target, that is, red to yellow to green. A "go" signal is then generated (target color turning into green), indicating that the actual movement could start. This signal can only be generated if either of the following conditions was fulfilled:

  (1) the subject successfully generated 5 ERDs or

  (2) the 3 sec time limit of waiting was reached.

In the "no imagery" experiments, only condition (2) was applied and the subjects had to wait for 1.5 to 3 sec randomly between target appearance and the "go" signal. On "go" signal, the subjects were required to move as fast and as accurate as possible. Subjects were encouraged to keep an

approximately constant movement timings and to avoid eye blinking and head movements or throat clearing during the imagery and movement phase. The next trial started as soon the subject placed the cursor inside the target at the central initial position.

Movements were performed under three different conditions: (i) null field (robot generated no force, 5 target sets); (ii) force field (velocity dependent force field was turned on, 5 target sets); (iii) after-effect (no field again, 2 target sets). During force field trials, the robot generated a viscous curl field that perturbed the reaching movements. The force field was perpendicular to the instantaneous hand velocity vector with magnitude proportional to the velocity

$$F = B \cdot v, \tag{2}$$

where,

$$B = \begin{bmatrix} 0 & -b \\ b & 0 \end{bmatrix} \text{N} \times \text{sm}^{-1}, \tag{3}$$

where the viscous coefficient b is $12 \, \text{N} \cdot \text{m}^{-1} \cdot \text{s}^{-1}$. The hand velocity vector (and its subsequent derivatives) was estimated online by means of a numerical differentiation technique. During the field sets, "catch trials" were inserted in which the force field was unexpectedly turned off. The probability of occurrence of one catch trial was set to 1/6, which corresponds to one catch trial per direction per set.

3.3. Data Analysis

3.3.1. Screening.
During screening phase, the recorded EEG data was arranged into 1 s long epochs and mean was removed. A 20th-order autoregressive model was used for estimating the power spectral density. The spectrum was calculated from 0 Hz to 40 Hz at every 0.2 Hz, and then spectral average was made into 2 Hz bins for 96 hand imagery trials and compared them with the rest period. The averaged spectral change (spectra at rest condition minus spectra during imagery) was also estimated during the screening process. Screening gave an overview about the most responsive electrode and the maximum change in the ERD. This information was the basis of online feedback.

3.3.2. Online Feedback.
EEG signals were recorded in 300 ms blocks, and for each block the software application estimated the power spectral density. The online ERD detection threshold was set at the 80% of the averaged spectral change from the base measurement during the rest period. Thus, for each subject the threshold was different and it was 80% of the maximum spectral change he/she could produce. As a result, a binary signal, that is, 1 (presence of a ERD) or a 0 (no ERD) was generated after every 300 ms and was used to change the color of the target from red to yellow to green.

3.3.3. Familiarization Session.
For each subject, we tested the error measurements for normal distribution using Shapiro-Wilk, Kolmogorov-Smirnov, and Lilliefors tests. It turned out

that the distributions were normal ($P \leq 0.01$). Equivalent variances were tested using Hartley, Cochran, and Bartlett tests.

3.3.4. Adaptation Session.

Hand trajectories were sampled at 100 Hz. The x and y components were smoothed with a 6th-order Savitzky-Golay filter (window size 270 ms, equivalent cut-off frequency of around 7 Hz). The first three-time derivative was estimated for the following indicators of motor performance

Aiming Error. Aiming error provides angular difference between the required target direction and the actual hand movement direction in the early phase of the movement, that is, 300 ms from movement onset. This error provides information about the lateral deviation and is used as a general measure of curvature.

Learning Index. The learning process was quantified by using an indicator similar to that proposed by [17]. This measure is independent of the magnitude of force field and other user-specific parameters such as the net compliance of the arm:

$$I_{\text{learning}} = \frac{-y_c}{|y_c - y_f|}, \tag{4}$$

where y_f and y_c are the 300 ms aiming errors in the field and catch trials, respectively. Both error measures were adjusted for any bias present in the last null field set. Therefore, errors were always referred to change from errors in the null set.

3.4. State Space Modeling.

Internal model developed by brain is composed of a set of primitives that translate desired movement trajectories into required motor commands. In an event of external perturbation, motor commands are issued to minimize its effects. The forces produced as a result can be expressed in terms of desired position and velocity primitive functions g_j [18]:

$$\mathcal{O} = W^T \cdot g\left(x, \frac{dx}{dt}\right) \mid g = \left[g_1, g_2, \ldots, g_j\right]^T, \tag{5}$$

W^T is the experience dependent weighted matrix which is adjusted according to

$$\Delta W_i = -\eta \cdot g\left(x_i, \frac{dx_i}{dt}\right). \tag{6}$$

The shape of the primitives in the above equations can be found out by fitting a linear state space model over experimental data. Such a fit is possible as explained in [17, 19]. Although, various types of models can be used for dynamic system modeling, we used prediction error estimate method (PEM) to identify a structured linear state space model. PEM algorithm is quite similar to maximum likelihood estimation used in time series analysis [20].

Let us suppose that we have eight dimensional input force field signal denoted by $f(n)$, which triggers maximum speed path error of $e(n)$ with sample number n. If we have data upto Nth sample a set of input output pairs can be defined as,

$$\mathcal{X} = \{f(n), e(n)\} \mid 1 \leq n \leq N. \tag{7}$$

Here, the input $f(n)$ is dependent on the trial which may be a force field trial (FF), simple null field trial (NF) or null field catch trial (C) after the removal of force field;

$$t \in \{C, NF, FF\}. \tag{8}$$

Linear state space model can be represented as a predictor model that estimates $(N + 1)$th output sample:

$$\hat{e}([N + 1] \mid N; \varphi) = \mathcal{F}(\mathcal{X}_N, \varphi). \tag{9}$$

Using an iterative procedure, an estimate of parameter vector $\hat{e}_{N+1}$ is generated for $(N + 1)$th output. $\hat{e}_{N+1}$ depends both on samples from $1 \cdots N$ and parameter vector φ. φ represents the parametrization, and $\mathcal{F}(\cdot)$ is the function defined on observed data [20]:

$$\mathcal{F}(\mathcal{X}_N, \varphi) = H_e(q, \varphi) e(n) + H_f(q, \varphi) f(n)$$
$$= \sum_{k=1}^{N} h_e(k) e(n-k) + \sum_{k=1}^{N} h_f(k) f(n-k), \tag{10}$$

where q is a shift operator and H_e and H_f are the linear time or shift invariant filters which we will specify in a further discussion. State space equations are given by

$$\dot{x}(n+1) = A(\varphi) x(n) + B(\varphi) f(n),$$
$$e(n) = C(\varphi) x(n) + Df(n). \tag{11}$$

The linear state space model is estimated based on the assumption that the data has been generated according to (11). PEM tries to minimize a weighted norm of estimation error. In our case, where there is only one output, this cost function $\xi_N(\cdot)$ is given by

$$\xi_N(R, S) = \frac{1}{S^2(q, \varphi)} \sum_{t=1}^{N} \Delta\Delta^T, \tag{12}$$
$$\Delta = e(n) - \hat{e}(n \mid \varphi),$$

where $\hat{e}(n \mid \varphi)$ is the output estimate of model, and PEM produces an output which is optimal in least squares sense. N is the number of data values of errors during hand-reaching experiments. In the cost function estimated output is supposed to be:

$$\hat{e}(n \mid \varphi) = R(q, \varphi) \cdot f(n), \tag{13}$$

where $f(n)$ is the input of the model. Here, $R(q, \varphi)$ and $S(q, \varphi)$ are the matrices that can be described in terms of state space matrices. In turn, they define filters as follows:

$$H_e(q, \varphi) = \left[I - S^{-1}(q, \varphi)\right],$$
$$H_f(q, \varphi) = S^{-1}(q, \varphi) R(q, \varphi). \tag{14}$$

PEM is a fast algorithm and has similar merits as that of maximum likelihood estimation. However, it requires accurate parameterization and may get stuck in local minima. The initial parameters were estimated using a numerical algorithm for subspace state space system identification that projects both input and output data to find optimal state sequence (N4SID Algorithm by van Overschee and de Moor [21]). These sequences can be interpreted in terms of states of a parallel bank of Kalman filters. By using this interpretation, state space system matrices can be easily determined from the given data with no requirement of providing parameterization for nonzero initial conditions [21]. This algorithm uses QR decomposition and singular value decomposition. Thus, it is numerically stable and always converges to a finite value. With these benefits, we used it for finding an initial estimate of state space matrices of linear model.

In our experiments, the force field magnitude and direction (anticlockwise) were kept constant and its presence or absence was recorded using normalized integers;

$$
f(n) = \begin{cases} +1, & \text{if } t \in \{\text{C, NF}\}, \\ -1, & \text{if } t \in \{\text{FF}\}. \end{cases} \tag{15}
$$

On each sampled input, a value of −1 indicates the presence of force field while a value of 1 indicates a catch trial or null field. Similar discrete scalar representation of force field magnitude was adopted by Thoroughman and Shadmehr [18] and Smith and Shadmehr [17].

Instead of using coordinate information in maximum errors, we used the relationship between actual arm compliance and the angular error. The details of the derivation can be found in [17]. In general, the two-dimensional compliance matrix is given by

$$
\begin{bmatrix} x \\ y \end{bmatrix} = \begin{bmatrix} D_{11} & D_{12} \\ D_{21} & D_{22} \end{bmatrix} \begin{bmatrix} f_x \\ f_y \end{bmatrix}. \tag{16}
$$

This two-dimensional compliance matrix can be transformed to one-dimensional oppositional compliance having a value in each direction of motion. The magnitude of one-dimensional compliance matrix depends on direction of force and three parameters D_{11}, D_{22}, D_{21}, and D_{12}, see [17] for details. Briefly,

$$
D_1(\varrho) = \frac{D_{11} + D_{22}}{2} + \frac{D_{11} - D_{22}}{2} \cos(2\varrho) \\ + \frac{D_{12} + D_{21}}{2} \sin(2\varrho). \tag{17}
$$

We parameterized D matrix of the state space model with the value of $D_1(\varrho)$.

3.5. Measuring Goodness of Fit.
We also compared the variances of estimated output and the actual errors (see Figure 2) to account for the goodness of fit of our model. We defined our goodness of measure by δ [19] as follows:

$$
\delta = 1 - \frac{\sum_{n=1}^{N} \|\widehat{e}(n) - e_0(n)\|}{\sum_{n=1}^{N} \|e(n) - e_0(n)\|}, \tag{18}
$$

where $e_0(n)$ is a *baseline* model obtained by setting matrices B and D to zero. In (11),

$$
\dot{x}(n+1) = A(\varphi) x(n), \\ e_0(n) = C(\varphi) x(n). \tag{19}
$$

For our experiments, the model fit was reasonably good in subjects data (with a mean $\mu \cong 82\%$ and standard deviation $\sigma \cong 0.078$). In comparison, Krakauer et al. in [11] do not report the error numerically, although authors state that model parameters are chosen such that the mean square error between model prediction and actual experimental data is minimized. Thoroughman and Shadmehr have reported 60% model fitness in their experiments related to human motor learning [18]. Donchin et al. have documented percentage deviation in model and actual output to be 77% [19]. Scheidt et al. report the variance accounted for (VAF) of 84% as the measure of error of their model [22]. In the nutshell, our model fit is competitive with the results reported in previous model-based studies.

4. Results and Discussion

Figure 4 shows the group averaged ERD patterns during the online feedback. The subjects in No-MI group were waiting for the "Go" signal, while the subjects from MI group were imagining upcoming movement. Both groups showed ERDs, however, ERDs in MI group were more prominent.

From the model parameters it is found that the directional changes of equal magnitude have nearly same estimated values. For the sake of convenience we reduced the number of free parameters to 5 by averaging the parameters on same directional difference values. Let B_j^i be the vector in direction j for user i. Thus, for each direction j, we can formulate a matrix $\mathscr{D}_j$ for both MI and No-MI subjects as follows:

$$
\mathscr{D}_j = \left[B_j^{\,1}, B_j^{\,2}, \ldots, B_j^{\,6} \right]^T. \tag{20}
$$

A new matrix $\mathscr{M}$ can be defined over to reduce the free parameters to 5 by averaging the values on similar distance from peak learning rate. Each column $\mathscr{M}_l$ can be defined by vectors

$$
\mathscr{M}_l = \frac{B_{j+k}^i + B_{j+k}^i}{2} \quad 0 \le k \le 4, \tag{21}
$$

where $j + k$ wraps around in an event of dimension outflow.

4.1. Statistical Analysis of Model Parameters.
The variables were found to be normally distributed when Shapiro-Wilk W-test was applied. Setting the null hypothesis that the variables came from a normal distribution, we found the P values which were greater than the threshold of 0.05 in all cases. Next, we made comparison of relationships between variables (the learning rate in various directions) belonging to MI and No-MI groups by a parametric statistical test named t-test. We found that the MI group has higher learning rate than the

(a) 1st subject

(b) 5th subject

—— Actual error
—— Model output

(c) 11th subject
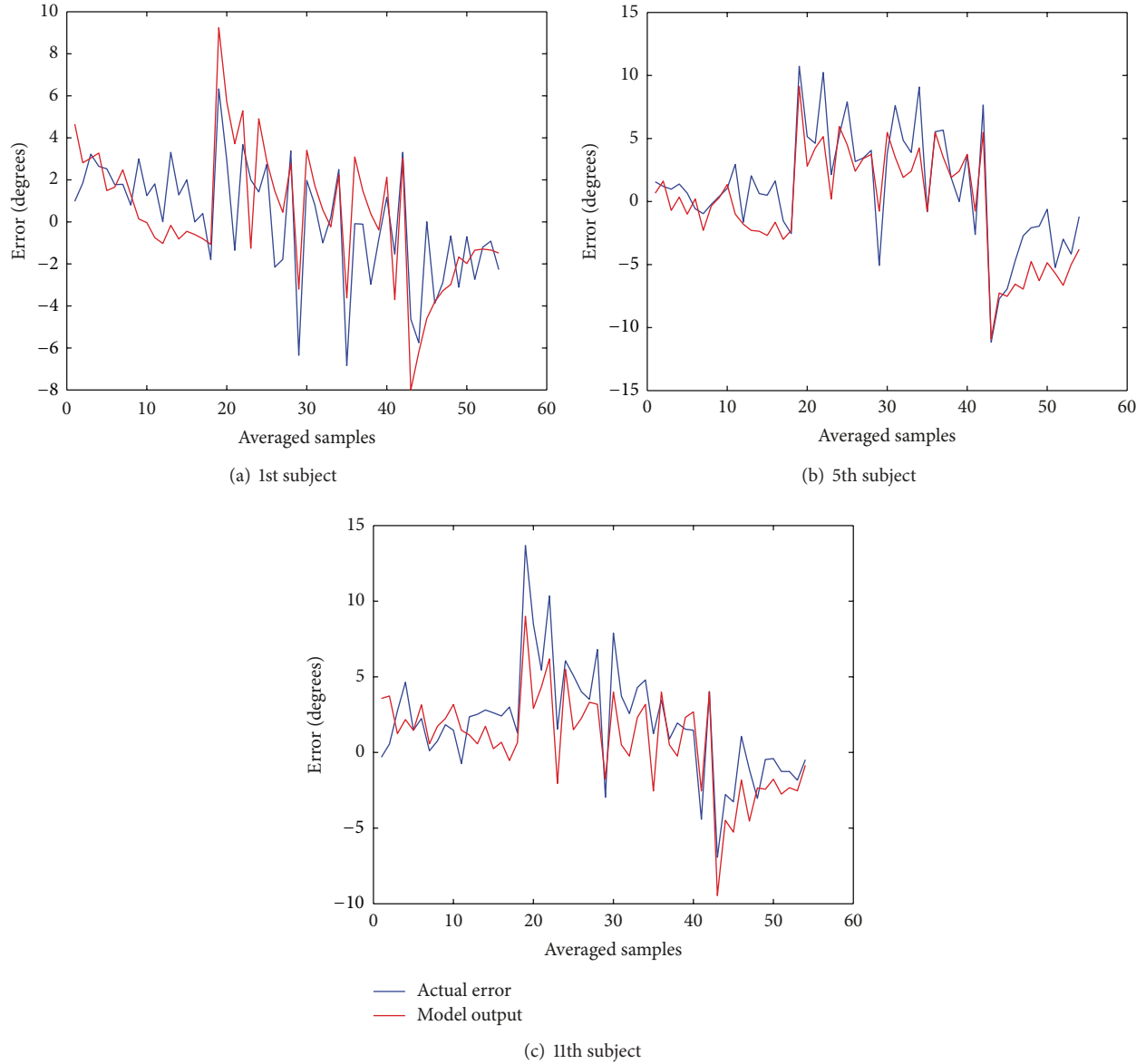
FIGURE 2: Time series of actual movement errors and the corresponding model predictions are shown. The changing trend of model output conforms with the actual movement errors. For the sake of clarity, the values are plotted after averaging every 5 samples.

corresponding No-MI group in all directions. In direction 0°, the learning rate of MI group is 0.203 ± 0.019 and for No-MI group's 0.175 ± 0.024 ($P = 0.046$). In direction 45°, MI group: 0.175 ± 0.026; No-MI group: 0.155 ± 0.023 ($P = 0.05$). In direction 90°, MI group has learning rate 0.184 ± 0.015 in contrast to No-MI group's 0.145 ± 0.031 ($P = 0.020$). In direction 135°, MI group: 0.195 ± 0.016; No-MI group: 0.155 ± 0.031 ($P = 0.023$). In direction 180°, MI group has learning rate 0.224 ± 0.019 in contrast to No-MI group 0.168 ± 0.033 ($P = 0.005$). In direction 225°, MI group: 0.197 ± 0.019, while No-MI group: 0.161 ± 0.030 ($P = 0.039$). In direction 270°, MI group has learning rate 0.189 ± 0.024, while No-MI group 0.148 ± 0.025 ($P = 0.016$). In direction

315°, MI group has learning rate of 0.207 ± 0.029 and No-MI group of 0.165 ± 0.022 ($P = 0.021$). See Figure 5 for a plot of comparison between MI and No-MI groups.

The effect of learning in one direction on immediate next direction was also analyzed. Along 0° the transfer of learning rate for MI group is = 0.112 ± 0.007, and for No-MI group it was 0.08 ± 0.009 ($P = 0.037$). In direction 45°, MI group has transfer of learning rate 0.125 ± 0.009 in contrast to No-MI group 0.092 ± 0.018 ($P = 0.021$). In direction 90°; MI group: 0.104 ± 0.006 and No-MI group: 0.087 ± 0.012 ($P = 0.039$). In direction 135°; MI group: 0.131 ± 0.004 in contrast to No-MI group: 0.077 ± 0.006 ($P = 0.019$). In direction 180°; MI group: 0.122 ± 0.009 and No-MI group: 0.087 ± 0.014 ($P =$

(a) 0°degree

(b) 45°degree

(c) 90°degree

(d) 135°degree
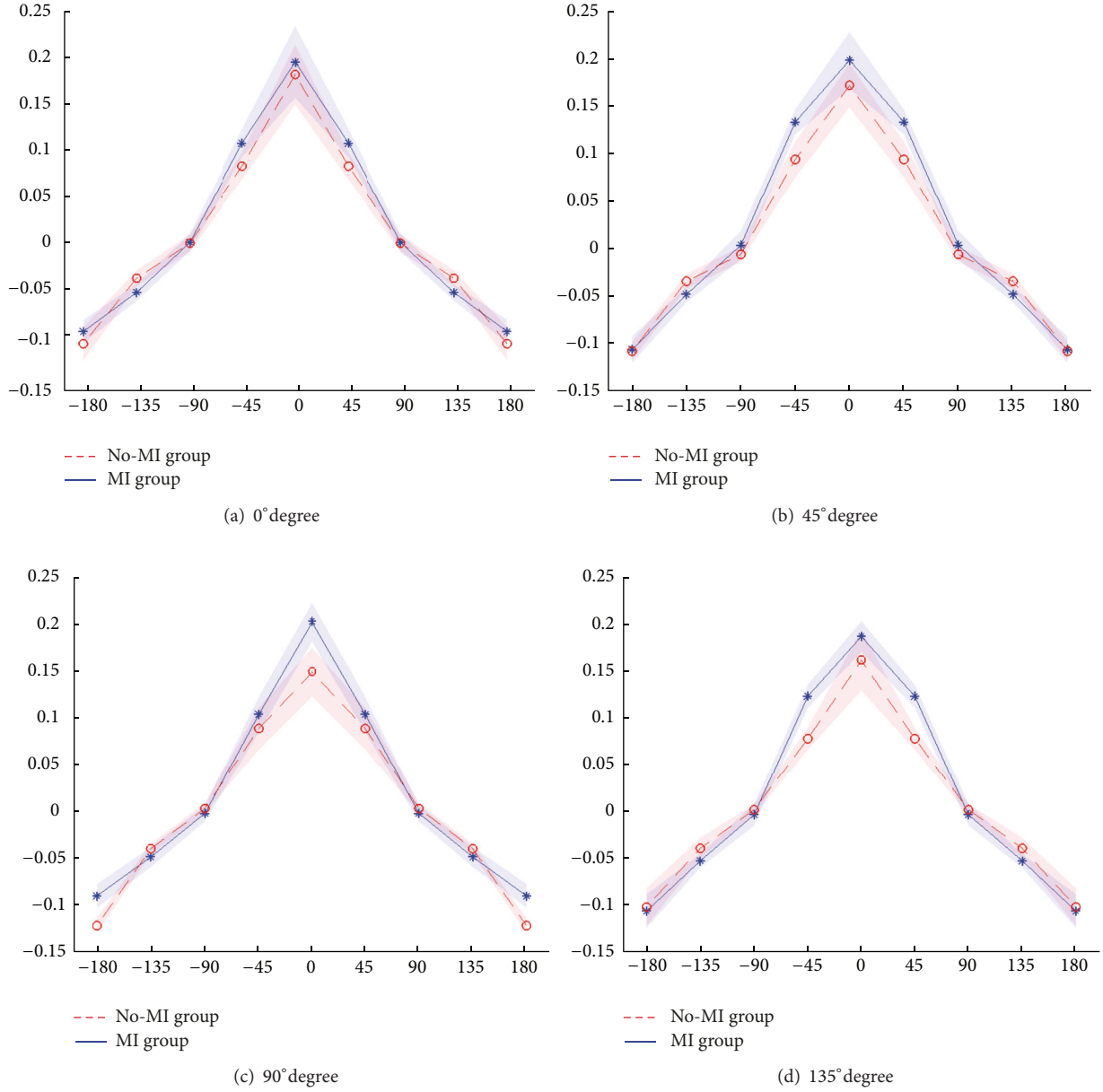
FIGURE 3: Generalization patterns in 4 directions are shown. Free parameters are reduced to 5 by averaging the parameters existing at same directional difference values. Shaded regions show the deviation in parameter values across all subjects.

0.025). In direction 225°; MI group: 0.099 ± 0.011 and No-MI group: 0.081 ± 0.023 ($P = 0.055$). In direction 270°; MI group: 0.114 ± 0.012 and No-MI group: 0.100 ± 0.016 ($P = 0.032$). In direction 315°; MI group: 0.108 ± 0.019 in contrast to No-MI group: 0.072 ± 0.022 ($P = 0.041$). See Figure 6 for a comparison between MI and No-MI groups.

Next, we studied the generalization patterns for MI and No-MI groups averaged over all the subjects in each group, see Figure 7. Student's t-test was performed to account for the significance level of results. Variables were found to be significantly different for MI and No-MI groups with P values < 0.05 in all directions except in direction 90°. The mean

values of learning rate of all users with associated standard deviation are shown in Figure 7. It must be noted that the absolute values of learning rates in directions 135° and 180° are shown for the sake of easy comparison with learning rates in other directions.

4.2. Insights. Generalization patterns along directions 0°, 45°, 90°, and 135° degrees are shown in Figure 3. Also from Figures 5, 6, and 7 it is evident that the subjects with motor imagery have higher learning rates as compared to those of No-MI subjects. Mental rehearsal has focused the learning
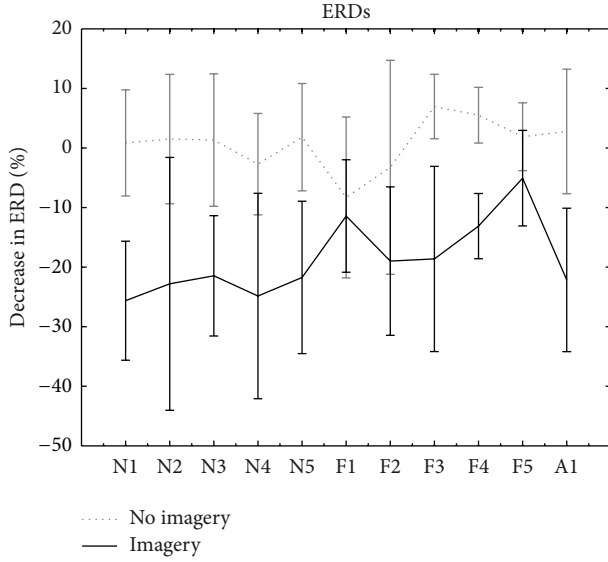
FIGURE 4: Figure shows averaged ERD patterns in both MI (in black) and No-MI (in dotted gray) groups. The ERD was calculated for each direction and was averaged within the sets. MI group has shown more prominent ERDs during imagery time.
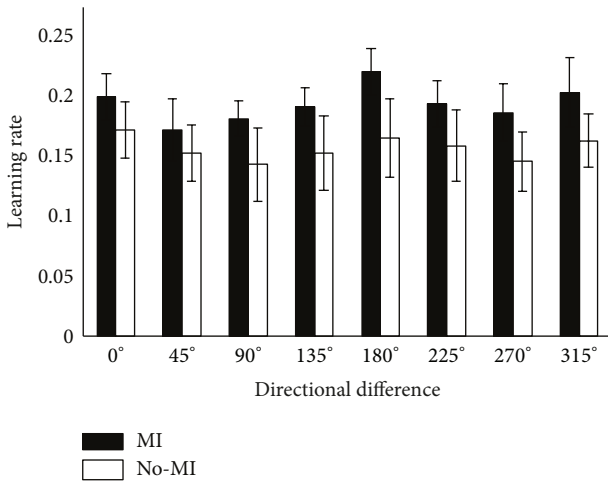
FIGURE 5: Motor learning rate in all directions is shown. The solid bars represent mean values while corresponding standard deviation values are represented by the limits put on bars.

rate in one particular direction (the one in which training is performed). Generally, in both groups the trial-to-trial transfer of learning has decreased as the directional difference increase, but the transfer rate is higher in MI group. In case of 90° directional difference, the averaged generalization pattern shows that the mean and SD for both MI ad No-MI are not significantly different. This can be attributed to the fact that the perpendicular motion is unique and not much difficult to perform. Thus the learning transfer is less as compared to other direction. All the models were found to have a good fit and stable eigenvalues as shown in Figure 8.
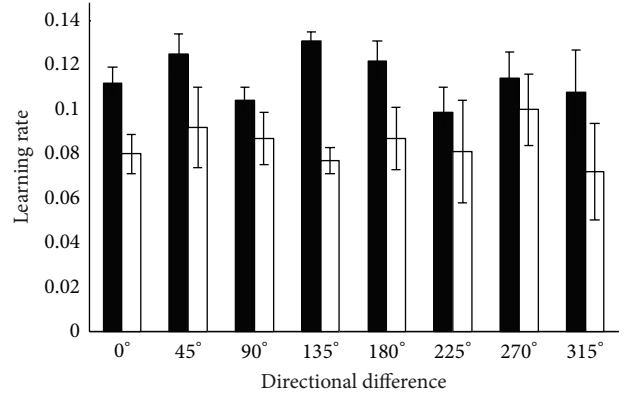
FIGURE 6: Motor learning rate that is, transferred in adjacent direction is shown. The impact of motor learning on immediate next direction (with 45° difference) is averaged across all subjects.
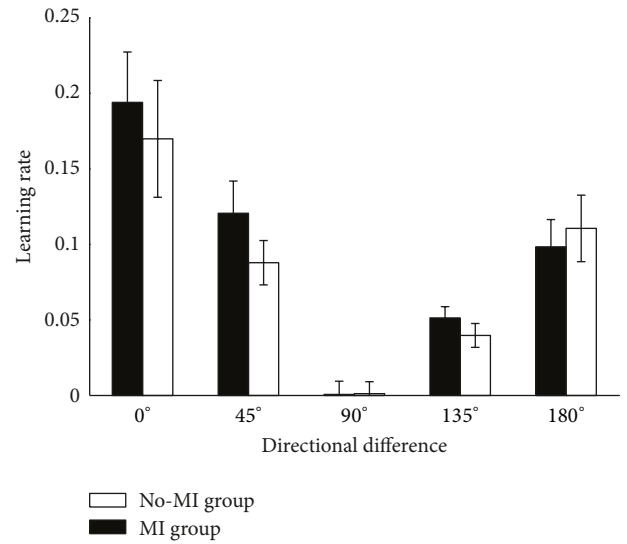
FIGURE 7: Averaged generalization pattern in all possible directional differences for MI and No-MI groups. Solid bars show the mean values, while the deviation is represented by the limits put on bars.

5. Conclusion

In this study we compared the performance of two groups of subjects (MI and No-MI) in a center out-reaching movement task under a force field. The small number of subjects in both groups is a limitation of this study and suggests the need for caution in the interpretation of our results. However, this study helped us to investigate the trial to trial effect of motor imagery on learning. It turned out that our initial three hypotheses were true (see Section 1). MI group has a higher learning rate and transfer of learning as compared to No-MI group and has a more focused generalization pattern. These results show positive influence of motor imagery and suggest that motor learning can be facilitated by mentally rehearsing the upcoming movement and could be used to increase the rate of adaptation.

(a) 3rd subject

(b) 5th subject

(c) 7th subject
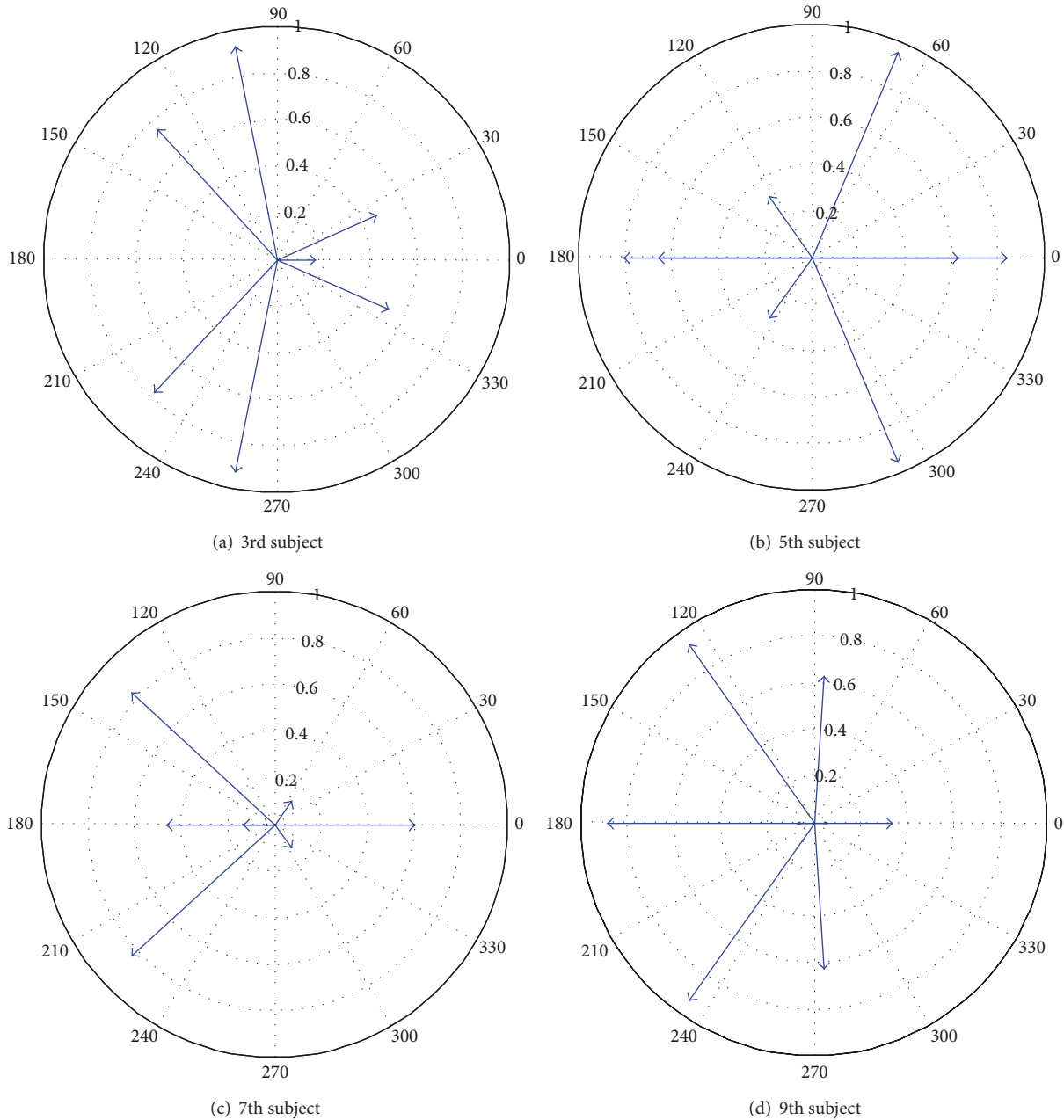
(d) 9th subject

Figure 8: Polar plots for the eigenvalues of all odd subjects are shown. These plots signify that the model built for each subject is stable with the eigenvalues lying inside the unit circle.

References

[1] C. Papaxanthis, T. Pozzo, R. Kasprinski, and A. Berthoz, "Comparison of actual and imagined execution of whole-body movements after a long exposure to microgravity," *Neuroscience Letters*, vol. 339, no. 1, pp. 41–44, 2003.

[2] M. Lotze and U. Halsband, "Motor imagery," *Journal of Physiology Paris*, vol. 99, no. 4–6, pp. 386–395, 2006.

[3] M. N. Anwar, N. Tomi, and K. Ito, "Motor imagery facilitates force field learning," *Brain Research*, vol. 1395, pp. 21–29, 2011.

[4] U. Debarnot, T. Creveaux, C. Collet et al., "Sleep-related improvements in motor learning following mental practice," *Brain and Cognition*, vol. 69, no. 2, pp. 398–405, 2009.

[5] R. Gentili, C. E. Han, N. Schweighofer, and C. Papaxanthis, "Motor learning without doing: trial-by-trial improvement in motor performance during mental training," *Journal of Neurophysiology*, vol. 104, no. 2, pp. 774–783, 2010.

[6] E. L. Shoenfelt and A. U. Griffith, "Evaluation of a mental skills program for serving for an intercollegiate volleyball team," *Perceptual and Motor Skills*, vol. 107, no. 1, pp. 293–306, 2008.

[7] J. Munzert, B. Lorey, and K. Zentgraf, "Cognitive motor processes: the role of motor imagery in the study of motor representations," *Brain Research Reviews*, vol. 60, no. 2, pp. 306–326, 2009.

[8] M. N. Anwar, V. Sanguineti, P. G. Morasso, and K. Ito, "Motor imagery in robot-assistive rehabilitation: a study with healthy subjects," in *Proceedings of the IEEE International Conference on Rehabilitation Robotics (ICORR '09)*, pp. 337–342, June 2009.

[9] R. Shadmehr and F. A. Mussa-Ivaldi, "Adaptive representation of dynamics during learning of a motor task," *The Journal of Neuroscience*, vol. 14, no. 5, pp. 3208–3224, 1994.

[10] U. Halsband and R. K. Lange, "Motor learning in man: a review of functional and clinical studies," *Journal of Physiology Paris*, vol. 99, no. 4–6, pp. 414–424, 2006.

[11] J. W. Krakauer, P. Mazzoni, A. Ghazizadeh, R. Ravindran, and R. Shadmehr, "Generalization of motor learning depends on the history of prior action," *PLoS Biology*, vol. 4, no. 10, p. e316, 2006.

[12] F. A. Mussa-Ivaldi and E. Bizzi, "Motor learning through the combination of primitives," *Philosophical Transactions of the Royal Society B*, vol. 355, no. 1404, pp. 1755–1769, 2000.

[13] L. Pignolo, "Robotics in neuro-rehabilitation," *Journal of Rehabilitation Medicine*, vol. 41, no. 12, pp. 955–960, 2009.

[14] S. J. Page, J. P. Szaflarski, J. C. Eliassen, H. Pan, and S. C. Cramer, "Cortical plasticity following motor skill learning during mental practice in stroke," *Neurorehabilitation and Neural Repair*, vol. 23, no. 4, pp. 382–388, 2009.

[15] M. Casadio, V. Sanguineti, C. Solaro, and P. G. Morasso, "A haptic robot reveals the adaptation capability of individuals with multiple sclerosis," *The International Journal of Robotics Research*, vol. 26, no. 11-12, pp. 1225–1233, 2007.

[16] G. Schalk, D. J. McFarland, T. Hinterberger, N. Birbaumer, and J. R. Wolpaw, "BCI2000: a general-purpose brain-computer interface (BCI) system," *IEEE Transactions on Biomedical Engineering*, vol. 51, no. 6, pp. 1034–1043, 2004.

[17] M. Smith and R. Shadmehr, "Intact ability to learn internal models of arm dynamics in huntington's disease but not cerebellar degeneration," *Journal of Neurophysiology*, vol. 93, no. 5, pp. 2809–2821, 2005.

[18] K. A. Thoroughman and R. Shadmehr, "Learning of action through adaptive combination of motor primitives," *Nature*, vol. 407, no. 6805, pp. 742–747, 2000.

[19] O. Donchin, J. T. Francis, and R. Shadmehr, "Quantifying generalization from trial-by-trial behavior of adaptive systems that learn with basis functions: theory and experiments in human motor control," *The Journal of Neuroscience*, vol. 23, no. 27, pp. 9032–9045, 2003.

[20] L. Ljung, "Prediction error estimation methods," *Circuits, Systems, and Signal Processing*, vol. 21, no. 1, pp. 11–21, 2002.

[21] P. van Overschee and B. de Moor, "N4SID: Subspace algorithms for the identification of combined deterministic-stochastic systems," *Automatica*, vol. 30, no. 1, pp. 75–93, 1994.

[22] R. A. Scheidt, J. B. Dingwell, and F. A. Mussa-Ivaldi, "Learning to move amid uncertainty," *Journal of Neurophysiology*, vol. 86, no. 2, pp. 971–985, 2001.

Research Article

Coercively Adjusted Auto Regression Model for Forecasting in Epilepsy EEG

Sun-Hee Kim,[1] Christos Faloutsos,[1] and Hyung-Jeong Yang[2]

[1] *Department of Computer Science, Carnegie Mellon University, Pittsburgh, PA 15213, USA*
[2] *Department of Computer Science, Chonnam National University, Gwangju 500-757, Republic of Korea*

Correspondence should be addressed to Hyung-Jeong Yang; hjyang@jnu.ac.kr

Recently, data with complex characteristics such as epilepsy electroencephalography (EEG) time series has emerged. Epilepsy EEG data has special characteristics including nonlinearity, nonnormality, and nonperiodicity. Therefore, it is important to find a suitable forecasting method that covers these special characteristics. In this paper, we propose a coercively adjusted autoregression (CA-AR) method that forecasts future values from a multivariable epilepsy EEG time series. We use the technique of random coefficients, which forcefully adjusts the coefficients with -1 and 1. The fractal dimension is used to determine the order of the CA-AR model. We applied the CA-AR method reflecting special characteristics of data to forecast the future value of epilepsy EEG data. Experimental results show that when compared to previous methods, the proposed method can forecast faster and accurately.

1. Introduction

Forecasting time series data predicts future values by discovering a set of rules or identifying patterns from past data. Linear regression models for forecasting time series such as autoregressive (AR), moving average (MA), and autoregressive moving average (ARMA) are widely used [1]. However, these methods have difficulty obtaining accurate forecasts when the time series data has nonlinear characteristics that constantly change. Thus, soft computing techniques, such as fuzzy logic and neural networks, have been developed to resolve the problems of linear approach considering nonlinear properties and uncertainty of time series data [2, 3].

EEG time series signals obtained from a brain have irregular and complex wave structures. They also include a large amount of noise. Epilepsy EEG data is a representative example of a complex time series. Epilepsy is a disease defined by abnormal electrical activity in the brain that is central to the diagnosis of epilepsy. Epilepsy EEG signals display changes over time through constant interaction with external factors [4]. Noise is included within the complexity of epilepsy EEG data during measurements. Epilepsy EEG data is difficult to forecast because it has special characteristics,

such as nonlinearity, abnormalities, and noise. Therefore, it is important to select an appropriate forecasting method because these characteristics affect the forecasting accuracy.

In recent years, studies have been conducted to automatically detect and predict epilepsy seizures using EEG data. Univariate, bivariate, and multivariate algorithms were proposed to solve the problem of seizure detection and prediction based on the EEG analysis of single or multiple electrodes [5–7]. Rabbi et al. applied nonlinear dynamics based on unvaried characteristic measurements to extract a correlation dimension from the intracranial EEG recordings and designed a fuzzy rule-based system for seizure prediction [8]. Iasemidis et al. proposed an adaptive seizure prediction algorithm (ASPA) based on the convergence of the short-term maximum Lyapunov exponents (STLmax) among critical electrodes in the preseizure phase [9]. Liu et al. introduced a seizure prediction approach using particle filtering [10]. Also, Shahidi Zandi et al. proposed a method to predict seizures by analyzing the entropy level corresponding to zero-crossing intervals in scalp EEG and its derivatives [11]. Many researchers also used autoregressive and spectral analysis for forecasting by extracting seizure precursors from the EEG data [12, 13]. However, these researchers used approaches that

were based on the linear data or unvaried characteristics of data.

We can give the following problem definition.

Problem Definition. Given a time series data which includes special characteristics such as nonlinearity, nonnormality, and nonperiodicity, a forecasting model attempts to forecast the values over some future time period. More formally, given a time series of Epilepsy EEG $X = x_1, x_2, \ldots, x_t$, we forecast the value of x_{t+n}. x_t is the value of the time series at time t, and n is the forecasting length.

In this paper, we propose an adaptive forecasting algorithm that adjusts its coefficients of the autoregressive (AR) model forcedly. To forecast the future values of epilepsy EEG data including special characteristics, we use the random coefficients with −1 and 1 and the fractal dimension which the order of the CA-AR model determines. We conduct experiments with sets of EEG time series to evaluate the suitability of our forecasting approach. The experimental results demonstrate that the proposed method provides better forecasting performance than previous methods. The proposed algorithm provides the following benefits: (1) seizure forecasting and warning to patients about seizures and (2) actively probing the characteristics of seizure onset.

The remainder of the paper is organized as follows. In Section 2, we describe the proposed method for forecasting. The experiment results are compared with the other methods in Section 3. In Section 4, we discuss the related work on the prediction and analysis of seizures. Finally, we present our conclusions in Section 5.

2. Materials and Methods

An autoregressive model is a simple model to estimate the future value of a series using previous input values. The AR(p) model represents a stochastic process using a general form of order p as shown in (1):

$$
\begin{aligned}
X_t &= c + \varphi_1 X_{t-1} + \varphi_2 X_{t-2} + \cdots + \varphi_p X_{t-p} + \varepsilon_t, \\
X_t &= c + \sum_{i=1}^{p} \varphi_i X_{t-i} + \varepsilon_t,
\end{aligned}
\tag{1}
$$

where X_t is the observation at time t, φ_p is the autoregressive coefficient of pth order, and ε_t is white noise normally distributed with mean zero and variance σ^2 at time t.

An important feature of the AR model is utilizing recent past observations in the process of estimating the current observation X_t at time t. That is, the current observation can be estimated by a linear weighted sum of previous observations. The weights denote the auto-regression coefficients. The problem in AR analysis is the assumption that data is stationary and linear, and it must derive the best values for coefficients given a series X_t. Several methods have been used to estimate AR parameters, such as Yule-Walker, least squares, and Burg's method [1]. It has been shown that for large data samples these estimation techniques should lead to approximately the same parameter values. The Yule-Walker method applied the AR model to the signals by minimizing

the forward forecasting error in a least squares sense. The unknown parameter φ is estimated as follows:

$$
\widehat{\varphi} = \frac{\sum_{i=1}^{p} X_t X_{t-i}}{\sum_{i=1}^{p} X_{t-i}^2}.
\tag{2}
$$

Under the assumption that ε_t is normally distributed, this is also the maximum likelihood estimate of φ. The distribution of $\widehat{\varphi}$ has been studied extensively. Unfortunately, the exact distribution of $\widehat{\varphi}$ is unknown. Asymptotically, if $|\varphi| < 1$, it has a normal distribution, while if $|\varphi| > 1$, it is a Cauchy distribution. In addition, if $|\varphi| = 1$, it is a nonstandard distribution [14]. These distributions can be used to approximate the finite sample distribution of $\widehat{\varphi}$. This suggests that the distribution would not adequately approximate the finite sample distribution, especially near the discontinuity point of $\varphi = 1$, because the exact distribution of $\widehat{\varphi}$ is continuous for all values of φ. It has been found that, unless φ is close to zero, these distributions do not approximate the distribution of finite samples well. The nonstandard limiting distribution when $|\varphi| = 1$ seems to give a good approximation of the finite sample distribution when $|\varphi|$ is close to 1. However, it is too complex for practical use since an accurate approximation to this nonstandard limiting distribution can be obtained from the asymptotic expansion [15]. In this study, our aim is to find a forecasting method suitable for epilepsy EEG data. More specifically, suppose that $\{\varphi_t\}$ is an independent and identically distributed sequence defined by

$$
\varphi_t = \begin{cases} \theta & \text{with probability } \alpha, \\ -\theta & \text{with probability } 1 - \alpha, \end{cases}
\tag{3}
$$

where $0 \leq \theta < \infty$ and $0 < \alpha < 1$. From (3), we have $\varphi = E(\varphi_t) = 2(\alpha - 1)\theta$, $E(\varphi_t^2) = \theta^2$, and $\sigma_\varphi^2 = \theta^2 - \varphi^2 = 4\alpha(1-\alpha)\theta^2$ [16].

In particular, if we take $\theta = p$, we obtain a special case of an AR(p) process [16]. We study this special case in this paper. As a motivation for the model in (3) for $\{\varphi_t\}$ with $\theta = p$, consider the order of the standard flexible coefficient AR(p) model given in (1). If $\varphi = 1$, we have (4) leading to the standard random model from (1):

$$
X_t^{(p)} = \sum_{i=1}^{t-p} \varepsilon_{t-i}.
\tag{4}
$$

If we put $\varphi = -1$, we have

$$
X_t^{(p)} = \sum_{i=1}^{t-p} -(1)^i \varepsilon_{t-i}.
\tag{5}
$$

Both models (4) and (5) correspond to the standard (critical case) unit root [17]. A model that generalizes (4) and (5) is

$$
X_t = \sum_{i=1}^{t-p} \xi_{ti} \varepsilon_{t-i},
\tag{6}
$$

where the random coefficients $\{\xi_{ti}\}$ take the values 1 or −1. The model in (6) can be viewed as a generalization of the standard

random where the successive jumps go up or down according as $\xi_{ti} = 1$ or -1.

Epilepsy EEG data has special characteristics, such as nonlinearity and abnormal and nonstandard distributions [4]. Therefore, in this study, when EEG data has an abnormal distribution, we forcefully adjust the coefficients of AR. In this paper, the AR model is the basis of our coercively adjusted AR model (CA-AR). This model can be expressed as follows:

$$X_t = c + \sum_{i=1}^{p} \pi_{tp} \cdot X_{t-i} + \varepsilon_t, \tag{7}$$

where π_{tp} is random coefficients with $\varphi = 1$ and $\varphi = -1$, with $\pi_{t1} = 1$ and $|\pi_{tp}| = 1$ for all t and p. p has an important role in AR modeling since it determines the order of the coefficients. In the autoregressive model, to determine the order of the AR model is an important issue [18]. The order of an AR model, p, must be appropriately selected because it determines the efficiency of the autoregressive model. If p is smaller, then the estimation error is higher while calculation speed is faster. On the other hand, if p is bigger, there are drawbacks requiring more computation time without any decreases in estimation error. Therefore, in order to resolve these drawbacks, an optimal way to determine the order of the AR model is required.

In this paper, the fractal dimension is used to determine the order of the CA-AR model. To calculate the fractal dimension, we apply the box-counting method [19]. The box-counting method is one of the most common methods to obtain the fractal dimensions using boxes that are big enough to cover the measured signal S [20]. In other words, when the length of one side of the square is ε $(\varepsilon > 0)$ and the number of square boxes is N_ε, the box-counting dimension of S is $N_\varepsilon(S) \sim 1/\varepsilon^d$ and $\varepsilon \to 0$. It can be expressed as the box-counting dimension of S, d, and the positive constant, k:

$$\lim_{\varepsilon \to 0} \frac{N_\varepsilon(S)}{1/\varepsilon^d} = k. \tag{8}$$

By taking logs on both sides of (8), we get

$$\lim_{\varepsilon \to 0} \left(\ln N_\varepsilon(S) + d \ln \varepsilon \right) = \ln k. \tag{9}$$

Fractal dimension d is given by (10):

$$d = \lim_{\varepsilon \to 0} \frac{\ln k - \ln N_\varepsilon(S)}{\ln \varepsilon} = -\lim_{\varepsilon \to 0} \frac{\ln N_\varepsilon(S)}{\ln \varepsilon}, \tag{10}$$

where $\ln k$ is excluded while the denominator $\varepsilon \to 0$. Also, $0 < \varepsilon < 1$, and if $\ln \varepsilon$ is a negative number, d will be a positive number. If the log-diagram of $\ln \varepsilon$ verses $\ln N_\varepsilon$ is a straight line, the fractal dimension is the slope of this straight line (as shown in Figure 3).

In this paper, the measured value d using (10) is defined as the order of AR, p, and it is applied to the CA-AR(p) model. In other words, to predict epileptic seizures from EEG data, the future value X_t is predicted using $X_{t-1}, \ldots, X_{t-p}$, the observed values from the past. This paper will show that special case of epileptic seizure where X_t is predicted by $X_{t-1}, \ldots, X_{t-p}$, where the series X_t is AR(p) using (7). The estimated AR model is then used for prediction by applying the least squares estimation.

3. Results

In this section we present the empirical verification of our data analysis to forecast epilepsy EEG data. EEG datasets are provided in [4], and epilepsy EEG data set composed the five EEG datasets 5 (denoted by A~E). A and B datasets are recorded in the relaxed awake state of healthy volunteers (eye open or closed). C and D are measured during seizure free intervals, and E contained seizure activity. These five EEG datasets contain 100 single channel EEG segments of 23.6 sec duration, and they are sampled at 173.61 Hz. For our experiments, we used only three datasets such as A, C, and E.

3.1. Detection of Special Characteristics. In this paper, we proposed a novel approach to help in the improvement of epileptic seizure forecasting in nonlinear and nonperiodic EEG signals. In this section, we first analyze the characteristics of epilepsy EEG data which show nonlinearity and periodicity by applying cepstrum and lag plots. The cepstrum is employed to extract periodicities or repeated patterns [21]. The cepstrum analysis of a spectrum will have peaks corresponding to the spacing of the harmonics and sidebands. The x-axis of the cepstrum shows frequency, and peaks in the cepstrum are related to periodicities. The cepstrum is employed to find the periodicity in Subjects A, C, and E. Figure 1(a) demonstrates the 50th original signal of Subject E recorded during seizure activity and Figure 1(b) displays the measured periodicity using the cepstrum. Figure 1(a) seems to have a periodic wave within the original signal. However, Figure 1(b) does not have any periodicity. In addition, Subjects A and C also do not show the periodicity.

Even though the periodicities in the original signal repeatedly appear as a sinusoidal wave during seizure activity, when we applied the cepstrum to the seizure activity signals, the results differ from the original signal. Seizure activity signals do not have any periodicity. We observed that our experimental results of the seizure activity signals by the cepstrum do not have any periodicity. Therefore, since most conventional forecasting or prediction approaches require periodicity in observed data, these approaches are not appropriate for the nonperiodic seizure activity signals.

In this paper we also applied lag plots to find hidden characteristics in the data. Lag plots are useful in the analysis of cyclical data [22]. A lag plot checks whether a dataset is random or not. In addition, they provide the autocorrelation of the data. Figure 2(a) shows the first raw signal of Subject A's epilepsy EEG time series. The lag plot of Subject A is shown in Figures 2(b) and 2(c), where the lag $L = 1$ and $L = 20$, respectively. Figure 2(b) shows a definite linear structure in the lag plot, which was hidden in Figure 2(a). That is, this lag plot exhibits a linear pattern. If the data is strongly nonrandom, we are able to apply an autoregressive model that might be appropriate for prediction. Figure 2(c) shows the Gaussian distribution of Subject A plotted with a lag of $L = 20$ by plotting x_t versus x_{t-20}. Figure 2(d) is the first raw signal of Subject C. Figures 2(e) and 2(f) show lag plots for $L = 1$ and $L = 20$, respectively. In the case of $L = 1$, linear patterns are shown for both Subject A and Subject C. Figure 2(f) shows similar results

(a) The 50th original signal of Subject E

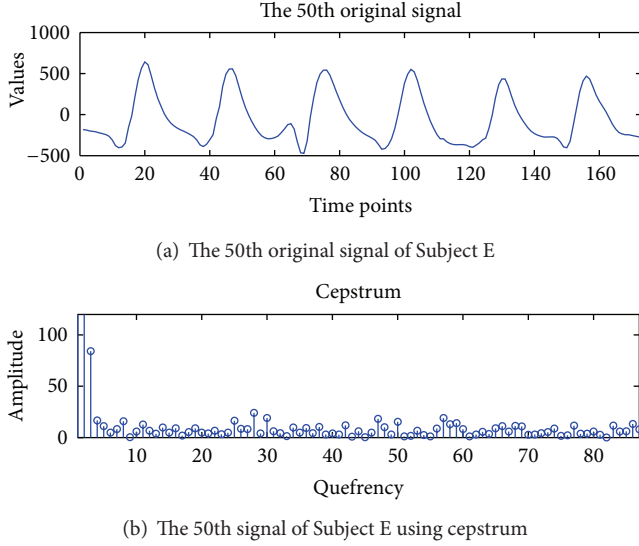(b) The 50th signal of Subject E using cepstrum

FIGURE 1: Periodicity detection using cepstrum in Subject E.

to Figure 2(c). However, Figures 2(h) and 2(i) for Subject E differ from Subject A and Subject C. In the case of $L = 20$ shown in Figure 2(i), it is a mixture of Gaussian distribution. Generally, when a lag plot has a nonrandom pattern, the data can be predicted using conventional methods. However, the epilepsy EEG dataset shows random patterns that are difficult to be predicted by conventional approaches. Thus, we need a suitable method for forecasting of EEG signals whose characteristics are nonlinearity and nonperiodicity.

3.2. The Order of CA-AR Choice (Box-Counting) for Forecasting. In this section, we present how the order of CA-AR is determined using fractal dimension. We use box-counting analysis which is a common method for fractal dimension estimation. It is also known that it is easy, automatically computable, and applicable to patterns with or without self-similarity [20]. However, this technique, including the processing of data and definition of the range of grid size, requires proper implementation to be effective in practice. In this study, the grid size is changed from 0.1 to 10000 in multiplication of 2 [22]. The slope of the linear part of the plot is the estimated fractal dimension d of the epilepsy dataset. In this method each signal is covered by a sequence of grids of ascending sizes. Two values are recorded for each of the grids: the number of square boxes intersected by the signal, $N_\varepsilon(S)$, and the side-length of the squares, ε. The slope d of the straight line formed by plotting $\log(N_\varepsilon(S))$ against $\log(1/\varepsilon)$ indicates the degree of complexity or fractal dimension between 1 and 2 ($1 \leq d \leq 2$) [23]. A signal with a fractal dimension of 1 or 2 is considered as completely differentiable or very rough and irregular, respectively.

We measured the fractal dimension of the 100 single signals from each subject to determine the order of CA-AR using box-counting analysis. Figure 3 illustrates the plot of $\log(N_\varepsilon(S))$ versus $\log(1/\varepsilon)$ based on the grid sizes. The log-log plots of Figure 3 are used to estimate the fractal dimension

that is computed from the slope of the plot. Figures 3(a), 3(b), and 3(c) are the log-log plot for the fractal dimension of the 1st signals of Subject A, Subject C, and Subject E. This graph clearly displays a horizontal straight line when the grid size is small or too big. Deviation from a linear straight line can be expected to lead to underestimation of the fractal dimension value for the skeleton of a signal.

We applied the box-counting method to estimate the fractal dimension of the Phase Space from a signal of each subject. The vector space of the delay coordinate vectors is termed the Phase Space [22]. The observation sequence is represented by the series x_t, which gives the value of the time series at time t. That is, we can define $V = [x_t, x_{t-\tau}, x_{t-2\tau}, \ldots, x_{t-L\tau}]$. τ is a real number greater than zero termed the time delay, and L is any integer greater than zero. The vector V is termed the delay coordinate vector, because its terms are the time-delayed data values from the time series. Given time series x_t and lag L, we form all the delay coordinate vectors from x_t. The Phase Space is a $(L + 1)$-dimensional space.

Figure 4 demonstrates the estimated fractal dimensions. The x-axis and y-axis denote the Phase Space (time delay space) and slope, respectively. This implies that a lag length of one is sufficient to reconstruct the state space.

Figure 4 shows fractal dimension of few signal, and we confirm some particular results; if the dimension of signal x_t increases, the fractal dimension (slope) increases. As a result of Figure 4, in the case of Subjects A and C, signals mostly have a fractal dimension between 5 and 7, while Subject E exhibits a fractal dimension between 2 and 4 when time delay is 20. That is, Subjects A and C exhibit an average slope between 4 and 5. However, in the case of Subject E, the seizure activity represents an average slope of 2.5. When the time delay dimension increases, the fractal dimension increases. However, the plot of fractal dimension versus lag length shows that fractal dimension does not significantly increase, as lag length is incremented. This experiment shows the determination of the value of parameters using log-log plots for time series prediction. That is, we select the round-up integer of the average slope values of all normal signals as Subjects A and C for the order p of CA-AR, because we must predict abnormal behavior that dropped out of the past pattern. We ran the CA-AR model with the round-up integer "5" of the average of the slope of all signals for forecasting. To verify that the selected $p = 5$ is the optimal order, we measured the forecasting error of each signal from each subject. That result can be confirmed in Section 3.3.

3.3. Forecast Accuracy. To evaluate the reliability of optimal order for our model, we measured Root Mean Square Error (RMSE) of forecasting from all signals of each subject. An autoregressive model of order p implies that the current value of the time series is being predicted based on past pth data of the same random variable. Thus, an autoregressive model of order p can be expressed using the p previous values of the time series. Let $X_1, X_2, \ldots$, be successive instances of the random variable X, measured at regular intervals of time. We applied the standard AR model and CA-AR (coercively
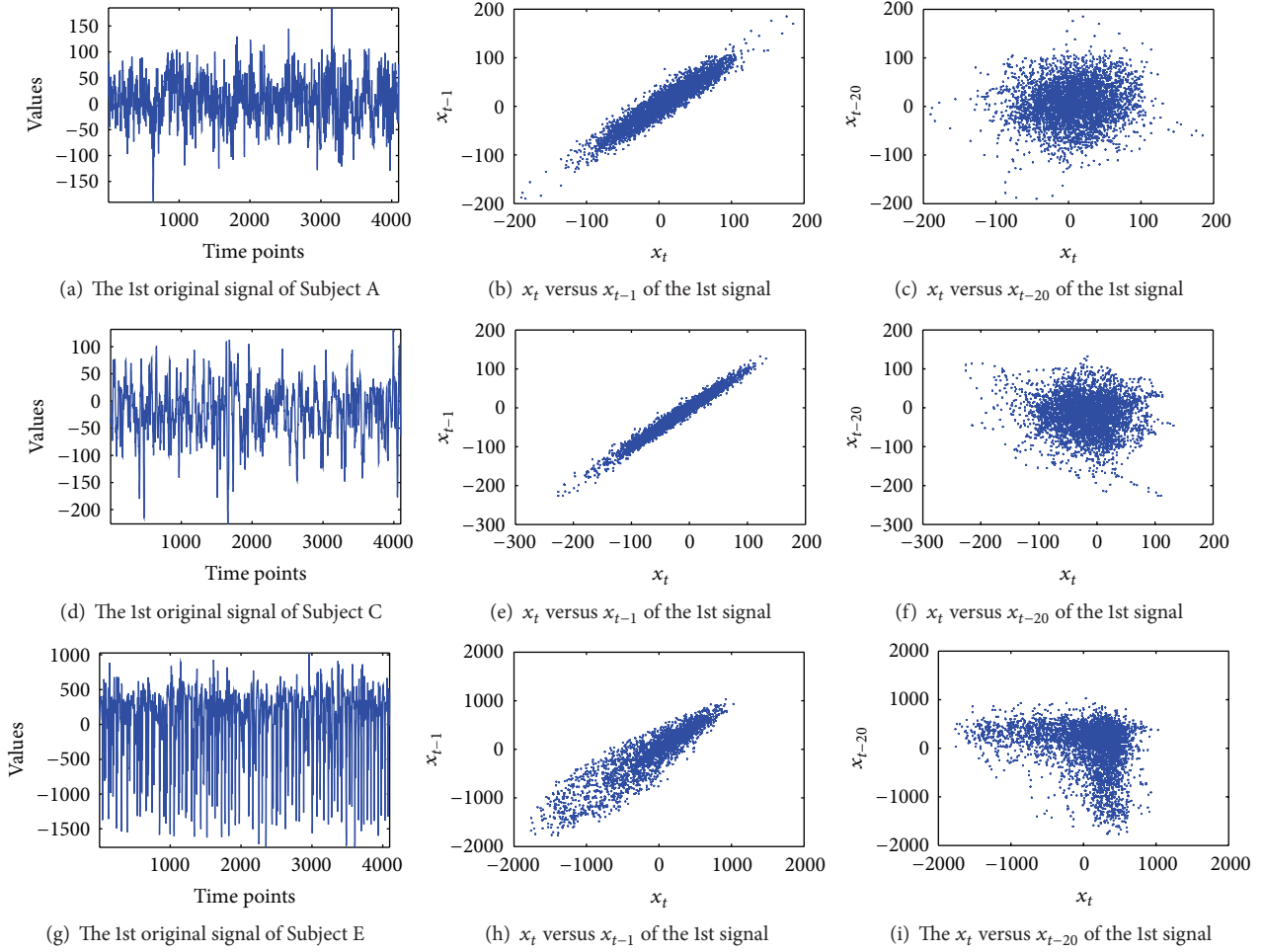
FIGURE 2: Lag plots: epilepsy EEG dataset. Subject A is shown in (a). This appears hard to predict. (d) is Subject C, and Subject E is shown in (g). (b), (e), and (h) show the two-dimensional lag plots of x_t versus x_{t-1}, for each subject. (c), (f), and (i) are lag plots of x_t versus x_{t-20}, respectively.

adjusted coefficient with $\varphi = 1$ or -1) model to forecast the new X_t of the epilepsy EEG data.

We forecasted the signals from 481 to 500 time points by the proposed model and compared the forecasting errors between the optimal order that decided by the average of fractal dimensions and the other orders. For forecasting, we used the p past values of time series, and p is selected by fractal dimension. If $p = 5$, our model uses from 476 to 480 time points to forecast 481 time point. Table 1 shows RMSE results of several signals that were measured between the original values and the generated values by the model. RMSE is compared when the orders are 3, 5, 10, and 15 for AR and the proposed method. In the case of $p = 5$ in the proposed model, RMSE has a higher accuracy than $p = 3$, $p = 10$, and $p = 15$ in Subjects A, C, and E. In case of the standard AR, Subjects A, C and E exhibited the lowest RMSE in $p = 5$, similar to the proposed method. As shown in Table 1, the proposed method is exhibits a lower error rate than standard AR, and when p is 5, the lowest RMSE exhibited in Subject E among the subjects. Thus, we confirm that optimal order is 5, and it is used as the order of the CA-AR during experiments to verify the

efficiency. The order of the proposed method is determined with the round-up integer of the average fractal dimension that it is measured from all normal signals as Subjects A and C.

Figure 5 shows the result of the forecast snapshot of Subjects A, C, and E, using the CA-AR and standard AR models. Plots (a), (c), and (e) show a specific case of a 20-time step prediction of the 20th electrode, and plots (b), (d), and (f) provide the prediction result for the 80th electrode signal. The original signal is shown in Figure 5(a), from time 481 to 500 in red line with the star point marker. The plus sign marker shows the forecasted signals by the proposed method (green line) and the point marker plots the forecasted signals by standard AR (blue line). These plots confirm that our forecasting method outperforms the conventional AR method.

In this paper, we compared the forecasting results among several existing methods and CA-AR method. Table 2 shows the forecasting results using existing methods of linear and nonlinear prediction (Artificial Neural Networks [3], Fuzzy [2, 24], Nearest Neighbors [25], and the proposed method) of

(a) Subject A

(b) Subject C
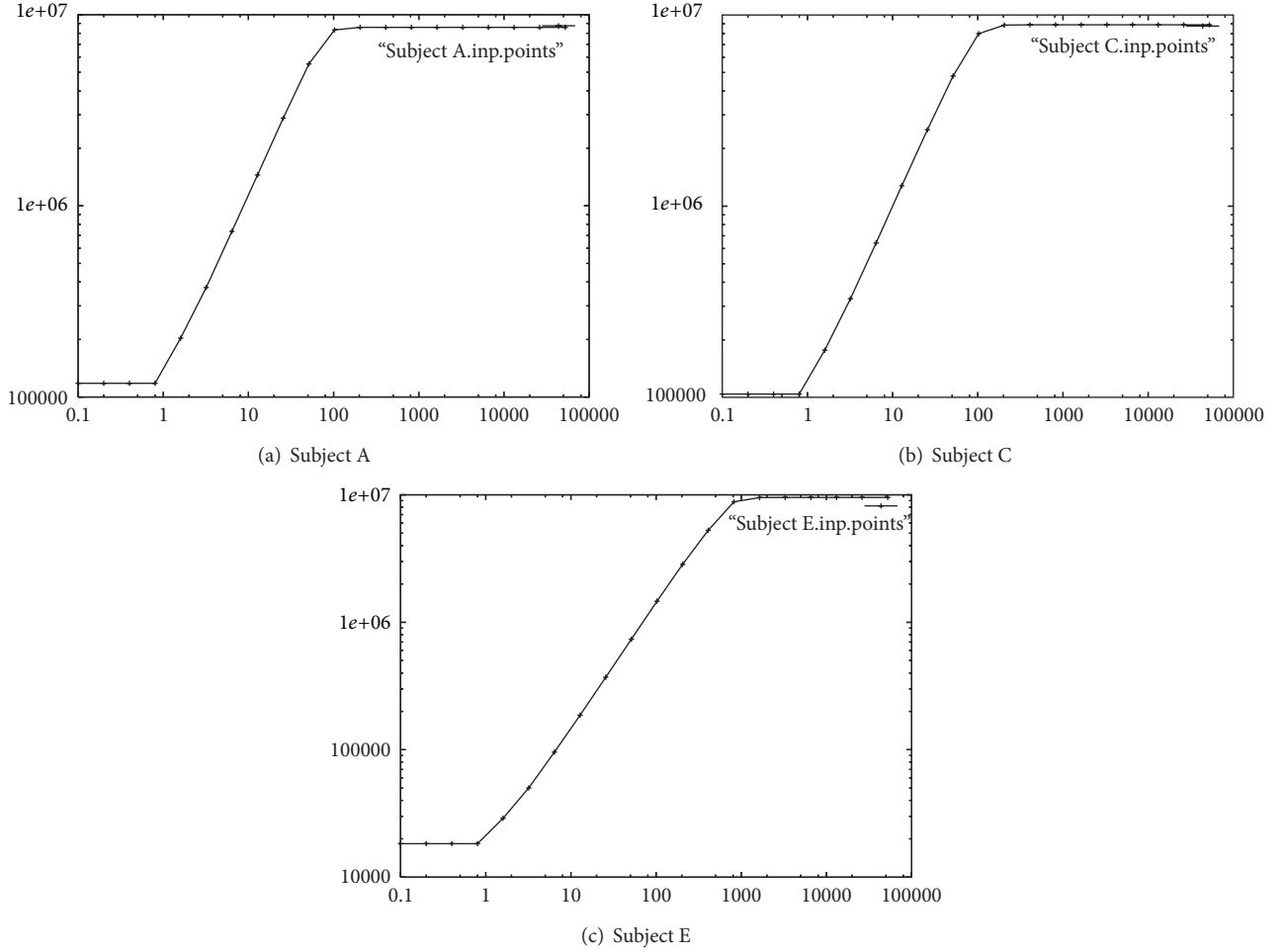
(c) Subject E

FIGURE 3: Fractal dimension: the log-log plot about the 1st signal (a vector x_t) for each of Subjects A, C, and E.

the 7th electrode signal in Subject E. For the experiments, we used a single signal of each subject to measure the forecasting error in each forecasting method. Also, to measure forecasting errors of existing methods, we derived the partial training signals from original signals that are from the starting points to 500 time points or 1000 time points of signal. For example, when the existing method tries to forecast the length of 150 time points, 1 to 500 time points or 1000 time point of the signal are used for training. However, our method still uses only 5 time points to forecast the future values of 150 time points. CA-AR considers from the time 496 to 500 to forecast the future values of the time 501, and it used from the time 497 to 501 to forecast the time 502.

As a result of Table 2, the proposed method shows lower error rates than existing forecasting methods. In case of ANN, RMSE is gradually increased when the forecasting time points increase. However, our proposed method is unaffected by the length of the forecasting time points because it used only the order p of AR. Besides, even though the length of forecasting time points increased, the error rate of the forecasting result did not show much change in our model. In case of the Fuzzy-based method, it performs the batch process using all of the previous values to estimate the new value. Thus, we quit

measuring the forecasting error because it requires very long execution time.

Table 3 measures the forecasting time using the existing methods as in Table 2. For example, if the training time duration of ANN (Artificial Neural Networks) is 500 and the forecasting time duration is 150, then 0.5304 represents the execution time to forecast from the time 501 to 650. Fuzzy-based method [2, 24] was excluded from the 1500-forecasting time point test, because it already exhibited the highest forecasting time compared to the other methods in the 150-time point forecasting test. The proposed method achieves much faster forecasting time than ANN (Artificial Neural Networks) and NN (Nearest Neighbors). When the training time point or forecasting time point increases, the existing methods incrementally increase the forecasting time. However, since the proposed CA-AR method uses only a few observed values, it maintains a steady time. In the case of epilepsy seizure, we assume that it should be able to inform a patient a few minutes or several hours before the beginning of a seizure.

We evaluated forecasting error with each signal in each subject, and Table 4 shows the results. This experiment is done to measure the future values of the length of 500 time
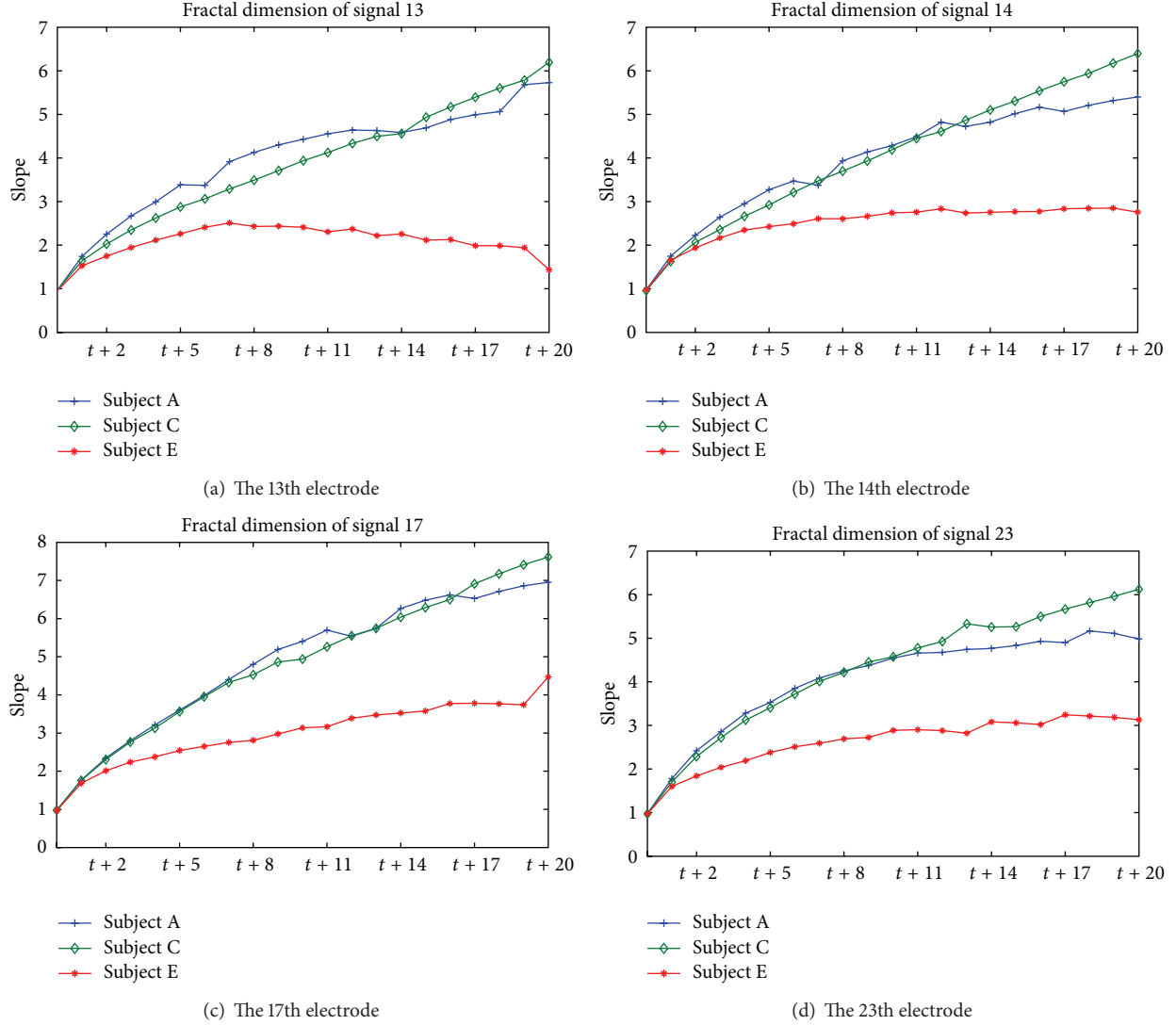
Figure 4: Fractal dimension of time delay space: (a) the 13th electrode of each subject, (b) the 14th electrode, (c) 17th electrode, and (d) 23rd electrode.

points using the observed signal from the time 1 to 500. That is, single signal has 4096 time points, and the existing method used from the time 1 to 500 of single signal for learning. Models forecast from the time 501 to 1000 through learning. In this paper, we measured RMSE between the original signals and the forecasted signals. As a result of Table 4, Subjects C and E indicated the lowest average forecasting error rate when NN algorithm was used. However, NN method required much learning time compared to our method. That is, the values of 1 to 500 in NN will be the training period for the forecasted value of 501. For the forecast of 502, the training period is $1:501$. On the other hand, our method provides the fast computation time because its training period is 407 to 501 for the forecast of 502. Besides, the difference of error rate between NN and CA-AR is very small.

Our method needs only the past values of p that are determined by fractal dimension to forecast the future values. Therefore, it guarantees the fastest computation time for

learning to forecast the epileptic seizure. We measured the execution time of each model during forecasting the time length of 1000, 2000, and 3000. We can confirm the result of several signals from Table 5. In this experiment, we used each signal of Subject E and training signal used from the time 1 to 500 or 1000 time points of each signal in the existing method. As a result of Table 5, the lowest RMSE of forecasting is appeared in NN method except when CA-AR forecasted the length of the 2000 times using the length of the 1000 times as training signals. However, we need to look at the execution time of the whole forecasting method. NN method provided good forecasting results. However, it needs longer execution time. In addition, when the length of forecasting time increases, the execution time also increases.

The accuracy of time series forecasting is a very important factor to many decision processes, and hence the research for improving the effectiveness of forecasting models has lasted. Both the neural network and the AR model capture all of the

TABLE 1: Root Mean Square Error of forecast using CA-AR and AR.

Electrode	Proposed method				Standard AR			
	$P = 3$	$P = 5$	$P = 10$	$P = 15$	$P = 3$	$P = 5$	$P = 10$	$P = 15$
				RMSE of Subject A				
7	0.1878	0.1320	0.0419	0.0523	1.0044	0.8149	0.5294	0.5399
15	0.3766	0.5306	0.9532	0.9942	0.9947	0.9514	0.9985	1.3158
20	0.2629	0.1525	0.1943	0.3741	1.0003	1.0071	1.0478	1.0128
27	0.1226	0.0757	0.1347	0.0897	1.0093	1.0961	1.2423	1.3061
35	0.0213	0.0559	0.0348	0.0563	0.9995	0.9299	0.8068	0.8334
50	0.1271	0.1436	0.1093	0.1339	1.0038	0.9907	1.0183	1.1479
60	0.0356	0.0273	0.0332	0.0070	0.8364	0.5043	0.7012	0.5120
70	0.0554	0.0449	0.0369	0.0402	0.9960	0.9987	0.9937	1.0352
80	0.0101	0.0068	0.0078	0.0110	0.4783	0.3180	0.2287	0.2108
87	0.1368	0.1458	0.1524	0.1370	1.0011	0.9736	1.0224	1.3125
95	0.0999	0.0677	0.0902	0.0385	1.0025	1.0141	1.0118	0.9709
Average	0.1306	**0.1257**	0.1626	0.1758	0.9388	0.8726	0.8728	0.9270
				RMSE of Subject C				
7	0.0302	0.0427	0.0372	0.0939	0.9501	0.5978	0.6480	0.6142
15	0.8090	0.7386	0.8873	1.5213	1.4048	1.1270	1.2222	1.8517
20	0.0384	0.0305	0.0335	0.0798	0.9979	0.9496	0.8857	0.8286
27	0.1288	0.1376	0.1122	0.1107	0.9469	1.02888	1.0845	0.7823
35	0.0495	0.0394	0.0428	0.1079	1.0635	1.0051	0.9715	0.9691
50	0.0369	0.0500	0.0437	0.0694	1.0187	0.9474	0.9118	0.8815
60	0.0319	0.0412	0.0282	0.1105	0.9208	0.6429	0.7676	0.7703
70	0.1612	0.1302	0.1527	0.0376	1.0973	1.3006	1.2392	1.3000
80	0.1068	0.1126	0.1087	0.1012	1.2428	1.4660	1.4313	1.4892
87	0.1478	0.1470	0.1621	0.0706	1.1839	1.5971	1.6903	1.9786
95	0.1158	0.1105	0.1141	0.0710	1.6958	1.7924	1.6513	1.6922
Average	0.1506	**0.1437**	0.1566	0.2158	1.1384	1.1322	1.1367	1.1962
				RMSE of Subject E				
7	0.2225	0.0098	0.0074	0.0272	0.9566	0.9761	0.7667	0.7669
15	0.0709	0.0749	0.0763	0.0739	1.0041	0.9226	0.9306	0.9534
20	0.1757	0.0540	0.1248	0.1429	1.2710	1.1595	0.9591	0.3047
27	0.0661	0.0494	0.0822	0.1094	1.1139	0.9623	1.1128	0.8602
35	0.1138	0.0375	0.0605	0.0774	1.0139	1.0181	1.2581	2.8540
50	0.0345	0.0310	0.0121	0.1890	0.7694	0.8749	0.8942	1.6892
60	0.0062	0.0343	0.0109	0.0794	0.8563	0.6543	0.8975	1.0238
70	0.0975	0.0246	0.0590	0.0450	0.1912	1.1594	1.7443	1.5908
80	0.0642	0.0237	0.0517	0.1455	0.5931	0.5950	3.4392	9.2907
87	0.0039	0.0802	0.1155	0.1507	1.0098	0.5522	0.5753	0.6716
95	0.1567	0.0389	0.1023	0.1285	1.2754	1.1505	1.0432	0.619
Average	0.0920	**0.0417**	0.0639	0.1063	0.9141	0.9114	1.2383	1.8749

patterns in the data [26]. Our method also can capture the patterns of data because it was based on the AR model. In epilepsy EEG data, the amplitude between normal and seizure signal presents a great difference. If a pattern of the generated signals by the proposed model deviates from the past pattern, CA-AR can regard these as the epileptic seizure. However, the proposed model does not separately determine or measure

the sliding time window length to detect the change of pattern in this paper. The goal of this study is to provide the fast run time and high forecasting accuracy in time series data that has special characteristics such as the nonperiodicity and nonlinearity. Through our experiments results, we can guarantee the fast execution time and accuracy between original signal and generated signal from our model.

TABLE 2: Root Mean Square Error of forecast comparison.

Forecasting time points	500 (training time points)				1000 (training time points)			
	ANN	Fuzzy	NN	CA-AR (5)	ANN	Fuzzy	NN	CA-AR (5)
150	0.2059	0.1210	0.1462	0.0162	0.1297	0.0721	0.0950	0.0114
1500	0.6174	—	0.1050	0.0541	0.3221	—	0.0887	0.0533
2000	0.6328	—	0.0998	0.0487	0.356	—	0.0918	0.0486
2500	0.7607	—	0.0995	0.0497	0.3741	—	0.0910	0.0507
3000	0.7801	—	0.0976	0.0480	0.3613	—	0.0874	0.0479

TABLE 3: Forecast time comparisons.

Forecasting time points	500 (training time points)				1000 (training time points)			
	ANN	Fuzzy	NN	CA-AR (5)	ANN	Fuzzy	NN	CA-AR (5)
150	0.5304	186.94	1.060	0.0780	4.430	675.38	1.669	0.0156
1500	0.9516	—	13.722	0.0499	5.004	—	13.887	0.0811
2000	0.9953	—	20.439	0.0749	4.995	—	20.689	0.0718
2500	0.9766	—	28.189	0.0967	5.098	—	29.178	0.0874
3000	1.0764	—	32.723	0.0748	5.248	—	37.272	0.0736

TABLE 4: The measured forecasting error with several signals from each subject.

Electrode	Subject A				Subject C				Subject E			
	NN	Fuzzy	ANN	CA-AR (5)	NN	Fuzzy	ANN	CA-AR (5)	NN	Fuzzy	ANN	CA-AR (5)
4	0.320	0.050	0.429	0.019	0.013	0.031	0.156	0.023	0.018	0.044	0.136	0.029
8	0.086	0.050	0.177	0.127	0.010	0.018	0.093	0.018	0.002	0.121	0.086	0.016
35	0.043	0.086	0.113	0.056	0.045	0.029	0.394	0.078	0.069	0.169	0.203	0.038
70	0.145	0.058	0.166	0.045	0.038	0.048	0.130	0.066	0.012	0.072	0.038	0.025
95	0.093	0.087	0.173	0.068	0.030	0.061	0.111	0.024	0.013	0.081	0.115	0.039
Average	0.137	0.066	0.212	**0.063**	**0.027**	0.037	0.177	0.042	**0.023**	0.097	0.115	0.029

4. Discussion

Epilepsy is a common neurological disorder in which some nerve cells spasmodically incur excessive electricity for a short time. Seizure predictions are mostly handled by statistical analysis methods from the EEG recordings of brain activity. The forecasting of epilepsy seizures can be used as a warning about seizures occurring on certain time scales by estimating the change in brain waves. That is, the forecasting of seizures alerts patients before an epilepsy seizure occurs. As a result, they could avoid potentially dangerous situations such as brain damage or injury during seizures.

In recent years, much research has looked into the prediction of epilepsy seizures using EEG data. Mormann et al. [27] analyzed bivariate EEG signals for seizure prediction. They analyzed the synchrony of EEG data using mean phase coherence (MPC) and maximum linear cross-correlation between EEG signal pairs. Schelter et al. [28] used MPC and obtained a proportion of seizures that were correctly predicted. Chávez et al. [29] analyzed the focal epilepsy EEG data for seizure prediction using non-linear regression analysis and phase synchrony. Winterhalder et al.

[30] suggested the "seizure prediction characteristic" based on clinical and statistical considerations and compared to the performance of seizure prediction methods using concepts of linear and nonlinear time series analysis. This work indicates the uncertainty of predictions made by the use of the seizure occurrence period (SOP), in which the seizure is expected. However, it can be expressed when the independent variables are continuous. Moreover, these methods assume that the data has normality and independence.

Li and Yao [31] proposed prediction methods based on the wavelet transform and fuzzy similarity measurements of EEG data. This method is divided into two steps: to calculate the entropy of the EEG data and to calculate similarity between variables. Li and Ouyang [32] proposed the dynamical similarity measure based on a similarity index to predict epileptic seizures using EEG data. Gigola et al. [33] analyzed the time domain of different types of epilepsy to predict epileptic seizures using wavelet analysis based on the evolution of accumulated energy. Maiwald et al. [34] evaluated three nonlinear methods for seizure prediction: dynamical similarity index, correlation dimension, and accumulated energy. These methods can extract robust features
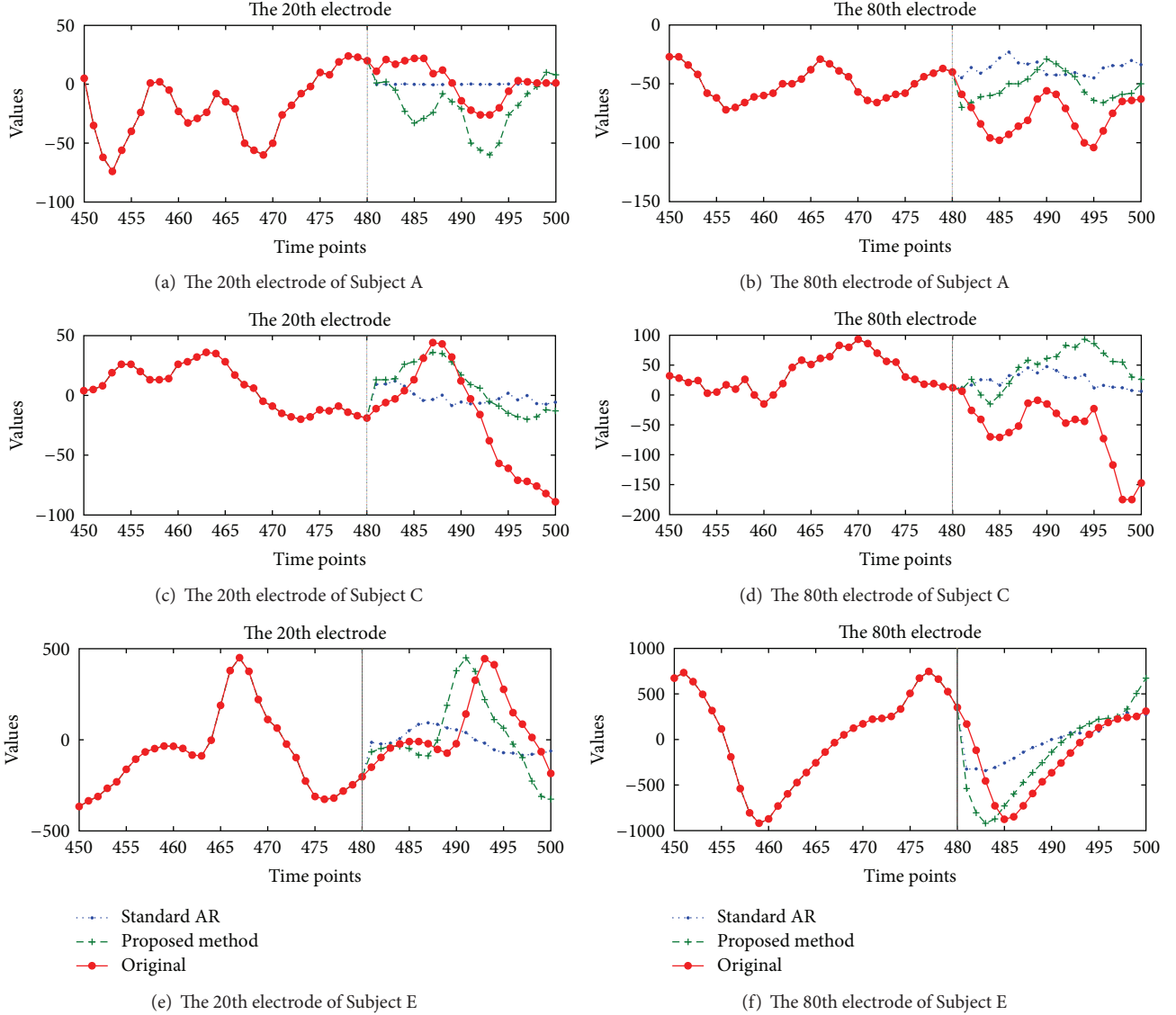
Figure 5: Forecast comparison: (a) and (b) plot forecasts of the 20th and 80th electrode of Subject A to compare the proposed and standard AR methods. (c) and (d) show forecast plots of Subject C. (e) and (f) display the forecast plot of the 20th and 80th electrode of Subject E, respectively.

from EEG data. However, part of these methods is performed based on the window unit and it is not sufficient for clinical applications.

Several techniques have been proposed to analyze characteristics of seizures via various methods. Liu et al. [35] measured the fractal dimension of the human cerebellum in magnetic resonance images (MRI) of 24 healthy young subjects using the box-counting method. Esteller et al. [36] determined the fractal dimension in the cortex electroencephalogram (IEEG, ECoG), using the Katz algorithm. Their results show that an electrographic seizure in the Electrocorticography (ECoG) occurs when there is an increase of complexity. Sackellares et al. [37] found that temporal lobe epilepsy is characterized by episodic paroxysmal electrical discharges (ictal activity). These discharges consist of organized synchronous activity of mesial temporal neurons,

particularly those of the hippocampus. However, proper interpretation of such analyses has not been thoroughly addressed.

In this paper, we proposed a new CA-AR forecasting method based on the AR model that can forecast the seizure of complex epilepsy EEG data by applying the property of nonstandard distribution from [14]. The CA-AR model is suited to time series data with special characteristics, such as abnormality, noise, nonlinearity, and nonperiodicity.

5. Conclusions

Epilepsy may be caused by a number of unrelated conditions, including damage resulting from high fever, stroke, toxicity, or electrolyte imbalances. An algorithm capable of effective real-time epileptic seizure prediction will allow the patient

TABLE 5: Comparison of the foresting error rates and the execution time between the existing methods and the proposed method.

Forecasting time points	Electrodes	RMSE						Execution time (sec)					
		500 (training)			1000 (training)			500 (training)			1000 (training)		
		ANN	NN	CA-AR (5)	ANN	NN	CA-AR (5)	ANN	NN	CA-AR (5)	ANN	NN	CA-AR (5)
1000	4	0.091	0.020	0.047	0.13	0.023	0.05	1.01	7.44	0.08	5.34	9.11	0.06
	8	0.039	0.006	0.043	0.055	0.016	0.051	0.08	7.75	0.03	5.01	8.86	0.06
	35	0.228	0.072	0.039	0.192	0.062	0.045	0.90	7.64	0.08	4.90	8.78	0.05
	70	0.057	0.010	0.056	0.049	0.011	0.054	0.10	7.57	0.08	4.48	8.63	0.06
	95	0.091	0.032	0.044	0.145	0.038	0.034	0.94	7.44	0.06	4.70	8.75	0.05
	Average	0.101	**0.028**	0.046	0.114	**0.03**	0.047	0.61	7.57	**0.07**	4.88	8.83	**0.06**
2000	4	0.217	0.021	0.046	0.245	0.03	0.038	1.11	20.55	0.08	4.87	20.14	0.05
	8	0.060	0.019	0.047	0.082	0.027	0.018	1.11	20.64	0.08	5.55	20.87	0.05
	35	0.253	0.063	0.052	0.191	0.088	0.048	0.83	20.31	0.06	4.91	21.03	0.05
	70	0.058	0.015	0.049	0.046	0.012	0.033	1.01	20.12	0.08	4.52	20.94	0.04
	95	0.173	0.037	0.048	0.198	0.038	0.048	0.92	20.58	0.08	5.12	20.47	0.05
	Average	0.152	**0.031**	0.048	0.152	0.039	**0.037**	1.00	20.44	**0.07**	5.00	20.69	**0.05**
3000	4	0.376	0.029	0.052	0.399	0.019	0.051	0.92	32.74	0.08	5.79	38.31	0.05
	8	0.094	0.015	0.051	0.112	0.032	0.051	1.22	32.39	0.03	5.68	36.47	0.05
	35	0.259	0.070	0.049	0.213	0.087	0.047	0.98	32.40	0.08	4.76	36.57	0.05
	70	0.055	0.023	0.048	0.044	0.013	0.046	1.33	32.79	0.08	5.13	37.53	0.05
	95	0.227	0.049	0.050	0.233	0.059	0.049	0.94	33.29	0.11	4.88	37.47	0.05
	Average	0.202	**0.037**	0.050	0.2	**0.042**	0.049	1.08	32.72	**0.07**	5.25	37.27	**0.05**

to take appropriate precautions minimizing the risk of a seizure attack or injuries resulting from such an attack. Conventional methods for forecasting or prediction of data require periodicity in the observed data. However, when we applied the cepstrum, seizure activity signals did not exhibit periodicity. In addition, we could distinguish whether the epilepsy EEG data is random or nonrandom using the lag plot. If the lag plot has a nonrandom pattern, it can be used for prediction by conventional approaches. However, our data appears to have a random distribution.

This study proposed the random coefficients appropriate for random distribution data. Further, we used the log-log plots (box-counting) using the concept of fractal dimensions to forecast epilepsy EEG data to estimate the vital forecasting optimal order p in our CA-AR model. Our experimental results demonstrate that CA-AR (coercively adjusted autoregressive) is the most suitable forecasting method for nonperiodic data. It does not require complex calculations and conducts fast forecasting compared to other methods. In addition, our method generates future values more accurately or similar than other methods. The experiments on epilepsy EEG data show that our method is not only fast and scalable but also accurate in achieving low prediction errors.

Future research could focus on extending CA-AR to perform forecasting on a multiple, coevolving time series which includes linear or non-linear correlations and periodicity or nonperiodicity. A more ambitious direction would be to automatically readjust the parameter and coefficient equations.

References

[1] M. J. L. D. Hoon, T. H. J. J. Van der Hagen, H. Schoonewelle, and H. van Dam, "Why Yule-Walker should not be used for autoregressive modelling," *Annals of Nuclear Energy*, vol. 23, no. 15, pp. 1219–1228, 1996.

[2] S. M. Chen and J. R. Hwang, "Temperature prediction using fuzzy time series," *IEEE Transactions on Systems, Man, and Cybernetics B*, vol. 30, no. 2, pp. 263–275, 2000.

[3] P. Kumar and E. Walia, "Cash forecasting: an application of artificial neural networks in finance," *International Journal of Computer Science and Applications*, vol. 3, no. 1, pp. 61–77, 2006.

[4] R. G. Andrzejak, K. Lehnertz, F. Mormann, C. Rieke, P. David, and C. E. Elger, "Indications of nonlinear deterministic and finite-dimensional structures in time series of brain electrical activity: dependence on recording region and brain state," *Physical Review E*, vol. 64, no. 6 I, pp. 061907/1–061907/8, 2001.

[5] M. E. Saab and J. Gotman, "A system to detect the onset of epileptic seizures in scalp EEG," *Clinical Neurophysiology*, vol.

116, no. 2, pp. 427–442, 2005.

[6] N. C. Bhavaraju, M. G. Frei, and I. Osorio, "Analog seizure detection and performance evaluation," *IEEE Transactions on Biomedical Engineering*, vol. 53, no. 2, pp. 238–245, 2006.

[7] C. Stöllberger, J. Finsterer, W. Lutz et al., "Multivariate analysis-based prediction rule for pulmonary embolism," *Thrombosis Research*, vol. 97, no. 5, pp. 267–273, 2000.

[8] A. F. Rabbi, A. Aarabi, and R. Fazel-Rezai, "Fuzzy rule-based seizure prediction based on correlation dimension changes in intracranial EEG," in *Proceedings of the IEEE Engineering in Medicine and Biology Society Conference*, pp. 3301–3304, 2010.

[9] L. D. Iasemidis, D. S. Shiau, W. Chaovalitwongse et al., "Adaptive epileptic seizure prediction system," *IEEE transactions on bio-medical engineering*, vol. 50, no. 5, pp. 616–627, 2003.

[10] D. Liu, Z. Pang, and Z. Wang, "Epileptic seizure prediction by a system of particle filter associated with a neural network," *Eurasip Journal on Advances in Signal Processing*, vol. 2009, Article ID 638534, 10 pages, 2009.

[11] A. Shahidi Zandi, G. A. Dumont, M. Javidan, and R. Tafreshi, "An entropy-based approach to predict seizures in temporal lobe epilepsy using scalp EEG," in *Proceedings of the Annual International Conference of the IEEE Engineering in Medicine and Biology Society*, pp. 228–2231, 2009.

[12] Z. Rogowski, I. Gath, and E. Bental, "On the prediction of epileptic seizures," *Biological Cybernetics*, vol. 42, no. 1, pp. 9–15, 1981.

[13] Y. Salant, I. Gath, and O. Henriksen, "Prediction of epileptic seizures from two-channel EEG," *Medical and Biological Engineering and Computing*, vol. 36, no. 5, pp. 549–556, 1998.

[14] M. M. Ali, "Distribution of the least squares estimator in a first-order autoregressive model," *Econometric Reviews*, vol. 21, no. 1, pp. 89–119, 1996.

[15] K. M. Abadir, "The limiting distribution of the autocorrelation coefficient under a unit root," *Annals of Statistics*, vol. 21, no. 2, pp. 1058–1070, 1993.

[16] S. Y. Hwang, I. V. Basawa, and T. Y. Kim, "Least squares estimation for critical random coefficient first-order autoregressive processes," *Statistics and Probability Letters*, vol. 76, no. 3, pp. 310–317, 2006.

[17] W. A. Fuller, *Introduction to Statistical Time Series*, Wiley, New York, NY, USA, 2nd edition, 1996.

[18] O. A. Sykes, "An Introduction to Regression Analysis," in *The Inaugural Coase Lecture*, University of Chicago, 1988, Chicago Working Paper in Law & Economics.

[19] L. S. Liebovitch and T. Toth, "A fast algorithm to determine fractal dimensions by box counting," *Physics Letters A*, vol. 141, no. 8-9, pp. 386–390, 1989.

[20] H. O. Peitgen, H. Jurgens, and D. Saupe, *Chaos and Fractals: New Frontiers of Science*, Springer, New York, NY, USA, 1992.

[21] D. G. Childers, D. P. Skinner, and R. C. Kemerait, "The cepstrum: a guide to processing," *Proceedings of the IEEE*, vol. 65, no. 10, pp. 1428–1443, 1977.

[22] D. Chakrabarti and C. Faloutsos, "F4: large-scale automated forecasting using fractals," in *Proceedings of the 11th International Conference on Information and Knowledge Management (CIKM '02)*, pp. 2–9, November 2002.

[23] B. B. Mandelbrot, *The Fractal Geometry of Nature*, Freeman, New York, NY, USA, 1983.

[24] M. Sarkar and T. Y. Leong, "Characterization of medical time series using fuzzy similarity-based fractal dimensions,"

Artificial Intelligence in Medicine, vol. 27, no. 2, pp. 201–222, 2003.

[25] F. Fernandex-Rodriguez, S. Sosvilla-Rivero, and J. Andrada-Felix, "Nearest neighbor predictions in foreign exchange markets," Working Papers from FEDEA, 2002.

[26] G. P. Zhang, "Time series forecasting using a hybrid ARIMA and neural network model," *Neurocomputing*, vol. 50, pp. 159–175, 2003.

[27] F. Mormann, T. Kreuz, C. Rieke et al., "On the predictability of epileptic seizures," *Clinical Neurophysiology*, vol. 116, no. 3, pp. 569–587, 2005.

[28] B. Schelter, M. Winterhalder, T. Maiwald et al., "Testing statistical significance of multivariate time series analysis techniques for epileptic seizure prediction," *Chaos*, vol. 16, no. 1, pp. 013108–013110, 2006.

[29] M. Chávez, M. Le Van Quyen, V. Navarro, M. Baulac, and J. Martinerie, "Spatio-temporal dynamics prior to neocortical seizures: amplitude versus phase couplings," *IEEE Transactions on Bio-Medical Engineering*, vol. 50, no. 5, pp. 571–583, 2003.

[30] M. Winterhalder, T. Maiwald, H. U. Voss, R. Aschenbrenner-Scheibe, J. Timmer, and A. Schulze-Bonhage, "The seizure prediction characteristics: a general framework to assess and compare seizure prediction methods," *Epilepsy and Behavior*, vol. 4, no. 3, pp. 318–325, 2003.

[31] X. Li and X. Yao, "Application of fuzzy similarity to prediction of epileptic seizures using EEG signals," in *Proceedings of the 2nd International Confernce on Fuzzy Systems and Knowledge Discovery (FSKD '05)*, vol. 3613, pp. 645–652, August 2005.

[32] X. Li and G. Ouyang, "Nonlinear similarity analysis for epileptic seizures prediction," *Nonlinear Analysis, Theory, Methods and Applications*, vol. 64, no. 8, pp. 1666–1678, 2006.

[33] S. Gigola, F. Ortiz, C. E. D'Attellis, W. Silva, and S. Kochen, "Prediction of epileptic seizures using accumulated energy in a multiresolution framework," *Journal of Neuroscience Methods*, vol. 138, no. 1-2, pp. 107–111, 2004.

[34] T. Maiwald, M. Winterhalder, R. Aschenbrenner-Scheibe, H. U. Voss, A. Schulze-Bonhage, and J. Timmer, "Comparison of three nonlinear seizure prediction methods by means of the seizure prediction characteristic," *Physica D*, vol. 194, no. 3-4, pp. 357–368, 2004.

[35] J. Z. Liu, L. D. Zhang, and G. H. Yue, "Fractal dimension in human cerebellum measured by magnetic resonance imaging," *Biophysical Journal*, vol. 85, no. 6, pp. 4041–4046, 2003.

[36] R. Esteller, J. Echauz, B. Pless, T. Tcheng, and B. Litt, "Real-time simulation of a seizure detection system suitable for an implantable device," *Epilepsia*, vol. 43, supplement 7, p. 46, 2002.

[37] J. C. Sackellares, L. D. Iasemidis, R. L. Gilmore et al., "Epilepsy—when chaos fails," in *Chaos in the Brain*, pp. 112–1133, World Scientific, 2000.

Research Article

Evaluation of EEG Features in Decoding Individual Finger Movements from One Hand

Ran Xiao[1] and Lei Ding[1,2]

[1] School of Electrical and Computer Engineering, University of Oklahoma, Norman, OK 73019, USA
[2] Center for Biomedical Engineering, University of Oklahoma, Norman, OK 73019, USA

Correspondence should be addressed to Lei Ding; leiding@ou.edu

With the advancements in modern signal processing techniques, the field of brain-computer interface (BCI) is progressing fast towards noninvasiveness. One challenge still impeding these developments is the limited number of features, especially movement-related features, available to generate control signals for noninvasive BCIs. A few recent studies investigated several movement-related features, such as spectral features in electrocorticography (ECoG) data obtained through a spectral principal component analysis (PCA) and direct use of EEG temporal data, and demonstrated the decoding of individual fingers. The present paper evaluated multiple movement-related features under the same task, that is, discriminating individual fingers from one hand using noninvasive EEG. The present results demonstrate the existence of a broadband feature in EEG to discriminate individual fingers, which has only been identified previously in ECoG. It further shows that multiple spectral features obtained from the spectral PCA yield an average decoding accuracy of 45.2%, which is significantly higher than the guess level ($P < 0.05$) and other features investigated ($P < 0.05$), including EEG spectral power changes in alpha and beta bands and EEG temporal data. The decoding of individual fingers using noninvasive EEG is promising to improve number of features for control, which can facilitate the development of noninvasive BCI applications with rich complexity.

1. Introduction

Brain-computer interface (BCI) is an assistive technology, which decodes neurophysiological signals from the human brain and translates them into commands to control external devices, such as computer programs, electrical wheelchairs, and neuroprosthesis [1–4]. For people with severe motor disabilities, BCI provides an alternative approach to communicate with the external world without going through damaged motor output pathways [5, 6].

In terms of measurements utilized, BCIs can be categorized into invasive and noninvasive ones. Invasive BCIs mainly use local field potential (LFP) and electrocorticography (ECoG) [7–12]. Both techniques record neuroelectrical activities of the brain with high spatiotemporal resolution and signal-to-noise ratio (SNR) [12], while the implantation of electrodes poses a potential risk for BCI users. On the other side, noninvasive BCIs take advantage of noninvasive measurements, for example, electroencephalography (EEG),

magnetoencephalography (MEG), and functional magnetic resonance imaging (fMRI) [13–19]. All of them require no surgeries for applications. Among these noninvasive techniques, EEG has been widely adopted in BCIs [2–4, 13–15, 20], due to its merits of easy setup, mobility, and low cost, as well as providing signals with reasonable SNR and high temporal resolution.

Due to the advancements in biomedical equipment and signal processing techniques, the field of noninvasive BCI grows rapidly with several patterns of brain activities that have been identified and applied for noninvasive applications. The most popular ones include features extracted from motor execution/imagery of certain human body parts [13, 14, 21], event-related P300 [22, 23], steady-state visual evoked potentials (SSVEP) [24], and some others. Motor execution/imagery elicits power changes in alpha/beta bands, that is, event-related desynchronization/synchronization (ERD/ERS) [21], which have been widely used in cursor tasks and neuroprosthesis [3, 13, 25, 26]. However, a remaining

challenge of applying movement-related features in noninvasive BCIs is the limited number of distinguishable patterns available in order to generate more control signals, which largely confines the complexity of noninvasive BCIs to only simple tasks.

During the past decade, many efforts have been made using EEG to decode movements of large body parts of the human. For example, Doud et al. decoded movements from upper limbs for continuous BCI control [27]; Gu et al. investigated the feasibility of discriminating type and speed of wrist movements [28]; Zhou et al. performed classification on movements from elbow and shoulder using EEG [29]; and one of our previous studies discriminated different types of motor imageries from both hands [30], only to name a few. To further increase the number of control signals for BCI, decoding movements of fine body parts, such as individual fingers from one hand, is a viable mean [31–34], while there are some difficulties, particularly with the use of noninvasive EEG. Compared to invasive measurements, the relatively poor spatial resolution of EEG makes it hard to decode individual finger movements, since they activate adjacent brain regions [35]. Furthermore, neural signals are further attenuated and smeared by the Dura mater, cerebrospinal fluid, and skull before reaching the head surface, which makes it even harder to discriminate movements from fine body parts using EEG. A recent study [36] has achieved promising decoding performance using temporal EEG data as features, when classifying movements from four fingers of one hand. It demonstrated the existence of discriminative information of individual finger movements in EEG. Another study uses information extracted from ECoG to decode individual finger movements [37], which are projections of spectral powers on spectral principal components (PCs) obtained by principal component analysis (PCA), and suggests a new type of decomposition for spectral feature extraction. While these studies provide possible approaches to extract features for decoding individual fingers from one hand, they are carried out under different experimental conditions and using different signals, making it hard to compare their performance in discriminating individual fingers. Furthermore, the efficacy of use of spectral PCs from EEG has not been demonstrated, particularly as compared with other features in decoding finger movements. The comparison of these features can provide a reference for feature extraction in such decoding tasks.

The present study evaluated three types of EEG features, including projections on spectral PC(s) (single PCs or multiple PCs), ERD/ERS (in both alpha and beta bands), and temporal data, when subjects performed the same task, that is, individual finger movements of one hand. Different features from a same set of channels were extracted and single-trial EEG data were then classified to decode individual fingers using a support vector machine (SVM) technique [38]. The decoding accuracies were statistically compared against the guess level and among different types of features. The confusion matrices classifying individual fingers using EEG were constructed. The present results indicated that EEG features using both spectral PC projection coefficients and temporal data produced decoding accuracies significantly higher than the guess level ($P < 0.05$), while the decoding accuracies using ERD/ERS features from individual frequency bands (i.e., alpha and beta bands) did not reach the significant level. The present results further suggested that the combined EEG features from the first three spectral PCs provide significant better decoding accuracies (an average accuracy of 45.2% across all subjects) for individual finger movements than all other features investigated ($P < 0.05$), which was supported by results in confusion matrices as well. These findings demonstrate a new way to extract EEG features for decoding individual fingers of one hand, which can facilitate the development of noninvasive BCI applications with rich complexity.

2. Materials and Methods

2.1. Subjects and Experimental Protocol. Six subjects (mean age: 27.3, range: 22~32, all right handed), who had no previous experience with the current experimental protocol, volunteered to participate in the study. All subjects provided written informed consents prior to taking up the experiments. The study was approved by the Institutional Review Board of the University of Oklahoma.

The experiments were conducted in a dim-lighted and electrically shielded chamber room to reduce environmental noise. During the experiments, subjects either rested or performed repetitive movements of individual fingers from one hand according to visually presented cues. The stimuli were presented using E-Prime software (Psychology Software Tools, Inc., Pittsburgh, PA, USA) as illustrated in Figure 1(a). In the first two seconds of the trial, the computer screen was black, allowing time of necessary blinking or swallowing for subjects. After that, a fixation appeared in the center of screen for two seconds. During this time window, subjects were instructed to sit still and stare at the fixation, which provided data for resting conditions without artifacts. In the last two seconds of the trial, one of five words (thumb, index, middle, ring, and little) was randomly chosen and presented on the screen, cueing subjects to perform repetitive movements of corresponding fingers. Most subjects finished one session including 80 trials for each finger in total 40 minutes. One subject reported difficulties in finishing the entire session and finished a session with 60 trials for each finger instead. Data from one subject were excluded from further analysis due to poor recording quality with large EEG artifacts.

2.2. EEG Recording and Preprocessing. EEG data were acquired from a 128-channel sensor net using the Geodesic EEG System 300 (Electrical Geodesic Inc., OR, USA). The channel layout is depicted as black dots in Figure 1(b). The EEG signals were sampled at 250 Hz and referenced to a channel on vertex.

The raw EEG data recorded were firstly high-pass filtered at 0.3 Hz. A 60 Hz notch filter with 0.3 Hz transition band was then applied to the data to reduce the influence from power line noise. To further increase the SNR of data, an independent component analysis (ICA) was performed using the EEGLAB toolbox [39, 40] to remove independent
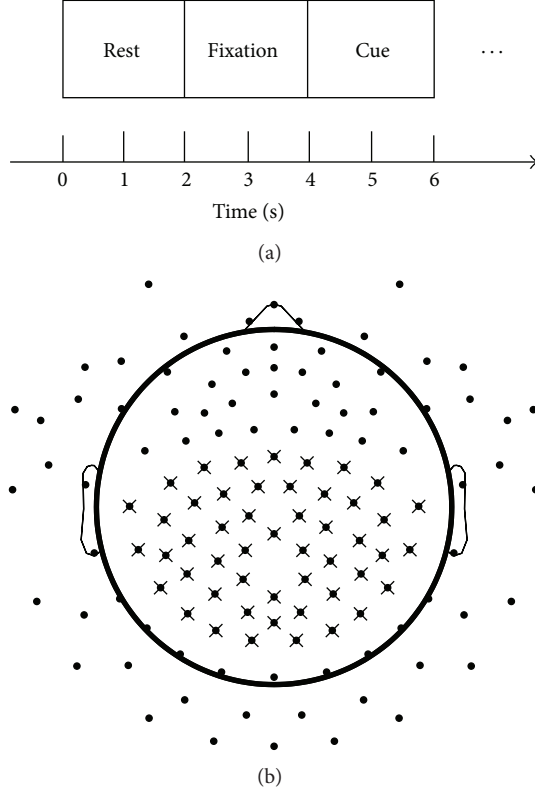
FIGURE 1: Experimental trial design and EEG sensor layout. (a) Each trial consists of three segments: 2 s for rest, 2 s for fixation, and 2 s for movement. (b) Channel locations for EEG sensor net. Each dot denotes an EEG sensor and each cross denotes a channel selected for decoding.

components (ICs) related to electrooculogram (EOG), electrocardiogram (ECG), electromyogram (EMG), and other common artifacts. There were usually 10 to 20 ICs identified and rejected as artifacts in each subject. After temporal filtering, the EEG data went through a spatial filter named as common average reference (CAR), which could further increase the SNR of data [41]:

$$V_{\mathrm{CAR}}(n,t) = V(n,t) - \frac{1}{N}\sum_{i=1}^{N} v(i,t), \tag{1}$$

where $V_{\mathrm{CAR}}(n,t)$ denotes the common average referenced potential at channel n and sample point t. It was calculated by subtracting EEG potential $V(n,t)$ at channel n and sample point t to the average potential of total N channels at that sample point.

After the previous preprocessing steps, the EEG data were segmented into 6-second epochs according to the trial structure depicted in Figure 1(a). One-second segment data centered at the last two seconds for movements, that is, 4.5–5.5 s of each epoch, were used to decode individual fingers, since maximal actions of fingers in most subjects were shown in this time window. 500 ms data from the onset of stimuli were not used for decoding, since subjects were preparing movements before execution [42]. In accordance with data

for movements, their corresponding resting data were also selected as one-second segments, which were located in the middle of fixation, that is, 2.5–3.5 s of each epoch. Movement data and resting data, together with the corresponding labels that indicate the fingers moved, were then combined for later processing.

2.3. Feature Extraction

2.3.1. Features from Spectral PCA Decomposition. The PCA method [43] was performed on EEG spectral powers to identify common spectral patterns across conditions. It transferred original signals into projections along uncorrelated principal components, which represented multiple common spectral patterns in all conditions. The use of PCA not only reduced the dimension of feature space but also identified features accounting for large variations in data. Both characteristics could improve decoding performance in classification problems.

The extraction of these spectral features involved multiple steps as the following. EEG segment data were firstly transferred into spectral powers, by calculating power spectral density (PSD) for each trial (both movement data and resting data) with

$$P_n(f,m) = \frac{1}{T}\left|\sum_{t=-(T/2)}^{(T/2)-1} V_{\mathrm{CAR}}\left(n, t + \frac{T}{2} + 1, m\right) \cdot H(t)\right.$$

$$\left. \cdot \exp\left(i\frac{2\pi}{T}(f-1)t\right)\right|^2, \tag{2}$$

$$H(t) = \frac{(1 + \cos(2\pi t/T))}{2},$$

where $P_n(f,m)$ denoted PSD at channel n and frequency f for segment m. $H(t)$ represented the Hanning window, with the window length T set as 250 sample points. The range of f was from 1 to 125 Hz, due to the sampling frequency of 250 Hz.

Before performing PCA on data, the PSDs for each trial were normalized by

$$\widetilde{P}_n(f,m) = \ln\left(P_n(f,m)\right) - \ln\left(\frac{1}{M}\cdot\sum_{p=1}^{M} P_n(f,m)\right), \tag{3}$$

where the normalized PSD $\widetilde{P}_n(f,m)$ was the log-transferred division between PSD of each segment data and the mean of all segment data (including movements and resting). The symbols f, m, n, and M denote frequency, segment, channel numbers, and the total number of segments, respectively. This operation compensated the uneven distribution characteristic of EEG spectral powers, which followed the power law and emphasized on low-frequency components. It also put the proportions of EEG spectral powers from 0 to 1 and from 1 to infinity on an equal footing, where one indicated the mean PSD of all segment data [37].

After the normalization, the spectral PCA decomposition started by calculating the second moment tensor of distribution function for EEG spectral powers [37] by

$$C\left(f, f'\right) = \sum_{m=1}^{M} \widetilde{P}_n\left(f, m\right) \cdot \widetilde{P}_n\left(f', m\right), \qquad (4)$$

where f and f' were frequencies from 1 to 125 Hz. The constructed matrix measured how well spectral powers at two frequencies vary together along different segment data (i.e., different trials). Then, eigenvalues and eigenvectors of the matrix were calculated using a MATLAB (R2011a, the MathWorks, Natick, MA) function named "eig." The eigenvectors were rearranged according to their corresponding eigenvalues in a descending order. These eigenvectors were spectral principal components (PCs) that represented different common spectral patterns in EEG spectral powers across conditions, ordered with decreasing significance. Each segment data was then projected onto these spectral PCs and the resulting projection coefficients were features used for classification.

The projection coefficients on the single PCs (i.e., the first PC and the second PC) and multiple PCs (i.e., combined first three PCs) were chosen to evaluate the decoding performance with features obtained from spectral PCs. The channels, marked by crosses in Figure 1(b), were selected for performing spectral PCA and decoding, which covered the posterior frontal cortex, motor cortex, and parietal cortex.

2.3.2. Features from Individual Frequency Bands and Temporal Data.

The extractions of both features from individual frequency bands and temporal data were performed on the same EEG segments used for spectral PCA analysis for the purpose of comparison. The first step in acquiring features in individual frequency bands was to transfer temporal EEG data into spectral powers in the frequency domain, which was achieved using (2) as well. After that, the spectral powers at 8–12 Hz (i.e., alpha band) and 13–30 Hz (i.e., beta band) were selected as movement-related features to decode individual finger movements. For using temporal data as movement-related features, EEG potentials from all movement segments were downsampled to 25 Hz by choosing one sample out of every ten samples, which was adopted from a previous study [36]. This operation reduced the computational workload for decoding tasks later, leaving 25 samples in each segment as decoding features.

2.4. Permutation and Classification.

To evaluate decoding accuracies, the sequence of segments was randomly permuted 30 times before feature extraction and classification. The corresponding labels were permuted as well, in line with the segments. After each permutation, 80% of the data were selected as the training set and the remaining as the testing set. The features being evaluated in the present study were obtained only from the training set, which made sure that no data in the testing set were involved in building classifiers.

A support vector machine (SVM) classifier [44] was adopted for decoding. The SVM classifier used a kernel method to map training data into a high dimensional space, where different classes of data could be linearly separated. Next, it searched for a hyperplane, which maximized the margin constructed by support vectors among different classes. The acquired hyperplane then served to distinguish data from different classes. In the present study, the LIBSVM toolbox was implemented using radial basis function (RBF) as kernel function [38]. For different features evaluated, the paired feature data and their labels in the training set were used to train the SVM classifiers. The trained classifiers were then used to predict labels of EEG segment data in the testing set. Finally, predicted labels were compared to true labels for these segments in the testing set to compute decoding accuracies with the use of different types of features.

2.5. Evaluation of Decoding Performance.

To evaluate the performance of decoding individual finger movements using these features, the decoding accuracies acquired by different features were compared with the guess level using one-sample t-test. The guess level for 5-class classification problems was 20%. To compare the decoding performance of each pair of features, pairwise t-tests were performed on decoding accuracy data obtained from them. All t-tests were implemented using a MATLAB function named "t-test." In addition, confusion matrices were constructed from data of decoding accuracies using each type of features to assess their decoding accuracies on individual fingers as well as their structures of misclassification.

3. Results

3.1. Features from Spectral PCA Decomposition.

Features from spectral PCA decomposition were evaluated from two aspects, that is, the profiles of PCs (i.e., the amplitude structure as a function of frequency) and the spatial patterns of projection coefficients over EEG electrodes (Figure 1(b)) for different fingers. Figure 2(a) presents the profiles of the first three spectral PCs, which account for most variations in data (over 90% in average among all subjects). The first PC for each subject (blue curves) presents a broadband phenomenon, which is flat and positive across all frequencies. The phenomenon is consistent with results in the recent ECoG study [37], suggesting that the similar spectral pattern indicative of finger movements can be identified in EEG as in invasive ECoG. The second PC (red curves) mainly peaks at alpha band and beta band, which suggests the similar ERD/ERS phenomena within alpha and beta bands as discussed in Section 2.3.2 (also see Figure 3(a)). The third PC (black curves) exhibits small variations in low-frequency bands, which may represent some residual activities in low-frequency bands besides the first two PCs.

To evaluate the spatial patterns of features from the spectral PCA, projection coefficients on the first PC for different fingers were plotted in Figure 2(b). It reveals that the projections of EEG data from different brain regions on the same spectral structure (as denoted by the spectral PC) present distinct patterns during finger movements. Projection coefficients on electrodes over both left and right
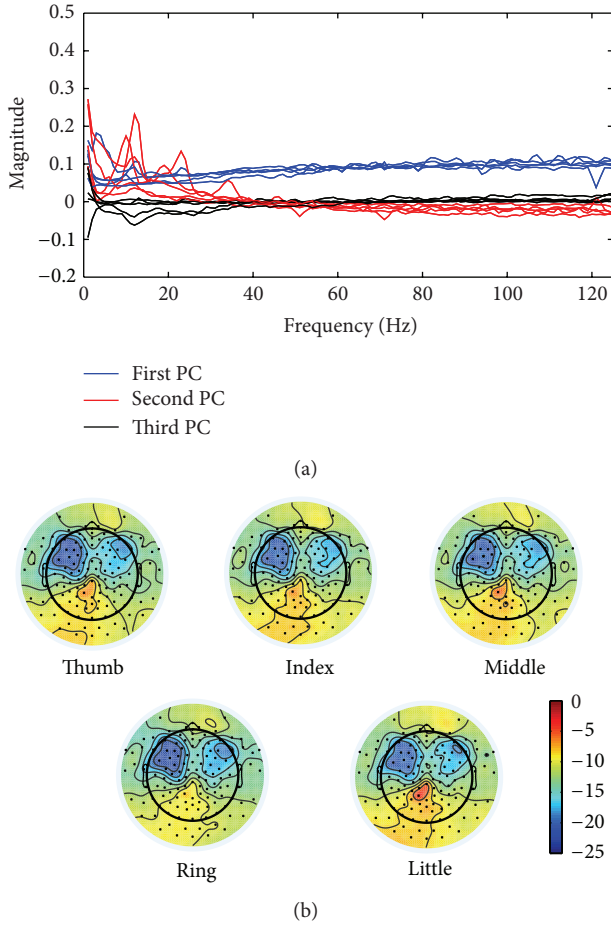
(a)

(b)

Figure 2: Spectral PC features from PCA decomposition. (a) Profiles of the first three PCs. (b) Topographies of projection coefficients on the first PC from movements of different fingers.

(a)

(b)

Figure 3: Illustration of averaged alpha/beta power changes and averaged temporal EEG data from a channel (the red dot) over the left motor cortex. (a) Average spectral powers as a function of frequency calculated from movement and resting segment data. (b) Average temporal EEG data from different fingers. Zero indicates the onset of movement cues.

motor cortices have large negative values, while they are more towards zeros on electrodes over the parietal cortex. More importantly, these distinct patterns covering different brain regions elicit variations to certain extents when moving different fingers from the same hand, with more obvious phenomena on the parietal cortex.

3.2. Features Using Spectral Powers and Temporal Data. All subjects moved fingers from the right hand, which elicited power changes in channels from the motor cortex on the left motor cortex (i.e., the contralateral side) [6, 21]. Hence, spectral powers averaged over all segments belonging to one condition from a channel on the left motor cortex were chosen to display (Figure 3(a)). The selected channel was marked by the red dot on the scalp map. It shows that all finger movements elicit power decreases in both alpha band (enclosed by 1st and 2nd vertical lines) and beta band (enclosed by 2nd and 3rd vertical lines) compared to the resting (denoted by the cyan curve), while spectral powers in alpha band present much larger decrease. However, no major differences in spectral powers among different finger movement conditions can be readily identified in

both frequency bands. This observation suggests features of spectral powers from individual frequency bands may not suffice the task of decoding movements of fine body parts, that is, individual finger movements.

The same channel on the left motor cortex was selected to present features in temporal data averaged over all segments belonging to one finger aligning to the onset of movements (Figure 3(b)). The first vertical line indicates the onset of movement cues, and the following two vertical lines define the segments of data selected for extracting temporal patterns to decode individual finger movements. Average temporal waveforms from movements of different fingers are depicted using different colors. It presents similar EEG patterns prior to onset of movements, while distinct fluctuations in amplitudes are shown from different finger movements after stimulus onsets, particularly in the window selected for decoding. This difference in temporal data is utilized to decode individual finger movements from one hand.

3.3. Classification Accuracies Using Different Features. Figure 4 summarizes the decoding accuracies in discriminating individual finger movements of one hand using differently computed features from EEG. Each bar in the figure presents the mean, together with the standard deviation, of decoding accuracies from all subjects and all permutations using one type of the features. The figure shows that all features produce average decoding accuracies above the guess level, which is indicated by the red dash dotted line. It also demonstrates that different features yield different average decoding accuracies, with projection coefficients on multiple spectral PCs, the highest (45.2%), followed by temporal data (39.2%), projection coefficients on single PCs (the first PC: 37.6% and the second PC: 32.2%), and then spectral powers in alpha band (29.3%) and beta band (26.8%).

3.4. Evaluation of Decoding Performance. To evaluate decoding performance using different features, one-sample t-tests were firstly conducted between different features and the guess level. The results, as presented in Table 1, indicate most features produce decoding accuracies significantly higher than the guess level ($P < 0.05$), except for spectral powers in alpha band and in beta band. Comparison of decoding performance among different features was achieved by conducting pair-wise t tests on every two different features. The results in Table 1 demonstrate that projection coefficients on multiple spectral PCs produce an average decoding accuracy significantly higher than those achieved by all other features ($P < 0.05$). The decoding performance of temporal data is better than the single PC and spectral powers in both alpha and beta bands, while the difference is not significant as compared with data from the first PC ($P > 0.05$). Furthermore, the second PC (with combined features from both alpha and beta bands since it peaks on both frequency bands) indicates significantly better decoding accuracy than individual features from either alpha band or beta band.

To further examine the decoding performance of different features, confusion matrices for decoding each finger were computed (Figure 5). The present results indicate that entries on the main diagonal are most prominent for all features. It suggests that labels of trials in the testing set are mostly classified to the corresponding fingers correctly. It also can be observed that other large entries are mainly on either superdiagonal or subdiagonal lines of each confusion matrix, suggesting most misclassified trials were classified to neighbored fingers, rather than other fingers far away. When comparing confusion matrices from different features, the EEG feature of spectral PC project coefficients shows much less confusions than other EEG features, which is supported by decoding accuracy data. The EEG features from the first spectral PC projection coefficients and the temporal data have similar general performance in terms of confusion matrices, while these matrices further indicate different performance of these features on different fingers (e.g., the most confused finger is the index finger using first spectral PC projection coefficients and is the ring finger using temporal EEG data). The similar phenomenon is also observed in comparing other
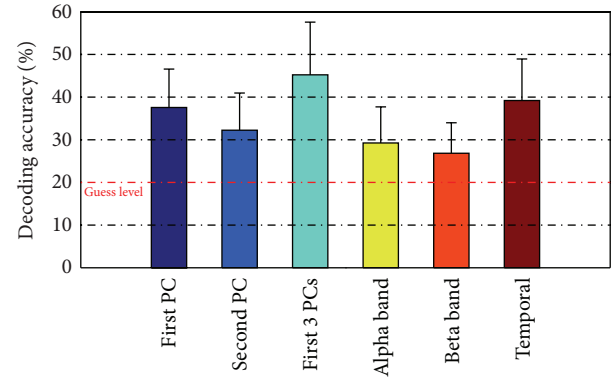
FIGURE 4: Comparison of decoding accuracies averaged over all subjects using different EEG features. The red dash dotted line indicates the guess level for 5-class classification problems.

pairs of features. Again, the confusion matrix data indicate that the feature of alpha or beta band EEG signal changes has less power in discriminating different fingers.

4. Discussion

In the development of noninvasive BCI applications, movement-related features are capable of providing BCI users with voluntary and intuitive control by extracting information from motor execution/imagination of certain body parts [45]. Movements of large body parts, such as hands, arms, and feet, have been successfully decoded using spectral powers from the low-frequency bands (i.e., alpha and beta bands) to generate control signals for noninvasive BCI [27–30, 46–48]. However, to develop BCI applications with rich complexity, the current available control features are not sufficient. Several BCI studies explored different aspects of movement-related information including projections from PCA decomposition and temporal waveforms [36, 37]. Their results suggest decoding movements from fine body parts, that is, individual finger movements, as one of promising approaches to improve the number of control features for BCI applications. These studies were carried out under different experimental conditions and using different signals, for example, invasive ECoG and noninvasive EEG, making it infeasible to compare the decoding performance of different features in discriminating individual finger movements from one hand in a unified configuration. The aim of present study is to evaluate features from a spectral PCA decomposition [37], spectral powers in individual frequency bands, and temporal data under the same protocol, that is, the discrimination of individual finger movements from one hand using noninvasive EEG.

For EEG features from spectral PCA decomposition, profiles and projections of the first three PCs are evaluated in the present study (Figure 2), since they account for most variations in data. The first PC shows a broadband phenomenon, which is consistent with the results in ECoG based BCI studies [37]. The result demonstrates, for the first time, that the features extracted from ECoG using spectral PCA

TABLE 1: Summary of t-test results on decoding accuracies using different features, as well as the guess level (20%). The bold entries indicate significant difference ($P < 0.05$).

	1st PC	2nd PC	First 3 PCs	Alpha band	Beta band	Temporal amplitudes	Guess level
1st PC	—	0.1390	**0.0470**	0.0595	**0.0191**	0.5030	**0.0092**
2nd PC	—	—	**0.0096**	0.5245	0.1552	**0.0290**	**0.0246**
First 3 PCs	—	—	—	**0.0310**	**0.0142**	**0.0446**	**0.0105**
Alpha band	—	—	—	—	0.2482	**0.0312**	0.0635
Beta band	—	—	—	—	—	**0.0089**	0.0763
Temporal amplitudes	—	—	—	—	—	—	**0.0099**
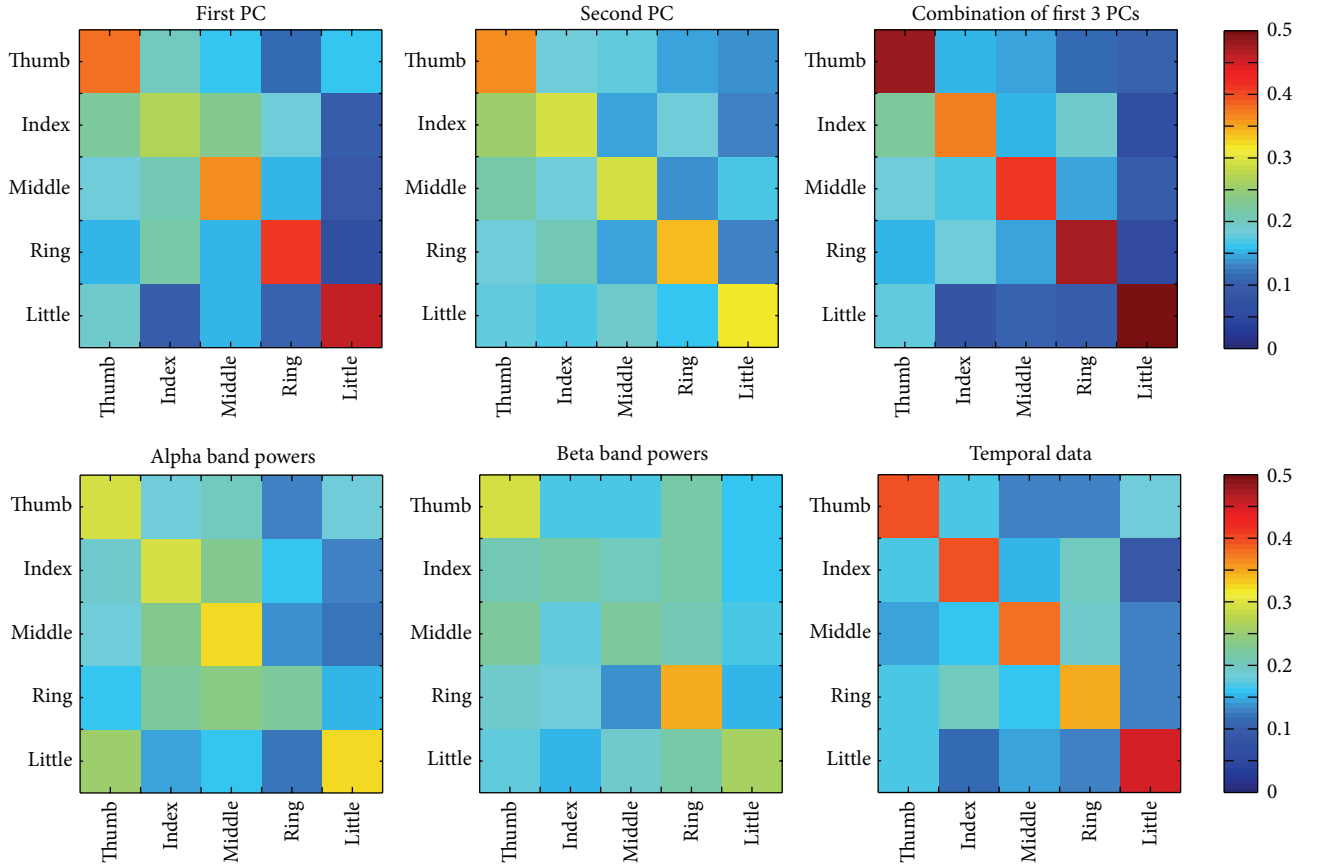
FIGURE 5: Confusion matrices for different types of EEG features. Horizontal axis: predicted labels for fingers; vertical axis: true labels for fingers.

decomposition also reside in EEG. In addition, the spatial patterns of projection coefficients on the first PC vary in movements of different fingers, suggesting that such a feature can be used to decode individual fingers from one hand. The resulting decoding accuracy that is significantly higher than the guess level ($P < 0.05$) further demonstrates the feasibility of using the broadband feature in EEG to discriminate individual fingers. Both the second and third PCs show large peaks in alpha and beta bands, which resemble ERD/ERS phenomena (particularly the second PC) [37] that are also demonstrated in EEG features of alpha/beta band spectral power changes (Figure 3(a)) in the present study. For EEG features of alpha/beta power changes, while they have

demonstrated the promising performance in discriminating movements of large body parts in the literature [27–29], their decoding accuracies are not significantly higher than the guess level ($P > 0.05$) in discriminating individual fingers. This is consistent with the previous reports using ECoG data [37, 49] that low-frequency EEG components are more smeared and not spatially specific to individual fingers as compared with high-frequency EEG components (e.g., gamma band). It is worth noting that the broadband feature of the first spectral PC encompasses both low- and high-frequency EEG components. Lastly, the difference in EEG temporal data caused by movement of different fingers can be observed in averaged EEG data (Figure 3(b)). The present

study further demonstrates the direct use of single-trial EEG temporal data (without any feature extraction techniques) in discriminating individual fingers, which shows comparable accuracies as reported in the literature [36].

These three types of EEG features have different discrimination performance in decoding individual fingers from one hand, as indicated by the data of decoding accuracy (Figure 4) and confusion matrix (Figure 5). In terms of decoding accuracy, the EEG feature from multiple spectral PCs yields the highest accuracy (i.e., 45.2% in decoding five fingers from one hand) among all studied features. The discrimination performance using multiple PCs exceeds those achieved from the use of any single PCs ($P < 0.05$), which suggest movement of fingers causes changes in EEG in a broad frequency range possibly contributed by multiple neural substrates, consistent with movement of other large body parts [27–29]. The better discrimination performance using multiple PCs further indicates movement-related changes in different frequency bands are independent, where all EEG frequency components contribute to the improved decoding accuracy. The discrimination performance using the first spectral PC is significantly better than the second PC ($P < 0.05$). The fact suggests that EEG spectral power changes in high-frequency bands (conveyed in the first PC) are more specific to individual finger movements than low-frequency EEG power changes [49, 50], similar to what is discussed above for ERD/ERS phenomena. Features from EEG temporal data produce the second best discrimination performance, which provides the direct evidence that useful information exists in noninvasive EEG data to decode individual fingers [36]. Its performance decrease as compared with the use of multiple spectral PCs might be caused by common changes presented in EEG data from all types of movements. It is noted that the use of the second PC yields significantly higher decoding accuracy than the guess level ($P < 0.05$) and higher decoding accuracy than individual alpha band or beta band power changes. Since the second PC resembles the combined phenomenon in both alpha and beta bands, the fact indicates the discrimination performance using EEG low-frequency components in decoding individual fingers can be improved when multiple frequency bands are integrated.

Meanwhile, it is important to note that the discrimination performance using EEG data is lower than those achieved by invasive measurements [33, 51, 52] due to relatively poor spatial resolution and low SNR of EEG. While the present study demonstrates a useful feature available in EEG to decoding individual fingers noninvasively, several practical factors can be considered to further improve the performance of EEG-based system in decoding fingers. EEG features can be enhanced by grouping and averaging a number of trials from the same fingers. Moreover, while a universe channel set is selected for different features to achieve a fair comparison in the present study, distinct channel sets should be investigated to acquire optimal discrimination performance. Furthermore, some spatial filtering algorithms, such as common spatial patterns (CSP) [53], are able to better reveal valuable spatial patterns of EEG features than simply selecting channel sets, which could improve the detection of features and, thus, the decoding performance.

5. Conclusion

The present study evaluated the discrimination performance from three types of EEG features, including spectral features obtained using PCA, alpha/beta band power changes, and EEG temporal data, in decoding individual finger movements from one hand. The experimental results demonstrate the feasibility of a broadband feature in EEG in discriminating individual fingers. Moreover, it is demonstrated that the use of multiple PCs (i.e., the first three PCs) can achieve the best decoding accuracy (45.2%) among all investigated EEG features. EEG temporal data yield a slightly lower decoding accuracy than spectral PC features. The present study further indicates that alpha/beta power changes do not contain sufficient information about fine individual finger movements, while they contribute to improved decoding accuracy when combined with other features. The findings in the present study provide a reference in selecting features for decoding individual fingers from one hand, which could largely increase the number of features for BCI applications and advance the state of the art of noninvasive BCI with rich complexity in control.

Conflict of Interests

The authors confirm that there is no conflict of interests in relation to this work.

Acknowledgment

References

[1] J. R. Wolpaw, N. Birbaumer, D. J. McFarland, G. Pfurtscheller, and T. M. Vaughan, "Brain-computer interfaces for communication and control," *Clinical Neurophysiology*, vol. 113, no. 6, pp. 767–791, 2002.

[2] D. J. McFarland, W. A. Sarnacki, and J. R. Wolpaw, "Electroencephalographic (EEG) control of three-dimensional movement," *Journal of Neural Engineering*, vol. 7, no. 3, Article ID 036007, 2010.

[3] J. A. Wilson, G. Schalk, L. M. Walton, and J. C. Williams, "Using an EEG-based brain-computer interface for virtual cursor movement with BCI2000," *Journal of Visualized Experiments*, no. 29, Article ID e1319, 2009.

[4] T. J. Bradberry, R. J. Gentili, and J. L. Contreras-Vidal, "Reconstructing three-dimensional hand movements from noninvasive electroencephalographic signals," *Journal of Neuroscience*, vol. 30, no. 9, pp. 3432–3437, 2010.

[5] J. R. Wolpaw, "Brain-computer interfaces as new brain output pathways," *Journal of Physiology*, vol. 579, no. 3, pp. 613–619, 2007.

[6] D. J. McFarland, L. A. Miner, T. M. Vaughan, and J. R. Wolpaw, "Mu and beta rhythm topographies during motor imagery and actual movements," *Brain Topography*, vol. 12, no. 3, pp. 177–186, 2000.

[7] J. E. O'Doherty, M. A. Lebedev, P. J. Ifft et al., "Active tactile exploration enabled by a brain-machine-brain interface," *Nature*, vol. 479, no. 7372, pp. 228–231, 2011.

[8] G. W. Fraser, S. M. Chase, A. Whitford, and A. B. Schwartz, "Control of a brain-computer interface without spike sorting," *Journal of Neural Engineering*, vol. 6, no. 5, Article ID 055004, 2009.

[9] E. C. Leuthardt, G. Schalk, J. R. Wolpaw, J. G. Ojemann, and D. W. Moran, "A brain-computer interface using electrocorticographic signals in humans," *Journal of Neural Engineering*, vol. 1, no. 2, pp. 63–71, 2004.

[10] A. Gunduz, J. C. Sanchez, P. R. Carney, and J. C. Principe, "Mapping broadband electrocorticographic recordings to two-dimensional hand trajectories in humans. Motor control features," *Neural Networks*, vol. 22, no. 9, pp. 1257–1270, 2009.

[11] D. Zhang, H. Song, R. Xu, W. Zhou, Z. Ling, and B. Hong, "Toward a minimally invasive brain-computer interface using a single subdural channel: a visual speller study," *Neuroimage*, vol. 71, pp. 30–41, 2013.

[12] G. Schalk and E. C. Leuthardt, "Brain-computer interfaces using electrocorticographic signals," *IEEE Reviews in Biomedical Engineering*, vol. 4, pp. 140–154, 2011.

[13] D. Huang, P. Lin, D. Y. Fei, X. Chen, and O. Bai, "Decoding human motor activity from EEG single trials for a discrete two-dimensional cursor control," *Journal of Neural Engineering*, vol. 6, no. 4, Article ID 046005, 2009.

[14] G. R. Müller, C. Neuper, R. Rupp, C. Keinrath, H. J. Gerner, and G. Pfurtscheller, "Event-related beta EEG changes during wrist movements induced by functional electrical stimulation of forearm muscles in man," *Neuroscience Letters*, vol. 340, no. 2, pp. 143–147, 2003.

[15] F. Cincotti, D. Mattia, F. Aloise et al., "High-resolution EEG techniques for brain-computer interface applications," *Journal of Neuroscience Methods*, vol. 167, no. 1, pp. 31–42, 2008.

[16] J. Mellinger, G. Schalk, C. Braun et al., "An MEG-based brain—computer interface (BCI)," *NeuroImage*, vol. 36, no. 3, pp. 581–593, 2007.

[17] A. P. Georgopoulos, F. J. P. Langheim, A. C. Leuthold, and A. N. Merkle, "Magnetoencephalographic signals predict movement trajectory in space," *Experimental Brain Research*, vol. 167, no. 1, pp. 132–135, 2005.

[18] S. S. Yoo, T. Fairneny, N. K. Chen et al., "Brain-computer interface using fMRI: spatial navigation by thoughts," *NeuroReport*, vol. 15, no. 10, pp. 1591–1595, 2004.

[19] A. Eklund, M. Andersson, H. Ohlsson, A. Ynnerman, and H. Knutsson, "A brain computer interface for communication using real-time fMRI," in *Proceedings of the 20th International Conference on Pattern Recognition (ICPR '10)*, pp. 3665–3669, August 2010.

[20] S. Makeig, C. Kothe, T. Mullen, N. Bigdely-Shamlo, Z. L. Zhang, and K. Kreutz-Delgado, "Evolving signal processing for brain-computer interfaces," *Proceedings of the IEEE*, vol. 2012, pp. 1567–1584, 2012.

[21] G. Pfurtscheller and F. H. Lopes Da Silva, "Event-related EEG/MEG synchronization and desynchronization: basic principles," *Clinical Neurophysiology*, vol. 110, no. 11, pp. 1842–1857, 1999.

[22] E. W. Sellers, D. J. Krusienski, D. J. McFarland, T. M. Vaughan, and J. R. Wolpaw, "A P300 event-related potential brain-computer interface (BCI): the effects of matrix size and inter stimulus interval on performance," *Biological Psychology*, vol. 73, no. 3, pp. 242–252, 2006.

[23] D. J. Krusienski, E. W. Sellers, D. J. McFarland, T. M. Vaughan, and J. R. Wolpaw, "Toward enhanced P300 speller performance," *Journal of Neuroscience Methods*, vol. 167, no. 1, pp. 15–21, 2008.

[24] Y. Wang, X. Gao, B. Hong, C. Jia, and S. Gao, "Brain-computer interfaces based on visual evoked potentials: feasibility of practical system designs," *IEEE Engineering in Medicine and Biology Magazine*, vol. 27, no. 5, pp. 64–71, 2008.

[25] G. R. Müller-Putz, R. Scherer, G. Pfurtscheller, and R. Rupp, "EEG-based neuroprosthesis control: a step towards clinical practice," *Neuroscience Letters*, vol. 382, no. 1-2, pp. 169–174, 2005.

[26] A. Chatterjee, V. Aggarwal, A. Ramos, S. Acharya, and N. V. Thakor, "A brain-computer interface with vibrotactile biofeedback for haptic information," *Journal of NeuroEngineering and Rehabilitation*, vol. 4, article 40, 2007.

[27] A. J. Doud, J. P. Lucas, M. T. Pisansky, and B. He, "Continuous three-dimensional control of a virtual helicopter using a motor imagery based brain-computer interface," *PLoS ONE*, vol. 6, no. 10, Article ID e26322, 2011.

[28] Y. Gu, K. Dremstrup, and D. Farina, "Single-trial discrimination of type and speed of wrist movements from EEG recordings," *Clinical Neurophysiology*, vol. 120, no. 8, pp. 1596–1600, 2009.

[29] J. Zhou, J. Yao, J. Deng, and J. P. A. Dewald, "EEG-based classification for elbow versus shoulder torque intentions involving stroke subjects," *Computers in Biology and Medicine*, vol. 39, no. 5, pp. 443–452, 2009.

[30] R. Xiao, K. Liao, and L. Ding, "Discriminating multiple motor imageries of human hands using EEG," in *Proceedings of the Annual International Conference of the IEEE Engineering in Medicine and Biology Society*, pp. 1773–1776, 2012.

[31] R. Scherer, S. P. Zanos, K. J. Miller, R. P. N. Rao, and J. G. Ojemann, "Classification of contralateral and ipsilateral finger movements for electrocorticographic brain-computer interfaces," *Neurosurgical Focus*, vol. 27, no. 1, article e12, 2009.

[32] R. Flamary and A. Rakotomamonjy, "Decoding finger movements from ECoG signals using switching linear models," *Frontiers in Neuroscience*, vol. 6, article 29, 2012.

[33] P. Shenoy, K. J. Miller, J. G. Ojemann, and R. P. N. Rao, "Finger movement classification for an electrocorticographic BCI," in *Proceedings of the 3rd International IEEE EMBS Conference on Neural Engineering*, pp. 192–195, May 2007.

[34] J. Lehtonen, P. Jyländki, L. Kauhanen, and M. Sams, "Online classification of single EEG trials during finger movements," *IEEE Transactions on Biomedical Engineering*, vol. 55, no. 2, pp. 713–720, 2008.

[35] B. Cottereau, K. Jerbi, and S. Baillet, "Multiresolution imaging of MEG cortical sources using an explicit piecewise model," *NeuroImage*, vol. 38, no. 3, pp. 439–451, 2007.

[36] F. Quandt, C. Reichert, H. Hinrichs, H. J. Heinze, R. T. Knight, and J. W. Rieger, "Single trial discrimination of individual finger movements on one hand: a combined MEG and EEG study," *NeuroImage*, vol. 59, no. 4, pp. 3316–3324, 2012.

[37] K. J. Miller, S. Zanos, E. E. Fetz, M. Den Nijs, and J. G. Ojemann, "Decoupling the cortical power spectrum reveals real-time representation of individual finger movements in humans," *Journal of Neuroscience*, vol. 29, no. 10, pp. 3132–3137, 2009.

[38] C. C. Chang and C. J. Lin, "LIBSVM: a Library for support vector machines," *ACM Transactions on Intelligent Systems and Technology*, vol. 2, no. 3, article 27, 2011.

[39] A. Delorme and S. Makeig, "EEGLAB: an open source toolbox for analysis of single-trial EEG dynamics including independent component analysis," *Journal of Neuroscience Methods*, vol. 134, no. 1, pp. 9–21, 2004.

[40] A. Delorme, T. Sejnowski, and S. Makeig, "Enhanced detection of artifacts in EEG data using higher-order statistics and

independent component analysis," *NeuroImage*, vol. 34, no. 4, pp. 1443–1449, 2007.

[41] D. J. McFarland, L. M. McCane, S. V. David, and J. R. Wolpaw, "Spatial filter selection for EEG-based communication," *Electroencephalography and Clinical Neurophysiology*, vol. 103, no. 3, pp. 386–394, 1997.

[42] A. T. Welford, *Reaction Times*, Academic Press, New York, NY, USA, 1980.

[43] E. M. Glaser and D. S. Ruchkin, *Principles of Neurobiological Signal Analysis*, Academic Press, New York, NY, USA, 1976.

[44] V. N. Vapnik, *Statistical Learning Theory*, Wiley-Interscience, New York, NY, USA, 1998.

[45] E. A. Curran and M. J. Stokes, "Learning to control brain activity: a review of the production and control of EEG components for driving brain-computer interface (BCI) systems," *Brain and Cognition*, vol. 51, no. 3, pp. 326–336, 2003.

[46] G. Pfurtscheller, C. Neuper, D. Flotzinger, and M. Pregenzer, "EEG-based discrimination between imagination of right and left hand movement," *Electroencephalography and Clinical Neurophysiology*, vol. 103, no. 6, pp. 642–651, 1997.

[47] C. C. Kuo, W. S. Lin, C. A. Dressel, and A. W. Chiu, "Classification of intended motor movement using surface EEG ensemble empirical mode decomposition," in *Proceedings of the Annual International Conference of the IEEE Engineering in Medicine and Biology Society*, pp. 6281–6284, 2011.

[48] T. Solis-Escalante, G. Müller-Putz, and G. Pfurtscheller, "Overt foot movement detection in one single Laplacian EEG derivation," *Journal of Neuroscience Methods*, vol. 175, no. 1, pp. 148–153, 2008.

[49] K. J. Miller, E. C. Leuthardt, G. Schalk et al., "Spectral changes in cortical surface potentials during motor movement," *Journal of Neuroscience*, vol. 27, no. 9, pp. 2424–2432, 2007.

[50] F. Aoki, E. E. Fetz, L. Shupe, E. Lettich, and G. A. Ojemann, "Increased gamma-range activity in human sensorimotor cortex during performance of visuomotor tasks," *Clinical Neurophysiology*, vol. 110, no. 3, pp. 524–537, 1999.

[51] S. Samiee, S. Hajipour, and M. B. Shamsollahi, "Five-class finger flexion classification using ECoG signals," in *Proceedings of the International Conference on Intelligent and Advanced Systems (ICIAS '10)*, pp. 1–4, June 2010.

[52] W. Wang, A. D. Degenhart, J. L. Collinger et al., "Human motor cortical activity recorded with Micro-ECoG electrodes, during individual finger movements," in *Proceedings of the Annual International Conference of the IEEE Engineering in Medicine and Biology Society*, pp. 586–589, 2009.

[53] H. Ramoser, J. Müller-Gerking, and G. Pfurtscheller, "Optimal spatial filtering of single trial EEG during imagined hand movement," *IEEE Transactions on Rehabilitation Engineering*, vol. 8, no. 4, pp. 441–446, 2000.

Research Article

A Sound Processor for Cochlear Implant Using a Simple Dual Path Nonlinear Model of Basilar Membrane

Kyung Hwan Kim,[1] Sung Jin Choi,[1] and Jin Ho Kim[1,2]

[1] Department of Biomedical Engineering, College of Health Science, Yonsei University, 234 Maeji-ri, Heungup-myun, Wonju, Kangwon-do 220-710, Republic of Korea
[2] School of Electrical Engineering, Seoul National University, Shillim-dong, Kwanak-gu, Building 301, Seoul 151-742, Republic of Korea

Correspondence should be addressed to Kyung Hwan Kim; khkim0604@yonsei.ac.kr

We propose a new active nonlinear model of the frequency response of the basilar membrane in biological cochlea called the simple dual path nonlinear (SDPN) model and a novel sound processing strategy for cochlear implants (CIs) based upon this model. The SDPN model was developed to utilize the advantages of the level-dependent frequency response characteristics of the basilar membrane for robust formant representation under noisy conditions. In comparison to the dual resonance nonlinear model (DRNL) which was previously proposed as an active nonlinear model of the basilar membrane, the SDPN model can reproduce similar level-dependent frequency responses with a much simpler structure and is thus better suited for incorporation into CI sound processors. By the analysis of dominant frequency component, it was confirmed that the formants of speech are more robustly represented after frequency decomposition by the nonlinear filterbank using SDPN, compared to a linear bandpass filter array which is used in conventional strategies. Acoustic simulation and hearing experiments in subjects with normal hearing showed that the proposed strategy results in better syllable recognition under speech-shaped noise compared to the conventional strategy based on fixed linear bandpass filters.

1. Introduction

Cochlear implants (CIs) have been used successfully for the restoration of hearing function in cases of profound sensorineural hearing loss by stimulation of spiral ganglia using electrical pulses. The parameters of the electrical pulses are determined from incoming sound via sound processing strategy. Despite the great progress over a period of more than two decades, many issues remain to be resolved to achieve successful restoration of hearing in noisy environments, melody recognition, and reduction of cognitive load in the patients [1]. Hearing in a noisy environment is especially important for practical purposes.

Several methods can be utilized for the improvement of CI. Among them, the development of novel sound processing strategies is particularly useful because it can be accomplished by modifying embedded programs in the speech processor and does not require a change of hardware.

A sound-processing strategy is defined here as an algorithm to generate electrical stimulation pulses based on the processing of incoming sound waveforms and is also called an encoding strategy. More accurate imitation of normal auditory function is a promising approach for CI sound-processing strategy development [1–3].

It has been suggested that speech perception performance can be improved considerably by adopting an active nonlinear model of the basilar membrane in the cochlea, called the dual resonance nonlinear (DRNL) model [2, 3]. The use of DRNL model was shown to be beneficial for the representation of the information of the formants, which mean the resonances in the vocal tract and are reflected in speech spectra as spectral peaks [2, 3]. The formants are known to be encoded in population responses of the auditory nerves [4, 5]. They are very important cues for speech perception, since the information on formants is crucial for the representation of vowels. It is also imperative for consonant representation, as
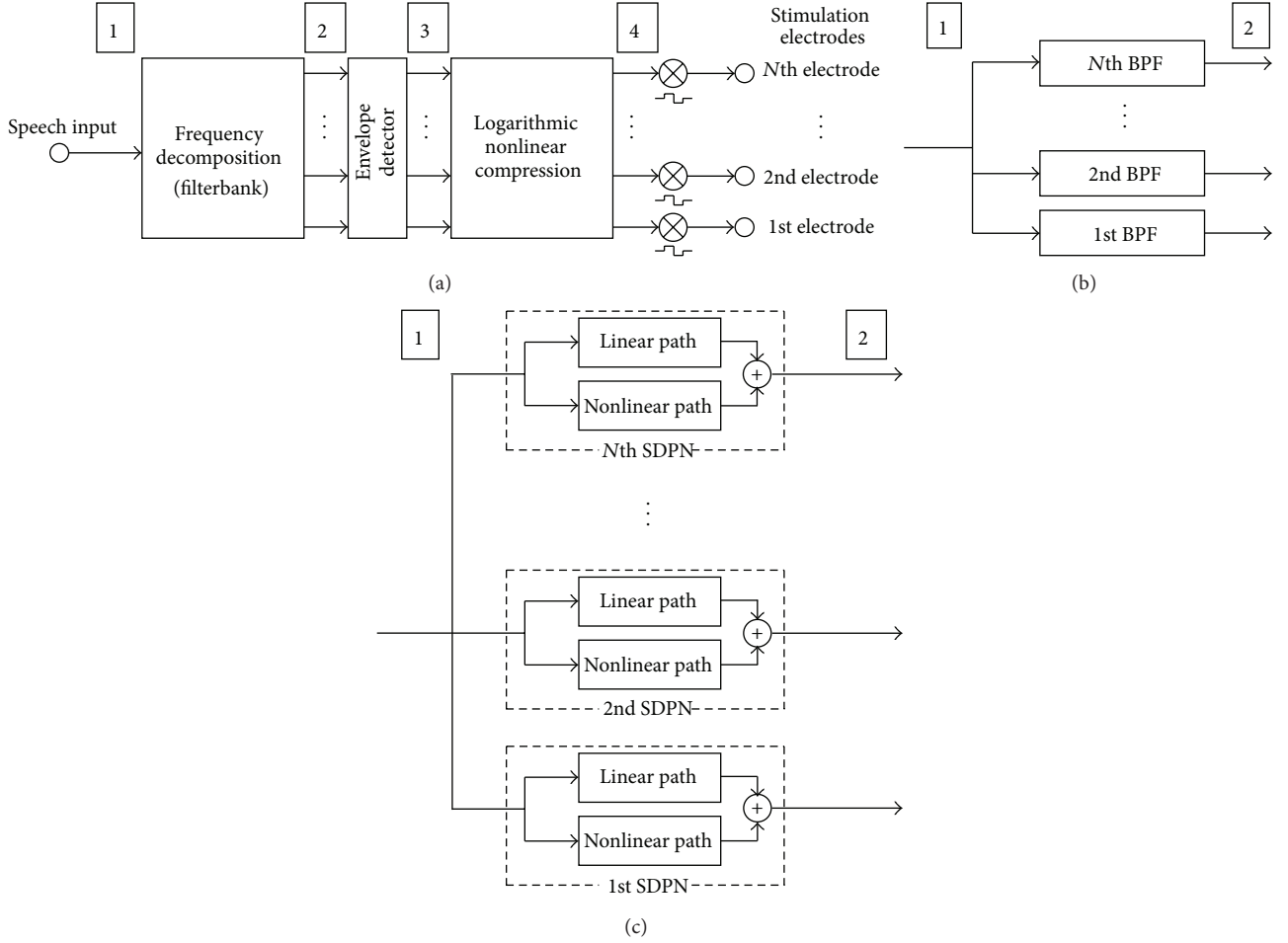
(a)

(b)

(c)

FIGURE 1: (a) General structure of CI sound-processing strategies. Incoming sound is decomposed into multiple frequency bands, and the relative strength of each subband is then determined with an envelope detector to modulate the amplitudes of stimulus pulses after logarithmic compression. (b) The frequency decomposition stage for the conventional strategy based on a fixed linear bandpass filter array. (c) The frequency decomposition stage for the proposed strategy based on the SDPN model.

formant transition provides a valuable piece of information for the identification of consonants, such as plosives, stops, and fricatives [6].

The aforementioned CI performance improvement by the use of active nonlinear model of the basilar membrane may result from robust representation of formants under noisy conditions. The DRNL model was first applied to a CI sound processor and improved speech perception performance was verified from one listener [2]. It was also reported that the DRNL-based sound-processing strategy provides robust formant representation characteristics and enhances vowel perception [3]. The DRNL model was originally developed for quantitative description of the physiological properties of the basilar membrane and to provide a satisfactory fit to experimental results. Thus, the DRNL model includes many parameters that should be determined from experimental data, and its structure is rather complicated for adoption in CI devices. Therefore, a simpler model may be implemented without compromising the advantages of the DRNL model.

Here, we propose a new active nonlinear model of the frequency response of the basilar membrane, called the simple dual path nonlinear (SDPN) model and a novel sound-processing strategy based on this model. The aim of the present study is only to utilize the advantages of the active nonlinear response and not to replicate the physiological properties of the basilar membrane in biological cochlea in detail. A subset of results has been presented in a conference proceeding [7].

2. Methods

2.1. Proposed Sound-Processing Strategy. Figure 1(a) shows the general structure of the sound processor for a CI. The incoming sound is decomposed into multiple frequency bands (stage 2 in Figure 1(a)), and then the relative strength of each subband is obtained from an envelope detector (stage 3) to modulate the amplitudes of stimulus pulses after logarithmic compression. This structure was motivated by place coding (tonotopy) of the basilar membrane and most modern CI devices are based on this structure [8–10]. In the strategy proposed in this paper, the frequency decomposition stage is replaced with a simple active nonlinear filter model
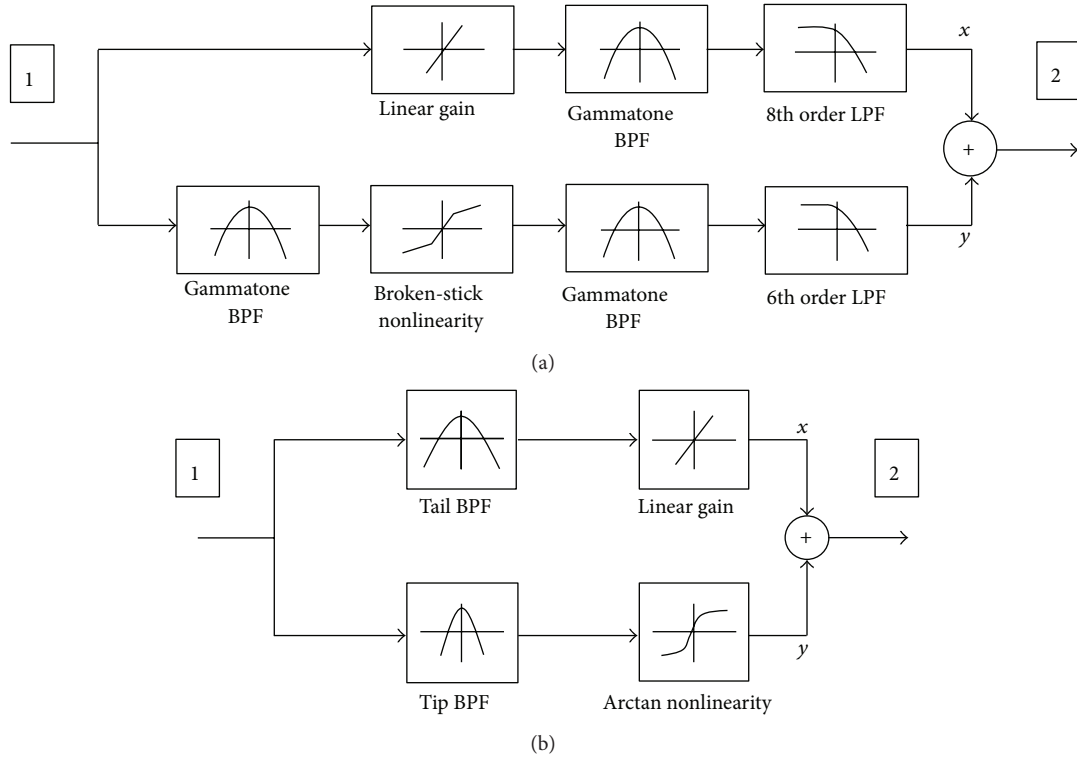
(a)

(b)

FIGURE 2: (a) Block diagram of the DRNL model. The output of each cochlear partition is represented as a summation of the outputs from a linear and a nonlinear pathway. (b) Block diagram of the proposed SDPN model.

of the basilar membrane with variable response instead of a fixed linear bandpass filter which is employed in conventional CIs. The variable response characteristic originates from the input-dependent tuning property of the basilar membrane resulting from active motility of outer hair cells (OHC) [11] and this active nonlinear response property contributes to robust representation of speech cues under noisy conditions [12].

Figures 1(b) and 1(c) illustrate the differences between the conventional and proposed strategies. Both can be regarded as having the structure shown in Figure 1(a). In the conventional strategy (Figure 1(b)), a fixed linear bandpass filter array, is adopted as the frequency decomposition block of Figure 1(a). In contrast, in the proposed strategy (Figure 1(c)), frequency decomposition is performed by the SDPN model array. The output from each channel can be regarded as a bandpass-filtered version of the input, similarly to the conventional strategy. However, the frequency response property is nonlinear and level dependent. Subsequently, the relative strength of each channel is calculated by applying envelope detectors to the outputs from each SDPN. The envelopes are used to modulate the amplitudes of the current pulses in clinical applications involving electrical stimulation; for acoustic simulation, the amplitudes of sinusoids are modulated instead of pulse amplitudes. This is described later in detail (Section 3.4).

Figure 2(a) illustrates the dual resonance nonlinear (DRNL) model which was developed for quantitative description of the physiological properties of the basilar membrane

and to provide a satisfactory fit to experimental results [12]. The output of each cochlear partition is represented as a summation of the outputs from linear and nonlinear pathways in the DRNL model. The linear pathway consists of a linear gain, a gammatone bandpass filter, and a Butterworth lowpass filter. The nonlinear path includes broken-stick nonlinearity between two bandpass filters so that its contribution to the total output is determined by the input signal level. The details of the DRNL model and parameters were reported in [12]. The effective center frequencies of the linear and nonlinear pathways are slightly different. The relative contributions of the two pathways are variable because of the nonlinear gain in the nonlinear pathway, and therefore the overall response characteristics such as gain and bandwidth are also variable. The DRNL model can replicate the frequency response of biological cochlea in that the level-dependent tuning and level-dependent gain properties could be reproduced successfully [12]. Compared to other models with similar purposes, it is relatively simple and computationally efficient. However, the DRNL model includes many parameters and its structure is rather too complicated for adoption in CI devices.

The block diagram of the SDPN model is shown in Figure 2(b). While developing the SDPN model, we did not attempt to reproduce experimental results regarding the neurophysiological properties of the basilar membranes to the numerical details.The purpose here was to implement the level-dependent frequency response characteristics of the biological cochlea. As in the DRNL model, the incoming sound is passed to two pathways. The linear pathway consists
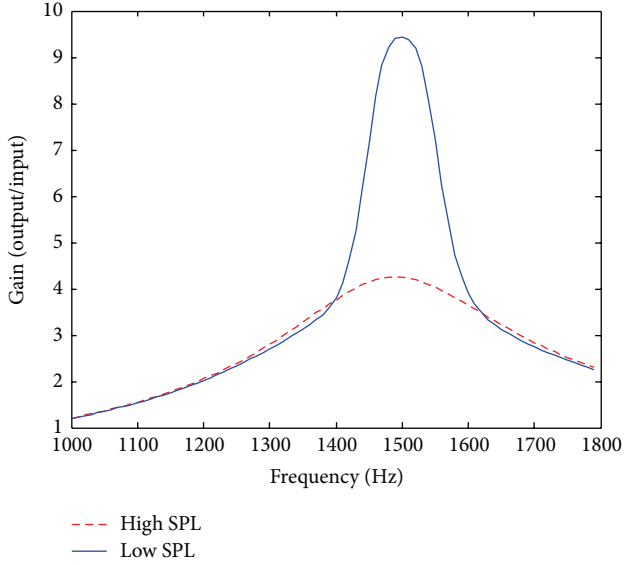
FIGURE 3: The frequency response of the proposed SDPN model when the center frequency is set to 1500 Hz. When the input amplitude is low, the contribution of the nonlinear pathway is relatively large so that the overall response shows a sharp frequency selectivity determined by the tip filter. As the amplitude increases, the contribution of linear pathway becomes dominant, and the overall frequency response therefore becomes broader.

of a linear gain (fixed to 6 here) and a broad bandpass filter, which is called the tail filter. The nonlinear pathway is made of a sharper bandpass filter, which is called the tip filter, and a compressive nonlinearity that is employed to mimic the saturation properties of the OHC. The nonlinearity is expressed as $y = 2 \arctan(15x)$. Both the tail and tip filters are composed of Butterworth bandpass filters (tail filter: 2nd order, tip filter: 4th order). The bandwidth of the tail filter is set to be three times larger than that of the tip filter. To realize the variable response properties, the relative contribution of each pathway is controlled according to the input level (root mean square value) by the nonlinearity. The overall output from one channel of the frequency decomposition block is obtained by summing the outputs from the two pathways. As discussed later in Section 3 (Figure 3), this method allows the implementation of active nonlinear frequency response characteristics of biological cochlea with much lower computational costs than the DRNL model.

After frequency decomposition, the envelopes of each channel output are obtained. We used a conventional envelope detector consisting of a rectifier and a low-pass filter. In addition, we also examined the advantages of using an enhanced envelope detector proposed by Geurts and Wouters [13]. This is based on the adaptation effect resulting from the synapse between inner hair cells and auditory nerves and utilizes a combination of two envelope detectors, namely, a standard envelope detector consisting of a full-wave rectifier and a 4th order Butterworth low-pass filter with 400-Hz cutoff frequency and another for extraction of slowly varying envelope with a low-pass filter cutoff frequency of 20 Hz.

By comparing the two envelopes, it is possible to determine the temporal points where rapid transient changes occur, and additional gain can be applied at these time points for emphasis of the transients. The detailed algorithm was reported in [13].

2.2. Acoustic Simulation. Acoustic simulation can be used to predict performance trends of CI sound-processing strategies and has therefore been utilized for many studies of the development of novel strategies [14]. We adopted sinusoidal modulation for the synthesis of acoustic waveforms, as in many previous studies on CI sound-processing strategy development [14, 15]. The center frequencies of the channels were chosen according to the method of Loizou et al. [16], as this enables systematic computation of the filter bandwidths and is used in current CI devices. Logarithmic filter spacing was used for 4-channel implementation, and semilogarithmic mel spacing was used for 8 and 12 channels. Detailed values of the center frequencies and bandwidths are listed in Table 1.

The method of acoustic simulation in the conventional strategy was similar to that of Dorman et al. [17]. After frequency decomposition of incoming sound by a linear band-pass filter array, an envelope detector consisting of a full-wave rectifier and a 4th order Butterworth low-pass filter (cutoff frequency: 400 Hz) was applied. The detected envelopes were used to modulate the sinusoids with frequencies the same as the center frequencies listed in Table 1. Finally, the amplitude-modulated sinusoids from all the channels were summed.

For the generation of an acoustic waveform corresponding to the proposed strategy, frequency decomposition was performed by an array of SDPN models, and then the envelopes of the outputs from each SDPN model were extracted by envelope detectors. Either conventional or enhanced envelope detectors were adopted. The amplitudes of sinusoids were modulated according to the outputs from the envelope detectors. The frequencies of sinusoids were the same as in the simulation using the conventional strategy. Note that we assigned one sinusoid per channel, as the center frequencies of the tail and tip filters were identical. Thus, the results of acoustic simulation can be readily compared to those of the conventional strategy. This is different from the case of acoustic simulation of the DRNL-based sound-processing strategy [2, 3], where two sinusoids should be used to simulate one channel due to the different center frequencies of linear and nonlinear pathways.

2.3. Hearing Experiment. Ten subjects with normal hearing volunteered to participate in the hearing experiment (mean ± SD age: 25.8 ± 4.08 years; 6 men, 4 women). All subjects were undergraduate or graduate students of Yonsei University. The experimental procedure was reviewed and approved by a local ethics review committee. The experiments were performed under two noise conditions: without any noise (i.e., signal-to-noise ratio (SNR) of ∞ dB) and with speech-shaped noise (SSN) of 2 dB SNR. The SSN here was generated by applying a 2nd order Butterworth low-pass filter (cutoff frequency 1100 Hz) to white Gaussian noise (WGN) as described previously [18] so that its spectral shape was similar

TABLE 1: Center frequencies and bandwidths of the filter arrays used for frequency decomposition.

(a) 4 Channel implementation

	Ch. 1	Ch. 2	Ch. 3	Ch. 4
CFs and BWs of BPFs (in conventional strategy)				
CF (Hz)	460	953	1971	4078
BW (Hz)	321	664	1373	2426
CFs and BWs of tip and tail BPFs (in proposed strategy)				
CF (Hz)	460	953	1971	4078
BW of tip filter (Hz)	321	664	1373	2426
BW of tail filter (Hz)	107	221.3	457.7	808.7

(b) 8 Channel implementation

	Ch. 1	Ch. 2	Ch. 3	Ch. 4	Ch. 5	Ch. 6	Ch. 7	Ch. 8
CFs and BWs of BPFs (in conventional strategy)								
CF (Hz)	394	692	1064	1528	2109	2834	3740	4871
BW (Hz)	265	331	431	516	645	805	1006	1257
CFs and BWs of tip and tail BPFs (in proposed strategy)								
CF (Hz)	394	692	1064	1528	2109	2834	3740	4871
BW of tip filter (Hz)	265	331	431	516	645	805	1006	1257
BW of tail filter (Hz)	83.3	110.3	143.7	172	215	268.3	335.3	419

(c) 12 Channel implementation

	Ch. 1	Ch. 2	Ch. 3	Ch. 4	Ch. 5	Ch. 6	Ch. 7	Ch. 8	Ch. 9	Ch. 10	Ch. 11	Ch. 12
CFs and BWs of BPFs (in conventional strategy)												
CF (Hz)	274	453	662	905	1190	1521	1908	2359	2885	3499	4215	5050
BW (Hz)	165	193	225	262	306	357	416	486	567	661	771	900
CFs and BWs of tip and tail BPFs (in proposed strategy)												
CF (Hz)	274	453	662	905	1190	1521	1908	2359	2885	3499	4215	5050
BW of tip filter (Hz)	165	193	225	262	306	357	416	486	567	661	771	900
BW of tail filter (Hz)	55	64.3	75	87.3	102	119	138.7	162	189	220.3	257	300

CF: center frequency, BPF: bandpass filter, BW: bandwidth.

to that of speech waveforms. The number of channels was varied to 4, 8, or 12 channels.

Syllable identification tests were performed using closed-set tasks. Consonant-vowel-consonant-vowel (CVCV) disyllables were constructed mainly to test vowel perception performance. Each speech token was fixed to the form of /sVda/; that is, only the first vowel was changed whereas the others were fixed to /s/, /d/, and /a/. The first vowel was selected from /a/, /ə/, /o/, /u/, /i/, and /e/. This CVCV form is more natural for the Korean language and was therefore used instead of the CVC-type monosyllables frequently utilized in vowel perception tests in previous studies [13, 17]. Vowel-consonant-vowel (VCV) type monosyllables were also constructed. The vowels at the beginning and end were the same and fixed to /a/. The consonants between vowels were selected from /g/, /b/, /m/, /n/, /s/, and /j/. Thus, the speech materials were of the /aCa/ type. A total of 72-/sVda-/ type disyllables and 72-/aCa-/ type monosyllables were generated (72 = 6 consonants/vowels × 2 strategies (conventional/SDPN-based) × 2 noise levels × 3 channel

types). Two experimental sessions were performed with the same subjects; the first compared conventional and SDPN-based strategies, and the second compared the conventional strategy with that based on the SDPN and the enhanced envelope detector.

The acoustic waveforms of speech tokens were generated by 16-bit mono analog-to-digital conversion at sampling rate of 22.050 kHz and stored as .wav files. The stored files were played by clicking icons displayed in a graphical user interface on a personal computer prepared for the experimental run. The speech tokens were presented binaurally using headphones (Sennheiser HD25SP1) and a 16-bit sound card (SoundMAX integrated digital audio soundcard). The sound level was controlled to be comfortable for each subject (range: ~70–80 dB). A 5 min training session was given before the main experiment. Each speech token was presented once. The conditions of sound processing strategies and noise conditions were randomized across subjects. If the subjects requested, the waveforms were played once more. After hearing each speech token, the subjects were instructed to
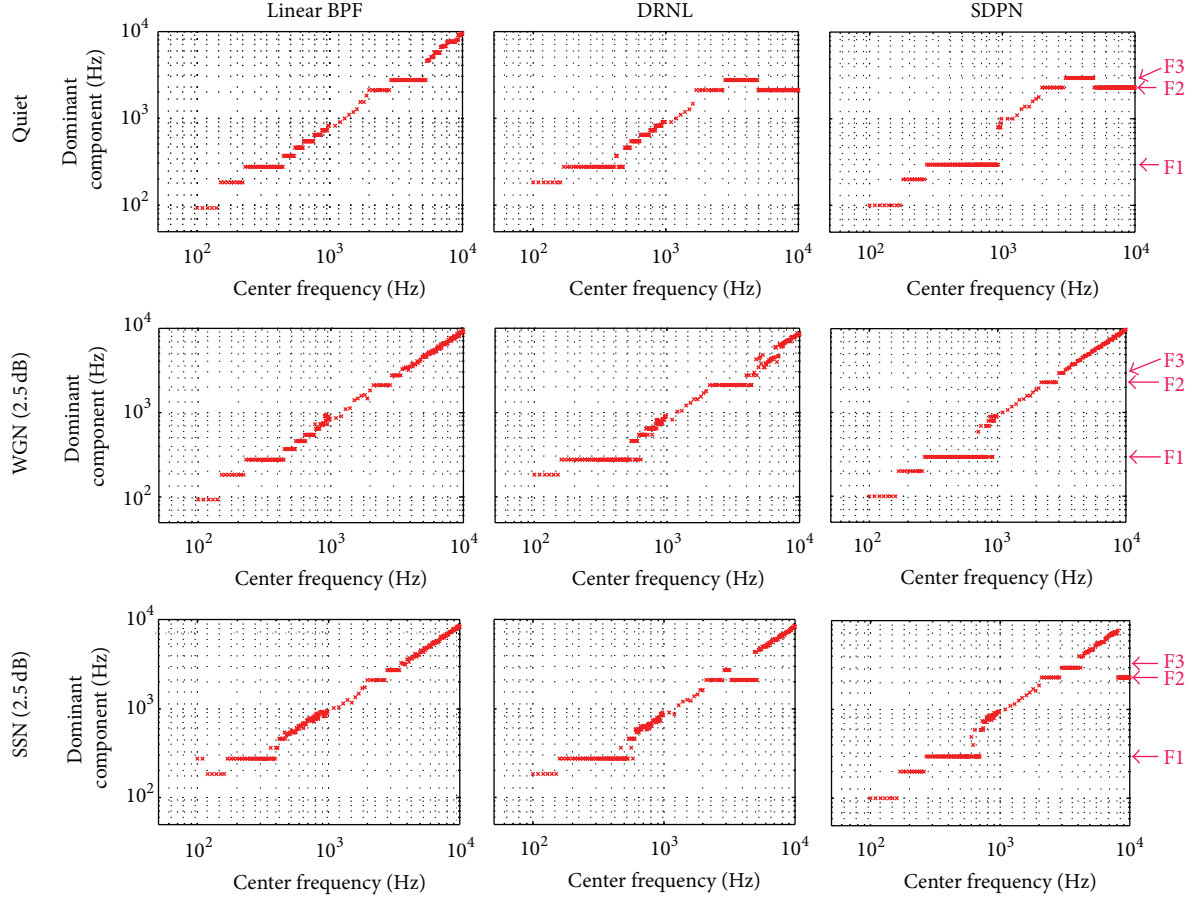
FIGURE 4: Dominant frequency component analysis for the vowel /i/. F1, F2, and F3 are at 270 Hz, 2290 Hz, and 3010 Hz, respectively. Upper row: under quiet conditions. Middle row: under 2.5 dB WGN. Lower row: under 2.5 dB SSN. Left column: by the linear BPF array. Middle columns: DRNL. Right column: SDPN.

choose the presented syllable among six given examples as correctly as possible, and the percentage of correct answers was scored.

3. Results

3.1. Variable Frequency Response of the SDPN Model. Figure 3 shows the frequency response of the proposed SDPN model with a center frequency of 1500 Hz. When the input amplitude was low (35 dB sound pressure level (SPL)), the contribution of the nonlinear pathway was relatively large, and so the overall response showed sharp frequency selectivity determined by the tip filter. Peak gain was 9.44, and the full width at half maximum (FWHM) was 140.27 Hz. As the amplitude increased (85 dB SPL), the contribution of the linear pathway became dominant, and the overall frequency response became broader (FWHM = 424.08 Hz). Meanwhile, the overall gain decreased due to the compressive nonlinearity (peak gain = 4.26). Overall, the frequency response of the SDPN model showed level-dependent behavior, which was similar to that of the biological cochlea. Compared to the DRNL model, the proposed simplified structure could be executed very quickly. For example, to process 1 s of sound, the CPU time was 0.054 ± 0.012 s (mean ± SD) for

the SDPN model, whereas that for the DRNL was 1.33 ± 0.034 s (average of 40 trials, Matlab implementation, 3.0 GHz Pentium 4 processor, 2 GB RAM). That is, the processing time for the proposed SDPN model was only about 1/24.6 that of the DRNL model.

3.2. Formant Representation under Noisy Conditions. The superiority of the active nonlinear models for robust representation of formants under noisy conditions could be demonstrated by dominant frequency component analysis, that is, by plotting the maximum frequencies of the output from each cochlear partition as a function of the center frequency [19]. We divided the frequency range from 100 Hz to 10 kHz in 181 partitions and observed the output from each cochlear partition. Figure 4 shows the results of dominant frequency component analysis after frequency decomposition using the fixed linear bandpass filter, the DRNL model, and the proposed SDPN model (input: vowel /i/, under quiet conditions, 5 dB WGN, and 5 dB SSN). Particularly under noisy conditions, the maximum frequencies of the outputs from active nonlinear models (DRNL and SDPN) were concentrated at the location of formant frequencies, as shown by the horizontal lines at the formants, whereas
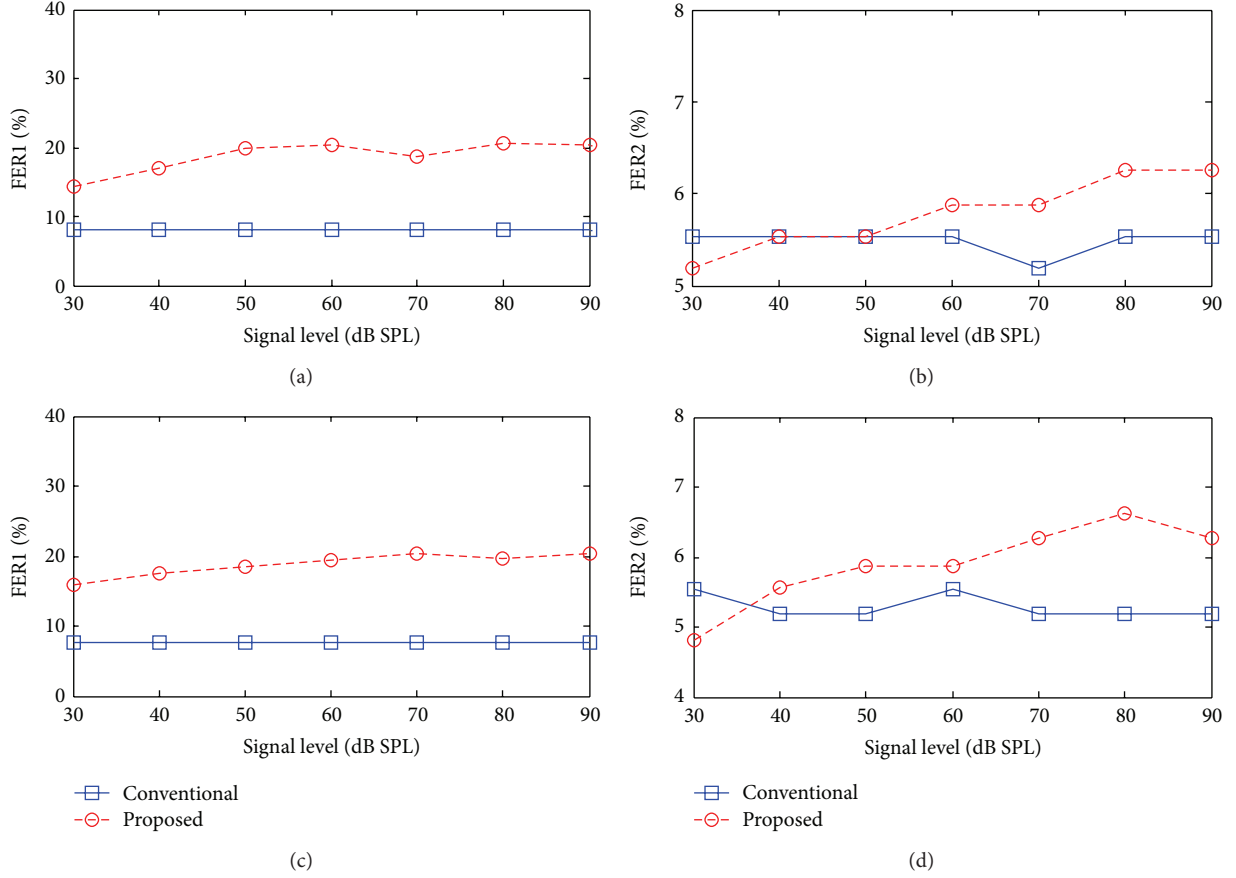
FIGURE 5: FER1 ((a) and (c)) and FER2 ((b) and (d)) at various sound pressure levels (SPLs) for the vowel /i/. (a) and (b) under WGN of 2.5 dB SNR. (c) and (d) under SSN of 2.5 dB SNR.

those from the linear filterbank model were determined by the center frequencies of each channel so that the data points were more concentrated at diagonal locations. Thus, the proposed SDPN model is more effective for robust formant representation under noisy conditions than the linear filter array and has advantages similar to those of the DRNL model. Similar results were also obtained for /a/ and /u/.

From the results of dominant frequency component analysis, formant representation performance could be quantified by counting the number of cochlear partitions the maximum output frequencies of which were determined by the formant frequencies. We defined two formant extraction ratios (FERs), FER1 and FER2, as the ratios of cochlear partitions with maximum output frequencies that were the same as the 1st and 2nd formant frequencies, respectively. FER1 and FER2 can be regarded as good quantitative measures of saliency of the formant representation in the output speech. Since the performance of nonlinear models could vary according to the input level as the response characteristic changes with respect to the input level, we observed the changes in formant representation performance at various SPLs. Figure 5 shows FER1 and FER2 for the vowel /i/ as functions of input amplitude under conditions of WGN and SSN of 5 dB SNR. For a wide range of input levels, the SDPN yielded higher FER1 and FER2 compared to the linear bandpass filter under both WGN and SSN. The FERs of the linear model remained

constant except for slight fluctuations due to error. As shown in Figures 5(a) and 5(b), the SDPN resulted in higher values of FER1 at all input amplitudes under WGN. The FER2 of the SDPN was also higher than that of the linear model when the SPL was higher than 40 dB. This indicated that the SDPN is advantageous for the formant representation for typical SPL levels. The SDPN was also superior when the SSN was added as background noise (Figures 5(b) and 5(d)).

3.3. Enhanced Envelope Detector. Figure 6 shows the envelopes of 4 channels obtained from conventional (Figure 6(a)) and enhanced (Figure 6(b)) envelope detectors after frequency decomposition using the SDPN model. The arrows in Figure 6(b) indicate the time points where the enhanced envelope detector effectively emphasized the point of speech onset. Particularly, for the input speech "/aka/," the onset point of /k/ was significantly accentuated in Figure 6(b).

3.4. Acoustic Simulation and Hearing Experiment. The results of hearing experiments using acoustic simulation of the proposed sound-processing strategy based on the SDPN model are shown in Figure 7. The percentages of correct answers were plotted as functions of the number of channels for 4, 8, and 12 channels. For all conditions, the proposed strategy was considerably superior to the conventional strategy. Although

(a)

(b)
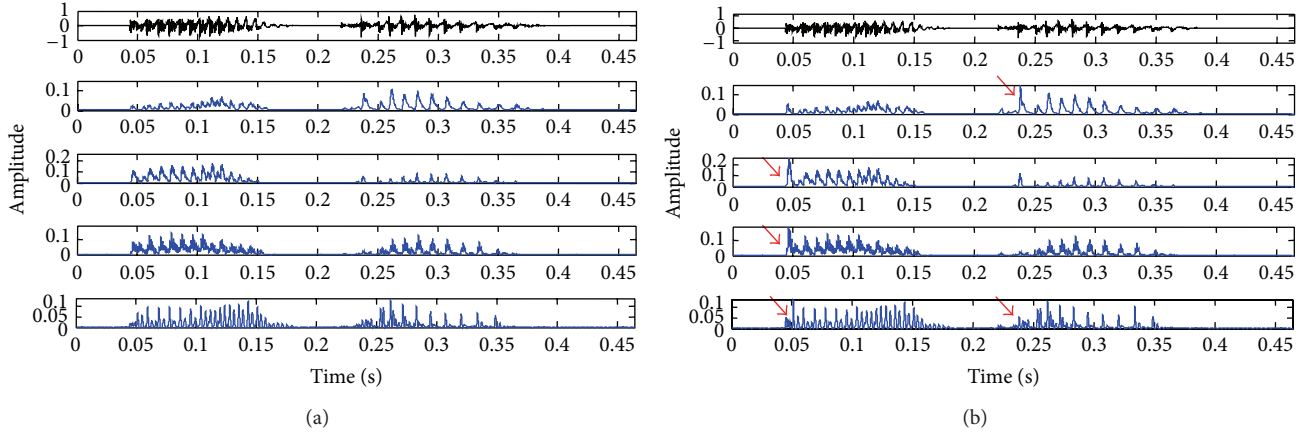
FIGURE 6: The envelopes obtained from (a) conventional and (b) enhanced envelope detectors after frequency decomposition by the SDPN model. The arrows in (b) indicate emphasis of speech onset.
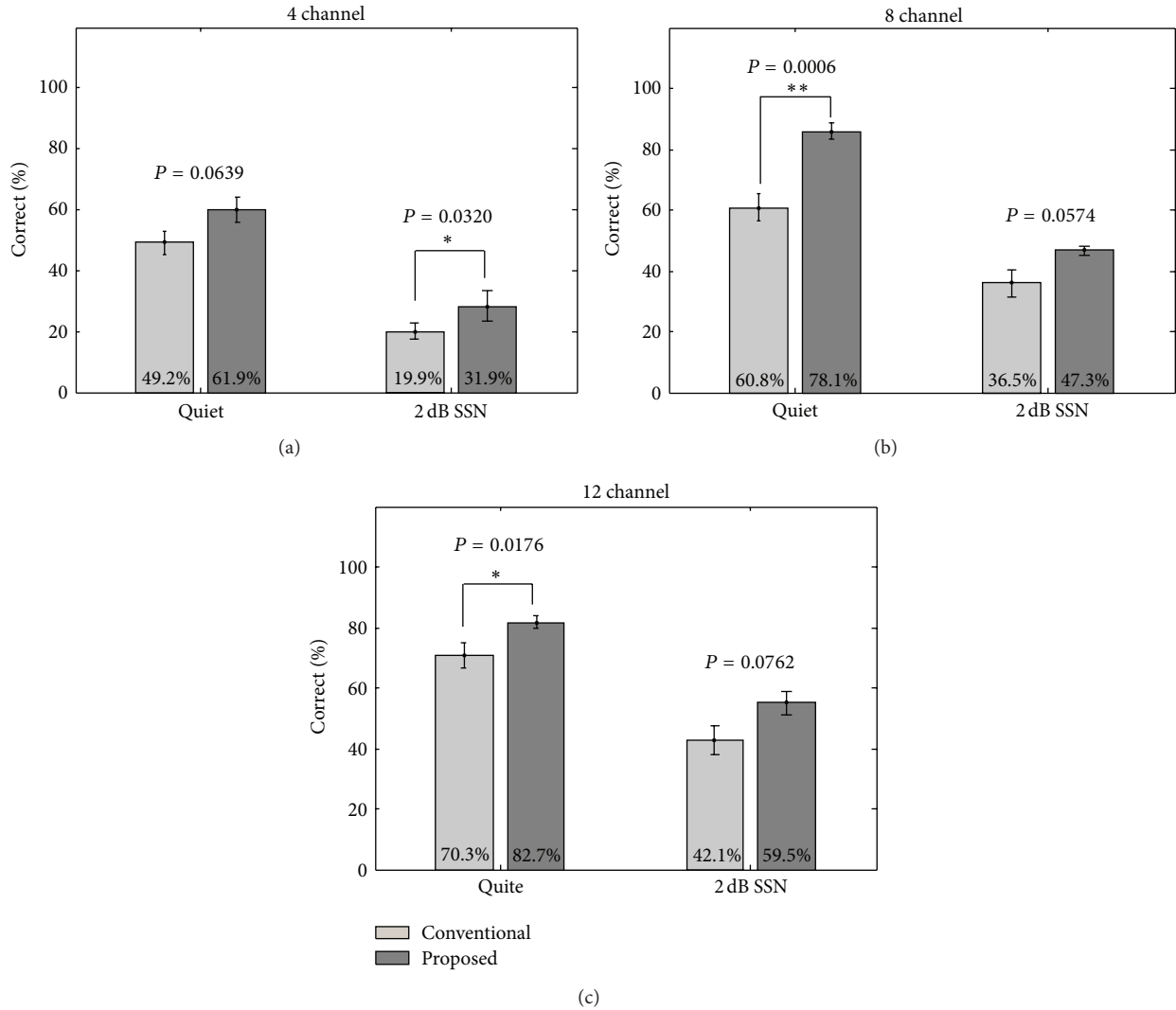

(a)

(b)

(c)

FIGURE 7: Results of syllable identification tests using the sound-processing strategy based on the SDPN and the conventional envelope detector (under quiet conditions or SSN of 2 dB SSN). (a) 4 channels. (b) 8 channels. (c) 12 channels.
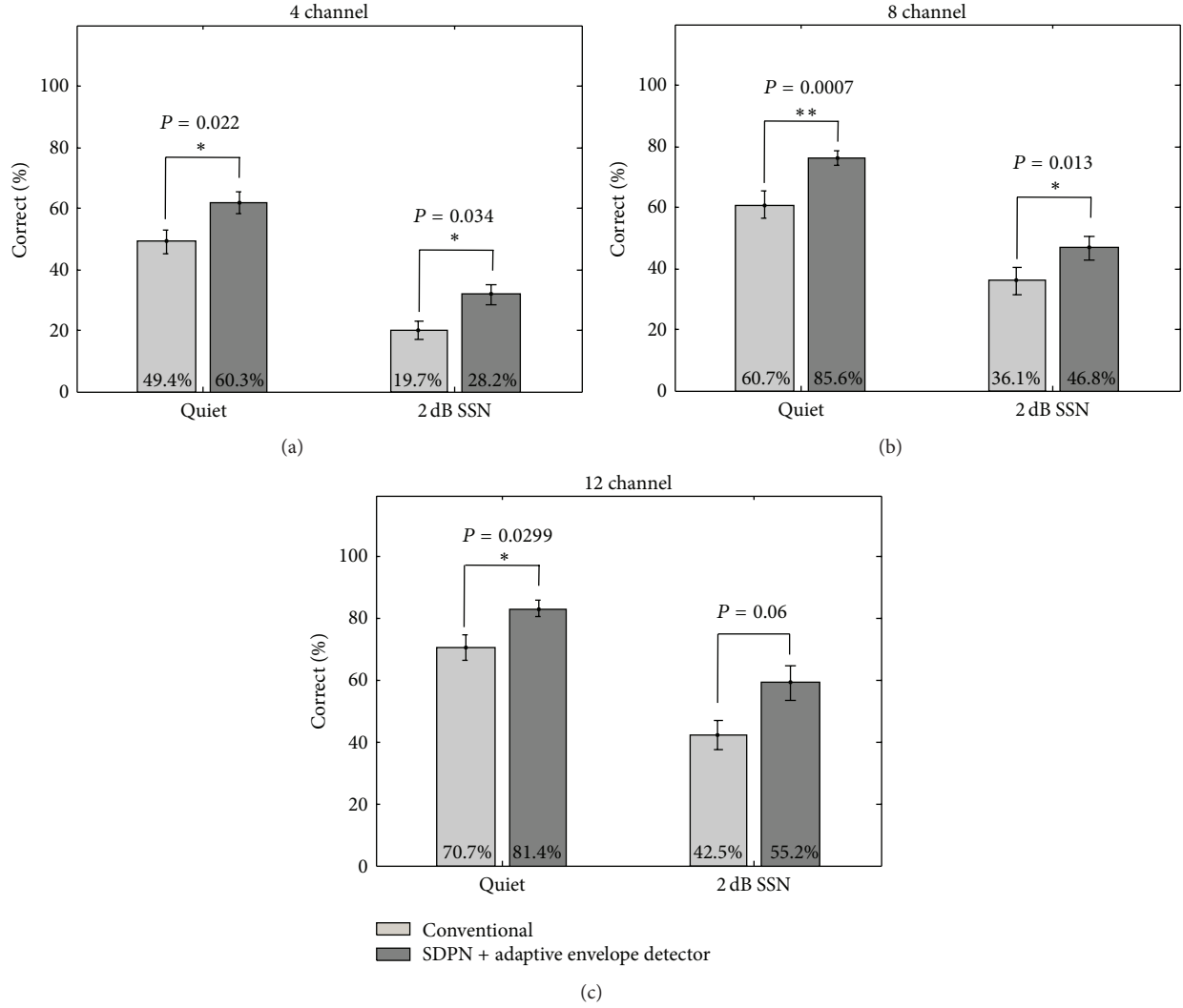
FIGURE 8: Results of syllable identification tests using the sound-processing strategy based on the SDPN and the enhanced envelope detector (under quiet conditions or SSN of 2 dB SSN). (a) 4 channels. (b) 8 channels. (c) 12 channels.

statistical significance ($P < 0.05$) was not reached for some conditions, the proposed strategy yielded much better speech perception performance for all conditions; all P-values were <0.0762 and approached statistical significance. Figure 8 shows the results of hearing experiments using a strategy based on the SDPN and the enhanced envelope detector. For quiet conditions, the proposed strategy was better than the conventional one for all channel conditions. The superiority was statistically significant for all channel conditions (t-test, $P < 0.05$ for 4 channels, and $P < 0.01$ for 8 and 12 channels). Under SSN of 2 dB SNR, the proposed strategy provided considerably better syllable identification for all channel conditions (t-test, $P < 0.05$ for 4 and 8 channels, $P = 0.06$ for 12 channels).

4. Discussion

In this study, we proposed a simple active nonlinear model of basilar membrane in the cochlea and developed a novel sound-processing strategy for the CIs based on this model.

Acoustic simulation and hearing experiments in subjects with normal hearing indicated that the proposed strategy provides enhanced syllable identification performance under conditions of speech-shaped noise, compared to the conventional strategy using a fixed linear bandpass filter array.

Some previous experimental studies indicated that the active nonlinear frequency response property contributes significantly to robust representation of formant information in noisy environments. Several models were suggested to reproduce this property [11, 20, 21]. For example, Deng and Geisler [11] proposed a nonlinear differential equation model with a variable damping term to simulate a level-dependent compression effect and successfully reconstructed the response characteristics of the biological cochlea that are beneficial for robust spectral cue representation under noise. This implies that the speech perception performance of CIs can be improved by adopting the active nonlinear response property, as demonstrated by the enhanced performance of CI sound-processing strategy based on the DRNL model [2, 3].

Although the DRNL model is one of the most efficient models in terms of computational costs, its purposes are to quantitative description of the physiological properties of the basilar membrane and to replicate detailed experimental results. The complicated structure and numerous parameters of the DRNL model make it unsuitable for the CI sound processor. The motivation for development of the SDPN model was to simplify the DRNL model without compromising its advantages due to the adaptive nonlinear frequency response. The SDPN model was developed as a further simplification of the DRNL model, with the purpose of developing a CI sound-processing strategy. The emphasis was on reproducing the input-dependent response characteristics of biological cochlea qualitatively. Many building blocks and parameters of the DRNL model were not necessary to implement the level-dependent frequency response of the biological cochlea, because they were adopted for the detailed replication of experimental results and are not essential to our goal here. The proposed SDPN is much simpler than the DRNL but can still provide the level-dependent frequency response, which is beneficial for real-time processing with lower power consumption due to less computation.

The results of dominant frequency analysis verified that more robust formant representation under SSN could be obtained from the proposed SDPN model. When the SDPN model was used, the output frequency was dominated by formant frequencies in much more cochlear partitions compared to the case of the linear bandpass filterbank (Figures 4 and 5). Despite the simplification, the formant representation performance of the SDPN model was comparable to that of the DRNL presented in [3], as can be verified by the results of dominant frequency component analysis and FERs. This suggests that the detailed imitation of the frequency response characteristics of the human basilar membrane is not essential for the improvement of CI speech perception performance. This is in contrast with a previous study [2] in which a detailed model of human basilar membrane based on the DRNL model was adopted in the CI sound processor.

The comparison between the envelopes extracted by two envelope detectors shown in Figure 6 showed that the enhanced envelope detector provides the emphasis of speech onset points, which is often weak in amplitude. This property may contribute to the improvement of the perception of stop, fricative, and plosive consonants. This was confirmed from the hearing experiments using acoustic simulation (Figures 7 and 8), as the use of the enhanced envelope detector provided further improvement of the SDPN-based strategy in speech perception.

A new sound-processing strategy for CI should be applied in clinical tests for more comprehensive verification. This requires the modulation of electrical pulse trains based on the sound processor output. The proposed SDPN-based strategy was developed so that it employs one amplitude-modulated pulse train per channel in actual CI devices. Thus, it is readily applicable to the existing hardware of current CIs.

In conclusion, we proposed a simple novel model of active nonlinear characteristics of biological cochlea and developed a sound-processing strategy for CI based on the model. The proposed SDPN model was based on the function of the basilar membrane so that a level-dependent frequency response can be reproduced; it is much simpler than the DRNL model and is thus better suited for incorporation into CI sound processors. The SDPN-based strategy was evaluated by spectral analysis and hearing experiments in subjects with normal hearing. The results indicated that the use of the SDPN model provides advantages similar to those of the DRNL-based strategy in that the formant is more robustly represented under noisy conditions. Further improvement in speech perception under noisy conditions was possible by adopting an enhanced envelope detector.

Conflict of Interests

The authors declare that there exists no conflict of interests.

Acknowledgment

References

[1] B. S. Wilson, D. T. Lawson, J. M. Muller, R. S. Tyler, and J. Kiefer, "Cochlear implants: some likely next steps," *Annual Review of Biomedical Engineering*, vol. 5, pp. 207–249, 2003.

[2] R. Schatzer, B. S. Wilson, R. D. Wolford, and D. T. Lawson, "Speech processors for auditory prostheses: signal processing strategy for a closer mimicking of normal auditory functions," Sixth Quatery Progress Report NIH N01-DC-2-1002, Neural Prosthesis Program, National Institute of Health, Bethesda, Md, USA, 2003.

[3] K. H. Kim, S. J. Choi, J. H. Kim, and D. H. Kim, "An improved speech processing strategy for cochlear implants based on an active nonlinear filterbank model of the biological cochlea," *IEEE Transactions on Biomedical Engineering*, vol. 56, no. 3, pp. 828–836, 2009.

[4] A. R. Palmer, I. M. Winter, and C. J. Darwin, "The representation of steady-state vowel sounds in the temporal discharge patterns of the guinea pig cochlear nerve and primarylike cochlear nucleus neurons," *Journal of the Acoustical Society of America*, vol. 79, no. 1, pp. 100–113, 1986.

[5] S. Bandyopadhyay and E. D. Young, "Discrimination of voiced stop consonants based on auditory nerve discharges," *Journal of Neuroscience*, vol. 24, no. 2, pp. 531–541, 2004.

[6] E. D. Young and M. B. Sachs, "Representation of steady-state vowels in the temporal aspects of the discharge patterns of populations of auditory-nerve fibers," *Journal of the Acoustical Society of America*, vol. 66, no. 5, pp. 1381–1403, 1979.

[7] K. H. Kim, S. J. Choi, and J. H. Kim, "A speech processing strategy for cochlear implant based on a simple dual path nonlinear model of Basilar membrane," in *Proceedings of the 13th International Conference on Biomedical Engineering*, Singapore, December 2008.

[8] B. Wilson and C. Finley, "Improved speech recognition with cochlear implants," *Nature*, vol. 352, pp. 236–238, 1991.

[9] P. Loizou, "Signal-processing techniques for cochlear implants," *IEEE Engineering in Medicine and Biology Magazine*, vol. 18, no. 3, pp. 34–46, 1999.

[10] J. T. Rubinstein, "How cochlear implants encode speech," *Current Opinion in Otolaryngology & Head and Neck Surgery*, vol. 12, no. 5, pp. 444–448, 2004.

[11] L. Deng and C. D. Geisler, "A composite auditory model for processing speech sounds," *Journal of the Acoustical Society of America*, vol. 82, no. 6, pp. 2001–2012, 1987.

[12] R. Meddis, L. P. O'Mard, and E. A. Lopez-Poveda, "A computational algorithm for computing nonlinear auditory frequency selectivity," *Journal of the Acoustical Society of America*, vol. 109, no. 6, pp. 2852–2861, 2001.

[13] B. L. Geurts and J. Wouters, "Enhancing the speech envelope of continuous interleaved sampling processors for cochlear implants," *Journal of the Acoustical Society of America*, vol. 105, no. 4, pp. 2476–2484, 1999.

[14] M. F. Dorman, A. J. Spahr, P. C. Loizou, C. J. Dana, and J. S. Schmidt, "Acoustic simulations of combined electric and acoustic hearing (EAS)," *Ear and Hearing*, vol. 26, no. 4, pp. 371–380, 2005.

[15] F. G. Zeng, K. Nie, G. S. Stickney et al., "Speech recognition with amplitude and frequency modulations," *Proceedings of the National Academy of Sciences of the United States of America*, vol. 102, no. 7, pp. 2293–2298, 2005.

[16] P. C. Loizou, M. Dorman, and Z. Tu, "On the number of channels needed to understand speech," *Journal of the Acoustical Society of America*, vol. 106, no. 4, pp. 2097–2103, 1999.

[17] M. F. Dorman, P. C. Loizou, and D. Rainey, "Speech intelligibility as a function of the number of channels of stimulation for signal processors using sine-wave and noise-band outputs," *Journal of the Acoustical Society of America*, vol. 102, no. 4, pp. 2403–2411, 1997.

[18] L. P. Yang and Q. J. Fu, "Spectral subtraction-based speech enhancement for cochlear implant patients in background noise," *Journal of the Acoustical Society of America*, vol. 117, no. 3, pp. 1001–1004, 2005.

[19] S. D. Holmes, C. J. Sumner, L. P. O'Mard, and R. Meddis, "The temporal representation of speech in a nonlinear model of the guinea pig cochlea," *Journal of the Acoustical Society of America*, vol. 116, no. 6, pp. 3534–3545, 2004.

[20] A. Robert and J. L. Eriksson, "A composite model of the auditory periphery for simulating responses to complex sounds," *Journal of the Acoustical Society of America*, vol. 106, no. 4, pp. 1852–1864, 1999.

[21] Q. Tan and L. H. Carney, "A phenomenological model for the responses of auditory-nerve fibers. II. Nonlinear tuning with a frequency glide," *Journal of the Acoustical Society of America*, vol. 114, no. 4, pp. 2007–2020, 2003.

Research Article

Corticomuscular Coherence Analysis on Hand Movement Distinction for Active Rehabilitation

Xinxin Lou,[1,2] Siyuan Xiao,[1,3] Yu Qi,[1,3] Xiaoling Hu,[4] Yiwen Wang,[1,5] and Xiaoxiang Zheng[1,2,5]

[1] *Qiushi Academy for Advanced Studies, Zhejiang University, Hangzhou, Zhejiang 310027, China*

[2] *College of Biomedical Engineering & Instrument Science, Zhejiang University, Hangzhou, Zhejiang 310027, China*

[3] *School of Computer Science and Technology, Zhejiang University, Hangzhou, Zhejiang 310027, China*

[4] *Interdisciplinary Division of Biomedical Engineering, Hong Kong Polytechnic University, Hong Kong*

[5] *Key Laboratory of Biomedical Engineering of Ministry of Education, Zhejiang University, Hangzhou, Zhejiang 310027, China*

Correspondence should be addressed to Yiwen Wang; eewangyw@zju.edu.cn

Active rehabilitation involves patient's voluntary thoughts as the control signals of restore device to assist stroke rehabilitation. Although restoration of hand opening stands importantly in patient's daily life, it is difficult to distinguish the voluntary finger extension from thumb adduction and finger flexion using stroke patients' electroencephalography (EMG) on single muscle activity. We propose to implement corticomuscular coherence analysis on electroencephalography (EEG) and EMG signals on Extensor Digitorum to extract their intention involved in hand opening. EEG and EMG signals of 8 subjects are simultaneously collected when executing 4 hand movement tasks (finger extension, thumb adduction, finger flexion, and rest). We explore the spatial and temporal distribution of the coherence and observe statistically significant corticomuscular coherence appearing at left motor cortical area and different patterns within beta frequency range for 4 movement tasks. Linear discriminate analysis is applied on the coherence pattern to distinguish finger extension from thumb adduction, finger flexion, and rest. The classification results are greater than those by EEG only. The results indicate the possibility to detect voluntary hand opening based on coherence analysis between single muscle EMG signal and single EEG channel located in motor cortical area, which potentially helps active hand rehabilitation for stroke patients.

1. Introduction

Stroke is one of the leading causes of death in the world [1, 2]. In addition to the high death rate, most stroke patients may lose many daily activities, such as walking, grasping, and speaking [3]. To restore the losing motor functions of a stroke patient, rehabilitation therapies are often necessary and proven to be effective [4–9]. Studies on fMRI, PET, and TMS had shown that some areas of the stroke patient's brain indicated reorganization [8–10], which played an important role for restore of patients' function. There are mainly two kinds of rehabilitation: passive rehabilitation and active rehabilitation. The passive rehabilitation directly stimulates

the affected muscles in therapies without involving patients' volition, such as physical training, electrical stimulation (ES) [11–14]. On the contrary, active rehabilitation is that stroke patients' volition is a necessary part in rehabilitation, in which the muscles are stimulated to be active only when the patients intent to do so. More importantly, active rehabilitation was proved to be more effective to restore stroke patient' motor function and improve the performance of brain plasticity [15–17]. Electromyography (EMG) or electroencephalography (EEG) signals had been utilized and proved to be as useful tools when volition was involved in active rehabilitation [18–21]. EMG, as the control signals of ES, could be adopted to help restore stroke patients' walk and grasp functions

[18–20]. However, the muscles are usually coactive, spastic, or amyotrophic for stroke patients [22]. The voluntary intention extract from such signals may not be reliable.

In therapies, restoration of hand function is usually a common procedure for stroke patients, since the loss of normal hand function can cause great difficulties in daily life. One of the most challenge movements is that the therapist needs to help patient to open hand, because the patient's hand is usually spastically closed [23, 24]. Extensor Digitorum is the muscle that mainly involved in finger extension (corresponding to hand opening). Although finger extension can be differentiated from thumb adduction and finger flexion (corresponding to hand closing) with EMG signals on extensor digitorum [25–27] for healthy subjects, it is not easy to classify different hand movements for stroke patients, since the muscles are coactive, spastic, or amyotrophic [22]. Therefore, extracting the intention of single muscle activity that involved in hand opening, and distinguishing from the hand closing, is meaningful for hand function restoration.

EEG is one of the approaches to interpret patient movement intentions [21]. For example, motor imagery (MI) can be used to distinguish rest from movements, or right from left motor imagery. In Pfurtscheller and Neuper's study, ES was controlled by EEG signals to help patient with spinal cord injury to restore grasp function [21]. However, EEG in his study utilize MI that could only distinguish left from right movement and it is difficult to classify different ipsilateral hand actions, such as finger extension (corresponding to hand opening), thumb adduction, and finger flexion (corresponding to hand closing) [28–31]. Since EMG signals are induced from EEG signals, the coherence is observed only in correlated EEG-EMG signals [32]. Even though coactive muscles or spasticity was observed in stroke patient's ipsilateral hand muscle, the cortico-muscular coherence (CMC) may not exist, because the collected EMG signals do not involve patient volition [32]. Conway et al. firstly described CMC existing in magnetocephalography (MEG) and first dorsal interosseous muscles surface EMG [33]. Mima and Hallett extracted coherence between EEG and right Abductor Pollicis Brevis muscle EMG and described CMC mechanism [34, 35]. The arm and hand coherence had overlap area shown in Mima and Steger's study [36].

In this paper, we propose to analyze cortico-muscular coherence between EMG and EEG signals to distinguish voluntary ipsilateral hand opening, hand closing, and rest state. The EMG signals of Extensor Digitorum (ED) muscle and 35 channels of EEG signals are simultaneously collected when 8 subjects are instructed to voluntarily execute right finger extension, thumb adduction, finger flexion, and rest. We observe the spatial distribution of the EEG channels when the cortico-muscular coherence reaches peak value. Then brain channel corresponding to the voluntary movement is fixed in left motor cortex, and CMC value over different frequency within beta range is explored for 4 different executions. After the temporal and spatial feature extraction, we apply t-test to check if the coherence between EMG on ED and EEG signals is statistically different among 4 movement states across all subjects. We finally implement linear discriminate analysis to classify finger extension from

Table 1: Character of subjects.

Subject	Age	Gender	Handedness
1	25	Male	Right
2	27	Male	Right
3	24	Male	Right
4	24	Male	Right
5	23	Female	Right
6	23	Male	Right
7	24	Male	Right
8	23	Male	Right

thumb adduction, from finger flexion, and from rest states based on cortico-muscular coherence value.

2. Materials and Methods

2.1. Subjects and Experiments Paradigm. We recruit 8 normal right-handed volunteers in this study without any healthy neurology disease history (7 males and 1 female, mean age 24.13 ± 1.36, as shown in Table 1). The subject's handedness is tested by the Edinburgh inventory [37]. All subjects are given informed written consent in the experiment and the protocol is approved by the ethics committees Zhejiang University.

The subjects are seated comfortably in front of table and asked to perform four simple hand movement tasks (finger extension (corresponding to hand opening), thumb adduction, finger flexion (corresponding to hand closing) and rest). The first three hand movements mainly correspond to Extensor Digitorum (ED), Abductor Pollicis Brevis (APB) and Flexor Digitorum (FD) muscles, respectively. In order to standardize experiment condition, an orthosis is used to fix subjects' finger and upper limb is fixed on the armrest (as shown in Figure 1(b)).

The total experiment contains two main parts. Firstly, the subjects are asked to finish the maximum volunteer contraction (MVC) test [38]. To compare different subject and same subject at different time, MVC test is necessary, because EMG amplitudes are different among subjects, so are the maximum EMG of the same subject. The subjects are asked to do three separately above-mentioned muscle MVC test, and the hand is fixed by a splint (as shown in Figure 1(b)). We take ED muscle for an example here.

There are three states in whole MVC test hinted on monitor (as shown in Figure 2(a)), ready, action, and rest. The subject should keep 10 s maximum finger extension with action hint in the monitor. The subject is asked to finish MVC test three times for each muscle. The average of this duration EMG amplitude is donated as $\text{EMG}_{\max}$ [38].

After the MVC test, each subject is asked to activate the target muscle with amplitude close to 25% of $\text{EMG}_{\max}$ as follows.

$$\text{EMG}_p = \frac{\text{EMG}_r}{\text{EMG}_{\max}}, \tag{1}$$

where EMG_r is real-time EMG signal displayed in real-time feedback bar and $\text{EMG}_{\max}$ is the maximum EMG signal from

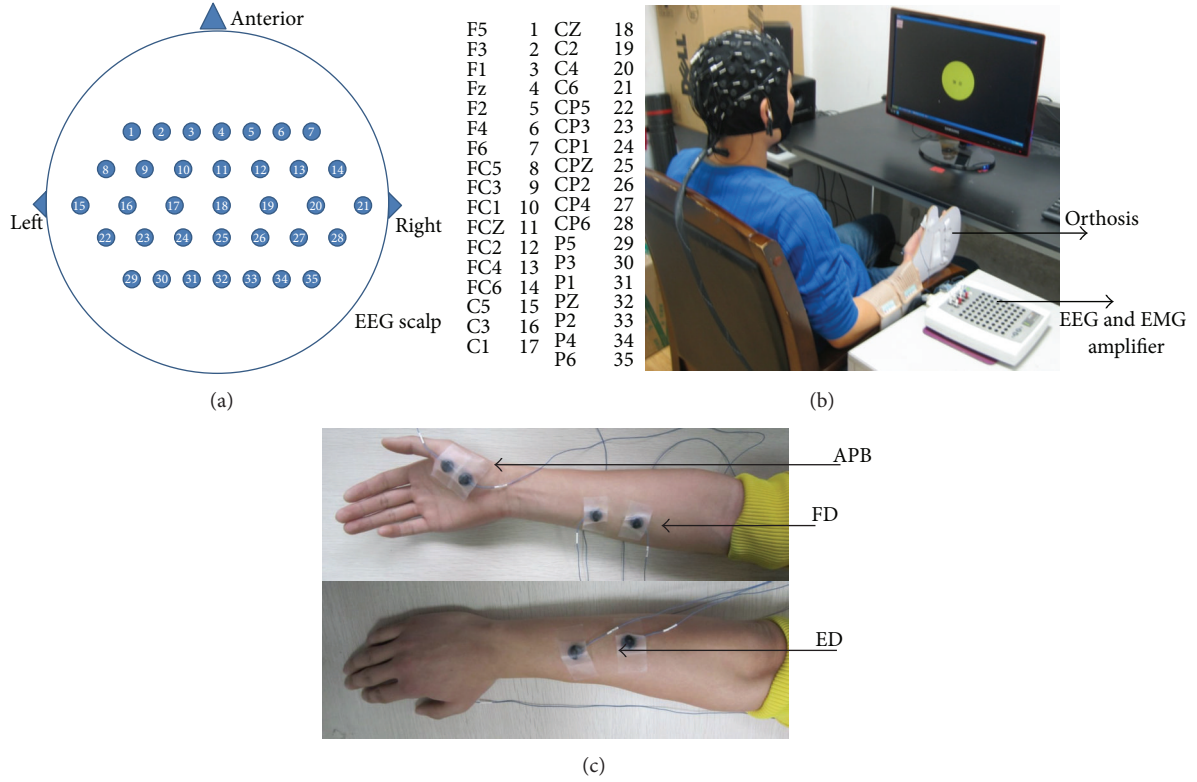|			
F5	1	CZ	18
F3	2	C2	19
F1	3	C4	20
Fz	4	C6	21
F2	5	CP5	22
F4	6	CP3	23
F6	7	CP1	24
FC5	8	CPZ	25
FC3	9	CP2	26
FC1	10	CP4	27
FCZ	11	CP6	28
FC2	12	P5	29
FC4	13	P3	30
FC6	14	P1	31
C5	15	PZ	32
C3	16	P2	33
C1	17	P4	34
		P6	35

(a)

(b)

(c)

FIGURE 1: (a) Top view of 35 channel quick cap and the mapping to 64 Ch quick cap name. (b) Demonstration of the experiment setup. (c) Extensor Digitorum (ED), Abductor Pollicis Brevis (APB), and Flexor Digitorum (FD) muscles position.

MVC. EMG_p is proportional of EMG signals and displayed in real time to instruct the subjects.

A real-time feedback bar is shown to the subject for precise control of the EMG amplitude (as shown in Figure 2(b)). The subject should keep the activity of any other muscle than the target one as minimal as possible. For example, when ED is the target muscle, APB and FD should be in the rest state. In each trial, the durations of the ready state, action state, and rest state are 1 s, 40 s, and 5 s, respectively, (as shown in Figure 2(b)). The subject should be prepared in the ready state to reduce onset artifacts in the action state and minimize eye blinks and irrelevant movements during the action state. There are total 6 trials for each hand movements. The subjects should perform four hand movements: finger extension, thumb adduction, finger flexion, and rest.

2.2. EEG and EMG Acquisition.
EEG signals are recorded from 64 scalp positions system using the international 10–20 system (Synamp2, Compumedics Inc., Charlotte, NC, USA) referenced to right mastoid and ground at AFz, and motor cortex related 35 positions are recorded (as shown in Figure 1(a)). EEG signals are filtered by a 1 Hz–200 Hz band-pass filter and sampling frequency is 1000 Hz. Before recording, the reference surface skin is prepared with neuroprep and alcohol to lower the impedance under 5 kΩ with Ag/AgCl electrodes.
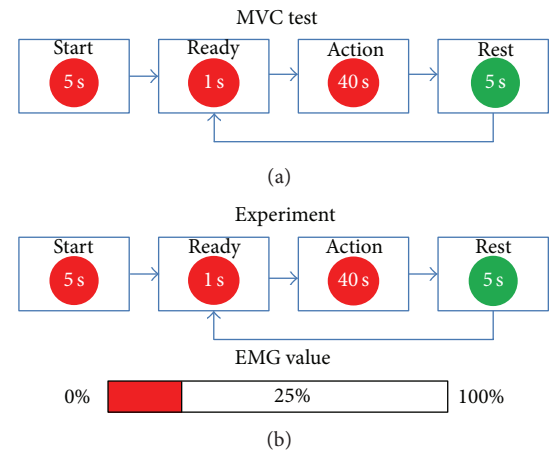
FIGURE 2: (a) The scheme of the MVC test and (b) upper is the scheme of the experiment and bottom is the real feedback bar. The subject is asked to maintain 25% EMG_{max}.

EMG signals are recorded by surface electrodes with band-pass filter between 5 and 200 Hz and sampling frequency is 1000 Hz using neuroscan Synamp2 EMG acquisition. The Ag/AgCl electrodes are applied on three surface muscles (ED, APB, and FD) with using electrical stimulation which fixed the position. The distance between a pair of electrodes is 5 cm in ED and FD muscles, 1 cm in APB muscle. All electrode impedances are kept under 5 kΩ.

2.3. Signal Analysis. EOG is recorded in EEG and EMG acquisition at the same time to remove signals contaminated with eye movement. After removing artifacts and EOG in the EEG and EMG signals trial by trial, we partition the EEG and EMG signals into nonoverlapping segments of 1024 ms, which has a frequency resolution of 0.976 Hz. There are 150–190 seconds of available data collected for all subjects. Here we adopt uniformly 150 segments to estimate CMC value over the whole frequency range. Coherence spectrum is calculated with a fast Fourier transform algorithm:

$$C(f, \text{ch}) = \frac{C_{xy}(f, \text{ch})}{C_{xx}(f, \text{ch}) C_{yy}(f, \text{ch})}, \tag{2}$$

where f is frequency and ch is channel. $C_{xy}(f, \text{ch})$ is cross-spectrum of EEG and EMG, and $C_{xx}(f, \text{ch})$ and $C_{yy}(f, \text{ch})$ are autospectrum of EEG and EMG signal, respectively. Therefore, CMC is function of frequency and channel. The confidence level is calculated in

$$\text{CL}_{\partial} = 1 - (1 - \partial)^{1/(N-1)}, \tag{3}$$

where α is confidence level, N is the number of segments. (α is 95% in our study and correspondence to P value is 0.05; N is 150 in our study.) CL represents the confidential limit. If the value is above CL, the coherence is considered to be significant.

In order to classify finger extension from thumb adduction, finger flexion, and rest, we explore the spatial and temporal distribution of CMC on ED muscle and EMG signals during the above-mentioned hand movements, which refers to channel and frequency respectively. For simple expression, here we define a few abbreviations below.

$\text{CMC}_{\text{FE\_max}}$ = ED muscle CMC peak value in finger extension movement. "FE" represents finger extension.

$\text{CMC}_{\text{TA\_max}}$ = ED muscle CMC peak value in thumb adduction movement. "TA" represents thumb adduction.

$\text{CMC}_{\text{FF\_max}}$ = ED muscle CMC peak value in finger flexion movement. "FF" represents finger flexion.

$\text{CMC}_{\text{REST\_max}}$ = ED muscle CMC peak value in rest.

$F_{\text{FE\_max}}$ = the frequency which reaches $\text{CMC}_{\text{FE\_max}}$.

$\text{Ch}_{\text{FE\_max}}$ = the channel which provides $\text{CMC}_{\text{FE\_max}}$.

We first compare the maximal CMC value of ED muscle ($\text{CMC}_{\text{FE\_max}}$ versus $\text{CMC}_{\text{TA\_max}}$, and $\text{CMC}_{\text{FE\_max}}$ versus $\text{CMC}_{\text{FF\_max}}$) across the all frequency and all EEG channels to see whether there is a significant difference across subjects in ED CMC peak value in finger extension other than thumb adduction or finger flexion. Next, we then generate the topographical distribution of CMC on the scalp, find out the most related cortical area, which means that the channel is fixed at $\text{Ch}_{\text{FE\_max}}$ and observe the maximal CMC value of ED muscle across the frequency range. t-test is applied to check if there is significant difference across subjects between finger extension and the 3 other movement tasks. Then, we obtain

Table 2: Number of segments for each subject.

Subject	1	2	3	4	5	8	7	8
Number of segments	25	23	25	22	20	25	21	23

the tuning frequency of finger extension ($F_{\text{FE\_max}}$) at the most related EEG channel. t-test is again used to check whether the ED CMC value acquired at $\text{Ch}_{\text{FE\_max}}$ and $F_{\text{FE\_max}}$ has a significant difference across subjects in finger extension from the other two above mentioned movements and rest.

If we could successfully classify the significant coherence of finger extension from other movement tasks, it provides promise to detect voluntary hand opening (versus hand closing) during active therapy. Here we divide signals into 20–30 segments for each subject (as shown in Table 2). The length of the segment is chosen when there is CMC value appeared above the significant value. We calculate CMC value within beta frequency between the collected EMG signals and the most related motor cortical channel. Linear discriminate analysis is applied on the CMC vector (across beta frequency) to calculate the classification accuracy in distinguishing finger extension from thumb adduction, finger extension, and rest for each subject.

3. Results

We first compare the maximal CMC value of ED muscle ($\text{CMC}_{\text{FE\_max}}$ versus $\text{CMC}_{\text{TA\_max}}$ and $\text{CMC}_{\text{FE\_max}}$ versus $\text{CMC}_{\text{FF\_max}}$) across the all frequency, and all EEG channels. With t-test, there is no significant difference in finger extension from thumb adduction and finger flexion in channel, frequency and peak coherence value.

An example of the topographical distribution of ED CMC value in the different actions is shown in Figure 3. At $F_{\text{FE\_max}}$, ED muscle CMC value is more obvious in finger extension and finger flexion than in thumb adduction, and rest. As seen from the Figure 3, the significant ED muscle CMC has overlap in channels on left motor cortex between finger extension with thumb adduction, finger flexion and rest.

We fix the channel at $\text{Ch}_{\text{FE\_max}}$ and observe the CMC value across frequencies. We calculate the maximal ED muscle CMC value of four movement tasks across frequencies at $\text{Ch}_{\text{FE\_max}}$ as shown in Table 3. With t-test, there is no significant difference between finger extension and finger flexion in ED CMC value. And there is no significant difference in finger extension from thumb adduction, finger flexion, and rest in frequency. But there is a significant difference at ED CMC value in finger extension from thumb adduction and rest; the P values are 0.0102 and 0.0161, respectively, at $\alpha = 0.05$.

Figure 4 shows an example of the distribution of ED CMC collected on $\text{Ch}_{\text{FE\_max}}$ across beta frequency range for 4 different movement tasks. We can see that the ED CMC peak value appears at different frequencies for four movement tasks.

Then, we obtain the tuning frequency of finger extension ($F_{\text{FE\_max}}$) at the most related EEG channel. The ED CMC values acquired at $\text{Ch}_{\text{FE\_max}}$ and $F_{\text{FE\_max}}$ for four movement
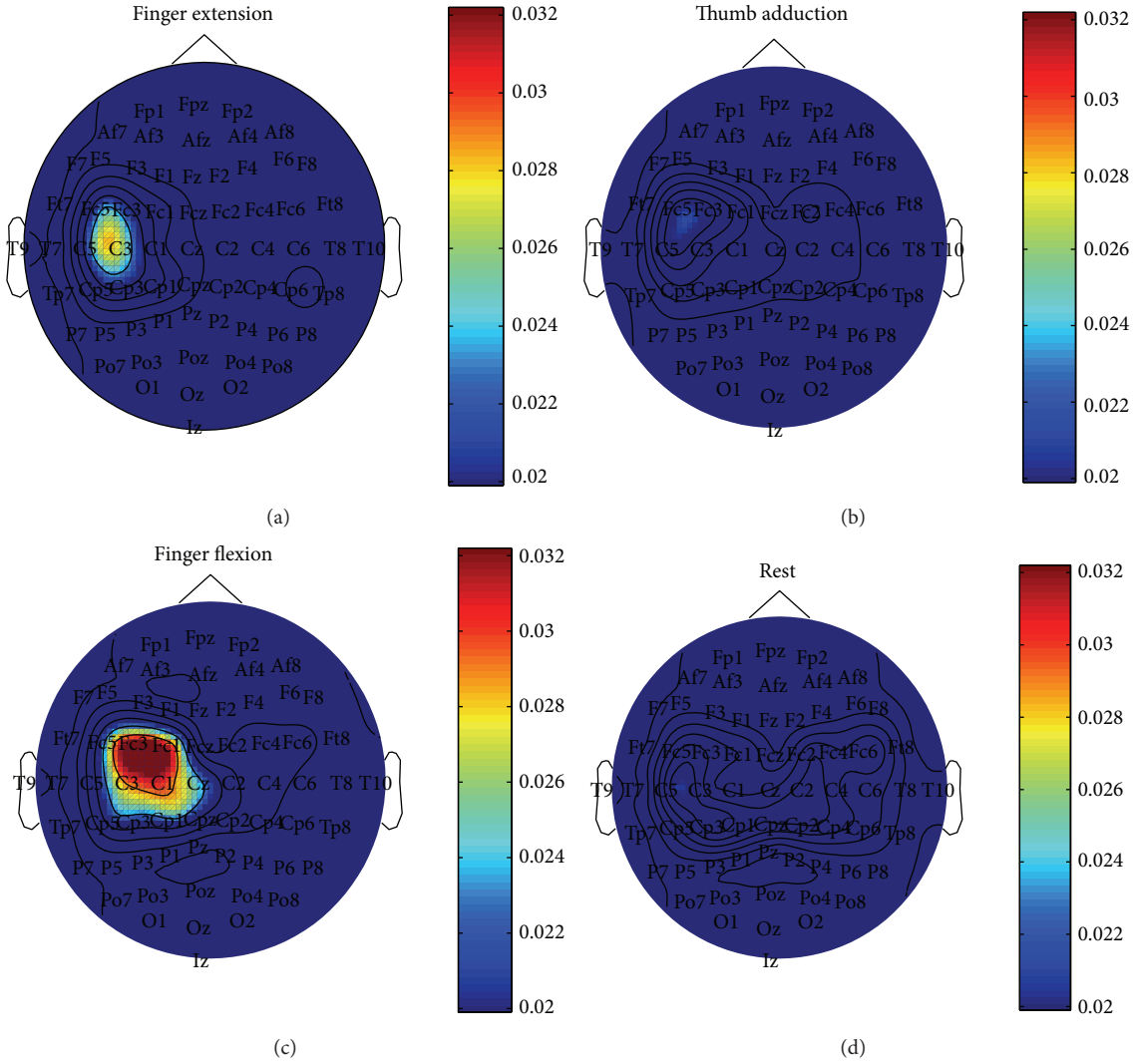
(a)

(b)

(c)

(d)

FIGURE 3: The topographical distribution of ED muscle CMC value on finger extension, thumb adduction, finger flexion, and rest. The significant ED muscle CMC has overlap in these mentioned movements around C3. The significant value was 0.0199, and the color bar was corresponding to CMC value bar. The peak coherence position and frequency are 15 and 20.51 Hz, respectively, in finger extension. The peak coherence position and frequency are 2 and 15.1367 Hz, respectively, in thumb adduction. The peak coherence position and frequency are 9 and 26.37 Hz, respectively, in finger flexion.

tasks that are shown in Table 4. The result of t-test shows there is significant difference across subjects in finger extension from the other three movements in ED muscle CMC value with the P values are 0.000000205, 0.000089, and 0.00012 respectively at $\alpha = 0.05$ (as shown in Table 4). It is obvious to linearly classify ED CMC in finger extension from other two movements and rest (as shown in Figure 5).

Without too finely tuning on the frequency, we calculated CMC value within beta frequency between the collected EMG signals and the most related motor cortical channel. Linear discriminate analysis is applied on the CMC vector (across beta frequency) to classify finger extension from thumb adduction, finger extension, and rest for each subject. Fourfold cross-validation is adopted in LDA analysis. To show the superiority of our method, the classification results by CMC are compared with EEG in this study. This is because in healthy subject, finger extension could be easily

classified from thumb adduction, finger extension and rest. But it is difficult in stroke patient due to abnormal coactive muscle and spasticity [22]. Study has shown that the average classification accuracy was 71.6% in moderately impaired subjects and only 37.9% in severely impaired subjects [22]. The voluntary intention extract from such signals may not be reliable. Therefore, good classification results by EMG do not necessarily result in good performance in patients. Here we classify finger extension from thumb adduction, finger flexion, and rest using CMC and by EEG only at the same channels (as shown in Figure 6).

The average accuracies across subjects by CMC are 78.96 ± 4.29%, 81.00 ± 7.34%, and 78.025 ± 9.39%, respectively, to distinguish finger extension from thumb adduction, finger flexion, and rest (see Table 5). It indicates the possibility to detect voluntary hand opening (versus hand closing) based on coherence analysis between EMG signal on one single
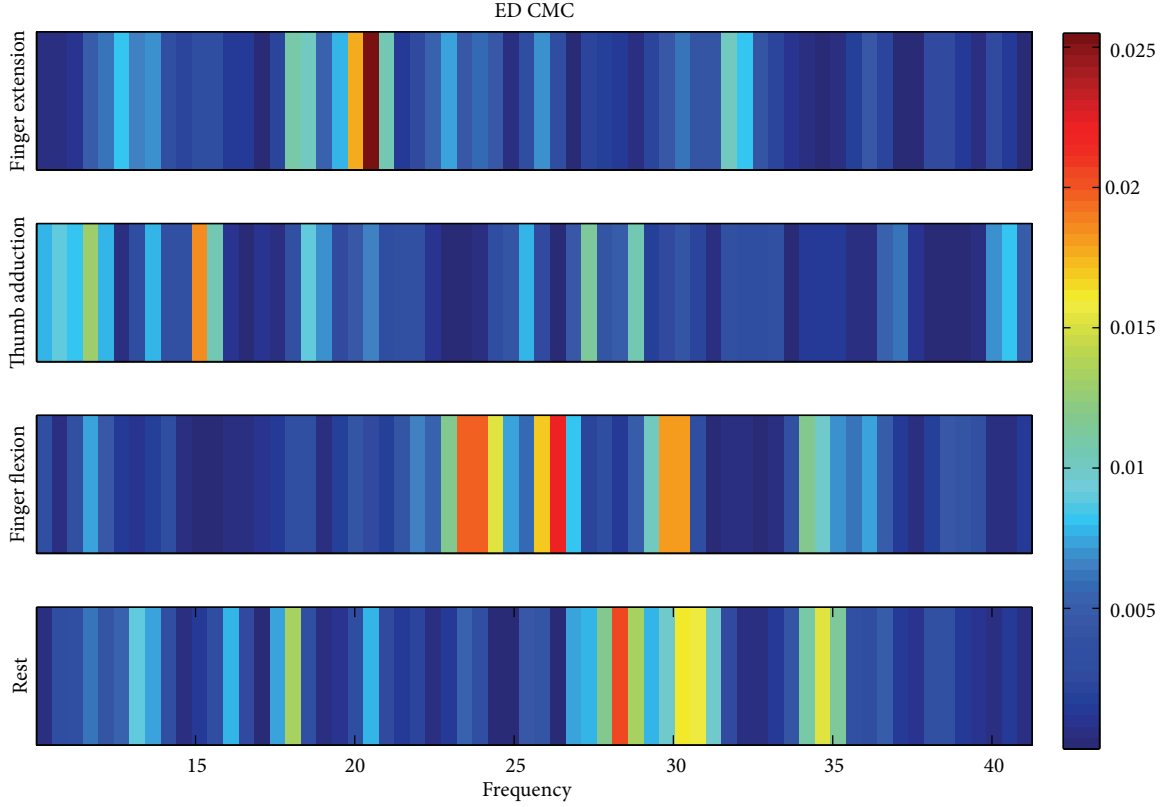
FIGURE 4: *Subject 3*. ED muscle CMC exists in finger extension, thumb adduction, finger flexion, and rest with peak appearing at different four hand movement tasks. ED muscle CMC peak value is in 20.51 Hz, 15.14 Hz, 26.37 Hz and 28.32 Hz for finger extension, thumb adduction, finger flexion, and rest, respectively.

muscle and one EEG channel located on motor cortical area. The average accuracies by EEG across subjects are 71.27 ± 12.32%, 71.12 ± 12.80%, and 81.39 ± 11.52%, respectively, (see Table 5). CMC classification accuracy is around 10% higher in average and less variance than EEG classification in thumb adduction and finger flexion, which is the main function (hand opening) we focused on for hand rehabilitation. The classification results on finger extension versus rest by CMC and EEG are similar (less average and less variance), which matches the good performance by EEG to distinguish movement from rest [39].

Furthermore, we do the 3-class classification (finger extension versus thumb adduction versus finger flexion) to extract finger extension. The best two subjects' accuracies by CMC are 75.80% and 79.56%. The mean accuracy of the 8 patients by CMC is 69%, which is greater than 64% by EEG.

4. Discussion and Conclusion

Active rehabilitation involves patients' voluntary movement intention. It is effective to restore stroke patient' motor function, such as hand opening (one of the most challenge movements) [23, 24]. In this study, we focus on finger extension, which is mainly involved in hand opening. EMG could be easily to extract such intention, while it is not reliable to extract such intention due to the abnormal coactive

muscles and spasticity in stroke patient [22]. EEG can be used to interpret patient movement intentions, but it is not good enough to distinguish ipsilateral hand movements [28–31]. Cortico-muscular coherence exists between EEG and EMG even on the abnormal muscle when stroke patient's intention appears [40]. We propose to analyze cortico-muscular coherence between EMG and EEG signals to distinguish voluntary ipsilateral hand opening, hand closing, and rest state. The EMG signals of Extensor Digitorum (ED) muscle and EEG signals are simultaneously collected when 8 subjects are instructed to voluntarily execute right finger extension, thumb adduction and finger flexion, and rest. We observe significant cortico-muscular coherence appearing at the left motor cortical area of the EEG channels, which is consistent with findings in Mima and Hallett's study [36] and shows different patterns within beta frequency range for 4 different executions. Statistical *t*-test shows that the coherence values of finger extension collected at tuning frequency and the most related channel are statically different from 3 other states, respectively, across all subjects. We apply linear discriminate analysis on the coherence pattern within beta range and average accuracy to distinguish finger extension state from thumb adduction, finger flexion, and rest. CMC classification accuracy is around 10% higher in average and less variance than the performance using EEG only in distinguishing finger extension from thumb adduction and finger flexion,
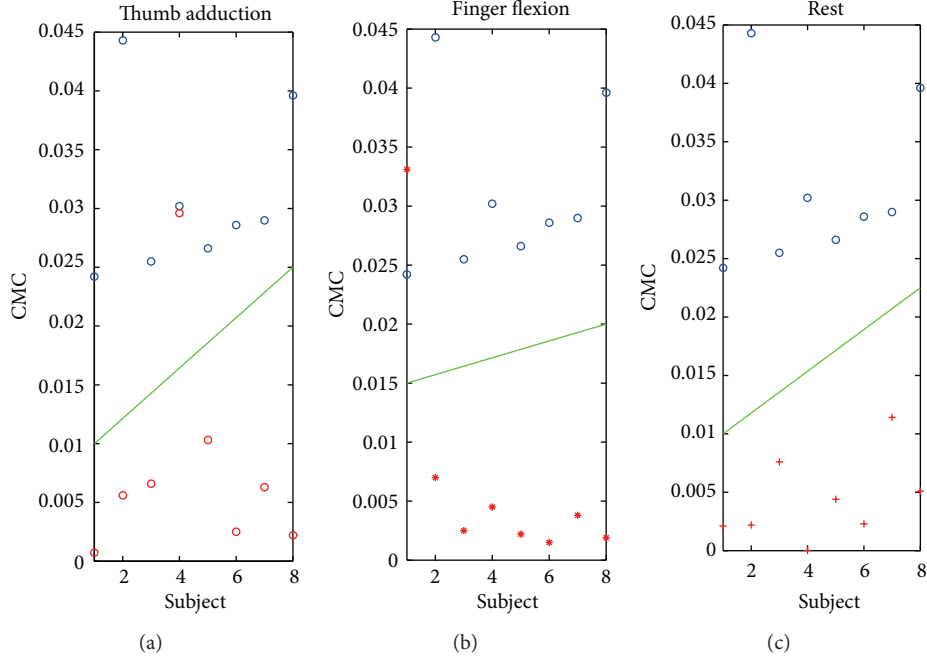
FIGURE 5: ED muscle CMC values at Ch_{FE_max} and F_{FE_max} in finger extension could be classified from thumb adduction, finger flexion, and rest. Finger extension versus thumb adduction (a). Finger extension versus finger flexion (b). Finger extension versus rest (c). Blue circle is ED muscle CMC values in finger extension. Red circle is ED muscle CMC value in thumb adduction. Red asterisk is ED muscle CMC value in finger flexion. Red cross is ED muscle CMC value in rest. Green l line distinctly classified ED EMC in finger extension from thumb adduction, finger flexion, and rest.

TABLE 3: ED muscle CMC on four movements at Ch_{FE_max} (Ch is channel).

Subject	Ch	Finger extension		Thumb adduction		Finger flexion		Rest	
		Peak CMC	Frequency (Hz)	Peak* CMC	Frequency (Hz)	Peak CMC	Frequency (Hz)	Peak* CMC	Frequency (Hz)
1	24	0.0242	35.64	0.0234	35.64	0.0377	35.16	0.0185	17.09
2	9	0.0443	15.63	0.0207	37.10	0.0356	30.27	0.0192	41.02
3	15	0.0255	20.51	0.0187	15.13	0.0222	26.37	0.0204	28.32
4	2	0.0302	12.70	0.0296	12.70	0.0346	10.25	0.0300	33.20
5	9	0.0266	36.62	0.0221	33.69	0.0128	12.70	0.0248	29.97
6	24	0.0286	13.18	0.0243	10.25	0.019	25.88	0.0255	30.76
7	16	0.029	37.60	0.0172	13.18	0.0116	32.23	0.0207	40.53
8	24	0.0396	21.00	0.024	13.67	0.0273	31.25	0.0211	10.25
Mean	/	0.031	24.11	0.0225	21.42	0.0251	25.51	0.0225	29.89
SD	/	0.0071	10.80	0.0038	11.75	0.0103	9.19	0.0039	10.64

*Represents that there is significant difference compared with finger extension. The ED CMC value compared in finger extension from thumb adduction and rest is significant and the P values are 0.0102 and 0.0161, respectively, at $\alpha = 0.05$.

which is the main function (hand opening) we focused on for hand rehabilitation. The classification results on finger extension versus rest by CMC and EEG are similar (less average but less variance), which matches the results that EEG can be used to distinguish movement from rest [39]. Furthermore, the classification results on finger extension out of 3 classes (finger extension versus thumb adduction versus finger flexion) by CMC are also greater than the performance by EEG only.

The results indicate the possibility to detect voluntary hand opening based on coherence analysis between one single muscle EMG signal and one EEG channel located on motor cortical area. One of the challenges is to accurately capture the instantaneous CMC value in real-time recoding. In the real application, EEG and EMC signals can be recorded from the patients at the same time. The significant coherence (CMC) value can be estimated to better classify the voluntary finger extension than EEG only and used as a more accurate

TABLE 4: ED muscle CMC value in four movements at Ch_{FE_max} and F_{FE_max}.

Subject	Channel	Frequency (Hz)	Finger extension Peak*	Thumb adduction Peak*	Finger flexion Peak*	Rest Peak*
1	24	35.64	0.0242	0.000736	0.0331	0.0021
2	9	15.63	0.0443	0.0056	0.007	0.0022
3	15	20.51	0.0255	0.0066	0.0025	0.0076
4	2	12.70	0.0302	0.0296	0.0045	0.000017
5	9	36.62	0.0266	0.0103	0.0022	0.0044
6	24	13.18	0.0286	0.0025	0.0015	0.0023
7	16	37.60	0.029	0.0063	0.0038	0.0114
8	24	21.00	0.0396	0.0022	0.0019	0.0051
Mean	/	24.11	0.0310	0.0080	0.0071	0.0044
SD	/	10.79	0.0071	0.0093	0.0107	0.0037

*represents that there is significant difference compared with finger extension. The P values are 0.000000205, 0.000089, and 0.00012, respectively, at $\alpha = 0.05$.
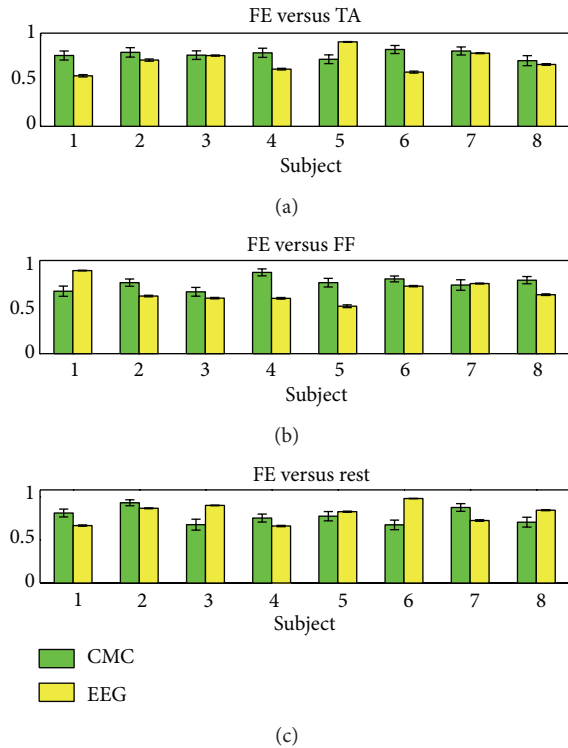

FIGURE 6: Classification accuracies are shown in the figure to distinguish finger extension from thumb adduction (a), finger flexion (b), and rest (c). FE, TA, FF are finger extension, thumb adduction and finger flexion, respectively. Green represents classification based on CMC and yellow represents classification based on EEG. The average accuracies by CMC and EEG are shown in Table 5.

TABLE 5: Average accuracies of CMC and EEG classification.

	FE versus TA	FE versus FF	FE versus REST
CMC	78.96 ± 4.29%	81.00 ± 7.34%	78.025 ± 9.39%
EEG	71.27 ± 12.32%	71.12 ± 12.80%	81.39 ± 11.52%

control signal to evoke the electrical stimulation in active rehabilitation for hand movement. With further experiments on stroke patients, CMC needs to be compared with EMG on abnormal muscles to classify the hand movement. It will eventually help develop a new rehabilitation protocol that can benefit the hand rehabilitation for stroke survivors.

Acknowledgments

References

[1] WHO, "The Atlas of Heart Disease and Stroke," http://www.who.int/cardiovascular_diseases/resources/atlas/en/.

[2] WHO, "The global burden of disease: 2004 update," http://www.who.int/healthinfo/global_burden_disease/2004_report_update/en/index.html.

[3] "Stroke Information Page: National Institute of Neurological Disorders and Stroke (NINDS)," http://www.ninds.nih.gov/disorders/stroke/stroke.htm#What_is_the_prognosis.

[4] S. J. Boniface, "Plasticity after acute ischaemic stroke studied by transcranial magnetic stimulation," *Journal of Neurology Neurosurgery and Psychiatry*, vol. 71, no. 6, pp. 713–715, 2001.

[5] R. J. Nudo, B. M. Wise, F. SiFuentes, and G. W. Milliken, "Neural substrates for the effects of rehabilitative training on motor recovery after ischemic infarct," *Science*, vol. 272, no. 5269, pp. 1791–1794, 1996.

[6] J. Liepert, I. Uhde, S. Gräf, O. Leidner, and C. Weiller, "Motor cortex plasticity during forced-use therapy in stroke patients: a preliminary study," *Journal of Neurology*, vol. 248, no. 4, pp. 315–321, 2001.

[7] J. Liepert, W. H. R. Miltner, H. Bauder et al., "Motor cortex plasticity during constraint,induced movement therapy in stroke patients," *Neuroscience Letters*, vol. 250, no. 1, pp. 5–8, 1998.

[8] R. Pineiro, S. Pendlebury, H. Johansen-Berg, and P. M. Matthews, "Functional MRI detects posterior shifts in primary sensorimotor cortex activation after stroke: evidence of local adaptive reorganization?" *Stroke*, vol. 32, no. 5, pp. 1134–1139, 2001.

[9] C. Calautti, F. Leroy, J. Y. Guincestre, and J. C. Baron, "Displacement of primary sensorimotor cortex activation after subcortical stroke: a longitudinal PET study with clinical correlation," *NeuroImage*, vol. 19, no. 4, pp. 1650–1654, 2003.

[10] T. Platz, S. Van Kaick, L. Möller, S. Freund, T. Winter, and I. H. Kim, "Impairment-oriented training and adaptive motor cortex reorganisation after stroke: a fTMS study," *Journal of Neurology*, vol. 252, no. 11, pp. 1363–1371, 2005.

[11] M. Glanz, S. Klawansky, W. Stason, C. Berkey, and T. C. Chalmers, "Functional electrostimulation in poststroke rehabilitation: a meta-analysis of the randomized controlled trials," *Archives of Physical Medicine and Rehabilitation*, vol. 77, no. 6, pp. 549–553, 1996.

[12] W. T. Liberson, H. J. Holmquest, D. Scot, and M. Dow, "Functional electrotherapy: stimulation of the peroneal nerve synchronized with the swing phase of the gait of hemiplegic patients," *Archives of Physical Medicine and Rehabilitation*, vol. 42, pp. 101–105, 1961.

[13] H. Igo Krebs, N. Hogan, M. L. Aisen, and B. T. Volpe, "Robot-aided neurorehabilitation," *IEEE Transactions on Rehabilitation Engineering*, vol. 6, no. 1, pp. 75–87, 1998.

[14] M. L. Aisen, H. I. Krebs, N. Hogan, F. McDowell, and B. T. Volpe, "The effect of robot-assisted therapy and rehabilitative training on motor recovery following stroke," *Archives of Neurology*, vol. 54, no. 4, pp. 443–446, 1997.

[15] S. L. Wolf, C. J. Winstein, J. P. Miller et al., "Effect of constraint-induced movement therapy on upper extremity function 3 to 9 months after stroke: the EXCITE randomized clinical trial," *Journal of the American Medical Association*, vol. 296, no. 17, pp. 2095–2104, 2006.

[16] P. L. Jackson, M. F. Lafleur, F. Malouin, C. Richards, and J. Doyon, "Potential role of mental practice using motor imagery in neurologic rehabilitation," *Archives of Physical Medicine and Rehabilitation*, vol. 82, no. 8, pp. 1133–1141, 2001.

[17] S. Hesse, C. Bertelt, M. T. Jahnke et al., "Treadmill training with partial body weight support compared with physiotherapy in nonambulatory hemiparetic patients," *Stroke*, vol. 26, no. 6, pp. 976–981, 1995.

[18] D. Graupe, "EMG pattern analysis for patient-responsive control of FES in paraplegics for walker-supported walking," *IEEE Transactions on Biomedical Engineering*, vol. 36, no. 7, pp. 711–719, 1989.

[19] S. Saxena, S. Nikolic, and D. Popovic, "An EMG-controlled grasping system for tetraplegics," *Journal of Rehabilitation Research and Development*, vol. 32, no. 1, pp. 17–24, 1995.

[20] R. Thorsen, R. Spadone, and M. Ferrarin, "A pilot study of myoelectrically controlled FES of upper extremity," *IEEE Transactions on Neural Systems and Rehabilitation Engineering*, vol. 9, no. 2, pp. 161–168, 2001.

[21] G. Pfurtscheller and C. Neuper, "Motor imagery direct communication," *Proceedings of the IEEE*, vol. 89, no. 7, pp. 1123–1134, 2001.

[22] S. W. Lee, K. M. Wilson, B. A. Lock, and D. G. Kamper, "Subject-specific myoelectric pattern classification of functional hand movements for stroke survivors," *IEEE Transactions on Neural Systems and Rehabilitation Engineering*, vol. 19, no. 5, Article ID 5585779, pp. 558–566, 2011.

[23] S. M. Lai, S. Studenski, P. W. Duncan, and S. Perera, "Persisting consequences of stroke measured by the stroke impact scale," *Stroke*, vol. 33, no. 7, pp. 1840–1844, 2002.

[24] D. G. Kamper, R. L. Harvey, S. Suresh, and W. Z. Rymer, "Relative contributions of neural mechanisms versus muscle mechanics in promoting finger extension deficits following stroke," *Muscle and Nerve*, vol. 28, no. 3, pp. 309–318, 2003.

[25] F. H. Y. Chan, Y. S. Yang, F. K. Lam, Y. T. Zhang, and P. A. Parker, "Fuzzy EMG classification for prosthesis control," *IEEE Transactions on Rehabilitation Engineering*, vol. 8, no. 3, pp. 305–311, 2000.

[26] J. U. Chu, I. Moon, and M. S. Mun, "A real-time EMG pattern recognition system based on linear-nonlinear feature projection for a multifunction myoelectric hand," *IEEE Transactions on Biomedical Engineering*, vol. 53, no. 11, pp. 2232–2239, 2006.

[27] K. Englehart, B. Hudgins, P. A. Parker, and M. Stevenson, "Classification of the myoelectric signal using time-frequency based representations," *Medical Engineering and Physics*, vol. 21, no. 6-7, pp. 431–438, 1999.

[28] B. Kamousi, Z. Liu, and B. He, "Classification of motor imagery tasks for brain-computer interface applications by means of two equivalent dipoles analysis," *IEEE Transactions on Neural Systems and Rehabilitation Engineering*, vol. 13, no. 2, pp. 166–171, 2005.

[29] T. Wang, J. Deng, and B. He, "Classifying EEG-based motor imagery tasks by means of time-frequency synthesized spatial patterns," *Clinical Neurophysiology*, vol. 115, no. 12, pp. 2744–2753, 2004.

[30] G. Pfurtscheller, C. Neuper, D. Flotzinger, and M. Pregenzer, "EEG-based discrimination between imagination of right and left hand movement," *Electroencephalography and Clinical Neurophysiology*, vol. 103, no. 6, pp. 642–651, 1997.

[31] C. Guger, S. Daban, E. Sellers et al., "How many people are able to control a P300-based brain-computer interface (BCI)?" *Neuroscience Letters*, vol. 462, no. 1, pp. 94–98, 2009.

[32] T. Mima, T. Matsuoka, and M. Hallett, "Information flow from the sensorimotor cortex to muscle in humans," *Clinical Neurophysiology*, vol. 112, no. 1, pp. 122–126, 2001.

[33] B. A. Conway, D. M. Halliday, S. F. Farmer et al., "Synchronization between motor cortex and spinal motoneuronal pool during the performance of a maintained motor task in man," *Journal of Physiology*, vol. 489, no. 3, pp. 917–924, 1995.

[34] T. Mima and M. Hallett, "Corticomuscular coherence: a review," *Journal of Clinical Neurophysiology*, vol. 16, no. 6, pp. 501–511, 1999.

[35] T. Mima and M. Hallett, "Electroencephalographic analysis of cortico-muscular coherence: reference effect, volume conduction and generator mechanism," *Clinical Neurophysiology*, vol. 110, no. 11, pp. 1892–1899, 1999.

[36] T. Mima, J. Steger, A. E. Schulman, C. Gerloff, and M. Hallett, "Electroencephalographic measurement of motor cortex control of muscle activity in humans," *Clinical Neurophysiology*, vol. 111, no. 2, pp. 326–337, 2000.

[37] R. C. Oldfield, "The assessment and analysis of handedness: the Edinburgh inventory," *Neuropsychologia*, vol. 9, no. 1, pp. 97–113, 1971.

[38] P. Konrad, "The abc of emg," *A Practical Introduction o Kinesiological*, pp. 1–60, 2005.

[39] G. Pfurtscheller, "Event-related synchronization (ERS): an electrophysiological correlate of cortical areas at rest," *Electroencephalography and Clinical Neurophysiology*, vol. 83, no. 1, pp. 62–69, 1992.

[40] T. Mima, K. Toma, B. Koshy, and M. Hallett, "Coherence between cortical and muscular activities after subcortical stroke," *Stroke*, vol. 32, no. 11, pp. 2597–2601, 2001.

Research Article

Continuous- and Discrete-Time Stimulus Sequences for High Stimulus Rate Paradigm in Evoked Potential Studies

Tao Wang, Jiang-hua Huang, Lin Lin, and Chang'an A. Zhan

School of Biomedical Engineering, Southern Medical University, Guangzhou, Guangdong 510515, China

Correspondence should be addressed to Chang'an A. Zhan; changan.zhan@gmail.com

To obtain reliable transient auditory evoked potentials (AEPs) from EEGs recorded using high stimulus rate (HSR) paradigm, it is critical to design the stimulus sequences of appropriate frequency properties. Traditionally, the individual stimulus events in a stimulus sequence occur only at discrete time points dependent on the sampling frequency of the recording system and the duration of stimulus sequence. This dependency likely causes the implementation of suboptimal stimulus sequences, sacrificing the reliability of resulting AEPs. In this paper, we explicate the use of continuous-time stimulus sequence for HSR paradigm, which is independent of the discrete electroencephalogram (EEG) recording system. We employ simulation studies to examine the applicability of the continuous-time stimulus sequences and the impacts of sampling frequency on AEPs in traditional studies using discrete-time design. Results from these studies show that the continuous-time sequences can offer better frequency properties and improve the reliability of recovered AEPs. Furthermore, we find that the errors in the recovered AEPs depend critically on the sampling frequencies of experimental systems, and their relationship can be fitted using a reciprocal function. As such, our study contributes to the literature by demonstrating the applicability and advantages of continuous-time stimulus sequences for HSR paradigm and by revealing the relationship between the reliability of AEPs and sampling frequencies of the experimental systems when discrete-time stimulus sequences are used in traditional manner for the HSR paradigm.

1. Introduction

In studying the auditory evoked potentials (AEPs), high stimulus-rate (HSR) paradigm featuring shorter and irregular interstimulus intervals (ISIs) has been proposed by Delgado and Özdamar [1] and applied to various investigations [2–4]. The specific technique proposed in [1] is generally named as continuous loop average deconvolution (CLAD). For CLAD, the presence of stimulus and silence is, respectively, represented by "1" and "0." As such a stimulus sweep containing multiple stimulus events is described by a binary sequence. A typical sweep contains a number of "1s" and a large number "0s." Due to the fact that the ISIs have to be so short for the HSR paradigm that the brain responses to consecutive stimulus events overlap, this binary sequence that constitutes a sweep of stimulus and the sweep response that contains a number of overlapped transient-responses are transformed into the frequency domain to solve the overlapping problem in order to recover the transient responses (see Section 2.1 for more details). This process is usually termed as deconvolution.

As shown by Jewett et al. [5], any chosen stimulus sweep needs to satisfy the noise attenuation property to avoid distorting transient responses in the deconvolution process. As far as this peroperty is concerned, the ISIs must be irregularly distributed in a sweep rather than a fixed ISI as in the conventional recording paradigm. On the other hand, most practical applications require that such ISI-jitters should be as small as possible so that the linear convolution model is valid [5, 6]. The noise attenuation property, which is a major criterion for judging its appropriateness, can be straightforwardly understood in Fourier domain (for details, please see (1d) and (5) below). The generation of stimulus sequences with the desired property is in essence an optimization problem, which is important and dependent on various factors in practice. Typically, a minimal temporal resolution (i.e., the analogy-to-digital (AD) conversion rate for EEG recording) and the number of stimulus events are

first chosen for the stimulus sweep for a given experiment. Since the stimulus sequence is optimized at given temporal resolution, we term it as discrete-time sequence. The temporal resolution is crucial for finding a good discrete-time stimulus sequence in that the AD rate is supposed to be as high as possible in order to increase the searching space for a sequence optimization method. However, the use of high temporal resolution imposes challenges for the search of optimal sequence. It either makes the optimization prone to local minima issue or increases computational expense when exhaustive searching strategy is used. Another issue is that when it is chosen, the optimal stimulus sequence should be used at the specific AD rate according to the chosen temporal resolution at which the optimal stimulus sequence is established.

In reality, different recording systems may not always be operated at the frequency exactly identical to that chosen for stimulus sweep design. When a recording system works at a different frequency, the timing of the onsets of stimulus events in the discrete-time stimulus sweep is to be resampled. It is unclear about the impacts of the resampling and actual AD rate on the deconvolution performance. Moreover, many optimization methods can only deal with continuous variables for the convenience of being exposed to certain mathematic operations [7, 8]. In this case, the optimal timing of stimulus events is a continuous variable, and we term the stimulus sweep as the continuous-time stimulus sequence, which need to be discretized in time domain to be used in actual experiments. The temporal resolution of the discretization is also determined by the AD rate for the actual application. As such, it is important to understand how the AD rate influences the performance of HSR paradigm no matter a resampling or discretization of optimal stimulus sequence is necessary.

To address these critical questions, in this paper, we derived the frequency representation of a continuous-time impulse sequence to solve the deconvolution problem for the HSR paradigm. Using simulated EEGs (based on real AEP data and simulated noises) and four optimized continuous-time stimulus sequences, we demonstrate the applicability and the advantages of continuous-time stimulus sequences for HSR paradigm. We also illustrate the relationship between the AD rate for discretizing a continuous-time sequence and the errors in terms of temporal locations of stimulus impulse, frequency properties of discretized stimulus sequence, and the deconvolved AEP as compared to the ground truth AEP.

2. The Convolution Model for HSR Paradigm

2.1. Discrete-Time Convolution.
Under discrete HSR condition, the observed sweep-response $y[n\Delta_t]$ can be modeled as a circulant discrete convolution between the binary stimulus sequence $s[n\Delta_t]$ and a transient response $x[n\Delta_t]$, that is,

$$
\begin{aligned}
y[n\Delta_t] &= s[n\Delta_t] \otimes x[n\Delta_t] + e[n\Delta_t] \\
&= \sum_{i=1}^{N} (s[n\Delta_t - i] \bmod N) x[n\Delta_t] + e[n\Delta_t],
\end{aligned}
\tag{1a}
$$

where $\otimes$ denotes circulant convolution; $e[n\Delta_t]$ represents an additive noise term for any undesired contribution to $y[n\Delta_t]$; Δ_t is the interval between two discrete samples, or in other word, the reciprocal of the analogue-to-digital (AD) rate f_s (i.e., $\Delta_t = 1/f_s$); N is the number of discrete samples for the duration of a stimulus sweep.

Note that the circulant convolution is adopted in (1a). This is because the stimulus sequence $s[n\Delta_t]$ is delivered to the subject repetitively in the HSR paradigm. As such, $y[n\Delta_t]$, $x[n\Delta_t]$, and $e[n\Delta_t]$ are of the same length N, or the same time duration $T = N/f_s$. In practice, the recorded raw electroencephalograms (EEGs) are epoched according to the stimulus sweep rather than to individual stimulus impulse (each stimulus sweep contains a number of stimulus impulses depending on the particular experiment design), and averaged over a number of sweeps to attenuate the noise level. Equation (1a) is usually referred to the case after averaging.

Equation (1a) can be represented in Fourier domain as

$$
Y[jmf_0] = S[jmf_0]X[jmf_0] + E[jmf_0], \tag{1b}
$$

where $f_0 = 1/T$ and the capital letters correspond to the discrete Fourier transforms of their counterparts (e.g., $X[jmf_0]$ denotes the discrete Fourier transform of $x[n\Delta_t]$),

$$
\begin{aligned}
X[jmf_0] &= \sum_{i=1}^{N} x[n\Delta_t] + e^{-j(2\pi/N)mn}, \\
m &= 1, 2, \ldots, N.
\end{aligned}
\tag{1c}
$$

From (1b) one can solve the transient response $x[n\Delta_t]$ in the frequency domain (i.e., $X[jmf_0]$) in a straightforward way using an inverse filter as done by the CLAD [1]. Consider

$$
\begin{aligned}
\widehat{X}[jmf_0] &= \frac{Y[jmf_0]}{S[jmf_0]} + \frac{E[jmf_0]}{S[jmf_0]} \\
&= X[jmf_0] + \frac{E[jmf_0]S^*[jmf_0]}{|S[jmf_0]|}.
\end{aligned}
\tag{1d}
$$

Based on (1d), it is obvious that distortion of the solution $X[jmf_0]$ can happen at some frequency bins where $|S[jmf_0]|$ approaches to zeros, since small $|S[jmf_0]|$ can amplify the noise components $E[jmf_0]$.

To address this issue, Jewett et al. [5] propose a scheme to examine the values of $|S[jmf_0]|$ within the frequency band of interest and make sure that these values are larger than a preset threshold. In a following study, Jewett et al. [7] offered a number of binary stimulus sequences according to this criterion.

2.2. Continuous-Time Convolution.
Knowing the frequency property of a stimulus sequence can assist the assessment of the noise attenuation performance of the inverse filter for the deconvolution problem [8]. Early studies such as those by Jewett et al. [5, 7] guiding the selection of appropriate stimulus sequences have made the HSR scheme practical for actual applications and thus significantly contributed to

the development of HSR paradigms. However, the optimal stimulus sequences used in the literature [7] so far are AD rate dependent and thus not generalizable due to the need of resampling when the actual AD rate differs from that used for stimulus sequence optimization. As such, there are two major drawbacks in optimizing the stimulus sequences in discrete form. First, the optimized sequence may not be optimal if the sequence is resampled with a different rate. This means that it is impossible to generate a sequence for general use; instead, optimization algorithm is to be employed to generate a good sequence according to the AD rate for each given experiment. Second, optimization in discrete form makes it hard to know how the AD rates influence the performance of an optimized sequence.

In this section, we derive the continuous-time convolution relationship between the stimulus sequence and transient response, and the estimation of transient response in a general form.

Similar to the $y[n\Delta_t]$ in (1a), the observable EEG sweep $y(t)$ can be represented as the circulant convolution between transient response $x(t)$ and stimulus $s(t)$, with error term $e(t)$:

$$y(t) = s(t) \otimes x(t) + e(t)$$
$$= \int_0^T s(\tau) x(t - \tau) \bmod T d\tau + e(t), \quad t \in [0, T]. \tag{2}$$

Since all the variables (except the error term $e(t)$) in (2) can be considered as periodical functions (with a period of T) due to the repetitive stimulation manner, the key difference here from (1a) is that the stimulus events in $s(t)$ can happen at any time point t within the period T, rather than the discrete time points determined by the AD rate. The Fourier transform of such signals as $x(t)$ is in discrete form:

$$F[x(t)] = X(jkf_0) = \int_0^T x(t) e^{-j2\pi kf_0} dt, \tag{3}$$

where $F[\cdot]$ denotes Fourier transform operator, and $f_0 = 1/T$ represents the repetition rate of the stimulus sweep and thus the discrete frequency resolution for signals (e.g., X in (3)) to be presented in Fourier domain. We can rewrite (2) in Fourier domain:

$$Y(jkf_0) = S(jkf_0) X(jkf_0) + E(jkf_0). \tag{4}$$

The transient response $x(t)$ can be estimated in Fourier domain as

$$\widehat{X}(jkf_0) = \frac{Y(jkf_0)}{S(jkf_0)} + \frac{E(jkf_0)}{S(jkf_0)}$$
$$= X(jkf_0) + \frac{E(jkf_0) S^*(jkf_0)}{|S(jkf_0)|}. \tag{5}$$

Distortion of the estimated transient response is introduced in the second term of the right hand side of (5). The noise term $E(jkf_0)$ is to be amplified by the inverse filter $S(jkf_0)^{-1}$ at some frequency bins where $|S(jkf_0)^{-1}|$ is small. As such, it is critical to study in detail the properties of the inverse filter $S(jkf_0)^{-1}$ and we will do so in Section 2.3.

Equation (5) shows that as far as these continuous periodical signals are concerned, the error term's contribution to the estimation of $x(t)$ depends only on f_0 but not the AD rate f_s as in (1d). Note that the frequency range of the solution can be infinite in theory, but in practice, the energy of transient signal $x(t)$ is bounded within a relatively narrow frequency band of interest and only the continuous-time stimulus sequences can be of unlimited frequency range, which is to be detailed below.

2.3. The Properties of Continuous-Time Stimulus Sequence. A stimulus sequence $s(t)$ for one experiment sweep can be described as a P impulses train. We use delta functions of delay $t_p (p = 1, 2, \ldots, P)$ to represent the occurrence of stimulus impulses and their summation to represent the stimulus sweep:

$$s(t) = \sum_{p=1}^P \delta(t - t_p). \tag{6}$$

In this continuous-time form of stimulus sequence, the t_p is a continuous variable, that is, $t_p \in [0, T]$. Figure 1(a) shows an example sweep with stimulus impulses occurring at 17 time points. The Fourier transform of (6) is

$$F[s(t)] = S(jf) = \sum_{p=1}^P e^{-j2\pi f t_p}. \tag{7}$$

This is a continuous function in the frequency domain [9]. In a given experiment, the stimulus sweep (Figure 1(a)) is repetitively delivered to the subject to stimulate the brain responses for EEG recording. As such, the whole stimulus sequence (Figure 1(b)) is modeled as a convolution between the impulses train $s(t)$ and a summation of delta functions $\delta_T(t)$:

$$s_T(t) = s(t) * \delta_T(t), \tag{8}$$

where $\delta_T(t)$ is a periodic function with period T defined as

$$\delta_T(t) = \sum_{q=-\infty}^{+\infty} \delta(t - qT). \tag{9}$$

The Fourier transform of (9) is

$$F[\delta_T(t)] = 2\pi f_0 \sum_{k=-\infty}^{\infty} \delta(f - kf_0). \tag{10}$$

Equation (10) shows that the Fourier transform of a periodical delta sequence is also a delta train with the interval of f_0.

Based on (8) and (10), the Fourier transform of the periodical stimulus $s_T(t)$ is

$$S_T(jf) = 2\pi f_0 S(jf) \sum_{k=-\infty}^{+\infty} \delta(f - kf_0). \tag{11}$$

Equation (11) indicates that the spectrum $S_T(jf)$ is a discrete sampling of the continuous function $S(jf)$ in (7) by

the delta function train at the interval of f_0. Plugging $S(jf)$ in (7) into (11), we get

$$S_T(jf) = 2\pi f_0 \sum_{p=1}^{P} \sum_{k=-\infty}^{+\infty} e^{-j2\pi f t_p} \delta(f - kf_0), \quad (12)$$

which can be rewritten as follow given the sampling property of the delta function $\delta(f - kf_0)$:

$$S_T(jkf_0) = 2\pi f_0 \sum_{p=1}^{P} e^{-j2\pi f_0 t_p}. \quad (13)$$

Equation (13) is the Fourier spectrum of the stimulus impulse-sequence, which includes infinite number of frequencies defined by kf_0 since k can be any integer. In real experiment, however, signals and noises are limited within a frequency band, say $[f_L, f_H]$. While f_L and f_H can be of arbitrary real values in theory, we should round off them to the multiples of f_0 in practice, say $[f'_L, f'_H]$, in the discrete frequency domain:

$$[f'_L, f'_H] = [k_L f_0, k_H f_0], \quad (14)$$

where $k_L = \lceil f_L/f_0 \rceil$ and $k_H = \lfloor f_H/f_0 \rfloor$ are the frequency domain indexes for the frequency band of interest.

As shown in (5), the inverse filter $S(jkf_0)^{-1}$ critically determines the error term's contribution to the distortion of deconvolved transient response $x(t)$. To limit the distortion, it is necessary to constrain the Fourier energy distribution of the stimulus sequence as follows so that the noise term $E(jkf_0)$ in (5) is at least not amplified. Assume

$$|S_T(jkf_0)|^{-1} \le \theta, \quad k = k_L, \dots, k_H, \quad (15)$$

where θ is a threshold usually set at 1 to make sure that the noise term within the frequency bins of interest is at most maintaining its original energy if not attenuated by the inverse filter.

Figure 1(c) illustrates that the example stimulus loop in Figure 1(a) meets this criterion in that the inverse filter satisfies $|S_T(jkf_0)|^{-1} < 1$ in the chosen frequency band $[f'_L, f'_H]$.

To further evaluate the overall quality of the stimulus sequence in (6), a measure called noise gain factor (NGF) can be defined accordingly [10] as

$$\text{NGF} = \frac{1}{f'_H - f'_L} \sum_{k=k_L}^{k_H} |S_T(jkf_0)|^{-1}, \quad (16)$$

which represents the average of noise gain factor at each frequency kf_0.

3. Experiments and Results

3.1. Stimulus Impulse Sequences.
In this section, we generate continuous-time stimulus sequences to be used for examining the impact of AD rates on the performance of inverse filtering in solving the transient AEPs. Using various optimization methods [11], these stimulus sequences can be found to satisfy the constraint in (15). Here we employed a modified optimization method called differential evolution algorithm [12] to obtain the optimal continuous-time stimulus sequences. The value of threshold θ in (15) was set to 1. Since the details of the optimization are beyond the scope of this paper, we directly provide the four impulse sequences (Table 1) generated for our study.

These four sequences are given in the form of ISI-series which can be expressed as $\Delta t_p = t_{p+1} - t_p$, where $t_p = T$ if $p = P$. Note that the temporal resolution of the stimulus events in the sequence is infinity in theory. In Table 1, we show Δt_p in the second decimal place only. These sequences are used to study the characteristics of 40 Hz steady-state responses which is a main application of HSR paradigms [2, 4]. Here, the jitter ratio (JR) in Table 1 is defined as JR = $[\max\{\Delta t_p\} - \min\{\Delta t_p\}]/\max\{\Delta t_p\}$ in percentage to measure the inhomogeneity of the stimulus interval. The applications of HSR paradigms usually requires a low jitter (small JR) stimulation to approach the case of steady state recordings while satisfying the constraint of (15) within the frequency band of interest (8–122 Hz, see Figures 4 and 5) in which the majority of energy of the simulated EEG signal falls.

3.2. EEG Data Simulation.
In actual experiments, the recorded EEGs (including transient AEPs and noises) are band-limited signals. They are digitized in time and amplitude according to Nyquist-Shannon sampling theorem. In this study, we use a real AEP signal previously measured using CLAD method [8] as the AEP component ($x(t)$) and the additive noise (i.e., $e(t)$) generated from a $1/f$ process [13] to simulate background EEGs mixed with inherent artifacts and noise. In our practice, the $e(t)$ is filtered by a band-pass filter to eliminate frequency outside [8, 500] Hz as a recording system usually does in experiments for the recording of middle latency response and 40 Hz steady state response. Note that $x(t)$ and $e(t)$ are both band-limited signals which in this case fall in frequency range [8, 500] Hz. In theory, there is no error when resampling them at a different AD rate as long as the sampling theorem is satisfied. In this study the original signals $x(t)$ and $e(t)$ were obtained at AD rate of 20 kHz and then resampled into other rates as needed. We chose a frequency band [8, 500] Hz for the simulated EEG signal to emulate the actual signal from recorded EEGs, which usually have a cut off frequency at 500 Hz in real experiment. However, this frequency band is broader than that ([8, 122] Hz) we used in optimizing our stimulus sequence in Section 3.1. Theoretically, we should avoid this inconsistency by either generating stimulus sequence satisfactory within [8, 500] Hz or filtering the EEG signal to [8, 122] Hz. In practice, we found it was much more difficult, if not impossible, to optimize the stimulus sequence for broad frequency range. Although the stimulus sequences in this paper are optimized for a frequency band narrower than that for the EEG signal, there was no data point of $|S_T(jkf_0)|^{-1}$ measure within the range of [0, 500] Hz to be extremely large. Moreover, the energy of EEG signals beyond range [8, 122] Hz is very low since the AEP is a very narrow band signal and the noise is simulated
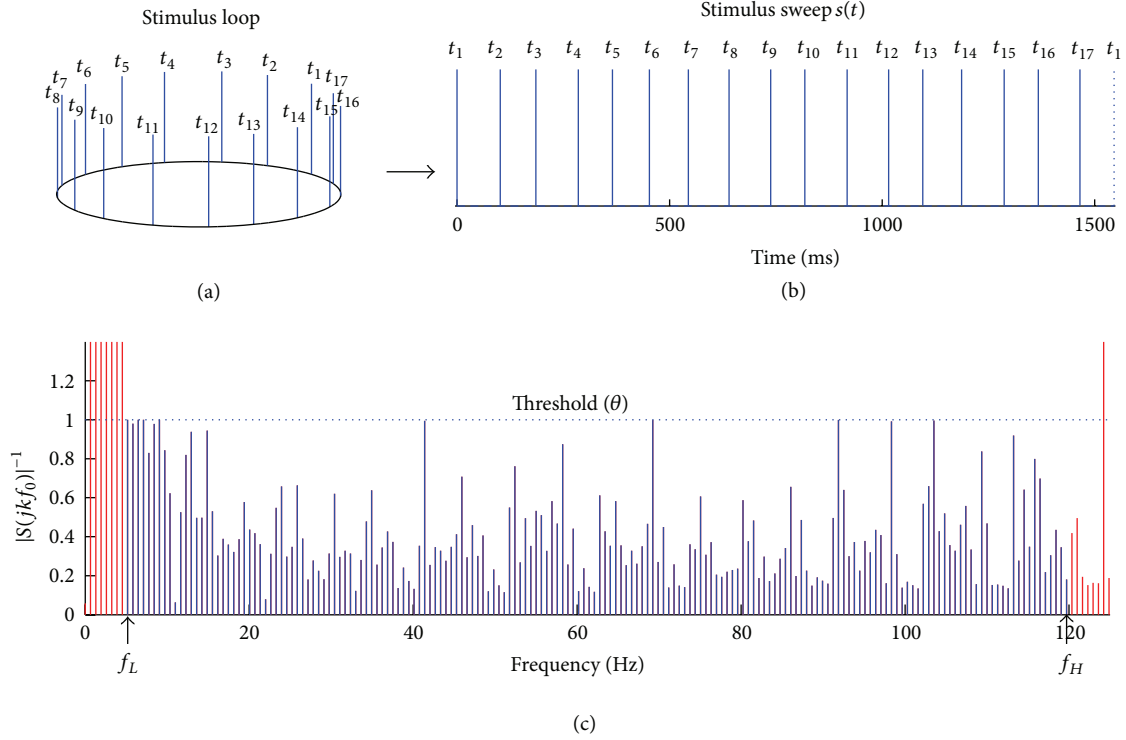
FIGURE 1: (a) A schematic diagram of a stimulus loop that contains 17 individual stimulus impulses to indicate the repetitive presentations in an experiment. (b) A sweep of stimulus sequence with impulses occurring at $t_p (p = 1, 2, 3, \ldots, 17)$ to represent a period of stimulus loop in time domain ($T = 1545.5$ ms; $f_0 = 0.647$ Hz). (c) A portion of the Fourier spectrum of the inverse filter $|S_T(jkf_0)|^{-1}$. Note that within the frequency band of interest ($[f'_L, f'_H] = [5, 120]$ Hz), $|S_T(jkf_0)|^{-1}$ is all below the threshold ($\theta = 1$).

TABLE 1: Four optimized stimulus impulse sequences obtained using differential evolution algorithm.

Sequence (ID, JR, NGF)	Stimulus interval (Δt_p in ms, rounded to the second decimal place for this table only)
Seq 1 11.95%, 0.43	27.21, 22.34, 27.16, 21.40, 21.43, 23.26, 27.18, 24.38, 26.19, 21.48, 27.16, 24.32, 27.05, 23.57, 24.02, 26.30, 27.04, 21.40, 23.41, 27.21, 22.16, 24.62, 21.47, 22.37, 22.54, 27.19, 27.21, 21.40, 21.40, 21.49, 27.21, 22.57, 25.52, 25.15, 27.21, 21.40, 21.40, 27.21, 24.92, 21.40, 25.93, 27.21, 27.21, 21.43, 21.74, 22.23, 27.20, 26.74, 27.21, 21.40, 24.39, 21.49, 24.38, 27.21, 22.54, 27.20, 21.40, 21.86, 27.21, 21.97, 22.59, 25.09, 27.15, 21.48, 26.27
Seq 2 12.40% 0.50	23.49, 21.91, 27.96, 27.96, 21.79, 21.79, 24.88, 27.96, 24.36, 21.79, 26.27, 23.13, 26.82, 27.96, 21.79, 27.96, 23.67, 22.83, 27.96, 21.79, 22.40, 27.96, 27.96, 21.91, 21.79, 27.96, 23.33, 27.96, 21.79, 27.96, 21.91, 27.94, 26.77, 21.79, 24.64, 27.25, 21.79, 24.89, 27.96, 25.00
Seq 3 12.88% 0.49	28.38, 21.90, 28.38, 23.20, 21.90, 28.38, 28.24, 21.90, 25.00, 28.38, 21.90, 28.38, 28.38, 22.24, 25.10, 28.38, 28.38, 24.72, 21.90, 28.37, 25.12, 27.13, 23.68, 21.90, 21.90, 28.38, 21.90, 24.35, 22.14, 28.24, 28.38, 23.78, 22.29, 28.38, 22.07, 25.35, 21.90, 28.38, 25.00, 21.90
Seq 4 12.60% 0.49	26.40, 27.75, 21.66, 27.90, 21.94, 27.91, 21.66, 22.67, 23.90, 27.64, 27.91, 21.88, 21.66, 21.66, 27.91, 27.91, 21.66, 27.03, 27.42, 26.29, 21.66, 25.65, 27.90, 21.66, 27.89, 25.77, 21.66, 21.66, 26.10, 27.91, 21.66, 24.73, 27.91, 21.66, 27.90, 24.01, 21.66, 27.90, 21.66, 23.63

using a $1/f$ process. As such, noise will not be over amplified by the inverse filtering in this study and their contribution to the distortion of deconvolved AEP is limited.

3.3. Errors Introduced by the Temporal Discretization. The interstimulus interval of continuous-time stimulus sequence can be discretized at required temporal resolution. The discretization will introduce round off errors no matter how high is sampling frequency f_s. Accordingly, the Fourier of the

discretized counterpart will differ from that of the original continuous-time stimulus sequence.

The discretized temporal location t'_p of a stimulus impulse at $t_p (p = 1, 2, \ldots, P)$ with respect to the onset of a stimulus-sweep is

$$t'_p = \text{round} \frac{(t_p f_s)}{f_s}. \tag{17}$$

TABLE 2: The errors between estimated and true solution at various AD rates for four sequences.

Seq. ID	SNR (dB)	AD rate (kHz)											
		Inf	1	2	3	4	5	7	9	11	15	20	25
Seq 1	9.5	2.02	20.53	12.65	10.31	8.85	7.87	6.67	5.94	5.29	4.58	3.96	3.54
	0	8.24	68.01	43.29	35.02	29.79	26.66	22.55	20.02	17.89	15.50	13.41	12.00
	−6.0	18.51	141.81	91.21	73.72	62.67	56.15	47.48	42.10	37.68	32.63	28.22	25.27
Seq 2	9.5	4.19	31.52	21.39	17.91	15.40	14.05	11.72	10.26	9.40	8.02	6.98	6.43
	0	9.52	78.32	52.98	44.67	38.33	35.15	29.23	25.55	23.44	19.99	17.44	6.23
	−6.0	18.14	149.64	101.20	85.47	73.32	67.31	55.94	48.87	44.83	38.25	33.39	31.15
Seq 3	9.5	5.02	27.32	18.70	15.48	13.67	11.78	10.07	8.83	8.00	6.85	5.96	5.32
	0	10.60	63.02	42.47	35.49	31.81	26.83	23.06	20.21	18.27	15.66	13.63	12.17
	−6.0	19.13	117.29	78.61	65.94	59.41	49.73	42.81	37.53	33.89	29.07	25.29	22.57
Seq 4	9.5	3.48	21.60	15.11	12.64	10.88	9.63	8.31	7.35	6.52	5.63	4.85	4.37
	0	10.79	67.96	47.93	39.82	34.17	30.32	26.14	23.13	20.61	17.75	15.30	13.76
	−6.0	22.53	139.85	98.80	81.91	70.28	62.39	53.76	47.56	42.44	36.51	31.48	28.31

FIGURE 2: The graphic representation of the relationship between γ_t and f_s. The data points for four datasets are fit using a reciprocal function: $\gamma_t = 11.78/f_s - 0.01363$, ($R^2 = 0.9982$). The location of maximal curvature is at $f_s = 3.43$ kHz.
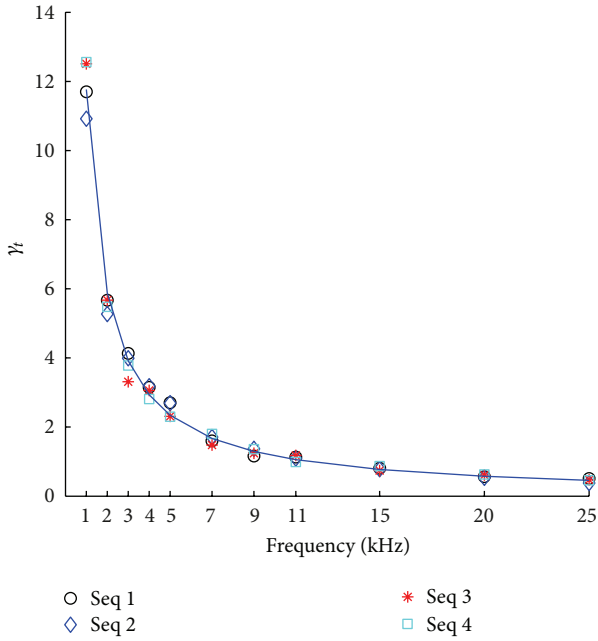

FIGURE 3: The graphic representation of the relationship between γ_f and f_s. The data points for four datasets are fit using a reciprocal function: $\gamma_f = 14.25/f_s - 0.003574$, ($R^2 = 0.9983$). The location of maximal curvature is at $f_s = 3.77$ kHz.

The normalized root-mean-square error is defined as an overall measure of the errors caused by the temporal discretization of the continuous-time stimulus impulse sequence

$$\gamma_t = \frac{P}{T}\sqrt{\frac{1}{P}\sum_{p=1}^{P}\left(t_p - t'_p\right)^2}. \tag{18}$$

To examine the error introduced by the temporal discretization of four stimulus sequences in Table 1, we calculated γ_t at different temporal resolutions determined by the AD rates (from 1 kHz to 25 kHz). The results are presented in

Figure 2. Consistent with results for the four sets of stimulus sequences, the γ_t decreases as sampling frequency increases. The results can be fit by a reciprocal function: $\gamma_t = 11.78/f_s - 0.01363$, ($R^2 = 0.9982$) and the location of maximal curvature $f_s = 3.43$ kHz.

As seen above, the temporal discretization introduces errors of the temporal location of the stimulus impulses, causing the difference between $S_T(jkf_0)$ and $S[jkf_0]$. We need to examine whether an optimized continuous-time stimulus sequence $s(t)$ still satisfies the constraint in (15) after
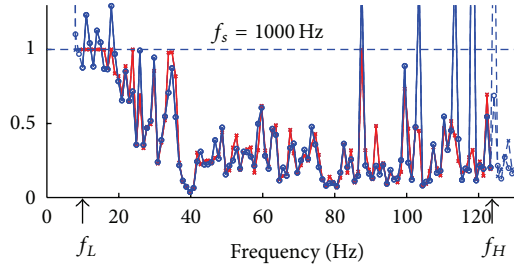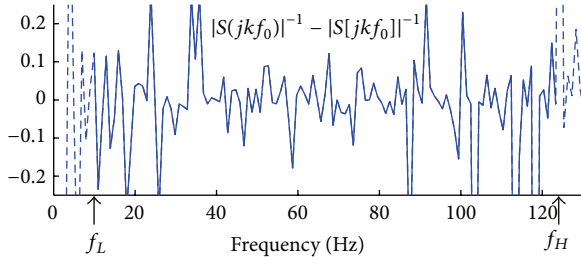
Figure 4: Comparison with respect to the $|S_T(jkf_0)|^{-1}$ measure between the continuous-time stimulus sequence and its discrete-time counterpart at discretization frequency of $f_s = 1$ kHz. (a) The plot of the $|S_T(jkf_0)|^{-1}$ measure for the continuous-time stimulus sequence (data points in "x") and that for the corresponding discrete-time stimulus sequence (data points in "o," discretization frequency $f_s = 1$ kHz). (b) The difference between the $|S_T(jkf_0)|^{-1}$ measures, respectively, for continuous-time and discrete-time stimulus sequences.

Figure 5: Comparison with respect to the $|S_T(jkf_0)|^{-1}$ measure between the continuous-time stimulus sequence and its discrete-time counterpart at discretization frequency of $f_s = 20$ kHz. (a) The plot of the $|S_T(jkf_0)|^{-1}$ measure for the continuous-time stimulus sequence (data points in "x") and that for the corresponding discrete-time stimulus sequence (data points in "o", discretization frequency $f_s = 20$ kHz). (b) The difference between the $|S_T(jkf_0)|^{-1}$ measures, respectively, for continuous-time and discrete-time stimulus sequences.

discretization. We define relative root-mean-square error in frequency domain as

$$\gamma_f = \frac{\sqrt{\sum_{k=k_L}^{k_H} \left(|S_T(jkf_0)| - |S[jkf_0]| \right)^2}}{\sqrt{\sum_{k=k_L}^{k_H} |S(jkf_0)|^2}} \times 100\%. \qquad (19)$$

Using the same four dataset in Table 1, we calculate γ_f with respect to each AD rate from 1 kHz to 25 kHz. The resulting γ_f is shown in Figure 3. Again, the data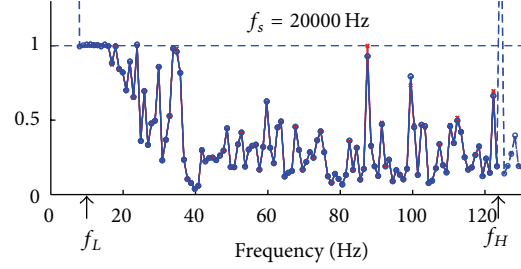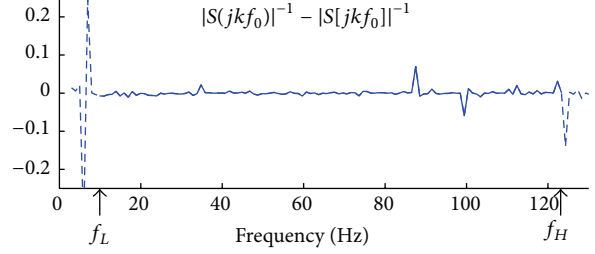 points can be well-fit with a reciprocal function: $\gamma_f = 14.25/f_s - 0.003574$, ($R^2 = 0.9983$), and the location of its maximal curvature is at $f_s = 3.77$ kHz.

Figure 3 shows that the error of stimulus sequence in Fourier domain caused by the temporal discretization decreases with the increase of sampling rate. But the error will not completely disappear. Based on the fit function $\gamma_f = 14.25/f_s - 0.003574$, the maximal curvature occurs at $f_{sc} = 3.77$ kHz, indicating that, in the range $[0, 3.77]$ kHz, γ_f decreases rapidly with the increase of f_s. However, γ_f decreases at a much low rate when f_s is greater than 3.77 kHz. These results suggest that the γ_f is very sensitive to low

AD rate, and that it is critical to increase the AD rate to a frequency higher than 3.77 kHz.

Here we use one stimulus sequence to exemplify the differences caused by discretization at two different AD rates: $f_{s1} = 1$ kHz, which is below the critical f_{sc} (3.77 kHz) and $f_{s2} = 20$ kHz, which is above the critical f_{sc} (3.77 kHz). Figure 4(a) illustrates the $|S_T(jkf_0)|^{-1}$ measure of the continuous-time stimulus sequence (data points labeled with cross "x") and that of the corresponding discrete-time stimulus sequence (data points labeled with open circle "o") at an AD rate of $f_s = 1$ kHz. Within the frequency range of interest $[f_L = 8$ Hz, $f_H = 122$ Hz$]$, the inverse filter based on the discretized stimulus sequence satisfies (15) at most frequency bins. However, at some frequency bins, its $|S_T(jkf_0)|^{-1}$ measure is greater than 1. The difference between the continuous-time and discrete-time stimulus sequence at each frequency bin is plotted in Figure 4(b). Clearly, the discretization causes errors at most frequency bins at amplitudes within the range from -0.25 to 0.25.

Figure 5 shows the similar contents as Figure 4, except that the continuous-time stimulus sequence is discretized at a higher AD rate of $f_s = 20$ kHz. Figure 5(a) depicts the $|S_T(jkf_0)|^{-1}$ measures for continuous-time (data points

labeled with "x") and discrete-time (data points in open circles "o") stimulus sequences. Again, the $|S_T(jkf_0)|^{-1}$ measure within most frequency bins for the discrete-time stimulus sequence satisfies (15). However, we can also see some data points stick out of the threshold of 1. The difference between the $|S_T(jkf_0)|^{-1}$ measures for the continuous-time and discrete-time stimulus sequences is shown in Figure 5(b). We can see that at $f_s = 20\,\text{kHz}$, the difference at most frequency bins is close to zero. When compared to Figure 4(b), Figure 5(b) clearly show that $f_s = 20\,\text{kHz}$ has substantial advantage over $f_s = 1\,\text{kHz}$ in maintaining the discrete stimulus sequence satisfactory to the condition described in (15). Importantly, if the AD rate is low, the discrete stimulus sequence may violate the condition and cause overamplification of noise components in the recorded EEG and distort the deconvolved transient AEPs. The results also suggest that using AD rate much higher than the Nyquist sampling rate is necessary to minimize the error introduced from temporal discretization.

3.4. Noise Attenuation Effects of Discretization Frequency.

Although the continuous-time stimulus sequence $s(t)$ is frequency unlimited ($S(jkf_0)$ in Fourier domain, where k can be any integer), the frequency range of interest is determined by the nonzero values of the product of $S(jkf_0)$ and $X(jkf_0)$ as indicated in (4). In this study, the recorded EEG is band-pass filtered within [8–500] Hz. The transient response $x(t)$ is obtained by applying inverse Fourier transform on $\widehat{X}(jkf_0)$ in (5):

$$\widehat{x}_c(n\Delta_t) = F^{-1}\left\{\widehat{X}(jkf_0)\right\}, \quad n = 1, 2, \dots, N;$$
$$8\,\text{Hz} \le kf_0 \le 500\,\text{Hz}. \tag{20}$$

Likewise, the inverse Fourier transform of $\widehat{X}[jmf_0]$ in (1d) will give the time domain signal for the discrete binary sequence:

$$\widehat{x}_d[n\Delta_t] = F^{-1}\left\{\widehat{X}[jmf_0]\right\}, \quad n = 1, 2, \dots, N;$$
$$8\,\text{Hz} \le mf_0 \le 500\,\text{Hz}. \tag{21}$$

To quantify the difference between the estimated and the true solutions for both continuous and discrete stimulus sequence, we can define root mean square error for $\widehat{x}_c(n\Delta_t)$

$$\gamma_{x_c} = \frac{\sqrt{\sum_{n=1}^{N}\left(\widehat{x}_c[n] - x(n\Delta_t)\right)^2}}{\sqrt{\sum_{n=1}^{N} x(n\Delta_t)^2}} \times 100\%. \tag{22}$$

By replacing $\widehat{x}_c(n\Delta_t)$ with $\widehat{x}_d[n\Delta_t]$ in (22), we can define the root mean square error γ_{x_d} for $\widehat{x}_d(n\Delta_t)$. As stated previously, an original copy of additive $1/f$ random noise is then rescaled and/or resampled to accommodate conditions with different AD rates and signal-to-noise ratios (SNRs), where the latter is defined as

$$\text{SNR} = 20\log\frac{\sqrt{\sum_{n=1}^{N} x(n\Delta_t)^2}}{\sqrt{\sum_{n=1}^{N} e(n\Delta_t)^2}}. \tag{23}$$
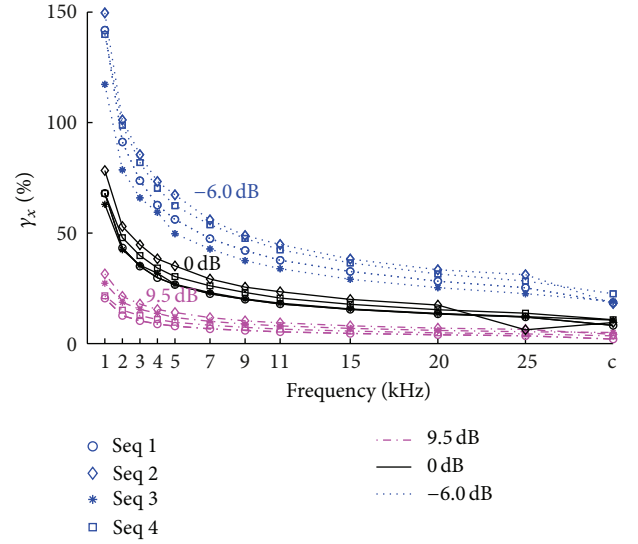

FIGURE 6: The errors between estimated and true solution at various AD rates (1–25 kHz) as well as the case of continuous-time sequence (tick "c" in the horizontal coordinate). Four sequences are examined under three SNR conditions (see the legend). γ_x in the vertical coordinate implies both errors of γ_{x_c} and γ_{x_d}.

To examine the relationship between AD rate and γ_{x_c}, we simulated the discretization at $f_s = 1$–25 kHz and three SNR conditions (9.5 dB, 0 dB, and −6.0 dB). The resulting γ_{x_c} is shown in Table 2, where in the first column (AD rate = Inf) means the errors for the continuous-time stimulus sequence condition and γ_{x_c} results for this condition serve the references for all other AD rates. From Table 2, we can see that the errors for high SNR EEGs are much smaller than those for low SNR EEGs, and the errors decrease as AD rate increases. These phenomena are consistent across four stimulus sequences. Figure 6 is a graphic representation of the results. It shows that low SNR EEGs are more vulnerable to low AD rates, and the increase AD rate is more beneficial for low SNR signal on the other hand.

To gain more straightforward understanding of above results, we choose to present the resulting AEPs from different SNR conditions and at two representative AD rates. Figure 7(a) shows the results at AD rate of 1 kHz. It is clear that the AEPs recovered from high SNR EEGs (the top panel) using continuous-time and discrete-time stimulus sequence are both very close to the original AEP used for the simulation study. However, the difference between the recovered AEPs becomes significant when the SNR is low (the third panel in Figure 7(a)). At same time, we can see that the AEPs recovered using continuous-time stimulus sequence are closer than the ones from discrete-time stimulus sequence to the original AEP. Figure 7(b) shows the results at AD rate of 20 kHz. Similar to the phenomena in Figure 7(a), the AEPs (the top panel in Figure 7(b)) recovered from high SNR EEGs are very close to the original AEP used in this study. When the SNR is getting worse, for example −6 dB as in the third panel in Figure 7(b), the recovered AEP is less
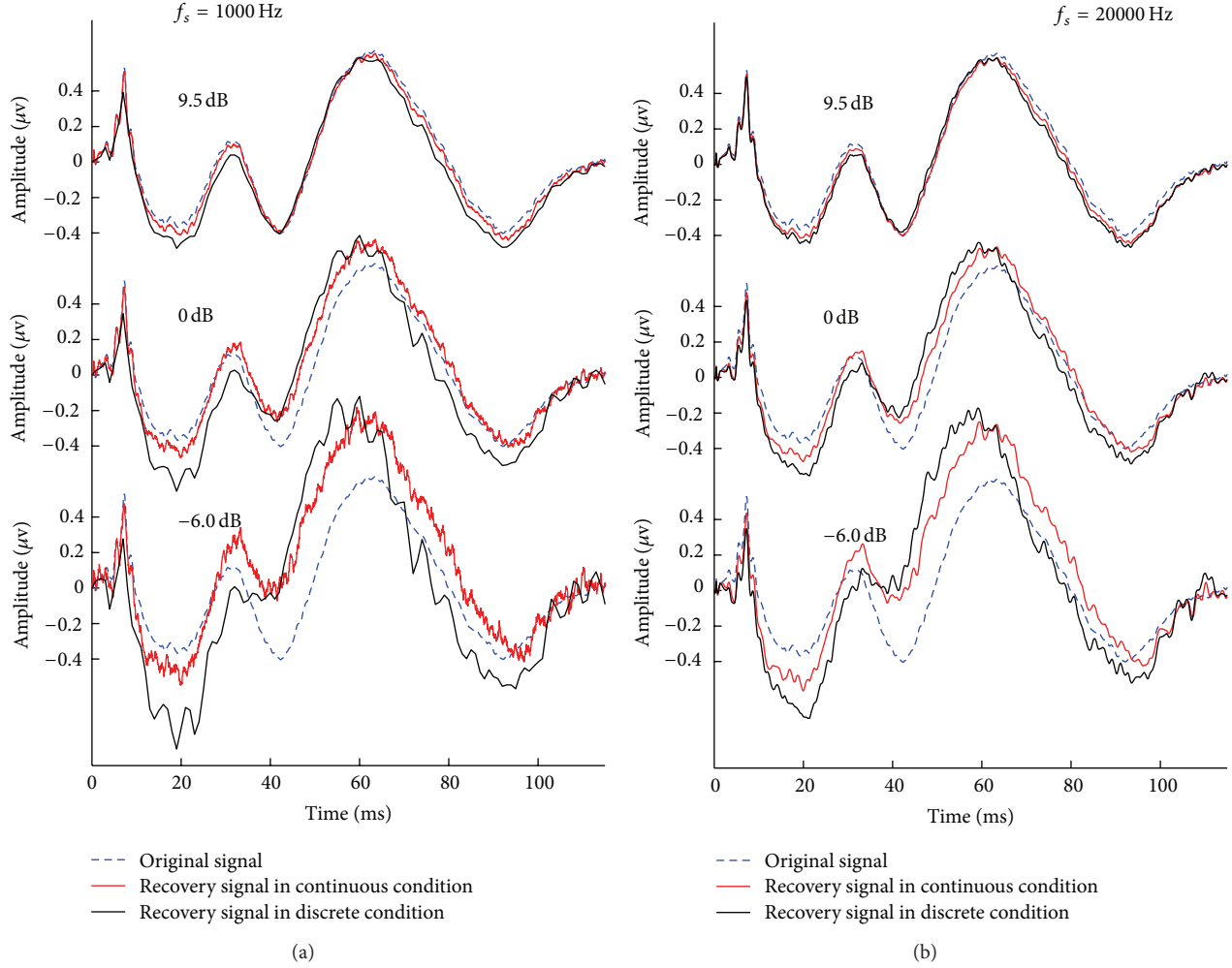
FIGURE 7: Comparison of transient AEPs solved by CLAD method at different SNR conditions and at two representative discretization frequencies. (a) AEPs (the original in dashed blue, the one recovered based on continuous-time stimulus sequence in thin red, and the one recovered based on discrete-time stimulus sequence in black). The discretization frequency (AD rate) $f_s = 1$ kHz; and the SNRs for three panels from top to bottom are, respectively, 9.5, 0 and −6.0 dB. (b) Same as (a) except the discretization frequency $f_s = 20$ kHz.

close to the original AEP. Consistent to that exemplified in Figure 7(a), the AEPs recovered based on continuous-time stimulus sequence better resemble the original AEP than those based on discrete-time stimulus sequence. Moreover, the AEPs from high AD rate ($f_s = 20$ kHz) of discretization resemble more closely to the original AEP than those from low AD rate of discretization. As such, it becomes obvious that increasing AD rate will reduce the distortions in the recovered transient AEP. More importantly, this positive impact of high AD rate is more significant for low SNR recordings.

4. Discussion and Conclusion

Solving the transient AEPs in frequency domain under HSR paradigm has been investigated and implemented recently using discrete-time stimulus sequences (e.g., in [1–5, 7, 8, 10]). Since the frequency characteristics of a stimulus sequence

critically influence the performance of deconvolution algorithms in the presence of noises in EEG recordings, one needs to select or generate appropriate sequences to satisfy certain criteria (e.g., (15)). However, it is challenging to generate an optimal discrete-time stimulus sequence when the occurring time points of stimulus impulses are subject to the constraint of the AD rate of the experiment systems. This is because theoretically it only has a limited number of possible solutions. Although continuous sequences generated by an optimum method might be ready for use, one needs to answer two more questions: (1) how to present such sequences into the practical recordings in digital form; (2) how to quantify the errors and impacts due to the discretization of the continuous-time stimulus sequences.

This paper answers the first question by explicating the frequency presentation of continuous-time stimulus sequences and its use in solving the transient AEP using deconvolution algorithm. As detailed before, the repetitive

continuous-time stimulus sequences have discrete frequencies in the Fourier domain and as such the convolution model and deconvolution algorithm can be similarly presented as for the discrete-time time system. In practice, the continuous-time stimulus sequences can be approximated using very high temporal resolution discrete-time stimulus sequences. For example, the temporal resolution for the stimulus sequences in Table 1 can be rounded to the 4th decimal place, equivalent to a sampling frequency at MHz level, which is well above the characteristic frequency (~4 kHz) in Figures 2 and 3 and makes the discretization errors negligible in applications. Furthermore, simulation studies are used to examine the applicability of the theory and quantify the errors and impacts when a continuous-time stimulus sequence is temporally discretized. The results show that using continuous-time stimulus sequences in the HSR paradigm has significant advantages over using discrete-time stimulus sequences in recovering the transient AEPs. This study also reveals a reciprocal relationship between errors introduced by the discretization of continuous-time stimulus sequence into discrete-time counterpart and the discretization frequencies. Note that we here used the absolute errors to quantify the impact of sampling rate of discrete-time stimulus sequences. But absolute errors should not be considered the only choice. In fact, other metrics such as correlation coefficient can be a good measure when the shape of waveform is of the researchers' only concern. In typical AEP studies, researchers are usually interested in both the shape and amplitude of the signals. In any case, the results in this paper suggest that when discrete-time stimulus sequence is used, a high frequency system is more likely to offer reliable recovered AEPs under HSR paradigm.

To conclude, this study demonstrates the applicability and advantages of continuous-time stimulus sequences for AEP studies using HSR paradigm and reveals the reciprocal relationship between the errors in recovered AEPs and the sampling frequencies of the experimental systems when discrete-time stimulus sequences are used in traditional manner for the HSR paradigm.

Acknowledgments

References

[1] R. E. Delgado and Ö. Özdamar, "Deconvolution of evoked responses obtained at high stimulus rates," *Journal of the Acoustical Society of America*, vol. 115, no. 3, pp. 1242–1251, 2004.

[2] Ö. Özdamar, J. Bohórquez, and S. S. Ray, "Pb(P1) resonance at 40 Hz: effects of high stimulus rate on auditory middle latency responses (MLRs) explored using deconvolution," *Clinical Neurophysiology*, vol. 118, no. 6, pp. 1261–1273, 2007.

[3] R. R. McNeer, J. Bohórquez, and Ö. Özdamar, "Influence of auditory stimulation rates on evoked potentials during general anesthesia: relation between the transient auditory middle-latency response and the 40-Hz auditory steady state response," *Anesthesiology*, vol. 110, no. 5, pp. 1026–1035, 2009.

[4] J. Bohórquez and Ö. Özdamar, "Generation of the 40-Hz auditory steady-state response (ASSR) explained using convolution," *Clinical Neurophysiology*, vol. 119, no. 11, pp. 2598–2607, 2008.

[5] D. L. Jewett, G. Caplovitz, B. Baird, M. Trumpis, M. P. Olson, and L. J. Larson-Prior, "The use of QSD (q-sequence deconvolution) to recover superposed, transient evoked-responses," *Clinical Neurophysiology*, vol. 115, no. 12, pp. 2754–2775, 2004.

[6] Y. Su, Z. Li, and T. Wang, "Deconvolution methods and applications of auditory evoked response using high rate stimulation," in *New Developments in Biomedical Engineering*, D. Campolo, Ed., pp. 105–122, InTech, Vukovar, Croatia, 2010.

[7] D. L. Jewett, T. Hart, L. J. Larson-Prior et al., "Human sensory-evoked responses differ coincident with either "fusion-memory" or "flash-memory", as shown by stimulus repetition-rate effects," *BMC Neuroscience*, vol. 7, article 18, 2006.

[8] T. Wang, Ö. Özdamar, J. Bohórquez, Q. Shen, and C. Marie, "Wiener filter deconvolution of overlapping evoked potentials," *Journal of Neuroscience Methods*, vol. 158, no. 2, pp. 260–270, 2006.

[9] M. J. Lighthill, *Introduction to Fourier Analysis and Generalised Functions*, Cambridge University Press, Cambridge, UK, 1970.

[10] Ö. Özdamar and J. Bohórquez, "Signal-to-noise ratio and frequency analysis of continuous loop averaging deconvolution (CLAD) of overlapping evoked potentials," *Journal of the Acoustical Society of America*, vol. 119, no. 1, pp. 429–438, 2006.

[11] J. D. Pintér, "Global optimization: software, test problems, and applications," in *Handbook of Global Optimization*, P. M. Pardalos and H. E. Romeijn, Eds., vol. 2, pp. 515–569, Publishing House of Kluwer Academic Publishers, Boston, Mass, USA, 2002.

[12] R. Storn and K. Price, "Differential evolution—a simple and efficient heuristic for global optimization over continuous spaces," *Journal of Global Optimization*, vol. 11, no. 4, pp. 341–359, 1997.

[13] W. S. Pritchard, "The brain in fractal time: 1/f-like power spectrum scaling of the human electroencephalogram," *International Journal of Neuroscience*, vol. 66, no. 1-2, pp. 119–129, 1992.

Review Article

A Review on the Computational Methods for Emotional State Estimation from the Human EEG

Min-Ki Kim,[1] Miyoung Kim,[2] Eunmi Oh,[2] and Sung-Phil Kim[3]

[1] *Department of Brain and Cognitive Engineering, Korea University, Seoul 136701, Republic of Korea*
[2] *Samsung Electronics, DMC R&D Center, Suwon 443742, Republic of Korea*
[3] *Research and Business Foundation, Korea University, Seoul 136701, Republic of Korea*

Correspondence should be addressed to Sung-Phil Kim; spkim@korea.ac.kr

A growing number of affective computing researches recently developed a computer system that can recognize an emotional state of the human user to establish affective human-computer interactions. Various measures have been used to estimate emotional states, including self-report, startle response, behavioral response, autonomic measurement, and neurophysiologic measurement. Among them, inferring emotional states from electroencephalography (EEG) has received considerable attention as EEG could directly reflect emotional states with relatively low costs and simplicity. Yet, EEG-based emotional state estimation requires well-designed computational methods to extract information from complex and noisy multichannel EEG data. In this paper, we review the computational methods that have been developed to deduct EEG indices of emotion, to extract emotion-related features, or to classify EEG signals into one of many emotional states. We also propose using sequential Bayesian inference to estimate the continuous emotional state in real time. We present current challenges for building an EEG-based emotion recognition system and suggest some future directions.

1. Introduction

An emotional state refers to a psychological and physiological state in which emotions and behaviors are interrelated and appraised within a context [1]. From the psychological aspects, the space of the emotional state can be built from the discrete model or the dimensional model. In the discrete model, an emotional state is defined as a set of a finite number of discrete states corresponding to one of core emotions, including anger, fear, disgust, surprise, happiness, and sadness, or a combination of them [2]. The dimensional model defines an emotional state spatially with the basic dimensions of emotion such as valence and arousal and interprets an emotion through the levels of each dimension [3]. These emotion models have been used for systematical and multilateral analyses of emotion [3]. Based on the emotion models, neurophysiologic mechanisms under the emotional state have been vigorously investigated. Broadly, it has been documented that the emotional processes performed at the ventral and dorsal systems in the human brain

are functionally different [4]. The ventral system, including ventral anterior cingulate gyrus and some ventral areas of prefrontal cortex (ventromedial prefrontal cortex and medial orbitofrontal cortex), is involved in the production of emotional states and the regulation of affective responses, whereas the dorsal system, including dorsal anterior cingulate gyrus, some dorsal areas of prefrontal cortex (dorsolateral, posterior dorsolateral, and mid-dorsolateral prefrontal cortex), and hippocampus, is involved in effortful emotion regulation and subsequent behavior [4, 5].

Recently, affective computing (AC) has emerged as a converging technology blending emotion into human computer interaction (HCI) [6]. AC, often called emotion aware computing, builds emotional interactions between a human and a computer by measuring the emotional state through behavioral and physiological signals and developing computational models for the emotional state [6, 7]. One of the key elements in AC is emotion recognition that estimates the emotional state of users from their behavioral and physiological responses [7]. Emotion recognition aims to advance

the intelligence of computer for creating affective user interfaces and to enhance the quality of psychiatric health care.

A variety of measures have been used for emotion recognition including self-report, startle response, behavioral response, autonomic measurement, and neurophysiologic measurement [3]. Self-report readily acquires emotional responses according to the emotion modeling framework but makes it difficult to track rapid affective changes and needs to rely on the outcome from self-estimation of the emotional state [3, 8]. The startle response magnitude using electromyography (EMG) measures unconscious myoneural responses but assesses only partial aspects of emotion (e.g., arousal level) [3, 9]. Behavioral measurement detects changes in facial and/or whole-body behavior using EMG or video image, but needs an assumption that EMG signals directly correspond to a specific emotional state [3, 10]. Autonomic measurement can objectively detect emotion-related physiological responses of autonomic nervous system (ANS), such as skin conductance responses (SCRs) and heart rate variability (HRV), but only access the subspaces of the emotional state [3, 11]. Neurophysiologic measurement based on electrophysiological and neuroimaging techniques can detect a wide range of dynamics of the emotional state by directly accessing the fundamental structure in the brain from which an emotional state emerges [3, 12]. Hence, neurophysiologic measurements clearly provide the most direct and comprehensive means for emotion recognition.

A large body of research has investigated neural correlates of emotion in humans using many noninvasive sensor modalities, each presenting unique characteristics with respect to spatiotemporal resolution and mobility. Functional magnetic resonance imaging (fMRI) has been used to find cortical and subcortical structures implicated in emotional states [13]. MEG has also been used to find emotion-related neural signals from specific sources in a timely manner with fine spatial and temporal resolutions [14]. But the cost and immobility of fMRI and MEG prevents these modalities from being used for practical emotion recognition systems [15, 16]. EEG, although suffering from its poor spatial resolution and high susceptibility to noise, has been widely used to investigate the brain dynamics relative to emotion as it enables the detection of immediate responses to emotional stimuli with an excellent temporal resolution [17–21]. Being developed to become more cost-effective and mobile with increased practicability and less physical restriction [22], EEG, not without its downsides, still carries critical advantages in practical usage and therefore has been a primary option for the development of online emotion recognition systems. In fact, there have been a growing number of efforts to recognize a person's emotion in real time using EEG. For example, EmoRate developed as a commercial product (Emotiv Corp., CA, USA) detects the flow of the emotional state while user is watching a film [23]. Brown et al. proposed an EEG-based affective computer system that measures the state of valence and transmits it via a wireless link [24].

The development of an EEG-based emotion recognition system requires computational models that describe how the emotional state is represented in EEG signals and how one can estimate an emotional state from EEG signals. Despite a long history of searching for EEG indices of emotion, less attention has been paid to the computational models for emotional state estimation. Hence, we feel needs for a review of the state-of-the-art computational models for emotional state estimation to subserve the development of advanced emotion recognition methods. This paper will review the current computational methods of emotional state estimation from the human EEG with discussion on challenges and some future directions.

This paper will particularly focus on the following aspects of EEG-based emotional state estimation models. First, it will start with a quick review on EEG correlates of emotion, including definition of the emotional state space, the design of emotional stimuli, and the EEG indices of emotion. Then, it will revisit the computational methods to extract EEG features relative to emotional states and to estimate emotional states from EEG. We will also propose a mathematical approach to the estimation of continuous emotional state based on Bayesian inference.

2. EEG Correlates of Emotion

Finding EEG correlates of emotional states should begin with how to define the emotional state space. The emotional state space can be largely categorized into a discrete space and a continuous space. The discrete state space draws upon the discrete emotion model and contains a set of discrete experiential emotional states. The discrete emotional state comprises seven to ten core emotions such as happiness, surprise, sadness, anger, disgust, contempt, and fear [2, 25] and sometimes expands to contain a large number of emotions with the synonyms of these core emotions [25]. The continuous state space is built from the dimensional emotion model and represents an emotional state as a vector in a multidimensional space. This vector space of the continuous emotional state depends on the definition a basis. For instance, the circumplex model, developed by Russell, describes an emotional state in a two-dimensional circular space with the arousal and valence dimensions [26]. Various psychological models define emotional dimensions that subsequently constitute the basis for the emotional state space [25, 27–30].

Based on the construction of the emotional state space, the investigation of EEG correlates of emotion should also address how to determine experimental stimuli to induce emotions. Typically, emotional stimuli are selected to cover desired arousal levels and valence states, and presented in different modalities including the visual, auditory, tactile, or odor stimulation. The ground truth of the emotional state induced by a stimulus is secured by exploiting the self-ratings of subjects or using the standard stimulus sets such as the international affective picture system (IAPS) or the international affective digitized sound system (IADS). The IAPS provides a set of normative pictures for emotional stimuli to induce emotional changes and attention levels [31]. The IADS embodies acoustic stimuli to induce emotions, sometimes together with the IAPS [32]. These international

affective systems are known to be independent of culture, sex, and age [33].

A number of neuropsychological studies have reported EEG correlates of emotion. These EEG features can be broadly placed in one of two domains: time domain and frequency domain. In the time domain, several components of event-related potentials (ERPs) reflected underlying emotional states [34]. These ERP components can be encapsulated in a chronological order: P1 and N1 components generated in a short latency from stimulus onset, N2 and P2 in a middle latency, and P3 and slow cortical potential (SCP) in a long latency. The ERP components of short to middle latencies have been shown to correlate with valence [34–37], whereas with the ERP components of middle to long latencies have been shown to correlate with arousal [38–41]. Basically, the computation of ERPs requires averaging EEG signals over multiple trials, rendering ERP features inappropriate for online computing. However, recent developments of the single-trial ERP computation methods increase a possibility to use ERP features for online emotional state estimation [42–46].

In the frequency domain, the spectral power in various frequency bands has been implicated in the emotional state. The alpha power varied with the valence state [47] or with discrete emotions such as happiness, sadness, and fear [18]. Specifically, the frontal asymmetry of the alpha power has been repeatedly reported as a steady correlate of valence [48]. The subsequent studies have suggested that the frontal alpha asymmetry may reflect the approach/avoidance aspects of emotion, rather than valence per se [49]. The event-related synchronization (ERS) and desynchronization (ERD) of the gamma power has been related to some emotions such as happiness and sadness [50–52]. The ERS of the theta power has also been modulated during transitions in the emotional state [18, 53–55].

Besides the waveforms and the spectral power, the interactive properties between a pair of EEG oscillations such as phase synchronization and coherence have also been implicated in emotional processes. For instance, the phase synchronization level between the frontal and right temporoparietal areas varied with the emotional states of energetic, tension, and hedonic arousal [56]. The EEG coherence across the prefrontal and posterior beta oscillations was increased by viewing high arousal images [57]. Also, increases in the gamma phase synchronization index were induced by unpleasant visual stimuli [58]. As the emotional process engages a large-scale network of the neural structures in the brain, these multichannel analyses of EEG across the brain will reveal more signatures of emotion as they do for other cognitive functions [59–64]. In short, a brief summary of the EEG correlates of emotion is presented in Table 1.

3. Computational Methods to Estimate Emotional States

The computational methods to estimate the emotional state have been designed based on various EEG features related to emotional processes. As most EEG analysis methods are
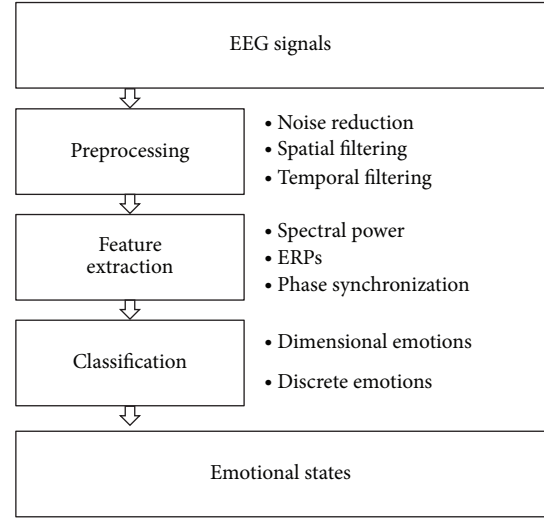

Figure 1: Overall emotional state estimation process. The overall emotional state estimation procedure. EEG signals are recorded during emotional situations and passed through the preprocessing step including noise reduction and spatial and temporal filtering. The features related with the emotional states such as spectral power, ERP, and phase synchronization are extracted from the preprocessed EEG signals. These features are used to estimate emotional states by classification methods.

accompanied by preprocesses for reducing the artifacts, so is the emotional state estimation method. Figure 1 illustrates overall processing steps to estimate the emotional state from EEG signals. The recorded EEG signals in response to affective stimuli pass through the preprocessing step in which noise reduction algorithms and spatiotemporal filtering methods are employed to enhance the signal-to-noise power ratio (SNR). Then, the feature extraction step determines specific band powers, ERPs, and phase coupling indices correlated with the target emotional states. Usually, this feature selection process is optimized by mathematical methods to achieve maximum emotional estimation accuracy. The classification step estimates the most probable emotional state from the selected EEG features. The number of class depends on the definition of the emotional state space, such as the continuous state of arousal and valence, or the discrete states.

As the preprocessing methods are relatively general to a variety of EEG signal processing applications, here we focus on the feature extraction and emotion classification methods. We first review the computational methods to extract emotion-related features from EEG, followed by the classification algorithms used to estimate the emotional state from the EEG features. The feature extraction methods usually build a computational model to find emotion-related features based on neurophysiologic and neuropsychological knowledge. Unlike the feature extraction methods, the classification methods draw more upon signal processing theories such as machine learning and statistical signal processing. It has been of interest how each of these two steps impact on estimation accuracy. On one hand, the feature extraction

TABLE 1: EEG correlates of emotion.

Authors	Year	#subjects	Stimulus (duration)	#EEG channels	Channel location	Emotional state	EEG features	Effects
Davidson et al. [48]	1990	37	Emotional film clips (60 sec)	8	F3, F4, C3, C4, T3, T4, P3, and P4	Happiness, disgust	Alpha power	Left-frontal: happiness < disgust; Right-frontal: happiness > disgust; Left-anterior temporal: happiness < disgust; Right-anterior temporal: happiness > disgust
Aftanas et al. [54]	2001	22	IAPS (7 sec)	128	IS	Valence (+/−)	Theta power (ERD/ERS)	Anterior temporal region (left-hemisphere); Negative: left < right; Positive: left > right; Parietotemporal region; Negative: left < right; Positive: left < right
Keil et al. [51]	2001	10	IAPS (1 sec)	128	IS	Arousal	Gamma power	Gamma power (46–65 Hz, 500 ms): arousing ↑
Kemp et al. [104]	2002	16	IAPS (13 Hz)	64	IS	Valence (+/−)	SSVEP amplitude	Negative: SSVEP ↓ at the bilateral anterior frontal area
Pollatos et al. [105]	2005	44	IAPS (6 sec)	61	IS	Arousal	ERP/ECG	Good heartbeat perceivers show higher P300 peak
Balconi and Lucchiari [18]	2006	20	Ekman's picture set (500 ms)	14	Fz, Cz, Pz, Oz, F3, F4, C3, C4, T3, T4, P3, P4, O1, and O2	Neutral versus emotions (happy, sad, angry, and fearful)	ERD (alpha, beta, delta, and theta)	ERD% of theta (150–250 ms) at the anterior regions; Emotional state > neutral state
Baumgartner et al. [106]	2006	24	IAPS + music (16 pictures/4.375 s)	16	F7, F3, FT7, FC3, F4, F8, FC4, FT8, TP7, CP3, P7, P3, CP4, TP8, P4, and P8	Happiness, sadness, and fear	Alpha power	Combining music with pictures evokes more intensive emotional experience
Sammler et al. [55]	2007	18	Music (22–44 sec)	63	IS	Valence (+/−)	Theta power	Frontal midline theta power is increased by positive emotion
Balconi and Mazza [47]	2009	19	Ekman's picture set (30 ms, 200 ms)	32	IS	Anger, fear, surprise, disgust, and happiness	Alpha power (ERD)	Right-frontal activity increase for negative emotions
Li and Lu [107]	2009	10	Picture (6 sec)	62	IS	Happiness, sadness	Gamma ERD	Gamma ERD for emotional stimuli
Petrantonakis and Hadjileontiadis [70]	2010	16	Ekman's picture set	3	Fp1, Fp2, and F3/F4 (bipolar)	Happiness, sadness, surprise, anger, fear, and disgust	Alpha and beta power	Higher-order crossing index improves performance
Lithari et al. [108]	2010	28	IAPS (2 sec)	19	IS	Arousal	ERP (N100, N200)	ERP peaks increase for unpleasant stimuli in female
Petrantonakis [69]	2011	16	IAPS (5 sec)	8	F3, F4, C3, C4, T3, T4, P3, P4	Arousal/valence	Alpha and beta power	Asymmetry index can detect arousal levels

TABLE 1: Continued.

Authors	Year	#subjects	Stimulus (duration)	#EEG channels	Channel location	Emotional state	EEG features	Effects
Park et al. [109]	2011	34	Video: comic, horror, sadness, and peaceful (10 min)	32	IS	Fear, sadness, peace, and happiness	Alpha, beta, and gamma	Fear emotion: beta wave ↑ at the left temporal lobe happy emotion: alpha wave ↓ at the C4 peaceful state: gamma wave ↑ at the T5, alpha wave ↓ at the CP5 Sadness emotion: alpha wave ↓ at the left temporal lobe
Degabriele et al. [110]	2011	18	Emotional go/no-go inhibition task (300 ms)	24	IS	Happiness, sadness	ERP (P100 and N170)	P100 amplitude: happiness > sadness N170 amplitude: bipolar disorder is less at all emotional state than normal subjects

seems to be more closely tied to estimation performance since without pointing to the very features correlated with emotion, it is implausible to build a correct model. On the other hand, the classification algorithms should also be carefully designed to fit to the characteristics of the feature space; for instance, using a linear classifier for highly nonlinear feature structures would not make much sense. In general, one should weigh coherence between a feature space and a classifier for increasing estimation accuracy.

3.1. Feature Extraction Methods. As for valence-related features, it has been shown that positive and negative emotions induce asymmetric modulations in the frontal alpha power of EEG, leading to a relative decrease in the left frontal alpha power for positive emotions and a decrease in the right for negative emotions [65]. This frontal alpha asymmetry provides an effective index for valence by computing a difference between the left and right alpha powers, here denoted as L and R respectively, divided by the sum of both:

$$\text{Index} = \frac{L - R}{L + R}. \tag{1}$$

The computation of the spectral power in the alpha band has been executed by a number of methods, including the squares of the EEG amplitude filtered through an alpha bandpass filter [53], Fourier transform [66], power spectral density [18, 21], and wavelet transform [7, 67, 68]. Most of these methods are well established and can readily be implemented in real time.

As for arousal-related features, one can extract the spectral power features such as the frontal midline theta power similar to the alpha power. Recently, more advanced computational methods have been proposed to evaluate emotional arousal. For instance, Asymmetry index (AsI) assesses emotion elicitation by computing a multidimensional directed information (MDI) between EEG channels [69]:

$$S_n = S_n^{XY} + S_n^{YX},$$
$$S_f = S_f^{XY} + S_f^{YX}, \tag{2}$$
$$\text{AsI} = \left(S_n - S_f\right) \times \frac{\sqrt{2}}{2}.$$

S_f^{XY} indicates the total amount of information flowing from left hemisphere signals, X, to right hemisphere signals, Y, when the subject has emotional feelings. S_f refers to the total bidirectional information with emotion. S_n^{XY} indicates the same directional information from X to Y but when the subject does not have emotional feelings, and S_n refers to the total bidirectional information without emotion. AsI can effectively indicate whether an emotional state is elicited or not [69]. Besides AsI, the variance of potentials from a specific channel over different EEG channels has been used as an emotion-related feature [68]. Also, the entropy of EEG signals has been used to extract information related to emotion from intrusive noise [68].

As for individual discrete emotions, a typical approach is to search through all the possible EEG channels, spectral bands, and time segments for a set of features that

maximizes the accuracy of emotional state estimation. This approach adopts a greedy search method with supervised learning, often resulting in different optimal feature sets for each individual. To overcome this issue of subject-by-subject variability, a higher order crossing (HOC) analysis was developed to implement a user-independent emotion recognition system [70]. The HOC analysis aims to find EEG features with respect to six affective traits, including surprise, disgust, anger, fear, happiness, and sadness [70]. The HOC model is given as:

$$D_n = \sum_{i=2}^{m} \left(X_i[n] - X_{i-1}[n]\right)^2,$$
$$i = 1, \ldots, m; \quad n = 1, 2, 3, \ldots, \tag{3}$$
$$FV_{\text{HOC}} = [D_1, D_2, \ldots, D_L], \quad 1 < L \le \text{Maximum order}.$$

D_n is the simplified version of the HOC feature that counts the number of zero-crossing from a high-pass filtered, standardized EEG time series. Zero-crossing indicates an event at which the signal amplitude passed through a zero-line with the change of polarity. The zero-crossing counts often represent oscillation properties more robustly than the spectral power. A vector of the simple HOCs is constructed to contain the features related to emotion. A higher value of n means decreases in the discrimination power of the simple HOC because different processes can yield almost the same D_n. $X_i[n]$ indicates a binary time series with zeros and ones: at time instant i where $X_i[n] = 0$ if the amplitude of the filtered signal is negative and $X_i[n] = 1$ otherwise. m indicates the length of the time series X_i. The EEG feature vector is defined as FV_{HOC} that consists of multiple simple HOCs [70]. The computational methods to extract emotional features from EEG are summarized in Table 2.

3.2. Emotion Classification Methods. The EEG feature vector provides observations from which an emotional state can be inferred. Commonly, a classifier has been used for decoding the feature vector into one of possible emotional states. A number of classification methods have been used for emotional state estimation, including discriminant analysis (DA), support vector machine (SVM), k-nearest neighbor (k-NN), and the Mahalanobis distance (MD) based method. DA performs dimensionality reduction in a high-dimensional feature space onto a low-dimensional space with an aim to maximize the Fisher discriminant ratio, S, of between-class scatter, C_B, to within-class scatter, C_W, [42, 71–76].

$$S = \text{tr}\left(C_B C_W^{-1}\right). \tag{4}$$

A larger S value indicates greater separation between classes. The dimensionality of the low-dimensional space varies from one up to the number of classes minus one.

SVM is derived from DA but determines a decision boundary in a kernel space instead of the original feature space. SVM finds an optimal hyperplane, $H(x)$, and the hypermargin of the decision boundary in the feature space

Table 2: Emotional state estimation model.

Author	Year	Stimulus (duration)	#channels	Channel location	Emotional states	EEG features	Feature extraction methods	Classifier	Accuracy (%)/#classes	Online versus offline
Li and Lu [107]	2009	Picture (6 sec)	62	IS	Happiness, sadness	Gamma ERD	CSP	SVM	93.5/2	Offline
Murugappan et al. [81]	2010	Video (−)	62	IS	Happiness, surprise, fear, disgust, and neutral	Delta, theta, alpha, beta, and gamma	Wavelet transform	kNN, LDA	83.04/5 (62 channels) 79.17/5 (24 channels)	Offline
Lin et al. [111]	2010	Music (30 sec)	24	Fp1-Fp2, F7-F8, F3-F4, FT7-FT8, FC3-FC4, T7-T8, P7-P8, C3-C4, TP7-TP8, CP3-CP4, P3-P4, O1-O2 (bipolar)	Joy, anger, sadness, and pleasure	Delta, theta, alpha, beta, and gamma	Short-time Fourier transform	SVM	82.29/4	Offline
Petrantonakis and Hadjileontiadis [70]	2010	Ekman's picture set (−)	3	Fp1, Fp2, F3/F4 (bipolar)	Happiness, sadness, surprise, anger, fear, and disgust	ERD/ERS	Higher-order crossing	QDA SVM	62.3/6 (QDA) 83.33/6 (SVM)	Offline
Hosseini et al. [112]	2010	IAPS (3 sec)	5	FP1, FP2, T3, T4, Pz	Calm-neutral, negative-excited	Delta, theta, alpha, beta, and gamma	Wavelet coefficients, Higuchi's algorithm	Elman ANN	82.7/2	Offline
Wang et al. [113]	2011	Video (4 min)	62	IS	Joy, relax, sad, and fear	Alpha, beta, and gamma	Minimum redundancy maximum relevance method	SVM	66.5/4	Offline
Brown et al. [24]	2011	IAPS (6 sec)	8	Fp1, Fp2, F3, F4, F7, F8, C3, C4	Positive, negative, and neutral	Alpha1 (6–8 Hz), Alpha2 (8–10 Hz), Alpha3 (10–12 Hz)	Spectral power features	kNN	85.0/3	Online
Petrantonakis [69]	2011	IAPS (5 sec)	8	F3, F4, C3, C4, T3, T4, P3, P4	Arousal, valence	Alpha and beta power	Asymmetry index	SVM	94.4/2	Offline
Stelios and Hadjidimitriou [114]	2012	Music (60 sec)	14	AF3, F7, F3, FC5, T7, P7, O1, O2, P8, T8, FC6, F4, F8, AF4	Arousal, neutral	Beta and gamma	Time-frequency (TF) analysis	SVM KNN QDA MDA	86.52/2	Offline
Konstantinidis et al. [22]	2012	IAPS (2D emotional space)	19	IS	Arousal, valence	ERP (N100, N200)	Amplitude of ERP	SVM	81.3/4	Online

(i) SVM: support vector machine; kNN: k-nearest neighbor; LDA: linear discriminant analysis; QDA: quadratic discriminant analysis; MDA: Mahalanobis distance based discriminant analysis; SOM: self-organization map; ANN: artificial neural networks.
(ii) IS: channel configuration followed the 10/20 International System.

using a supervised learning method. The classifier $u(x_i)$ classifies a new input feature vector x_j using a classification rule given by

$$u(x_i) = \text{sgn}\left(\sum_{x_i \in \mathbf{v}} \alpha_i t_i F(x_i, x_j) + b\right), \quad t_i \in \text{target space.} \tag{5}$$

Here, $\mathbf{v}$ indicates a set of the support vectors that are used to determine the maximum margin hyperplane, and $F(x_i, x_j)$ denotes the kernel function of the SVM classifier. b denotes an offset parameter, x_i does training input vectors, and α_i does nonzero weights on each support vector [7, 77–80]. Various kernel functions have been proposed such as the Gaussian function or polynomials. SVM offers advantages of good generalizability for nonlinear feature spaces.

The k-NN algorithm determines the class of a new feature vector according to the number of nearest vectors in the training set surrounding a new feature vector [73, 81]. k is a parameter determining the encircled boundary. The k-NN algorithm depends on how to define a distance between feature vectors, which is subject to be affected by the curse of dimensionality [81, 82].

The MD-based method, has been widely used in the clustering analysis, not only for distance, but also with correlation coefficient and the standard deviation [83, 84]:

$$\text{MD} = (\mathbf{x} - \boldsymbol{\mu}_c)^T \mathbf{C}_c^{-1} (\mathbf{x} - \boldsymbol{\mu}_c). \tag{6}$$

$\mathbf{C}^{-1}$ and $\boldsymbol{\mu}_c$ indicate the inverse of the covariance matrix and the mean vector of a class c, respectively. MD converges to Euclidean distance when the covariance matrix of feature vectors becomes the identify matrix [84]. Basically, when a new feature vector arrives, the MD-based classifier compares the distance of the vector to each class using MD and chooses the class with the smallest distance. The classification methods that have been used for emotional state estimation are summarized in Table 2.

4. A Generative Model for Online Tracking of Emotional States

As described earlier, most computational models estimating emotional states have focused on the discrete state space and classified EEG features into one of a finite number of emotional states. This approach generally suits well to the case of a static determination of which emotion is induced by a given stimulus. Yet, for the development of an online emotion recognition system, where continuous tracking of the emotional state may play an important role, the current approach might be suboptimal because they do not take temporal dynamics of the emotional state into account. Another downside of the current approach originates from their direct modeling framework. A model in this framework builds a direct input-output mapping from the observed EEG signal to the emotional state. Although this framework may be able to provide a reasonable solution just for the purpose of improving classification accuracy, it does not exploit prior

information of the emotional state as well as dynamics of the emotional state. These shortcomings make it difficult to gain useful insights on the neural mechanism of emotion. Also, it is often desirable to incorporate prior information of the dynamics of the emotional state within a model, especially for tracking emotional state continuously over time.

To address these issues, we propose a computational modeling approach based on the generative modeling framework [85–87]. Our approach focuses on tracking the change of the emotional state over time from EEG signal. In this approach, a generative model depicts how EEG signal is generated from a hidden emotional state. Also, a prior model explains how the emotional state changes over time. Integrating these two models, we infer a most likely emotional state from an observed EEG signal. Differences between the generative and direct models can be illustrated in a probabilistic view where a goal is to estimate a conditional probability of emotional state variables given EEG observations as accurately as possible. Suppose that a random vector $\mathbf{x}$ denotes hidden emotional states and a random vector $\mathbf{y}$ denotes observed EEG data (e.g., an EEG feature vector). An estimation model aims to optimize a parameter set, θ, for the following conditional probability:

$$p(\mathbf{x} \mid \mathbf{y}, \theta). \tag{7}$$

A direct model forms a functional relationship from $\mathbf{y}$ to $\mathbf{x}$ with θ, the parameter set of a function $f(\cdot)$,

$$\mathbf{x} = f(\mathbf{y}; \theta) + \mathbf{e}, \tag{8}$$

where $\mathbf{e}$ is a residual vector. In many cases, the residual vector is assumed to follow the Gaussian distribution. Parameter estimation of θ can be accomplished by many standard solutions such as maximum likelihood [88]. On the other hand, a generative model uses maximum a posteriori (MAP) or the Bayesian inference to estimate the conditional probability,

$$p(\mathbf{x} \mid \mathbf{y}, \theta) = \frac{1}{D} p(\mathbf{y} \mid \mathbf{x}, \theta) p(\mathbf{x}), \tag{9}$$

where D represents a constant representing the integral of $p(\mathbf{y})$. The posterior $p(\mathbf{x} \mid \mathbf{y}, \theta)$ is estimated by the product of $p(\mathbf{y} \mid \mathbf{x}, \theta)$, the likelihood of observation $\mathbf{y}$ given a state $\mathbf{x}$, and $p(\mathbf{x})$, the prior of the state $\mathbf{x}$. The parameter set θ is used to model a generative relation from $\mathbf{x}$ to $\mathbf{y}$. In terms of the EEG correlate of the emotional state, the likelihood describes how the observed EEG signal is generated from an emotional state, the prior describes a probability of each emotional state, and the posterior describes which emotional state most likely elicits the observed EEG signal.

Here, we extend this generative approach to take into account the temporal dynamics of the emotional state. We use sequential Bayesian inference to track a time-varying emotional state from EEG signal [89]. To this end, we first assume that the emotional state is defined in a continuous space. An example of a continuous state space consists of two emotional dimensions, such as valence and arousal. The valence dimension ranges from negative values to positive values. The arousal dimension ranges from low to high

arousal levels. A key point is that an emotional state varies over a continuous space, instead of altering between discrete values. This does not mean that we need to assign an explicit emotion to every possible point in the emotional state space. A specific area or volume in the state space can represent a single emotion.

The generative model is then formulated as follows. Let $\mathbf{x}_t$ be an emotional state vector and $\mathbf{y}_t$ an EEG signal vector at time instant t. $\mathbf{x}_t$ contains a set of emotional state variables (e.g., $\mathbf{x}_t = [x_{1,t}, x_{2,t}, x_{3,t}]$, where $x_{1,t}$ is the valence dimension, $x_{2,t}$ is the arousal dimension, and $x_{3,t}$ is the dominance dimension). $\mathbf{y}_t$ contains a set of EEG features selected to be related to emotion (e.g., the power of certain frequency band at a selected channel). The goal of the model is to find the most probable emotional state given a series of observation from the beginning, $\mathbf{y}_1, \ldots, \mathbf{y}_t$ (assuming observation begins at $t = 1$). The posterior is formed as

$$p\left(\mathbf{x}_t \mid \mathbf{y}_1, \ldots \mathbf{y}_t\right). \tag{10}$$

The posterior can be rewritten as a recursive equation,

$$
\begin{aligned}
&p\left(\mathbf{x}_t \mid \mathbf{y}_1, \ldots, \mathbf{y}_t\right) \\
&= p\left(\mathbf{y}_t \mid \mathbf{x}_t\right) \int p\left(\mathbf{x}_t \mid \mathbf{x}_{t-1}\right) p\left(\mathbf{x}_{t-1} \mid \mathbf{y}_t, \ldots, \mathbf{y}_{t-1}\right) d\mathbf{x}_{t-1}.
\end{aligned}
\tag{11}
$$

Note that the likelihood, $p(\mathbf{y}_t \mid \mathbf{x}_t)$, depends only on the current time t. The prior, $p(\mathbf{x}_t \mid \mathbf{y}_{t-1})$, represents state transition from $t - 1$ to t, assuming the first-order Markov process. The dynamics of emotional state is embedded in the prior, whereas the generative process of the EEG features from an emotional state is modeled by the likelihood. The integral can be approximately computed by a number of methods with different model assumptions [89].

As this approximation relies on the recursion of the posterior, inference of an emotional state from EEG signal operates sequentially over time. This property enables our model fit well to the purpose of tracking emotional states continuously. In fact, the sequential Bayesian inference model (or called a Bayesian filter) has been widely adopted for many neuroengineering studies (e.g., see [90–94]). Our model may provide an effective way for online emotion aware computing, especially when we need to keep track of changes in the emotional state from EEG measurements continuously over time, for instance, tracking emotional changes while a subject is watching movies [95].

5. Discussion

In this paper, we overviewed the computational methods used for emotional state estimation. We first briefly gave an overview of the EEG correlates of emotion. Then, we revisited the computational methods to extract EEG features correlated with the continuous and discrete emotional states. We also described the classification methods to discriminate a particular emotional state from EEG features. Finally, we proposed a computational approach based on the generative modeling framework that may suit well to tracking the emotional state over time. These computational methods for emotional state estimation will serve as a key element for practical online emotion recognition systems for affective computing.

While affective computing has attracted attentions in the HCI field with a promise to develop a novel user interface, the development of the computational methods to estimate the emotional state still requires further understanding of emotion processes and their neurophysiologic substrates [96]. Especially, the estimation of emotional states from the human EEG has been posed only as a relatively simple classification problem with a few discrete emotions. The development of a real-time emotional state tracking system would require a more rigorous definition of the emotional state space suitable for estimation models.

Exploration of the EEG signatures of emotion that can span a broad area of the emotional state space or represent a number of different discrete emotions should continue. Such investigations may need to overcome many existing challenges. In particular, finding such EEG signatures of emotion that are invariant across individuals will be important for general emotion recognition systems [69]. As the emotion-related features have been mostly found in the frontal EEG signal, online algorithms to overcome the eye movement artifact should be continuously developed [97–99]. Also, bringing the EEG-based emotion recognition system out to the normal users would require a simple yet efficient EEG sensor. A new EEG sensor should meet some criteria such as stabilization of a signal to noise ratio (SNR), reduction of noise elicited from hair, optimization of active dry electrodes, development of multi-channel wireless communication, and sustainment of the quality of EEG signals over a long period [100–103]. Many previous studies have estimated the emotional state by analyzing the EEG responding to specific emotional stimuli. However, this emotion-induction paradigm has a limitation that the EEG signals can be modulated by the stimulus properties irrelevant to emotion [21]. Hence, a computational model that can predict the emotional state with various stimuli may be required for real-world applications.

The computational methods to estimate the emotional state may improve further with several advances in computational models. First, a model that can associate the dynamics of EEG signal with the dynamics of cognitive emotional process will provide a basis for constructing a novel emotional state estimation method. The current methods only capture the static properties in the EEG pattern in response to emotional stimuli. If a new model can embrace the temporal dynamics of emotional information processing in the human cognitive system and find EEG correlates of those dynamical properties, it will estimate the emotional state more precisely. Second, the quest for novel EEG signatures of the emotional state should be pursued. In particular, interactive properties between EEG signals such as cross-frequency coupling and effective connectivity pattern may be worth exploring to find novel EEG correlates of emotion. Third, inference of emotion-related information from high-dimensional and nonlinear EEG data poses an interesting problem to develop and apply the state-of-the-art

machine learning algorithms. So far, only a few basic learning algorithms have been applied for emotional state estimation, but it is likely that emotion recognition would benefit from more advanced statistical learning and pattern recognition algorithms. With these advances, we foresee that the computational models of emotional estimation would play a key role in future consumer devices. Before long, they can bring serendipity to device users by estimating emotional states in a natural and nonintrusive way.

Conflict of Interests

The authors declare that there is no conflict of interests.

Acknowledgments

References

[1] K. R. Scherer, "What are emotions? and how can they be measured?" *Social Science Information*, vol. 44, no. 4, pp. 695–729, 2005.

[2] L. F. Barrett, "Discrete emotions or dimensions? the role of valence focus and arousal focus," *Cognition and Emotion*, vol. 12, no. 4, pp. 579–599, 1998.

[3] I. B. Mauss and M. D. Robinson, "Measures of emotion: a review," *Cognition and Emotion*, vol. 23, no. 2, pp. 209–237, 2009.

[4] M. L. Phillips, W. C. Drevets, S. L. Rauch, and R. Lane, "Neurobiology of emotion perception II: implications for major psychiatric disorders," *Biological Psychiatry*, vol. 54, no. 5, pp. 515–528, 2003.

[5] M. L. Phillips, W. C. Drevets, S. L. Rauch, and R. Lane, "Neurobiology of emotion perception I: the neural basis of normal emotion perception," *Biological Psychiatry*, vol. 54, no. 5, pp. 504–514, 2003.

[6] A. Luneski, E. Konstantinidis, and P. D. Bamidis, "Affective medicine: a review of affective computing efforts in medical informatics," *Methods of Information in Medicine*, vol. 49, no. 3, pp. 207–218, 2010.

[7] C. A. Frantzidis, C. Bratsas, C. L. Papadelis, E. Konstantinidis, C. Pappas, and P. D. Bamidis, "Toward emotion aware computing: an integrated approach using multichannel neurophysiological recordings and affective visual stimuli," *IEEE Transactions on Information Technology in Biomedicine*, vol. 14, no. 3, pp. 589–597, 2010.

[8] M. D. Robinson and G. L. Clore, "Belief and feeling: evidence for an accessibility model of emotional self-report," *Psychological Bulletin*, vol. 128, no. 6, pp. 934–960, 2002.

[9] B. N. Cuthbert, M. M. Bradley, and P. J. Lang, "Fear and anxiety: theoretical distinction and clinical test," *Psychophysiology*, vol. 33, supplement 1, pp. S15–S15, 1996.

[10] R. Adolphs, "Neural systems for recognizing emotion," *Current Opinion in Neurobiology*, vol. 12, no. 2, pp. 169–177, 2002.

[11] I. C. Christie and B. H. Friedman, "Autonomic specificity of discrete emotion and dimensions of affective space: a multivariate approach," *International Journal of Psychophysiology*, vol. 51, no. 2, pp. 143–153, 2004.

[12] J. Panksepp, "Neuro-psychoanalysis may enliven the mindbrain sciences," *Cortex*, vol. 43, no. 8, pp. 1106–1107, 2007.

[13] K. Vytal and S. Hamann, "Neuroimaging support for discrete neural correlates of basic emotions: a voxel-based meta-analysis," *Journal of Cognitive Neuroscience*, vol. 22, no. 12, pp. 2864–2885, 2010.

[14] P. Peyk, H. T. Schupp, T. Elbert, and M. Junghöfer, "Emotion processing in the visual brain: a MEG analysis," *Brain Topography*, vol. 20, no. 4, pp. 205–215, 2008.

[15] M. Hämäläinen, R. Hari, R. J. Ilmoniemi, J. Knuutila, and O. V. Lounasmaa, "Magnetoencephalography—theory, instrumentation, and applications to noninvasive studies of the working human brain," *Reviews of Modern Physics*, vol. 65, no. 2, pp. 413–497, 1993.

[16] A. Ray and S. M. Bowyer, "Clinical applications of magnetoencephalography in epilepsy," *Annals of Indian Academy of Neurology*, vol. 13, no. 1, pp. 14–22, 2010.

[17] P. R. Davidson, R. D. Jones, and M. T. Peiris, "EEG-based lapse detection with high temporal resolution," *IEEE Transactions on Biomedical Engineering*, vol. 54, no. 5, pp. 832–839, 2007.

[18] M. Balconi and C. Lucchiari, "EEG correlates (event-related desynchronization) of emotional face elaboration: a temporal analysis," *Neuroscience Letters*, vol. 392, no. 1-2, pp. 118–123, 2006.

[19] M. Balconi and U. Pozzoli, "Event-related oscillations (ERO) and event-related potentials (ERP) in emotional face recognition," *International Journal of Neuroscience*, vol. 118, no. 10, pp. 1412–1424, 2008.

[20] A. A. Beaton, N. C. Fouquet, N. C. Maycock, E. Platt, L. S. Payne, and A. Derrett, "Processing emotion from the eyes: a divided visual field and ERP study," *Laterality*, vol. 17, no. 4, pp. 486–514, 2012.

[21] M. Y. Bekkedal, J. Rossi III, and J. Panksepp, "Human brain EEG indices of emotions: delineating responses to affective vocalizations by measuring frontal theta event-related synchronization," *Neuroscience & Biobehavioral Reviews*, vol. 35, no. 9, pp. 1959–1970, 2011.

[22] E. I. Konstantinidis, C. A. Frantzidis, C. Pappas, and P. D. Bamidis, "Real time emotion aware applications: a case study employing emotion evocative pictures and neuro-physiological sensing enhanced by Graphic Processor Units," *Computer Methods and Programs in Biomedicine*, vol. 107, no. 1, pp. 16–27, 2012.

[23] O. Sourina and Y. Liu, "A fractal-based algorithm of emotion recognition from EEG using arousal-valence model," in *Proceedings of the International Conference on Bio-Inspired Systems and Signal Processing (BIOSIGNALS '11)*, pp. 209–214, Rome, Italy, January 2011.

[24] L. Brown, B. Grundlehner, and J. Penders, "Towards wireless emotional valence detection from EEG," *IEEE Engineering in Medicine and Biology Society*, vol. 2011, pp. 2188–2191, 2011.

[25] J. A. Russell, "Core affect and the psychological construction of emotion," *Psychological Review*, vol. 110, no. 1, pp. 145–172, 2003.

[26] E. S. Schaefer, "A circumplex model for maternal behavior," *Journal of Abnormal and Social Psychology*, vol. 59, no. 2, pp. 226–235, 1959.

[27] A. Mehrabian, *Basic Dimensions for a General Psychological Theory :Implications for Personality, Social, Environmental, and Developmental Studies*, Oelgeschlager, Gunn & Hain, Cambridge, UK, 1980.

[28] J. R. Fontaine, K. R. Scherer, E. B. Roesch, and P. C. Ellsworth, "The world of emotions is not two-dimensional," *Psychological Science*, vol. 18, no. 12, pp. 1050–1057, 2007.

[29] S. Hamann, "Mapping discrete and dimensional emotions onto the brain: controversies and consensus," *Trends in Cognitive Sciences*, vol. 16, no. 9, pp. 458–466, 2012.

[30] D. C. Rubin and J. M. Talarico, "A comparison of dimensional models of emotion: evidence from emotions, prototypical events, autobiographical memories, and words," *Memory*, vol. 17, no. 8, pp. 802–808, 2009.

[31] J. A. Mikels, B. L. Fredrickson, G. R. Larkin, C. M. Lindberg, S. J. Maglio, and P. A. Reuter-Lorenz, "Emotional category data on images from the international affective picture system," *Behavior Research Methods*, vol. 37, no. 4, pp. 626–630, 2005.

[32] J. Redondo, I. Fraga, I. Padrón, and A. Piñeiro, "Affective ratings of sound stimuli," *Behavior Research Methods*, vol. 40, no. 3, pp. 784–790, 2008.

[33] R. L. Ribeiro, S. Pompéia, and O. F. Amodeo Bueno, "Comparison of Brazilian and American norms for the International Affective Picture System (IAPS)," *Revista Brasileira de Psiquiatria*, vol. 27, no. 3, pp. 208–215, 2005.

[34] J. K. Olofsson, S. Nordin, H. Sequeira, and J. Polich, "Affective picture processing: an integrative review of ERP findings," *Biological Psychology*, vol. 77, no. 3, pp. 247–265, 2008.

[35] M. Codispoti, V. Ferrari, and M. M. Bradley, "Repetition and event-related potentials: distinguishing early and late processes in affective picture perception," *Journal of Cognitive Neuroscience*, vol. 19, no. 4, pp. 577–586, 2007.

[36] J. K. Olofsson and J. Polich, "Affective visual event-related potentials: arousal, repetition, and time-on-task," *Biological Psychology*, vol. 75, no. 1, pp. 101–108, 2007.

[37] L. R. R. Gianotti, P. L. Faber, M. Schuler, R. D. Pascual-Marqui, K. Kochi, and D. Lehmann, "First valence, then arousal: the temporal dynamics of brain electric activity evoked by emotional stimuli," *Brain Topography*, vol. 20, no. 3, pp. 143–156, 2008.

[38] E. Bernat, S. Bunce, and H. Shevrin, "Event-related brain potentials differentiate positive and negative mood adjectives during both supraliminal and subliminal visual processing," *International Journal of Psychophysiology*, vol. 42, no. 1, pp. 11–34, 2001.

[39] B. N. Cuthbert, H. T. Schupp, M. M. Bradley, N. Birbaumer, and P. J. Lang, "Brain potentials in affective picture processing: covariation with autonomic arousal and affective report," *Biological Psychology*, vol. 52, no. 2, pp. 95–111, 2000.

[40] R. Roschmann and W. Wittling, "Topographic brain mapping of emotion-related hemisphere asymmetries," *International Journal of Neuroscience*, vol. 63, no. 1-2, pp. 5–16, 1992.

[41] C. M. Yee and G. A. Miller, "Affective valence and information processing," *Electroencephalography and Clinical Neurophysiology*, vol. 40, pp. 300–307, 1987.

[42] B. Blankertz, S. Lemm, M. Treder, S. Haufe, and K. R. Müller, "Single-trial analysis and classification of ERP components—a tutorial," *NeuroImage*, vol. 56, no. 2, pp. 814–825, 2011.

[43] L. Hu, M. Liang, A. Mouraux, R. G. Wise, Y. Hu, and G. D. Iannetti, "Taking into account latency, amplitude, and morphology: improved estimation of single-trial ERPs by wavelet filtering and multiple linear regression," *Journal of Neurophysiology*, vol. 106, no. 6, pp. 3216–3229, 2011.

[44] M. Ahmadi and R. Quian Quiroga, "Automatic denoising of single-trial evoked potentials," *NeuroImage*, vol. 66, pp. 672–680, 2012.

[45] K. Vanderperren, B. Mijovic, N. Novitskiy et al., "Single trial ERP reading based on parallel factor analysis," *Psychophysiology*, vol. 50, no. 1, pp. 97–110, 2013.

[46] D. Jarchi, S. Sanei, J. C. Principe, and B. Makkiabadi, "A new spatiotemporal filtering method for single-trial estimation of correlated ERP subcomponents," *IEEE Transactions on Biomedical Engineering*, vol. 58, no. 1, pp. 132–143, 2011.

[47] M. Balconi and G. Mazza, "Brain oscillations and BIS/BAS (behavioral inhibition/activation system) effects on processing masked emotional cues. ERS/ERD and coherence measures of alpha band," *International Journal of Psychophysiology*, vol. 74, no. 2, pp. 158–165, 2009.

[48] R. J. Davidson, "Anterior cerebral asymmetry and the nature of emotion," *Brain and Cognition*, vol. 20, no. 1, pp. 125–151, 1992.

[49] I. H. Gotlib, C. Ranganath, and J. P. Rosenfeld, "Frontal EEG alpha asymmetry, depression, and cognitive functioning," *Cognition and Emotion*, vol. 12, no. 3, pp. 449–478, 1998.

[50] M. Balconi and C. Lucchiari, "Consciousness and arousal effects on emotional face processing as revealed by brain oscillations. A gamma band analysis," *International Journal of Psychophysiology*, vol. 67, no. 1, pp. 41–46, 2008.

[51] A. Keil, M. M. Müller, T. Gruber, C. Wienbruch, M. Stolarova, and T. Elbert, "Effects of emotional arousal in the cerebral hemispheres: a study of oscillatory brain activity and event-related potentials," *Clinical Neurophysiology*, vol. 112, no. 11, pp. 2057–2068, 2001.

[52] M. M. Müller, A. Keil, T. Gruber, and T. Elbert, "Processing of affective pictures modulates right-hemispheric gamma band EEG activity," *Clinical Neurophysiology*, vol. 110, no. 11, pp. 1913–1920, 1999.

[53] L. I. Aftanas, N. V. Reva, A. A. Varlamov, S. V. Pavlov, and V. P. Makhnev, "Analysis of evoked EEG synchronization and desynchronization in conditions of emotional activation in humans: temporal and topographic characteristics," *Neuroscience and Behavioral Physiology*, vol. 34, no. 8, pp. 859–867, 2004.

[54] L. I. Aftanas, A. A. Varlamov, S. V. Pavlov, V. P. Makhnev, and N. V. Reva, "Affective picture processing: event-related synchronization within individually defined human theta band is modulated by valence dimension," *Neuroscience Letters*, vol. 303, no. 2, pp. 115–118, 2001.

[55] D. Sammler, M. Grigutsch, T. Fritz, and S. Koelsch, "Music and emotion: electrophysiological correlates of the processing of pleasant and unpleasant music," *Psychophysiology*, vol. 44, no. 2, pp. 293–304, 2007.

[56] M. Wyczesany, S. J. Grzybowski, R. J. Barry, J. Kaiser, A. M. L. Coenen, and A. Potoczek, "Covariation of EEG synchronization and emotional state as modified by anxiolytics," *Journal of Clinical Neurophysiology*, vol. 28, no. 3, pp. 289–296, 2011.

[57] V. Miskovic and L. A. Schmidt, "Cross-regional cortical synchronization during affective image viewing," *Brain Research*, vol. 1362, pp. 102–111, 2010.

[58] N. Martini, D. Menicucci, L. Sebastiani et al., "The dynamics of EEG gamma responses to unpleasant visual stimuli: from local activity to functional connectivity," *NeuroImage*, vol. 60, no. 2, pp. 922–932, 2012.

[59] J. Fell and N. Axmacher, "The role of phase synchronization in memory processes," *Nature Reviews Neuroscience*, vol. 12, no. 2, pp. 105–118, 2011.

[60] P. Sauseng and W. Klimesch, "What does phase information of oscillatory brain activity tell us about cognitive processes?" *Neuroscience and Biobehavioral Reviews*, vol. 32, no. 5, pp. 1001–1013, 2008.

[61] P. Fries, "Neuronal gamma-band synchronization as a fundamental process in cortical computation," *Annual Review of Neuroscience*, vol. 32, pp. 209–224, 2009.

[62] S. Pockett and M. D. Holmes, "Intracranial EEG power spectra and phase synchrony during consciousness and unconsciousness," *Consciousness and Cognition*, vol. 18, no. 4, pp. 1049–1055, 2009.

[63] L. Melloni, C. Molina, M. Pena, D. Torres, W. Singer, and E. Rodriguez, "Synchronization of neural activity across cortical areas correlates with conscious perception," *Journal of Neuroscience*, vol. 27, no. 11, pp. 2858–2865, 2007.

[64] S. M. Doesburg, A. B. Roggeveen, K. Kitajo, and L. M. Ward, "Large-scale gamma-band phase synchronization and selective attention," *Cerebral Cortex*, vol. 18, no. 2, pp. 386–396, 2008.

[65] A. J. Tomarken, R. J. Davidson, and J. B. Henriques, "Resting frontal brain asymmetry predicts affective responses to films," *Journal of Personality and Social Psychology*, vol. 59, no. 4, pp. 791–801, 1990.

[66] B. Güntekin and E. Basar, "Emotional face expressions are differentiated with brain oscillations," *International Journal of Psychophysiology*, vol. 64, no. 1, pp. 91–100, 2007.

[67] E. Gross, A. S. El-Baz, G. E. Sokhadze, L. Sears, M. F. Casanova, and E. M. Sokhadze, "Induced eeg gamma oscillation alignment improves differentiation between autism and adhd group responses in a facial categorization task," *Journal of Neurotherapy*, vol. 16, no. 2, pp. 78–91, 2012.

[68] M. Murugappan, R. Nagarajan, and S. Yaacob, "Combining spatial filtering and wavelet transform for classifying human emotions using EEG Signals," *Journal of Medical and Biological Engineering*, vol. 31, no. 1, pp. 45–51, 2011.

[69] L. J. H. Panagiotis C. Petrantonakis, "A novel emotion elicitation index using frontal brain asymmetry for enhanced EEG-based emotion recognition," *IEEE Transactions on Information Technology in Biomedicine*, vol. 15, no. 5, pp. 737–746, 2011.

[70] P. C. Petrantonakis and L. J. Hadjileontiadis, "Emotion recognition from EEG using higher order crossings," *IEEE Transactions on Information Technology in Biomedicine*, vol. 14, no. 2, pp. 186–197, 2010.

[71] C. Bandt, M. Weymar, D. Samaga, and A. O. Hamm, "A simple classification tool for single-trial analysis of ERP components," *Psychophysiology*, vol. 46, no. 4, pp. 747–757, 2009.

[72] R. L. Horst and E. Donchin, "Beyond averaging. II. Single-trial classification of exogenous event-related potentials using stepwise discriminant analysis," *Electroencephalography and Clinical Neurophysiology*, vol. 48, no. 2, pp. 113–126, 1980.

[73] V. Kolodyazhniy, S. D. Kreibig, J. J. Gross, W. T. Roth, and F. H. Wilhelm, "An affective computing approach to physiological emotion specificity: toward subject-independent and stimulus-independent classification of film-induced emotions," *Psychophysiology*, vol. 48, no. 7, pp. 908–922, 2011.

[74] P. Poolman, R. M. Frank, P. Luu, S. M. Pederson, and D. M. Tucker, "A single-trial analytic framework for EEG analysis and its application to target detection and classification," *NeuroImage*, vol. 42, no. 2, pp. 787–798, 2008.

[75] C. Wang, S. Xiong, X. Hu, L. Yao, and J. Zhang, "Combining features from ERP components in single-trial EEG for discriminating four-category visual objects," *Journal of Neural Engineering*, vol. 9, no. 5, Article ID 056013, 2012.

[76] Y. Zhang, Q. Zhao, J. Jin, X. Wang, and A. Cichocki, "A novel BCI based on ERP components sensitive to configural processing of human faces," *Journal of Neural Engineering*, vol. 9, no. 2, Article ID 026018, 2012.

[77] I. Guler and E. D. Ubeyli, "Multiclass support vector machines for EEG-signals classification," *IEEE Transactions on Information Technology in Biomedicine*, vol. 11, no. 2, pp. 117–126, 2007.

[78] K. Gouizi, F. Bereksi Reguig, and C. Maaoui, "Emotion recognition from physiological signals," *Journal of Medical Engineering & Technology*, vol. 35, no. 6-7, pp. 300–307, 2011.

[79] I. Martisius, R. Damasevicius, V. Jusas, and D. Birvinskas, "Using higher order nonlinear operators for SVM classification of EEG data," *Elektronika ir Elektrotechnika*, vol. 119, no. 3, pp. 99–102, 2012.

[80] L. Guo, Y. Wu, L. Zhao, T. Cao, W. Yan, and X. Shen, "Classification of mental task from EEG signals using immune feature weighted support vector machines," *IEEE Transactions on Magnetics*, vol. 47, no. 5, pp. 866–869, 2011.

[81] M. Murugappan, R. Nagarajan, and S. Yaacob, "Combining spatial filtering and wavelet transform for classifying human emotions using EEG Signals," *Journal of Medical and Biological Engineering*, vol. 31, no. 1, pp. 45–51, 2010.

[82] Md. Rafiul Hassan, M. Marufhossain, J. Bailey, and K. Ramamohanarao, "Improving k-nearest neighbour classification with distance functions based on receiver operating characteristics," in *Proceedings of the 2008 European Conference on Machine Learning and Knowledge Discovery in Databases-Part I*, pp. 489–504.

[83] F. Babiloni, L. Bianchi, F. Semeraro et al., "Mahalanobis distance-based classifiers are able to recognize EEG patterns by using few EEG electrodes," in *Proceedings of the 23rd Annual International Conference of the IEEE Engineering in Medicine and Biology Society*, pp. 651–654, October 2001.

[84] P. C. Mahalanobis, "On the generalized distance in statistics," *Proceedings National Institute of Science, India*, vol. 2, no. 1, pp. 49–55, 1936.

[85] S. M. M. Martens and J. M. Leiva, "A generative model approach for decoding in the visual event-related potential-based brain-computer interface speller," *Journal of Neural Engineering*, vol. 7, no. 2, Article ID 026003, 2010.

[86] M. A. J. van Gerven, F. P. de Lange, and T. Heskes, "Neural decoding with hierarchical generative models," *Neural Computation*, vol. 22, no. 12, pp. 3127–3142, 2010.

[87] K. H. Brodersen, T. M. Schofield, A. P. Leff et al., "Generative embedding for model-based classification of fMRI data," *PLOS Computational Biology*, vol. 7, no. 6, Article ID e1002079, 2011.

[88] C. Kemere, K. V. Shenoy, and T. H. Meng, "Model-based neural decoding of reaching movements: a maximum likelihood approach," *IEEE Transactions on Biomedical Engineering*, vol. 51, no. 6, pp. 925–932, 2004.

[89] M. HB, "Sequential Bayesian Inference," in *Data Fusion: Concepts and Ideas*, pp. 239–272, Springer, 2012.

[90] S. Wu, D. Chen, M. Niranjan, and S. I. Amari, "Sequential Bayesian decoding with a population of neurons," *Neural Computation*, vol. 15, no. 5, pp. 993–1012, 2003.

[91] J. W. Yoon, S. J. Roberts, M. Dyson, and J. Q. Gan, "Adaptive classification for brain computer interface systems using sequential monte carlo sampling," *Neural Networks*, vol. 22, no. 9, pp. 1286–1294, 2009.

[92] Y. Wang, A. R. Paiva, J. C. Príncipe, and J. C. Sanchez, "Sequential Monte Carlo point-process estimation of kinematics from neural spiking activity for brain-machine interfaces," *Neural Computation*, vol. 21, no. 10, pp. 2894–2930, 2009.

[93] A. Sorrentino, L. Parkkonen, A. Pascarella, C. Campi, and M. Piana, "Dynamical MEG source modeling with multi-target

bayesian filtering," *Human Brain Mapping*, vol. 30, no. 6, pp. 1911–1921, 2009.

[94] T. D. Sanger, "Bayesian filtering of myoelectric signals," *Journal of Neurophysiology*, vol. 97, no. 2, pp. 1839–1845, 2007.

[95] D. Nie, X. W. Wang, L. C. Shi, and B. L. Lu, "EEG-based emotion recognition during watching movies," in *Proceedings of the 2011 5th International IEEE/EMBS Conference on Neural Engineering (NER '11)*, pp. 667–670, Cancun, Mexico, May 2011.

[96] E. Cutrell and D. Tan, "BCI for passive input in HCI," in *Proceedings ACM CHI Conference on Human Factors in Computing Systems Workshop on Brain-Computer Interfaces for HCI and Games*, 2007.

[97] J. F. Gao, Y. Yang, P. Lin, P. Wang, and C. X. Zheng, "Automatic removal of eye-movement and blink artifacts from eeg signals," *Brain Topography*, vol. 23, no. 1, pp. 105–114, 2010.

[98] C. A. Joyce, I. F. Gorodnitsky, and M. Kutas, "Automatic removal of eye movement and blink artifacts from EEG data using blind component separation," *Psychophysiology*, vol. 41, no. 2, pp. 313–325, 2004.

[99] S. Romero, M. A. Mañanas, and M. J. Barbanoj, "A comparative study of automatic techniques for ocular artifact reduction in spontaneous EEG signals based on clinical target variables: a simulation case," *Computers in Biology and Medicine*, vol. 38, no. 3, pp. 348–360, 2008.

[100] Y. M. Chi, Y. T. Wang, Y. Wang, C. Maier, T. P. Jung, and G. Cauwenberghs, "Dry and noncontact EEG sensors for mobile brain-computer interfaces," *IEEE Trans Neural Syst Rehabil Eng*, vol. 20, no. 2, pp. 228–235, 2012.

[101] L. D. Liao, I. J. Wang, S. F. Chen, J. Y. Chang, and C. T. Lin, "Design, fabrication and experimental validation of a novel dry-contact sensor for measuring electroencephalography signals without skin preparation," *Sensors*, vol. 11, no. 6, pp. 5819–5834, 2011.

[102] Y. M. Chi, T. P. Jung, and G. Cauwenberghs, "Dry-contact and noncontact biopotential electrodes: methodological review," *IEEE Reviews in Biomedical Engineering*, vol. 3, pp. 106–119, 2010.

[103] C. T. Lin, L. D. Liao, Y. H. Liu, I. J. Wang, B. S. Lin, and J. Y. Chang, "Novel dry polymer foam electrodes for long-term EEG measurement," *IEEE Transactions on Biomedical Engineering*, vol. 58, no. 5, pp. 1200–1207, 2011.

[104] A. H. Kemp, M. A. Gray, P. Eide, R. B. Silberstein, and P. J. Nathan, "Steady-state visually evoked potential topography during processing of emotional valence in healthy subjects," *NeuroImage*, vol. 17, no. 4, pp. 1684–1692, 2002.

[105] O. Pollatos, W. Kirsch, and R. Schandry, "On the relationship between interoceptive awareness, emotional experience, and brain processes," *Cognitive Brain Research*, vol. 25, no. 3, pp. 948–962, 2005.

[106] T. Baumgartner, M. Esslen, and L. Jäncke, "From emotion perception to emotion experience: emotions evoked by pictures and classical music," *International Journal of Psychophysiology*, vol. 60, no. 1, pp. 34–43, 2006.

[107] M. Li and B. L. Lu, "Emotion classification based on gamma-band EEG," *Conference Proceedings: IEEE Engineering in Medicine and Biology Society*, vol. 2009, pp. 1323–1326, 2009.

[108] C. Lithari, C. A. Frantzidis, C. Papadelis et al., "Are females more responsive to emotional stimuli? A neurophysiological study across arousal and valence dimensions," *Brain Topography*, vol. 23, no. 1, pp. 27–40, 2010.

[109] K. S. Park, H. Choi, K. J. Lee, J. Y. Lee, K. O. An, and E. J. Kim, "Emotion recognition based on the asymmetric left and right activation," *International Journal of Medicine and Medical Sciences*, vol. 3, no. 6, pp. 201–209, 2011.

[110] R. Degabriele, J. Lagopoulos, and G. Malhi, "Neural correlates of emotional face processing in bipolar disorder: an event-related potential study," *Journal of Affective Disorders*, vol. 133, no. 1-2, pp. 212–220, 2011.

[111] Y. P. Lin, C. H. Wang, T. P. Jung et al., "EEG-based emotion recognition in music listening," *IEEE Transactions on Biomedical Engineering*, vol. 57, no. 7, pp. 1798–1806, 2010.

[112] S. A. Hosseini, M. A. Khalilzadeh, M. B. Naghibi-Sistani, and V. Niazmand, "Higher order spectra analysis of EEG signals in emotional stress states," in *Proceedings of the 2nd International Conference on Information Technology and Computer Science (ITCS '10)*, pp. 60–63, Kiev, Ukraine, July 2010.

[113] X. W. Wang, D. Nie, and B. L. Lu, "EEG-based emotion recognition using frequency domain features and support vector machines," in *Neural Information Processing*, vol. 7062 of *Lecture Notes in Computer Science*, pp. 734–743, 2011.

[114] K. Stelios and L. J. Hadjidimitriou, "Toward an EEG-based recognition of music liking using time-frequency analysis," *IEEE Transactions on Biomedical Engineering*, vol. 59, no. 12, pp. 3498–3510, 2012.